

A neural probe to sample brain fluid in nanoliter volumes for quantitative molecular studies

Présentée le 11 novembre 2022

Faculté des sciences et techniques de l'ingénieur
Laboratoire de microsystemes 4
Programme doctoral en microsystemes et microélectronique

pour l'obtention du grade de Docteur ès Sciences

par

Joan TEIXIDOR

Acceptée sur proposition du jury

Prof. J. Brugger, président du jury
Prof. Ph. Renaud, Dr A. Bertsch, directeurs de thèse
Prof. C. Pollo, rapporteur
Dr N. Nakatsuka, rapporteuse
Prof. S. Lacour, rapporteuse

Salid y disfrutad.

— Johan Cruyff

A Jean et Hans-Peter.

Acknowledgements

My PhD was an incredible personal and professional journey, and I would like to thank the people who supported me along the way. First, I want to thank Philippe Renaud for all the research opportunities, for sharing his brilliant intuitions, but also for challenging my ideas and for guiding me. I also wish to thank Arnaud Bertsch, for sharing his scientific/life/sports expertise throughout the years. Arnaud was the victim of my keyboard experiments and he helped me improve each manuscript I sent him. I wish to acknowledge Christine Vuichoud, who ensured that the lab business rolled smoothly so that I could simply enjoy doing research. I also wish to thank the members of my jury, Prof. Stéphanie Lacour, Prof. Dr. med. Claudio Pollo, Dr. Nako Nakatsuka, and Prof. Jürgen Brugger who agreed to dedicate their time to reviewing my work and improving it. I also acknowledge Lucie Auberson who coordinated the organization for the doctoral school, as well as my EDMI mentor Prof. Martin Gijs for granting me access to some equipment in his group, but also Prof. Carlotta Guiducci and Prof. François Gallaire who helped me plan this journey during the candidacy exam.

Moreover, I would like to thank Prof. Hilal A. Lashuel for providing the resources to achieve the *in vivo* experiments and for his preciously sharp advice for the paper. Special acknowledgement to Salvatore Novello, who helped with the *in vivo* experiments. All the discussions, regardless of the topic, were a delight. I honestly do not know who will be next crack at Juventus, nor at Barcelona but I will keep our theories in mind. I also wish to thank Johannes Burtscher and Prof. Hubert van den Bergh. Furthermore, I want to thank Laure Menin, Daniel Ortiz and Francisco Sepulveda from the Mass Spectrometry and Elemental Analysis Platform (MSEAP). Laure and Daniel spent a significant amount of time helping me set up these mea-

surements and I am grateful for their dedication, but also for all the discussions we had about research, life, sports, and for their kind support when the clock suggested that the day was far from over.

During my thesis, I was also lucky to have access to multiple EPFL platforms run by experts in many fields. I spent considerable time in clean room at the EPFL Center of MicroNanoTechnology (CMi) and I want to thank all the members of CMi, especially Rémy, Joffrey, Cyrille, Niccoló, Julien, Giovanni, Gatera and Patrick. I also acknowledge the staff of the Proteomics Core Facility for the training on the MALDI-TOF, especially Adrien and Jonathan, as well as the staff of the Center for PhenoGenomics, especially to Vincent, Khaled, and Isabelle, and the staff of the Gene Expression Core Facility. I am also thankful to José Artacho from the Bio Imaging and Optics Platform and the members of the Atelier de Fabrication Additive, the Atelier de Circuits Imprimés, the Atelier de l'Institut des Matériaux and the Atelier de Production et Robotique.

I am grateful for all the scientific feedback, but also for the friendly lunches with the great minds and great friends from the lab, who surrounded me throughout the years. I would like to thank Benoît *Hombre* Desbiolles for the warm integration in the group on day one, but also for your joy and your relentless dedication to helping others reach their goals while surpassing yours. I also want to thank Sébastien Jiguet. You were always there to share you experience, to provide customized SU-8, to teach the handling of chemicals, and to frustrate me at badminton. I also wish to thank Guillaume Petit-Pierre for all the tips that you shared and for bequeathing your office to me and that included a Stefano Varricchio LvL 4 and a Ludovic Serex LvL 2.5 in pretty good condition. Thank you for all the laughs, to Stefano for your sharp graphical eyesight and to Ludo for showing me on how to get things done.

I have also been incredibly lucky to share the office with Clémentine Lipp and Miguel *Not-that-much-of-a-catalan-name-compared-to-me-but-still-an-ok-guy* Solsona for about 3 years. I'm thankful to you, for setting such good vibes, for the thoughtful attentions, and for making me smile behind the mask nearly every day. Friends, you are N.O.I.C.E, or should I say I.N.C.R.O.Y.A-BLES! Special thanks to Clémentine for the awesome holiday/lab visits/road trip to microTAS, for the countless discussions on anything and for all the fun moments, even when you tried to throw a cactus at me. Thank you Nicolas Maïno for your funny and sharp spirit, and your electrochemical knowledge; Margaux Duchamp for our many clean

room discussions and tips to keep moving forward; Albert Leroy for your dedication to the electrochemical chip paper; Nadya Ostromohov for the fun coffee breaks, the ITP tests and the cat stories; Lucas Yerly for spreading the culture from Fribourg "Canton of Dreams" and for your precious help in the lab; Jiande Zhou for laughing at my silly jokes and the sports discussions; William Courbat for your cool spirit on an explosive project; Jonathan Cottet for your friendly advice on navigating academia; Daniel Migliozi for the optics advice; Evgenii Glushkov for your nice spirit and involvement in the lab-EPFL-and-beyond communities; and Fatemeh Navaee for the best X-mas contest cookies. Thank you friends, you made this PhD experience a five-star journey.

And I also want to thank the brilliant start up leaders and scientists at all levels: Elodie Dahan, David Bonzon, Colin Darbellay, Mohammadmatin Behzadi, Silvia Demuru, Patrick Burch, Thamani Dahoun, Marie Vionnet, Marc Boers, Georges Muller, David Forchelet, Marc Heuschkel, Amélie Béduer, Clarisse Vaillier, Thomas Braschler, Antoine Herzog, Martina Genta, Weida Chen, and Harald van Lintel. Special thanks to fellow researchers from the LMIS1, LMIS2, CLSE and other groups, with whom I enjoyed the exchanges, the teaching duties, and the classes. I am also grateful to the students who worked with me: Quentin Wannebroucq, Benjamin Leis, Albert Leroy, William Larsen, Tarek Jabri, and Gabrielle Saint-Girons, who shared the pride when things worked and kept working harder when our goals kept escaping. I hope that I helped you learn even more than you helped me.

I was also well surrounded outside EPFL and I would like to thank Julien, John, Ben, Gabi, Tio, Pierre and Sam, with whom we shared so many passions that work was barely a topic of interest; my football coach Pym; and "les vieux hiboux" Dumuret, Eddy, Cihan, TT, Bob, and the Philippe's for countless epic moments throughout the years. J'aimerais aussi remercier les membres de ma famille pour leur soutien et leur générosité sans fin, particulièrement Minelle et Charly; Valérie et Jean-Luc et leurs sbires qui me servent de cousins; Isa et Pierre; et Cécile et Jean. Je voudrais aussi remercier Ursula et Hans-Peter, qui n'ont eu cesse de me soutenir dans tout, allant même jusqu'à m'envoyer des publications et me conseiller des conférences. Merci aussi à Xavi et Lirón pour leurs divertissants points de vue "out of the box". Je tiens également à remercier mes parents Colette et Laurent, pour votre amour, votre guidance et tout ce que vous m'avez transmis, chacun avec votre sensibilité, pour me mettre dans les meilleures conditions possibles pour toutes les étapes de la vie. Vous êtes des modèles.

Finale­ment, je veux remercier Stephanie, qui m'accompagne dans tous les projets de la vie. Merci pour ton indéfectible soutien et ta compréhension lorsque je passais mon temps derrière mon setup, merci pour les pétales de magie que tu disperses tout autour de toi et merci d'être une telle source de bonheur et d'inspiration. Sous tes yeux pétillants, tu as du cran et tu m'impressionnes.

Lausanne, le 2 juin 2022.

J. T.

Abstract

Neural functions operate in tightly controlled conditions that are mediated by multiple electrical and chemical phenomena. Brain disorders such as Parkinson's Disease and Alzheimer's Disease perturb these conditions and cause a loss of neurons, which impairs the motor and cognitive functions. Thus, an access to the concentration of the neurochemicals in the brain and to their temporal evolution would be an asset to understand these diseases better and develop treatments that could stop their progression and even restore neural functions.

Among the techniques to measure neurochemicals in the brain, fluid sampling approaches such as microdialysis allow the continuous collection of molecules from the extracellular fluid (ECF), by diffusion in a perfusate that can be retrieved and analyzed offline. However, these experiments can be long and the real concentration of the molecules in the ECF cannot be quantified directly from the samples. This thesis aims to propose a solution to these limitations; thus, a new sampling approach called Droplet on Demand (DoD) and a neural probe for it were developed.

The DoD approach is inspired by the theoretical foundations of microdialysis and by the limitations of continuous sampling methods. Thus, it is proposed as a sequential sampling method in steps: a perfusion step to create a pocket of perfusate in the brain, a diffusion step to capture molecules in this pocket, a sampling step to collect the pocket and the molecules in a droplet, and a phase to let the concentration in the ECF equilibrate. This offers a way to collect samples that closely reflect the molecular concentration in the ECF for quantitative molecular studies. Moreover, the DoD can be applied on-demand, to probe the molecules in the ECF at specific experimental times, punctually or repeatedly.

The neural probe was fabricated with polyimide and SU-8 technologies to implement the DoD approach during acute experiments in the brain of mice. It integrates microfluidic channels, droplet-sensing electrodes, and a stimulation electrode in its 320 μm wide and 80 μm thick needle. An optical fiber was also added to it for optical stimulation.

The concepts of the DoD were illustrated in simulations and confirmed in experiments in agarose brain phantoms *in vitro*. They showed that the diffusion time allows tuning the concentration of the molecules collected in the samples, with stable characteristics over repeated sampling events. Acute *in vivo* experiments were also performed in mice and samples of typically 24.4 nL were collected every 1 to 2 minutes, 20 minutes after inserting the probe. The samples were stored in a capillary and an analytical procedure with mass spectrometry was developed to confirm the properties of the DoD for the quantification of glucose in the brain. This also allowed the detection of acetylcholine and glutamate. Finally, a module for chronoamperometric measurement of dopamine (DA) was developed with pyrolyzed carbon electrodes, and proof-of-concept experiments showed that it could be coupled to the outlet of the probe for DA measurement in droplets.

By combining the probe and the DoD with the appropriate analytical methods, quantitative molecular studies of neurotransmitters, metabolites, proteins, or even ribonucleic acids (RNAs) could now be envisioned. They would benefit from the electrical, chemical, and optical stimulation features of the probe and from the accurate chemical recording enabled by the DoD approach.

Key words: Brain fluid sampling, neural probe, microdialysis, neurochemicals, neurotransmitters, neuroscience, droplets, microfluidics, mass spectrometry, multimodal stimulation.

Résumé

Les fonctions neurales opèrent dans des conditions étroitement contrôlées qui sont régulées par des phénomènes électriques et chimiques. Les pathologies du cerveau telles que la maladie de Parkinson ou d'Alzheimer perturbent ces conditions et provoquent la perte de neurones, ce qui induit des troubles des fonctions motrices et cognitives. Ainsi, un accès à la concentration des molécules neurochimiques dans le cerveau et à leur évolution temporelle serait un atout afin de mieux comprendre ces maladies et de développer des traitements qui pourraient freiner leur progression, voire même rétablir les fonctions neurales.

Parmi les techniques de mesure des molécules neurochimiques du cerveau, les méthodes de collecte fluidiques telles que la microdialyse permettent de collecter des molécules du fluide extracellulaire (ECF) en continu, par diffusion dans un perfusat, qui peut être récupéré et analysé a posteriori. Cependant, ces expériences peuvent être longues et la véritable concentration des molécules dans l'ECF ne peut pas être quantifiée directement à partir des échantillons. Cette thèse a pour but de proposer une solution à ces limitations. Ainsi une nouvelle méthode de collecte appelée Gouttelette à la Demande (DoD) et une sonde neurale pour cette méthode ont été développées à cet effet.

La DoD est inspirée par les fondements théoriques de la microdialyse et par les limitations des méthodes de collecte fluidiques en continu. De ce fait, elle est proposée comme une solution de collecte séquentielle par étapes : une étape de perfusion pour créer une poche de perfusat dans le cerveau, une étape de diffusion pour capturer des molécules dans cette poche, une étape d'aspiration pour collecter la poche chargée en molécules sous forme de gouttelette, et enfin une phase pour laisser la concentration dans l'ECF s'équilibrer. Ceci permet de collecter

des échantillons qui reflètent de près la concentration moléculaire de l'ECF pour effectuer des études moléculaires quantitatives. De plus, la DoD peut être appliquée à la demande pour mesurer les molécules de l'ECF à des moments précis d'une expérience, ponctuellement et de manière répétée.

De son côté, la sonde a été fabriquée en exploitant les technologies du polyimide et du SU-8 pour implémenter la méthode de la DoD au cours d'expériences aiguës dans le cerveau de souris. Elle contient des canaux microfluidiques, des électrodes de détection des gouttelettes, et une électrode de stimulation dans son aiguille de 320 μm de large et de 80 μm d'épais. Une fibre optique lui a aussi été ajoutée pour de la stimulation lumineuse.

Les concepts de la DoD ont été illustrés par des simulations et confirmés par des expériences dans des cerveaux artificiels en agarose, in vitro. Cela a montré que le temps de diffusion permet d'ajuster la concentration des molécules collectées dans les échantillons, avec des caractéristiques stables au cours de collectes répétées. Des expériences in vivo aiguës ont aussi été effectuées sur des souris et des échantillons de 24.4 nL ont typiquement été collectés toutes les 1 à 2 minutes, dès 20 minutes après insertion de la sonde. Les échantillons ont été stockés dans un capillaire et une procédure analytique par spectrométrie de masse a été développée pour confirmer les propriétés de la DoD pour la collecte de glucose dans le cerveau. Ceci a aussi permis la détection d'acétylcholine et de glutamate. Finalement, un module pour la mesure de dopamine (DA) par chronoampérométrie a été développé avec des électrodes en carbone pyrolysé, et des expériences de preuve de concept ont montré que ce module pouvait être couplé à la sortie de la sonde pour la mesure de DA dans des gouttelettes.

En combinant la sonde et la DoD avec des méthodes d'analyse appropriées, des études moléculaires quantitatives de neurotransmetteurs, de métabolites, de protéines, voire d'acides ribonucléiques (ARNs) pourraient à présent être envisagées. Ces études tireraient partie des fonctions de stimulation électrique, chimique et optique de la sonde et de l'enregistrement chimique précis proposé par la DoD.

Mots clés : Collection de fluide du cerveau, sonde neurale, microdialyse, molécules neurochimiques, neurotransmetteurs, neuroscience, gouttelettes, microfluidique, spectrométrie de masse, stimulation multimodale.

Contents

Acknowledgements	i
Abstracts	v
Contents	ix
List of figures	xv
List of tables	xxxi
List of Symbols	xxxiii
1 Introduction	1
1.1 Scope of the thesis	2
1.2 Molecules and electrical signals in the brain	3
1.2.1 Neurotransmission	3
1.2.2 Molecular signaling in the brain	4
1.2.3 The Blood-Brain Barrier (BBB)	5
1.2.4 Brain pathologies	5
1.2.5 Molecules and signals in the extracellular fluid	7
1.2.6 Microfabrication technologies for BioMEMS	8
1.2.7 Methods for neurochemical monitoring in the brain	11
1.2.8 Summary	14
1.3 State of the Art of brain fluid sampling probes	15
1.3.1 Sampling probes	15
1.3.2 Microtechnologies for sampling probes	19
	ix

1.4 Thesis positioning	22
1.4.1 Thesis objectives	24
1.4.2 Thesis structure	26
2 Theoretical bases of sampling systems	27
2.1 Theory of continuous sampling by microdialysis	27
2.1.1 Model of the system	28
2.1.2 Mathematical model of microdialysis	30
2.1.3 Results of the microdialysis model	37
2.1.4 Extension to push-pull sampling	38
2.1.5 Discussion	39
2.2 Definition of the Droplet on Demand approach	41
2.2.1 The objectives of the DoD	41
2.2.2 The steps of DoD sampling	41
2.3 Simulation of DoD sampling	46
2.3.1 Finite element analysis model	46
2.3.2 Effects of the parameters in a DoD sequence	47
2.3.3 Repeated DoD cycles	49
2.3.4 Summary of the DoD simulations	54
2.4 Conclusion	55
3 Implementation of DoD in a neural probe	57
3.1 Presentation of the probe for DoD	57
3.2 Fabrication of the probe	60
3.2.1 Polyimide layer - PI-i	62
3.2.2 Metallic layer - ELEC	63
3.2.3 Polyimide layer - PI-ii	64
3.2.4 SU-8 channels - SU8-i	64
3.2.5 SU-8 cover - SU8-ii	64
3.2.6 Anodic release and titanium etching	65
3.2.7 Interfacing	66
3.2.8 Surface treatments	66

3.3	Characterization of the fluidic system	68
3.3.1	Materials	68
3.3.2	Implementation of DoD	69
3.3.3	Implementation of continuous sampling	71
3.3.4	Model of the fluidic system	71
3.3.5	Calibration of the outlet flow rate	74
3.4	Conclusion	75
4	Sampling models	77
4.1	<i>In vitro</i> model - agarose brain phantom	77
4.1.1	Materials	78
4.1.2	Electrical measurement of the NaCl in droplets	79
4.1.3	Droplet generation by DoD	80
4.1.4	Effect of the diffusion time on the recovery fraction	80
4.1.5	Effect of the equilibration time on the recovery fraction	84
4.1.6	DoD and continuous sampling	84
4.1.7	Discussion	86
4.2	<i>In vivo</i> model - mouse striatum	87
4.2.1	Surgical procedure	87
4.2.2	Experimental procedure	87
4.2.3	Application of DoD <i>in vivo</i>	89
4.2.4	Discussion	94
4.3	Conclusion	95
5	Glucose collection with the DoD approach	97
5.1	Analytical methods for droplet samples	97
5.2	Development of the nanoESI-FTMS method	99
5.2.1	Materials and methods	100
5.2.2	Characterization of the signals	102
5.2.3	Quantification of glucose	104
5.3	Properties of DoD for the collection of glucose	106
5.3.1	The stability of the concentration	106

5.3.2	The diffusion time and the concentration	108
5.3.3	The recovery fraction of glucose in the brain	110
5.4	Conclusion	113
6	Measurement of neurotransmitters in droplets	115
6.1	Measurement of neurotransmitters by nanoESI-FTMS	116
6.1.1	Materials and methods	116
6.1.2	Detection and fragmentation	116
6.1.3	Measurement in complex matrices	117
6.1.4	Conclusion	119
6.2	Electrochemical measurement of dopamine in droplets	119
6.2.1	Fabrication of the electrochemical module	121
6.2.2	Materials and methods	123
6.2.3	Measurement of FcMeOH in droplets	125
6.2.4	Measurement of dopamine in droplets	127
6.2.5	Discussion and conclusion	131
6.3	Conclusion	133
7	Conclusion and future perspectives	135
7.1	Conclusion	135
7.2	Future perspectives	142
A	Supplementary information related to Chapter 2	147
A.1	Mass balance in the intracellular space	147
A.2	Quasi-steady-state mass balances for the probe	148
A.2.1	Mass balance in the membrane	148
A.2.2	Boundary conditions	149
A.2.3	Mass balance for the dialysate	150
A.3	Parameters for the simulations	151
B	Supplementary information related to Chapter 3	153
B.1	Hydraulic resistances	153
B.2	Details of the fabrication	154

C Characterization of the capacitive sensor	159
C.1 Definition of the model	159
C.2 Optimization of the design	161
C.3 Analytical computations	161
C.4 Simulations	163
C.5 Results	164
C.6 Discussion and conclusion	166
D Supplementary information related to Chapter 4	167
D.1 Characterization of the electrodes for conductivity measurements	167
D.2 Recovery of fluorescein from a gel with DoD sampling	170
D.3 Tissue sections	171
E Supplementary information related to Chapter 5	173
E.1 Droplets of glucose	173
E.2 Droplets of glucose and additive	174
E.3 Calibration curve for <i>in vivo</i> samples	175
F Measurement of miRNAs	177
F.1 Selection of the miRNAs	177
F.2 Objectives and materials of the study	178
F.3 Experimental protocol	179
Bibliography	181
List of publications	209
Acronyms	211
Curriculum Vitae	215

List of Figures

1.1	Biological signaling examples with molecules. a Neurotransmission occurs at the synaptic cleft between the presynaptic neuron emitting an AP, and a postsynaptic neuron receiving a chemical signal of neurotransmitters at its dendrite. Upon release, the neurotransmitters bind to receptors on the membrane of the postsynaptic neuron. This induces a cascade of ion fluxes and contributes to the propagation of the electrical signal. b Mechanisms of paracrine signaling and volume transmission. A cell releases molecules, that diffuse in the extracellular space to transmit a signal to remote cells by different means: modification of the environment, binding to receptors, uptake by the cell.	4
1.2	Passive droplet generation geometries. $Q_{carrier}$ and $Q_{dispersed}$ respectively represent the flow rates of the carrier and dispersed phase. a T-junction. b Flow focusing. c Co-flow.	10

- 1.3 Electrochemical probes. **a** Flexible polyimide neuroelectronic interface with pyrolyzed carbon electrodes. Flexibility was demonstrated in (A), with retrieval of the initial shape was after flexing in (B). Moreover, different electrode configurations were allowed: for DBS in (C), for retinal stimulation in (D), and for electrochemical measurements at different locations with linear arrays in (E) and (F). Scale bars: C:2000 μm , D:800 μm , E-F:500 μm . *Reprinted from VanDersarl et al. (2015) with permission.* **b** Minimally invasive probe for neurochemical recording with carbon fibers. Array of 8 neurochemical probes integrated on a circuit board for electrical interfacing in (A). The outlined box indicates the zoomed region of the next panel. 8 parylene-coated carbon fiber probes are shown in (B) and a scanning electron microscope image shows the tip of a carbon fiber that protrudes out of the parylene insulation in (C). The fibers are very small and the arrowhead show the delineation between the exposed sensing fiber (diameter 7 μm) and the parylene insulation (diameter 8.5 μm) in (D). *Reprinted from Schwerdt et al. (2017) with permission.* 14
- 1.4 Microdialysis and push-pull sampling probes. **a** Pictures of the commercial microdialysis probe CMA 7 and its guide cannula. The inlet (blue) brings perfusate at the tip with the membrane, to collect analytes before exiting at the outlet. The probe can be inserted into the brain through a guide cannula. *Adapted from CMA Microdialysis AB.* **b** Schematic of the tip of microdialysis and push-pull probes in the ECF. The analytes in the ECF diffuse through the ECF itself, through the membrane and through the perfusate. In microdialysis, the perfusate interacts with the membrane while flowing from the tip to the outlet and it captures analytes of which the size is small enough to go through the membrane. In push-pull probes, the perfusate interacts with the tissue directly and is sampled back at the outlet. 16

- 1.5 Microfabricated fluid sampling technologies. **a** SEM image of a nanoporous membrane integrated above a fluidic channel on chip. *Adapted with permission from Metz, Trautmann, et al. (2004).* **b** Silicon microdialysis probe with integrated silicon dialysis membrane. *Adapted with permission from W. H. Lee et al. (2016). Copyright 2016 American Chemical Society.* **c** Silicon push-pull probe with channels and fluidic openings at the tip. *Adapted with permission from W. H. Lee et al. (2013). Copyright 2013 American Chemical Society.* **d** Cross-section and tip of a silicon push-pull probe combining fluidic channels and electrodes. *Adapted with permission from Chae et al. (2021).* **e** Silicon-glass push-pull probe that integrates a frit to capture molecules while filtering the debris of the extracellular matrix. *Adapted with permission from van den Brink et al. (2019).* **f** Polyimide/SU-8 neural probe integrating microfluidic channels and electrodes for stimulation and recording of neural activity. The channels form a T-junction at the tip, that allows segmenting the sampled fluid into droplets within a carrier phase. *Reprinted with permission from Petit-Pierre et al. (2016).* 20
- 2.1 Schematic of the system with a cylindrical microdialysis probe. It consists of 3 domains: the annulus of perfusate/dialysate ($r_{cann} \leq r \leq r_i$) with a concentration C_d , the membrane ($r_i < r \leq r_o$) with a concentration C_m , and the tissue ($r > r_o$) with the extracellular concentration C_e . The analyte from the tissue reaches the perfusate by radial diffusion through the ECF and through the membrane. It gets collected in the dialysate, flowing along the z-axis, with a flow rate Q_d . Physiological interactions occur in the tissue, within the ECF, within the cells and with the vasculature. A traumatized tissue could be considered ($r_o < r \leq r_t$), with perturbed interactions with respect to the normal tissue ($r > r_t$), but the tissue is considered normal in this development, after a healing period. At $r = \infty$, the tissue has a concentration C_e^∞ , that should be reflected in the dialysate for a quantitative analysis. 28

- 2.2 The concentration profiles and the recovery fraction predicted by the solutions of the microdialysis model. **a** Temporal evolution of the axially-averaged concentration profile $\langle C \rangle[r, t]$ relative to C_e^∞ , predicted by the solution for the transient regime. The recovery fraction E_d is added. **b** Concentration profile of $\langle C \rangle[r, t]$ relative to C_e^∞ in the entire system, for different CL_m , at steady-state. **c** Temporal evolution of the recovery fraction E_d , predicted by the solution for the transient regime, for different CL_m . *Adapted with permissions from Bungay et al. (2006).* 38
- 2.3 Concepts of DoD. **a** Objectives of DoD sampling in terms of recovery fraction. DoD aims to collect samples punctually or repeatedly while maintaining a high recovery fraction without transient regime. A sketch of the recovery fraction of continuous sampling methods (with and without droplet segmentation of the dialysate) is added for comparison and inspired by Figure 2.2c and η_{ss} is the steady-state level. **b** Overview of the tip of the 320 μm wide and 80 μm high probe that contains 3 microfluidic channels. The first one allows infusing perfusate in the tissue to create a pocket of perfusate. The second one is filled with oil and allows aspiration of the perfusate pocket loaded with molecules that diffused into it. The third one is filled with oil and allows segmenting the perfusate into droplets at the T-junction. 42
- 2.4 Concept of the DoD approach implemented at the tip of a probe. Only the perfusion and outlet lines are represented to illustrate the sampling of an analyte in the tissue. After insertion of the probe, the tissue and the probe are initially at rest, in the idle state (left). Thus, the tissue is unperturbed and a sketch of the spatially uniform concentration profile of the analyte in the ECF is shown at the top. 1) A cycle starts when desired by the operator with local infusion of perfusate. This creates a pocket of perfusate between the probe and the tissue, and a concentration gradient appears. 2) The analyte is progressively collected in the liquid pocket by diffusion. 3) The pocket is aspirated within the oil phase at the T-junction. 4) A droplet is formed and moved to the outlet. 5) No flow is applied in the recovery step and the analyte concentration equilibrates in the tissue only, by diffusion. The idle state resumes. 44

- 2.5 Finite element analysis model to study DoD. **a** The model considers glucose diffusing from the cube of medium (1 μM), into a perfusate pocket (0 μM) of 30 nL and with variable thickness (40 μm here) at the tip of the 320 μm wide probe. **b** Evolution of the glucose concentration in the system illustrated on the cut surface, during a diffusion step. The black rectangle shows the domain of an 80 μm thick pocket. 47
- 2.6 Simulations of glucose diffusion in the pocket and in the medium, during a 60 s diffusion step. **a** Spatiotemporal evolution of the glucose concentration along the cut line, in an 80 μm thick pocket. The insets show the concentration over the cut surface defined in Figure 2.5a. **b** Evolution of the recovery fraction against the DoD parameter $t_{\text{diffusion}}$ in 30 nL pockets of perfusate with a thickness varying from 20 to 160 μm 48
- 2.7 Simulations of glucose diffusion in the medium only, during equilibration steps that follow a 10 s diffusion step. **a** Spatiotemporal evolution of the concentration along the cut line, over a 60 s equilibration step. It starts with the concentration profile at the end of the diffusion step (dotted blue line). For comparison, the concentration profile before the diffusion step is also added (thick black line). **b** Starting conditions of the concentration in the medium, for subsequent sampling cycles, using 10 s of $t_{\text{diffusion}}$ and 1, 10 and 60 s of $t_{\text{equilibration}}$ 50
- 2.8 Simulations of the recovery fraction of glucose in a 40 μm thick perfusate pocket of 30 nL, over repeated DoD cycles. **a** Three cycles were simulated subsequently, by alternating steps of 10 s of diffusion in the pocket and in the medium, and steps of 10 s of equilibration in the medium only. The recovery fraction at sampling is represented by a star symbol between the diffusion and equilibration steps. **b** Evolution of the recovery fraction in subsequent samples. A steady diffusion time of 10 s was used, and the $t_{\text{equilibration}}$ was varied from 1 s (fast DoD) to 60 s (stable DoD). 51
- 2.9 DoD for high and steady recovery fraction η for repetitive sampling cycles. $t_{\text{diffusion}}$ was varied from 10 s to 120 s, while the 60 s equilibration time was fixed. The thickness of the perfusate pocket was 40 μm for all sets of parameters, except for two sets with 80 μm and 160 μm respectively. 53

- 3.1 Overview of the features of the polyimide/SU-8 probe for DoD sampling. **a** Picture of the probe. The body allows fluidic and electrical interfacing, and all channels lead to the tip of the flexible needle, where droplets are collected and later moved to a storage capillary at the outlet. **b** Schematic of a sampling cycle at the tip of the probe. The perfusion channel is filled with perfusate, while the inlet and outlet channels are filled with PFD and intersect at the T-junction. During the perfusion step, a pocket of perfusate is created at the tip. Molecules diffuse into the pocket during the diffusion step, and the pocket is aspirated within the PFD phases during the sampling step. This forms a droplet at the T-junction, that is moved towards the outlet in the move step and detected by the electrodes. **c** SEM picture of the AA' cross section of the needle, showing the channels defined between the polyimide base (PI-i, ELEC, PI-ii) and two SU-8 layers (SU8-i and SU8-ii). **d** Picture of the probe with an optical fiber (false colored in red) inserted through a microdialysis cannula CMA7. **e** Picture of the storage capillary that keeps the droplets separated by PFD until analysis. 59
- 3.2 Probe fabrication process. **a** Deposition of the metallic sacrificial layers by sputtering and spin coating of the 3 μm thick polyimide base layer (PI-i) on the main wafer. **b** Coating and exposure of the positive PR AZ10XT on a mask aligner. **c** Reflow of the PR. **d** O_2 plasma etching of the unprotected PI-i and transfer of pattern and profile of the PR. **e** Deposition of the 500 nm thick Ti-Pt-Ti metallic layer for the electrodes by sputtering, photolithography, and patterning by ion beam etching. **f** Spin coating of the 1 μm thick polyimide passivation layer (PI-ii), photolithography, and patterning of PI-ii by O_2 plasma etching. **g** Spin coating and photolithography of SU-8 to pattern the channels (SU8-i). **h** Preparation of the SU-8 cover layer (SU8-ii) on a flexible film. The flexible PET film is laminated to a secondary wafer and held by capillary force by water. It allows production of a dry SU-8 film (SU8-ii) on a flexible PET substrate. **i** The flexible carrier is peeled off the secondary wafer and the main wafer is laminated to the SU-8 dry film. **j** The cover is patterned through the flexible PET film by photolithography. 61

- 3.3 Probe fabrication process at CMi - slanted polyimide base layer. **a** At the location of the electrical contact pads, the slanted edges ensure a smooth transition of the metallic layer between two levels. The rectangular area is shown in the next frame. **b** The pristine PI-i layer is smooth, whereas the slanted edged is rough due to partial etching during PR profile transfer and the grains of the aluminum base layer are visible. 62
- 3.4 Probe fabrication process at CMi - electrodes and fluidic channels. **a** The Ti-Pt-Ti electrodes deposited on PI-i access the fluidic channel defined by SU8-i through an opening in PI-ii. **b** The T-junction at the tip of the probe is formed by the SU8-i layer. **c** Finalized probe after SU8-ii development. The inlet, perfusion and outlet channels patterned in SU8-i are integrated in the needle. The perfusion aperture allows perfusate delivery into the tissue with the perfusion channel. The inlet and outlet channels intersect at the T-junction that leads to the sampling aperture through PI-i and PI-ii. Interdigitated droplet-sensing electrodes in the outlet channel allow droplet detection directly after sampling. A stimulation electrode is also available at the tip, which contacts the tissue on the PI-i side. The scale bar is 100 μm 63
- 3.5 Post-fabrication of the probes. **a** Before release, a wafer contains 18 probes surrounded by characterization devices on the sides. **b** Schematic of the fluidic interface to transfer droplets from the probe to the storage capillary with no dead volume. **c** Top and side views of the probe after gluing of the optical fiber at the tip of the probe, on the SU-8 side. **d** Picture of the tip of the probe, for local delivery of light through the fiber. 66
- 3.6 Wetting of the surfaces by the aqueous phase and the PFD, for different treatments, in *in vitro* conditions. A microfluidic channel with polyimide and SU-8 surfaces is shown in the left column, with flowing droplets. The glass surface of the outlet capillary is in the right column with static droplets. In both columns, the scale bars represent 100 μm . **a-b** Pristine surfaces. **c-d** Surfaces after plasma treatment and Sigmacote functionalization. **e-f** Surfaces after plasma treatment and PFOTS functionalization. 67

- 3.7 Fluidic setup. The perfusion and inlet lines are driven by syringe-pumps, while the outlet line is controlled with pressure and uses a flow sensor. All three lines reach the tip of the probe and access the tissue. The perfusate is delivered to the brain at the perfusion aperture. The inlet and outlet lines form a T-junction with the sampling channel that accesses the brain through the sampling aperture and from which droplets are collected. After sampling, the droplets are moved and stored in the storage capillary at the outlet. 69
- 3.8 Implementation of the flow rate in the DoD steps in the inlet, perfusion, and outlet lines, that respectively contain PFD, perfusate and droplets within PFD. The inlet and perfusion lines are controlled in volume, while the outlet line is controlled in pressure. Positive flow rates go from the setup to the tip. 70
- 3.9 Hydraulic model of the fluidic setup. **a** Hydraulic model of the perfusion line driven by a syringe pump to infuse perfusate in the tissue. **b** Hydraulic model of the inlet and outlet lines connected to the sampling channel via the T-junction. The inlet line is driven by a syringe pump, whereas the outlet line is controlled in pressure. 72
- 3.10 Calibration of the pressure-flow rate relationship at the outlet of the probe, for PFD sampling from a beaker. 75
- 4.1 Electrical measurement of the NaCl concentration in the droplets. **a** Current I_i and phase $|\phi_i|$ measured through droplets flowing over the electrodes in the probe and containing between 0 mM (0%) and 150 mM NaCl (100%). **b** Calibration curve of the peak current I_i through the droplets against their NaCl concentration. The insets show the current and phase signals of two droplets, with the variation of $|\phi_i|$ to 90° at the arrival and departure of the droplets from the electrodes. 79

- 4.2 In vitro experiments of DoD in an agarose gel phantom. **a** The tip of the probe was inserted in a cube of 0.6% agarose. The inlet and perfusion flow rates were controlled by syringe-pumps whereas the outlet line was controlled by a pressure controller, connected to a flow sensor. Electrodes in the outlet channel measured the current through the droplets. **b** In idle state, the full probe is loaded with PFD, except the perfusion line filled with perfusate. Example of a 1.8 nL droplet generated during a *sampling* step from 0 s to 1 s and followed by a *move* step that started circulating the droplet at 1 s. 81
- 4.3 Effect of $t_{\text{diffusion}}$ measured *in vitro*. **a** The trace of the current, converted into the recovery fraction of NaCl, shows the recovery fraction of NaCl from the gel in 3 droplets generated by DoD with $t_{\text{diffusion}}$ values of 1 s, 5 s and 10 s. **b** Summary of the recovery fraction measured in the droplets against $t_{\text{diffusion}}$. The simulated recovery fraction of Na^+ and Cl^- is added for qualitative comparison. 82
- 4.4 Recovery fraction and transient regime in DoD and continuous sampling conditions *in vitro*. **a** The recovery fraction η of subsequently sampled droplets with DoD cycles using $t_{\text{diffusion}}$ values of 1 s, 5 s and 10 s and $t_{\text{equilibration}}$ of 60 s. Two sets with $t_{\text{diffusion}}$ of 10 s and $t_{\text{equilibration}}$ of 21 s and 1 s are also reported. **b** The steady-state recovery fraction η_{ss} obtained for continuous push-pull sampling without and with segmentation into droplets. The perfusion flow rate $Q_{\text{perfusion}}$ was varied, and the outlet flow rate was adjusted accordingly. The inset shows the instantaneous evolution of $\eta(t)$, with a short transient regime and the steady-state η_{ss} 85
- 4.5 *In vivo* sampling in the brain of a mouse. **a** Fluidic and electrical interfacing of the probe, for the collection of the droplets in the storage capillary. **b** Real sampling conditions, with the endoscope in the background that monitors the droplets in the storage capillary. In these experiments, no cannula was used, and the needle was directly inserted in the brain through a small hole in the skull. The infrared lamp to maintain the body temperature is not shown. 88

- 4.6 Electrical signal recorded by the droplet-sensing electrodes in the outlet channel during 15 DoD cycles *in vivo*. The amplitude of the current I_i increased when a droplet moved over the electrodes, whereas the absolute value of the phase ϕ_i reduced. In this example, 14 out of 15 cycles successfully produced a droplet. 90
- 4.7 Outlet flow rate Q_{outlet} (left axis) and pressure P_{outlet} applied to the outlet line (right axis) for two DoD cycles executed *in vivo* at different stages of a sampling experiment. **a** Behavior of the flow rate during a cycle at the beginning of an experiment. Fast droplet aspiration occurred during the *sampling* step (iv), and Q_{outlet} reduced to 0 nL/min when the probe became in direct contact with the tissue (vi). This illustrated the high hydraulic resistance of the tissue and the need to adjust the parameters of DoD to prevent this. The parameters were $V_{\text{perfusion}} = 60$ nL at 3 nL/s, $t_{\text{diffusion}} = 10$ s, $P_{\text{outlet}} = -300$ mbar during $t_{\text{sampling}} = 15$ s, $Q_{\text{inlet}} = 300$ nL/min during $t_{\text{move}} = 20$ s, and $t_{\text{recovery}} = 1$ s. **b** A cycle was applied later in the same experiment, with modified sampling parameters to compensate for the changes of hydraulic resistance in the outlet line and to allow a smooth transition between the end of the *sampling* step and the *move* step. The parameters were $V_{\text{perfusion}} = 60$ nL at 3 nL/s over 20 s, $t_{\text{diffusion}} = 45$ s, $P_{\text{outlet}} = -350$ mbar during $t_{\text{sampling}} = 20$ s, $Q_{\text{inlet}} = 200$ nL/min during $t_{\text{move}} = 20$ s, and $t_{\text{recovery}} = 1$ s. 91
- 5.1 Setup for nanoESI-FTMS measurements. **a** Schematic of the setup. A syringe-pump drives the flow of PFD that infuses the droplets into the emitter at high voltage, at the inlet of the mass spectrometer. The drain helps remove the PFD that accumulates at the tip. **b** Picture of the experimental setup. The endoscope verifies seamless droplet transfer from the capillary to the emitter. The air blower blows filtered air at the emitter tip. **c** Close up on the emitter tip (130 μm OD) during droplet spraying. **d** Close up on the emitter tip during a long phase of PFD during two droplets, with PFD accumulation at the tip in absence of drain. 101

5.2	Glucose and internal standard measured in calibration solutions. a Ion chromatogram of a solution of 50 μM of glucose (203.05 m/z) and 100 μM of IS (209.07 m/z) in CNS Perfusion fluid and additive. b Ion chromatogram after fragmentation of the glucose (CID energy 28 eV at 203.05 m/z). c Ion chromatogram after fragmentation of the IS (CID energy 35 eV at 209.07 m/z).	102
5.3	Calibration of the signals of glucose and IS with reference droplets. a Raw signals and their ratio, for three droplets containing 750 μM of glucose and 250 μM of IS. b Calibration of the signals for glucose concentrations of 0, 10, 100, 200, 500, 750, 1000 and 1500 μM , with 250 μM of IS in reference droplets.	103
5.4	Signals of glucose and IS with <i>in vivo</i> sampled droplets. a Glucose signal of raw droplets, directly infused at 120 nL/min. b Picoinjection of additive is done with a custom T-junction. A raw droplet of volume V is moved to the junction and measured optically. Then, the appropriate volume of additive is injected to form a diluted droplet of volume V+X. c Signals of droplets diluted with additive (1:4 ratio). Final ACN and IS concentrations of 30% and 200 μM . The ratio of the signals and its median are added with respect to the right axis.	104
5.5	Glucose measured in 3 sets of DoD sampling parameters with respective diffusion times of 10 s, 5 s, and 1 s, in the same animal. The 10 first subsequently sampled droplets of each set are reported. All sets used 30 nL of perfusion over 10 s, 20 s of sampling time and 30 s of equilibration time.	106
5.6	Glucose quantified in droplets sampled <i>in vivo</i> , with sets of DoD parameters that varied the perfusion volume between 30 nL and 70 nL and the diffusion time from 1 s to 60 s.	109
6.1	Ion chromatogram of GABA, ACh, Glu and DA at 1 μM in 50% deionized water and 50% ESI buffer.	117

- 6.2 Detection of glucose, ACh and Glu in an *in vivo* sample diluted 10 times in the additive for glucose quantification. **a** Signals of glucose at 203.05 m/z in SIM mode, ACh in PRM at 87.04 m/z (30eV CID at 146.12 m/z) and Glu in PRM at 130.05 m/z (30eV CID at 148.06 m/z). **b** Ion chromatogram of glucose and IS in SIM mode. **c** Ion chromatogram of the main fragment of ACh in PRM. **d** Ion chromatogram of the main fragment of Glu in PRM, with an interferent at 130.09 m/z. 118
- 6.3 Fabrication of the electrochemical module. The fabrication of the bottom layer with pyrolyzed carbon electrodes is shown in the panels a-c, whereas the fabrication of the top PDMS layer is shown in the panels d-f. **a** Photolithography of a 2.6 μm thick layer of AZ1512-HS on a fused silica wafer. **b** Development and hardbake of the PR. **c** Pyrolysis at 180°C and 900°C. **d** Photolithography of a 2.6 μm thick layer of AZ1512-HS on a silicon wafer. **e** Etching of the unprotected silicon over a depth of 16 μm by Bosch process. **f** After cleaning and silanization of the mold, PDMS was cast over the mold and cured. **g** After cutting, punching, and cleaning of the PDMS layer, oxygen plasma bonding of the top and bottom layers was achieved. 122
- 6.4 Chip with T-junction for droplet generation and electrochemical measurement in droplets. The PFD inlet is used to flow the continuous phase into the chip, whereas the sample inlet allows infusion of the dispersed phase (FcMeOH or DA in PBS). Droplets are formed at the T-junction and the current I_{pc} is measured at the electrodes by potentiostatic chronoamperometry, with a voltage V_{pc} applied to WE with respect to REF. The channels are 100 μm wide (w_p) and 16 μm high (h_p). The electrodes are 5 μm wide (w_{pc}) and separated by 75 μm (s_{pc}). 123
- 6.5 Chronoamperometric measurement of FcMeOH in droplets. **a** Typical signal of the current I_{pc} across a droplet of 1 mM FcMeOH, with three distinct phases: a rapid rise of capacitive current (*i*), a decay due to the growth of the depletion layer (*ii*), and a quasi-steady-state plateau until the end of the droplet (*iii*). **b** Verification of the Levich law with FcMeOH in droplets. For a constant concentration, the current I_{pc} varies linearly with $u_{droplet}^{1/3}$ 125

- 6.6 Electrochemical measurements of DA in droplets. **a** Evaluation of the voltage V_{pc} to maximize the faradaic current from the oxidation of DA, I_{DA} , with respect to the current from PBS, I_{PBS} . The curves report the average end-of-plateau current for droplets of 100 μM of DA and droplets of PBS at different values of V_{pc} . The relative difference in current is also reported. **b** A typical signal of current I_{pc} obtained from the passage of a 21 nL droplet with 1.6 μM of DA and with V_{pc} of 0.8 V. The three phases *i*, *ii*, and *iii* are the same as for FcMeOH. . . . 127
- 6.7 Calibration curves of the end-of-plateau current I_{DA} against the concentration of DA, C_{DA} , varied from 0 μM to 20 μM . The flow rate $Q_{droplet}$ was set to 250 nL/min. The insets show the measurement points in the 0 μM to 2 μM range. **a** Calibration in 2 nL to 4 nL droplets separated by PFD. **b** Calibration in continuous sample phase without PFD. 128
- 6.8 Proof of concept experiment where the electrochemical chip was coupled to the outlet of the sampling probe. **a** The tip of the probe was inserted in a beaker of PBS spiked with DA. Droplets were generated by adjusting the flow rates Q_{inlet} and Q_{outlet} with syringe pumps. After generation, the droplets were transferred to the electrochemical chip for online measurement of I_{DA} in the droplets. **b** The current I_{DA} is reported for the analyzed droplets (black dots) over five step changes of the concentration C_{DA} in the beaker, from 0 μM to 101 μM . The blue circled dots represent the current obtained from droplets of different concentrations that merged in the interconnects. The center of the pink rectangles represents the average current for each step of C_{DA} , whereas the top and bottom boundaries represent the standard deviation. 130
- C.1 Side-view of the channel with a droplet of ECF in PFD. The equivalent capacitances encountered by the field lines between the two fingers are shown. . . . 160

- C.2 Simulations and analytical estimations of the capacitive sensor. **a** Map of the relative variation of the capacitance relative to the baseline capacitance with PFD, for different combinations of s_{el} and w_{el} . The simulation considered the capacitance over 4 electrodes. The red star represents the estimation for a sensor with $s_{el} = 10 \mu\text{m}$ and $w_{el} = 20 \mu\text{m}$. The dashed black line represents the condition $w_{el} + s_{el} = 31.25 \mu\text{m}$. **b** Sensitivity of the signal to the droplet size as a function of thickness of the polyimide layer over the electrodes. The experimentally measured sensitivity with a probe is added for comparison. 163
- C.3 Droplet characterization by capacitive sensing electrodes. **a** With untreated probes, the signal does not allow accurate detection, nor characterization of the droplets. **b** With PFOTS-treated probes, the signal allows clear identification and characterization of the droplets. The capacitance variation can be translated into the droplet size using the 39 fF/nL sensibility obtained after calibration. **c** A droplet produces a signal with a trapezoidal shape. The slopes allow velocity measurement while the height of the plateau reflects the size of the droplet. **d** Two subsequent droplets on the sensor can be discriminated and measured since they produce superposed trapezoidal signals. 165
- D.1 Complex impedance \bar{Z}_0 of a pair of $20 \mu\text{m} \times 70 \mu\text{m}$ electrodes, separated by $20 \mu\text{m}$, and exposed to an electrolyte. **a** Electrical model of the impedance, with the resistance to charge transfer R_{Ct} of the electrode, the constant phase element \bar{Z}_{CPE} for the double layer capacitance, the resistance of the bulk electrolyte R_{bulk} , and the capacitance of the dielectric insulation C_d . **b** Bode diagram of the impedance spectra for electrolytes with a NaCl concentration ranging from 0 mM (0%) to 150 mM (100%) NaCl. 168
- D.2 Plot of $1/Z_{el}$ against the concentration of NaCl. Z_{el} was extracted with the PRF method at different frequencies determined by the frequency where the phase was closest to 0° 170
- D.3 Effect of $t_{\text{diffusion}}$ measured *in vitro*. Summary of the recovery fraction measured by the fluorescence of fluorescein recovered in the droplets against $t_{\text{diffusion}}$. . . 171

D.4	Pictures of the medial striatum (a) and of the caudal striatum (b), after probe insertion, ink infusion, ink aspiration, and probe removal. The arrow shows the ink spot and the rectangular zone highlights the area where the tract should be visible.	171
E.1	Analysis of glucose and IS signals in 30 nL <i>in vitro</i> droplets. a Step concentration change of glucose in droplets, from 500 μM to 1000 μM . b Raw signals of 200 μM IS and 100 μM glucose. c Ratio of glucose and IS signals, with the median ratio over the duration of each droplet displayed as a black diamond \diamond	174
E.2	Calibration curve obtained at the end the measurement of <i>in vivo</i> samples, that links the measured ratio to the real glucose concentration that was initially in the reference samples. The IS concentration was 200 μM and the dilution factor was 10. The data represents the median of the ratio, and the error bars represent the quantiles 0.25 and 0.75.	175
E.1	Initial workflow of the TaqMan Advanced Assay for quantification of the selected miRNAs in the DoD samples.	179

List of Tables

1.1	Summary of four main families of methods to measure neurochemicals in the brain	25
2.1	Parameters of the DoD	44
4.1	DoD parameters used for the <i>in vitro</i> experiments.	82
4.2	Properties of the droplets collected <i>in vivo</i>	93
5.1	DoD parameters for glucose quantification <i>in vivo</i>	107
5.2	Summary of the glucose measurements presented in Figure 5.6	109
6.1	Main peaks and fragments of the neurotransmitters	117
7.1	Synthesis of the sampling methods in the literature	141
A.1	Parameters for the simulations of microdialysis in Bungay et al. (2006)	151
B.1	Parameters of the hydraulic circuit	154
E.1	Selection of miRNAs for experiments in DoD samples	178

List of Symbols

Physical constants

ϵ_0	Dielectric permittivity of vacuum = $8.854 \cdot 10^{-12}$ [F/m]
F	Faraday constant = 96485.332 [C/mol]
q_e	Elementary charge = $1.602 \cdot 10^{-19}$ [C]
U_{th}	Thermal voltage = 26 [mV]

General notation

ϵ	Dielectric permittivity [-]
$\eta(t)$	Instantaneous recovery fraction [-]
η	Recovery fraction [-]
η_{ss}	Recovery fraction at steady state [-]
Γ	Penetration depth of the depletion layer [m]
λ	Tortuosity factor [-]
\mathcal{P}	Permeability for theoretical analysis of microdialysis [m/s]
μ	Viscosity [kg/m/s ²]
ω	Pulsation [radians/s]
\bar{Z}	Complex hydraulic impedance [kg/m ⁴ /s] or complex electrical impedance [Ohm]
Φ	Volume fraction [-]
ϕ	Phase [-]
ρ	Density [kg/m ³]
b	Equilibrium binding ratio [-]
C	Analyte concentration [mol/m ³] or Capacitance [F]
D	Diffusion coefficient [m ² /s]

d	Diameter of circular channel/capillary [m]
f	Frequency [1/s]
G	Zero order analyte generation rate [kg/m ³ /s]
h	Height of rectangular channel [m]
k^r	First order degradation rate [1/s]
k^x	First order exchange rate [1/s]
P	Pressure [kg/m/s ²]
Q	Flow rate [m ³ /s]
r	Distance from the axis of the microdialysis probe [m]
R_h	Hydraulic resistance [kg/m ⁴ /s]
t	Time [s]
V	Volume [m ³] or voltage [V]
w	Width of a rectangular channel [m]
z	Axial distance from the end of the microdialysis probe [m]

Other symbols

K_0	Modified Bessel function of the second kind of zero order
K_1	Modified Bessel function of the second kind of first order
Pe	Peclet number [-]

Subscripts

c	Subscript for the intracellular space
d	Subscript for the dialysate
e	Subscript for the extracellular space/ECF
f	Subscript for the fluid phase of the membrane
m	Subscript for the membrane
s	Subscript for the solid phase of the membrane
t	Subscript for the tissue
pa	Subscript for the plasma

Specific variables and parameters

$\bar{C}_d[z, t]$	Radially averaged concentration in the dialysate in the transient regime [mol/m ³]
$\bar{C}_d[z]$	Radially averaged concentration in the dialysate in the steady-state regime [mol/m ³]

ϵ_{brain}	Relative dielectric permittivity of brain tissue [-]
ϵ_{ECF}	Relative dielectric permittivity of the ECF [-]
ϵ_{holder}	Relative dielectric permittivity of the probe holder [-]
ϵ_{PFD}	Relative dielectric permittivity of PFD [-]
ϵ_{Pi}	Relative dielectric permittivity of polyimide [-]
ϵ_r	Relative dielectric permittivity of the double layer for the Helmholtz capacitance [-]
ϵ_{SU-8}	Relative dielectric permittivity of SU-8 [-]
η_{NaCl}	Recovery fraction of NaCl in the DoD sample [-]
$\langle C \rangle [r]$	Axially averaged analyte concentration at distance r from the probe in the steady-state regime [mol/m ³]
\mathcal{P}_{di}	Permeability of the dialysate from the inner surface of the membrane [m/s]
\mathcal{P}_{do}	Permeability of the dialysate from the outer surface of the probe [m/s]
\mathcal{P}_{mo}	Permeability of the membrane from the outer surface of the probe [m/s]
\mathcal{P}_o	Permeability of the whole system [m/s]
\mathcal{P}_{P_o}	Permeability of the probe [m/s]
\mathcal{P}_{t_o}	Permeability of the tissue [m/s]
\overline{Z}_b	Complex hydraulic impedance of the brain [kg/m ⁴ /s]
\overline{Z}_g	Complex hydraulic impedance of the gap between the brain and the probe [kg/m ⁴ /s]
\overline{Z}_0	Complex impedance of the interface of the pair of electrodes in the channel [Ohm]
\overline{Z}_{CPE}	Complex constant phase element [Ohm]
ϕ_{el}	Phase of \overline{Z}_0 [radians]
ϕ_i	Phase of the current i(t) [A]
A	Area of the annulus of dialysate [m ²]
A_{el}	Area of the electrode [m ²]
a_{el}	Half spacing between the electrodes [m]
$C[r, z, t]$	Analyte concentration at distance r from the probe, at distance z along the membrane and at time t in the transient regime [mol/m ³]
$C[r, z]$	Analyte concentration at distance r from the probe, at distance z along the

	membrane in the steady-state regime [mol/m ³]
C_0	Concentration of the bulk electrolyte [mol/m ³]
C_1	Capacitance for the field lines going through the channel and the cover [F]
C_2	Capacitance for the field lines going through the channel [F]
C_3	Capacitance for the field lines going through the polyimide between the fingers [F]
C_4	Capacitance of the field lines going through the external medium [F]
C_{real}	Analyte concentration in the medium [mol/m ³]
C_{sample}	Analyte concentration in the sample [mol/m ³]
C_{brain}	Capacitance of the external medium as brain [F]
C_{Ch}	Capacitance of the channel [F]
C_{Cover}	Capacitance of the cover layer [F]
C_c	Analyte concentration in the intracellular space [mol/m ³]
C_d	Analyte concentration in the dialysate [mol/m ³]
C_d	Capacitance of the polyimide dielectric insulation that surrounds the electrodes [Ohm]
C_d^{in}	Analyte concentration in the perfusate [mol/m ³]
C_d^{out}	Analyte concentration in the dialysate [mol/m ³]
C_{eff}	Effective capacitance measured by the electrodes [F]
C_{ext}	Capacitance of the external medium [F]
C_e	Analyte concentration in the ECF [mol/m ³]
C_e^∞	Analyte concentration in the ECF in unperturbed tissue [mol/m ³]
C_{FcMeOH}	Concentration of the analyte in the droplet [mol/m ³]
C_f	Analyte concentration in the fluid phase of the membrane [mol/m ³]
C_G	Gouy-Chapman capacitance [F]
C_H	Helmoltz capacitance [F]
C_I	Capacitance of the Gouy-Chapman-Stern model [F]
C_{pa}	Analyte concentration in the plasma [mol/m ³]
C_p	Capacitance of the passivation layer above the electrodes [F]
$C_{\text{sub},2}$	Capacitance of the substrate layer between the electrodes [F]
C_{sub}	Capacitance of the substrate layer below the electrodes [F]

$C_{tot,ECF}$	Total capacitance of the system in presence of ECF only [F]
$C_{tot,PFD}$	Total capacitance of the system in presence of PFD only [F]
C_{tot}	Total capacitance of the system [F]
CL	Analyte clearance [m^3/s]
CL_m	Analyte clearance normalized by the mass of the tissue [$m^3/s/kg$]
D_0	Diffusion coefficient of an analyte in water [m^2/s]
D_d	Diffusion coefficient of an analyte in the dialysate [m^2/s]
D_m	Effective diffusion coefficient of an analyte in the membrane [m^2/s]
D_t	Effective diffusion coefficient of an analyte through the whole tissue [m^2/s]
D_{0,Cl^-}	Diffusion coefficient of Cl^- in water at $20^\circ C = 2030 \text{ } [\mu m^2/s]$
$D_{0,fluor}$	Diffusion coefficient of fluorescein in water at $20^\circ C = 425 \text{ } [\mu m^2/s]$
D_{0,Na^+}	Diffusion coefficient of Na^+ in water at $20^\circ C = 1330 \text{ } [\mu m^2/s]$
D_{FcMeOH}	Diffusion coefficient of FcMeOH in water at $20^\circ C = 610 \text{ } [\mu m^2/s]$
d_{OHP}	Thickness of the double-layer for the Helmholtz capacitance [F]
$E_d(t)$	Extraction fraction, also called the recovery fraction η [-]
G_t	Total generation rate for the whole tissue [$kg/m^3/s$]
$h_{channel}$	Height of probe channel [m]
h_{PI-ii}	Thickness of the polyimide PI-ii layer [m]
h_{PI-i}	Thickness of the polyimide PI-i layer [m]
h_{el}	Thickness of the electrodes [m]
h_p	Height of the channel in PDMS [m]
$i(t)$	Instantaneous current across the pair of the droplet-sensing electrodes [A]
I_{DA}	Current measured across droplets of DA [A]
I_i	Amplitude of the current $i(t)$ [A]
I_{Levich}	Current of the Levich regime [A]
I_{PBS}	Current measured across droplets of PBS [A]
I_{pc}	Current measured between the carbon electrodes [A]
k_t	Analyte elimination rate constant for the whole tissue [$1/s$]
K_{ce}	Equilibrium ratio of the cellular concentration for the chosen analyte to its free extracellular concentration [-]
K_{mf}	Membrane-to-fluid equilibrium partition coefficient [-]

K_{sf}	Solid-to-fluid partition coefficient in the membrane [-]
K_{te}	Equilibrium ratio of the total tissue concentration for the chosen analyte to its free extracellular concentration [-]
l_m	Length of the microdialysis membrane along the z-axis [m]
L_D	Debye length [m]
L_{el}	Length of the electrodes [m]
M_0	Impedance magnitude of the constant phase element [F]
n	Parameter of the constant phase element [-]
n_q	Number of electrons exchanged per molecule [-]
P_{outlet}	Pressure applied to the outlet of the system [kg/m/s ²]
$P_{sampling}$	Sampling pressure applied to the outlet of the system [kg/m/s ²]
Q_d	Flow rate of the perfusate/dialysate [m ³ /s]
Q_{brain}	Flow rate from or to the brain tissue [m ³ /s]
Q_{inlet}	Inlet flow rate in the probe [m ³ /s]
Q_{leak}	Leaking flow rate to the brain surface, through the gap between the probe and the tissue [m ³ /s]
Q_{outlet}	Outlet flow rate in the probe [m ³ /s]
$Q_{perfusion}$	Perfusion flow rate in the probe [m ³ /s]
Q_{pocket}	Flow rate that contributes to the pocket of perfusate in the brain [m ³ /s]
$Q_{sampling}$	Sampling flow rate in the probe [m ³ /s]
$Q_{carrier}$	Flow rate of the carrier phase for droplet generation [m ³ /s]
$Q_{dispersed}$	Flow rate of the dispersed phase for droplet generation [m ³ /s]
$Q_{droplet}$	Flow rate of the droplets over the carbon electrodes [m ³ /s]
R_{bulk}	Resistance of the bulk electrolyte [Ohm]
r_{cann}	Radius of the inner cannula of a microdialysis probe [m]
R_{Ct}	Resistance to charge transfer [Ohm]
r_c	Radius of the cylindrical catheter [m]
R_{ip}	Hydraulic resistance for the inlet channel of the probe [kg/m ⁴ /s]
R_{it}	Hydraulic resistance for the inlet tubing [kg/m ⁴ /s]
r_i	Radius of the dialysate-membrane interface [m]
$R_{o,max}$	Maximal hydraulic resistance for the outlet line [kg/m ⁴ /s]

$R_{o,min}$	Minimal hydraulic resistance for the outlet line [kg/m ⁴ /s]
R_{oc}	Hydraulic resistance for the outlet capillary [kg/m ⁴ /s]
$R_{op,max}$	Maximal hydraulic resistance for the outlet channel of the probe [kg/m ⁴ /s]
$R_{op,min}$	Minimal hydraulic resistance for the outlet channel of the probe [kg/m ⁴ /s]
R_{ot}	Hydraulic resistance for the outlet tubing [kg/m ⁴ /s]
r_o	Radius of the membrane-tissue interface [m]
R_{pp}	Hydraulic resistance for the perfusion channel of the probe [kg/m ⁴ /s]
R_{pt}	Hydraulic resistance for the perfusion tubing [kg/m ⁴ /s]
R_r	Hydraulic resistance for the flow resistor [kg/m ⁴ /s]
$R_{sc,max}$	Maximal hydraulic resistance for the storage capillary [kg/m ⁴ /s]
$R_{sc,min}$	Minimal Hydraulic resistance for the storage capillary [kg/m ⁴ /s]
R_{se}	Hydraulic resistance for the flow sensor [kg/m ⁴ /s]
$R_{sp,max}$	Maximal hydraulic resistance for the sampling channel of the probe [kg/m ⁴ /s]
$R_{sp,min}$	Minimal hydraulic resistance for the sampling channel of the probe [kg/m ⁴ /s]
r_t	Distance of the traumatized-normal tissue interface [m]
s_{el}	Spacing of the electrodes for the capacitive sensor [m]
S_o	Outer surface area of the microdialysis membrane [m ²]
s_{pc}	Spacing between the pyrolyzed carbon electrodes [m]
t_{cycle}	Cycle time [s]
$t_{diffusion}$	Diffusion duration [s]
$t_{equilibration}$	Tissue equilibration time [s]
t_{move}	Droplet move duration [s]
$t_{perfusion}$	Perfusion duration [s]
$t_{recovery}$	Tissue recovery duration [s]
$t_{sampling}$	Sampling duration [s]
T_{el}	Penetration depth of the electrodes for the capacitive sensor [m]
$u_{droplet}$	Velocity of the droplets over the carbon electrodes [m/s]
V_0	Amplitude of the voltage applied to the electrode [V]
V_{move}	Volume of PFD to dispensed during a <i>move</i> step [m ³]
$V_{perfusion}$	Volume of perfusate dispensed during a <i>perfusion</i> step [m ³]
V_{pc}	Voltage applied across the carbon electrodes [V]

w_{outlet}	Width of the outlet channel [m]
w_{pc}	Width of a pyrolyzed carbon electrode [m]
w_p	Width of the channel in PDMS [m]
W_{WE}	Normalized electrode length in the channel [-]
x_b	Length of the backflow along the probe [m]
z_0	Charge of the ion in solution [-]
Z_{el}	Module of \bar{Z}_0 [Ohm]

Chapter 1

Introduction

In biology, a cell is considered the smallest living unit. Mature cells differentiate into specialized cells with defined functions. Among these, neurons are responsible for neural functions and estimates provide that 86 billion neurons populate the human brain (Azevedo et al., 2009). Neurons form the nervous system, which is traditionally split into three structures: the central nervous system (CNS), the peripheral nervous system (PNS), and the enteric nervous system. The CNS comprises the brain and the spinal cord. The brain is the processing center of sensory stimuli and the decision unit to initiate voluntary motor actions. The spinal cord is responsible for reflexes and acts as an interface between the brain and the PNS. The PNS is composed of nerves and ganglia that respectively transduce and relay nervous signals throughout the rest of the body. Finally, the independent enteric nervous system is responsible for control functions in the gastrointestinal tract and is a major unit of the gut-brain axis. Bilateral communication occurs between these three structures through a network of nerves, that is regulated by electrical cues and supported by neurochemicals such as neurotransmitters, proteins, and neuromodulators (Kandel et al., 2014; Z. Wu et al., 2022). This network is difficult to study *in vivo* due to the limited access to the brain. As a corollary, unveiling the mechanisms of its pathologies is also a challenging task. Thus, further studies are required to get to know the brain better, and to cure it better.

Nevertheless, accessing the brain and its mechanisms is possible, with specialized tools and technological developments have allowed scientists to produce a large library of solutions to study the brain (Wan et al., 2022). Thus, brain-on-chip systems were developed, that enable to study neural cells *in vitro*, in conditions that emulate the real conditions in the brain. Solutions were also developed for acute *in vivo* studies, and after years of technological developments, chronically implantable systems were made available, that allowed treating severe cerebral impairments in humans. Among these revolutionary systems, Deep Brain Stimulation (DBS) devices can alleviate the symptoms of Parkinson's disease (PD) in humans by delivering localized electrical signals (Mercanzini et al., 2017). Moreover, Epidural Electrical Stimulation (EES) recently restored the ability to walk in patients with spinal cord injury (Rowald et al., 2022). Despite these outstanding breakthroughs, much remains unknown about the multiple gears of the brain. However, the advanced microfabrication technologies that helped these advancements happen, now provide systems to allow researchers to investigate the brain (Frank et al., 2019; Vázquez-Guardado et al., 2020; Y. Zhang et al., 2021).

1.1 Scope of the thesis

Together, biology and microtechnology have made it possible to develop systems to improve health, to a point that measurement of blood biomarkers is now part of the clinical routine. This is not yet the case with brain biomarkers. However, microtechnologies can help with this task, by providing the right tools to access the molecules in the brain. Thus, fluid sampling probes such as push-pull and microdialysis probes have allowed the measurement of many biomarkers in the brain since their development in the 1960s-1970s and the measurement of monoamine neurotransmitters in the brain of rats (Chefer et al., 2009; Ungerstedt & Pycock, 1974). Moreover, microfabrication technologies and microfluidics now permit their miniaturization and augmentation, with electrical functionalities for stimulation and sensing. Combined with accurate sampling protocols, they can accurately probe the chemistry of the brain. This will allow quantitative molecular studies of metabolites, neurotransmitters, and possibly larger molecules such as proteins or even microRNAs (miRNAs) in extracellular vesicles, that all contribute to the machinery of this organ.

1.2 Molecules and electrical signals in the brain

1.2.1 Neurotransmission

Neurons are electroactive cells capable of transmitting electrical signals. They are classified into 3 types: sensory neurons, motor neurons, and interneurons. Sensory neurons sense external stimuli and communicate them upstream, to the spinal cord, or to the brain. In contrast, motor neurons receive signals from the brain or from the spinal cord, that they relay to specific biological actuators. Finally, interneurons form complex signal processing layers that connect sensory neurons to motor neurons (Kandel et al., 2014). These different neurons are organized into systems that regulate high-level functions, such as motor functions for walking and cognitive functions for learning. In these systems, neurons present different molecular receptors and release different neurotransmitters (Alberts et al., 2009).

To simplify, a neuron possesses a soma, multiple dendrites and one axon that are all involved in neurotransmission, a principle illustrated in Figure 1.1a. The soma, which has a typical diameter of 10-25 μm , is the core of the neuron, where information is processed and from where signals are emitted. Signal transmission between neurons is mediated by electrical signals called Action Potentials (APs). APs are variations in electrical potential across the cell membrane that occur in a few milliseconds. After an AP is emitted in the soma, it propagates along the axon, a long filament that protrudes from the soma and that is sheathed by myelin. The axon has a typical diameter of 1 μm (Costa et al., 2018) and usually undergoes branching to communicate with multiple neurons, at structures called synapses. Fine neuromodulation can occur during propagation and when the AP reaches a synapse, a Ca^{2+} influx triggers the fusion of vesicles with the membrane, that release their neurotransmitters into the synaptic cleft. Neurotransmitters diffuse in the extracellular space and bind to specific receptors at the dendrite of the postsynaptic neuron. This triggers a cascade of ion fluxes of Na^+ and of K^+ and contributes to the propagation of the AP in the postsynaptic neuron. The typical extracellular signal of an AP is shown in Figure 1.1a. After this, the neurotransmitters diffuse in the extracellular fluid (ECF) that surrounds the neurons until neurotransmitter uptake occurs, thus bringing them back inside the neurons for a new cycle (Alberts et al., 2009).

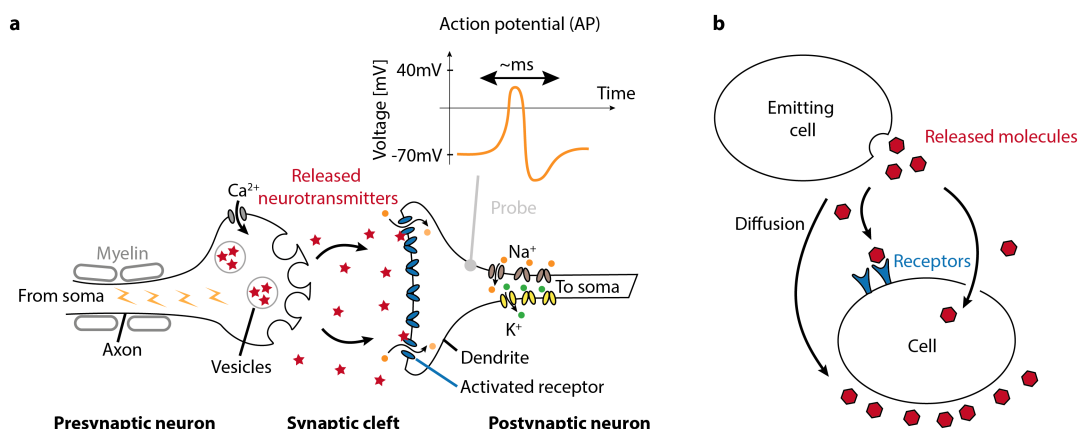


Figure 1.1: Biological signaling examples with molecules. **a** Neurotransmission occurs at the synaptic cleft between the presynaptic neuron emitting an AP, and a postsynaptic neuron receiving a chemical signal of neurotransmitters at its dendrite. Upon release, the neurotransmitters bind to receptors on the membrane of the postsynaptic neuron. This induces a cascade of ion fluxes and contributes to the propagation of the electrical signal. **b** Mechanisms of paracrine signaling and volume transmission. A cell releases molecules, that diffuse in the extracellular space to transmit a signal to remote cells by different means: modification of the environment, binding to receptors, uptake by the cell.

From this, it stands out that neurotransmission combines electrical signals via fluxes of charge carriers (i.e., ions) and chemical signals via molecules (i.e., neurotransmitters).

1.2.2 Molecular signaling in the brain

In fact, the brain does not contain only neurons, it also contains glial cells that are not electroactive, but which are responsible for supporting the operation of the neurons (Azevedo et al., 2009). Although these cells do not propagate APs, they participate in brain activity through the regulation of brain molecules. Moreover, they contribute to biological signaling via paracrine signaling or volume transmission. This consists of releasing molecules in the extracellular fluid, to act on remote cells in the surroundings. The molecules can alter the cellular environment, activate receptors, or be taken by the receiving cells (Syková & Nicholson, 2008; Zoli et al., 1998). In fact, volume transmission is a specific signaling process in the brain that usually involves neurotransmitters and neuropeptides to produce effects far from their release site (Morgan & Christie, 2010). These processes are illustrated in Figure 1.1b.

1.2.3 The Blood-Brain Barrier (BBB)

The brain requires a tightly controlled environment to operate normally. Therefore, it is separated from the rest of the body by the Blood-Brain Barrier (BBB), that consists of a layer of endothelial cells that line the capillaries in the brain. Thus, it restricts the access of the brain to selective molecules to protect it from blood-borne agents, such as neurotoxins. Consequently, drugs that target the CNS might be filtered out by the BBB and fail to produce any effects. Consequently, this prevents direct administration of dopamine (DA) to patients affected by PD. In addition to protection, the BBB also regulates the effluxes of molecules out of the brain, thus contributing to maintaining homeostasis. Homeostasis can be defined as an optimal functioning equilibrium of living organisms, that includes optimal physical and chemical conditions of temperature, pH, concentration gradients, energy sources, etc. (Kadry et al., 2020; McEwen, 2016; Roh et al., 2016). In other words, the BBB regulates the microenvironment of the cells in the brain, which are surrounded by ECF. Using specific ion channels, it ensures optimal conditions for synaptic activity, such as by maintaining high Na^+ and low K^+ levels in the ECF, that are necessary for the propagation of APs.

1.2.4 Brain pathologies

Despite the BBB, brain homeostasis can be altered, namely by drugs or lack of sleep, but also by brain pathologies. While the former ones have obvious solutions, treating, and possibly reversing brain pathologies is a major challenge of neuroscience. These pathologies notably include ischemic stroke and epilepsy, but also pathologies related to neurodegenerative diseases such as PD, Alzheimer's disease (AD), Huntington's disease, and Amyotrophic Lateral Sclerosis (ALS). Neurodegenerative diseases refer to disorders that cause a progressive death of neurons, that are followed by impairments of different cerebral functions over time. Among them, PD and AD are probably the most common ones.

The exact causes and mechanisms of PD are still unclear, but PD appears to be linked with genetic mutations of the protein α -synuclein. In the Parkinson's brain, they form fibrils and accumulate as Lewy bodies in the neurons, in a localized brain region called substantia nigra. This region contains dopaminergic cells that project DA to the striatum, where it contributes to the regulation of motor functions, in coordination with glutamate (Glu) and gamma-aminobutyric acid (GABA). PD causes the death of dopaminergic cells; thus, it induces an imbalance in the system that results in an over-activated motor cortex. This translates into loss of motor functions, and resting tremors or bradykinesia (Stayte & Vissel, 2014). Alternatively, the AD brain features a generalized accumulation of β -amyloid plaques in the ECF, that results from disintegration of microtubules in nerve cells. They cause the progressive death of the neurons across large areas of the brain, that notably translate into memory and cognitive impairments (Johnstone et al., 2016).

Treatment options for AD are limited to certain drugs that slow down cognitive decline, however they do not work in all patients and only alleviate the symptoms. Similarly, PD cannot be cured, but treatments exist to alleviate the symptoms, such as administration of L-dopa to compensate for the loss of DA. The alternative stands in DBS systems. These consist in electrodes implanted in the deep brain with a stimulator that delivers accurate electrical stimulation to the subthalamic nucleus (Mercanzini et al., 2017). In fact, these are systems that benefit from microtechnologies to allow accurate adjustment of the position of the electrodes and of the stimulation parameters.

Nevertheless, despite these advancements in PD management, there is no cure to reverse the progression of PD and AD. The reasons for this are simple. First, the exact causes of PD and AD remain unclear. Therefore, this impairs the development of efficient drugs and explains why many clinical trials have failed (Hamblin, 2019). Second, these are progressive diseases, and the symptoms usually appear at a late stage of their development, when significant neural loss has occurred and when it might be too late already. Earlier diagnostic would probably allow easier identification of the causes, but this requires appropriate biomarkers that have not all been identified yet (Kalia, 2018; Lausted et al., 2014; Lotankar et al., 2017).

Meanwhile, alternative treatments were proposed to induce neuroprotection and prevent these pathologies from evolving to critical states (Blivet et al., 2018; Che et al., 2018; Saliba et al., 2017). These approaches notably include photobiomodulation (PBM), a treatment based on near-infrared light shone on the head or directly in the brain (Hamblin, 2016). Invasive and non-invasive treatments were studied, that provided remarkable effects against PD in animal models and that suggested neuroprotective effects (Darlot et al., 2016; Moro et al., 2014). Nevertheless, discrepancies exist in the results and comparing the studies proves difficult due to the lack of standardized protocols (Salehpour & Hamblin, 2020). But more importantly, the precise mechanisms of PBM remain unclear and are debated (Sommer et al., 2020). Despite this, many molecular changes have been reported following PBM treatments, that include changes in ATP, in oxidative stress, in growth factor release, but also in gene expression (Benson et al., 2020; de Freitas & Hamblin, 2016; Glass, 2021). This confirmed that PBM produces effect, but scientists do not know yet the exact conditions that make these treatments work.

Based on these considerations, many unknowns remain in the understanding of the diseases and of the tested treatments. They would require further studies of the brain, and technological improvements such as artificial brain models (brain-on-a-chip) have already allowed this *in vitro*. However, because of the complexity of the brain, translation from *in vitro* to *in vivo* is challenging due to the lack of accurate *in vitro* models. For these reasons, *in vivo* studies are required, that focus on the molecular processes in the brain. This would provide valuable insights on what to act on and to develop efficient treatments that really stop these diseases.

1.2.5 Molecules and signals in the extracellular fluid

The extracellular fluid that surrounds the neurons is rich in many types of biomarkers that could help understand the brain and its pathologies: proteins, peptides, enzymes, extracellular vesicles, etc. (Shetty & Zanirati, 2020). Moreover, their concentrations vary at different time scales and with different amplitudes. In fact, neurotransmission, volume transmission, and protein aggregation provide good examples of these scales. Thus, during neurotransmission, the release of Glu (molecular mass of 147 Da) occurs in the 20 nm wide synaptic cleft between two neurons. When it binds to a receptor, an AP is initiated, that is mediated by Na^+ (23 Da)

and K^+ ions (39 Da) and that lasts about a millisecond (Kandel et al., 2014). In comparison, volume transmission with Glu is a slower process since Glu needs to diffuse through the ECF to reach a remote target, that can be millimeters away. On the other side of the spectrum, the aggregation of α -synuclein proteins (14 kDa) and the formation of Lewy bodies in nerve cells, which are associated with Parkinson's disease, take years to produce detectable motor and cognitive dysfunctions (Jagust & Landau, 2021; H.-J. Lee et al., 2014). For these reasons, measuring molecules in the brain requires specific systems.

1.2.6 Microfabrication technologies for BioMEMS

Microfabrication technologies are key to the development of systems to probe the brain and biology in general. These technologies are covered by the field of microelectromechanical systems (MEMS), which encompasses the production of miniaturized devices that combine electrical and mechanical functions at small scales, with features in the nanometer (10^{-9} m) to micrometer (10^{-6} m) range (Villanueva et al., 2016). Given their dimensions, these systems are fabricated in a clean room environment and use processes developed for the fabrication of integrated circuits. They consist in depositing and patterning layers of different materials subsequently. Certain layers serve as structural features, whereas others are masking structures (photosensitive resins), to protect the former ones during etching steps. By the repetition of deposition, photolithography and etching steps, microfabrication processes allow the production of multimaterial microdevices that can combine semiconductors, metals, oxides, polymers, etc. (Franssila, 2010; Madou, 2018) These include accelerometers, gyroscopes, and microphones in mobile phones, surface scanning probes for atomic force microscope (AFM) (Martinez et al., 2016), optical switches (Seok et al., 2016), micro-mirrors (Schweizer et al., 1999), and much more (Vladisavljević et al., 2013).

BioMEMS and microfluidics

With microfabrication technologies, features can be achieved that match the scales of cells and that allow studying biological processes. This is the field of biological MEMS (BioMEMS), also referred to as lab-on-a-chip and micro total analysis systems, and that was introduced

in 1990 (Grayson et al., 2004; Manz et al., 1990). In addition to mechanical and electronic functionalities, fluidic features are frequently integrated to BioMEMS (Whitesides, 2006), that enable to infuse, change, block (Gomez-Sjöberg et al., 2007; Hansen et al., 2002) or mix fluids on chip (Bertsch et al., 2020; Kee & Gavrilidis, 2008). In fact, microfluidics is a field of microtechnologies that encompasses the operations performed on small volumes of fluids in the range of nanoliters and below (Whitesides, 2006). It allows reduced reagent consumption and faster reactions due to the scaling of the dimensions, and accurate control of the fluidic environment due to laminar flow conditions (Berthier & Silberzan, 2010; Taylor et al., 2022). This field has gained significant popularity with the development of polydimethylsiloxane (PDMS), a silicone elastomer that allows fast molding of microfluidic channels, that can later be assembled to MEMS (McDonald & Whitesides, 2002).

Droplets microfluidics is a field of microfluidics, that allows handling fluids at dimensions below the dimensions of the channels, thus scaling down operations such as phase extraction (Wells & Kennedy, 2020) or mixing of reagents (Amirifar et al., 2022; Duchamp et al., 2021). The core concept relies on the use of non-miscible phases to create emulsions of independent microreactors. In life sciences, an aqueous phase and silicone oils, fluorinated oils, or hydrocarbon oils are commonly used, that can be supplemented with surfactants to help stabilize the emulsion (Baret, 2012; Elvira et al., 2022). Droplets allow high throughput operations such as fluorescence-activated cell sorting (FACS) (Bai et al., 2014), or droplet digital polymerase chain reaction (PCR) for quantification of deoxyribonucleic acids (DNA) and ribonucleic acids (RNA) sequences (Lindner et al., 2021). Droplets also serve for single cell and chemical assays (Hümmer et al., 2016; S. Lee et al., 2022), and they can segment samples to preserve bands of separate analytes after chromatography (Peretzki et al., 2020).

Passive and active droplet generation strategies exist that allow the generation of droplets with variable sizes (from hundreds of nanometers in diameter) and at generation frequencies up to tens of kHz (Baroud et al., 2010; Battat et al., 2022; P. Zhu & Wang, 2017). The T-junction geometry figures among the most used designs. It is illustrated in Figure 1.2a. It is a passive approach that uses a carrier phase in the main channel and a dispersed phase in the side channel. Both channels intersect at 90° with respective flow rates $Q_{carrier}$ and $Q_{dispersed}$. As the dispersed phase enters the main channel, shear forces elongate its head into the main

channel, and narrow its neck until a breakup point, where the dispersed phase splits, thus forming a droplet. The size and the rate of generation can be tuned by the geometry and the control of the flow rates, or by changing the relative viscosity between the two phases (Baroud et al., 2010; Garstecki et al., 2006). Flow focusing and co-flow geometries are two alternative passive droplet generation geometries illustrated in Figure 1.2b-c. In a planar geometry, flow focusing allows the generation of smaller droplets than T-junctions and in 3D systems, the co-flow geometry allows the production of droplets directly in the carrier phase without interactions between the dispersed phase and the walls.

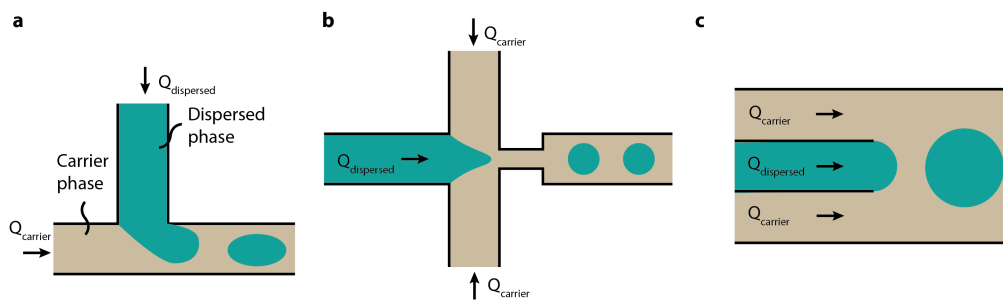


Figure 1.2: Passive droplet generation geometries. $Q_{carrier}$ and $Q_{dispersed}$ respectively represent the flow rates of the carrier and dispersed phase. **a** T-junction. **b** Flow focusing. **c** Co-flow.

Applications of BioMEMS

Over more than 30 years of research in microfluidics, a library of solutions to study biology was developed (Convery & Gadegaard, 2019). Thus, BioMEMS allow applications as different as characterization of cells by impedance spectroscopy (Gawad et al., 2001) and biomarker detection in biological fluids (Inglis et al., 2021; Kikkeri et al., 2022). Moreover, systems were also developed that study cellular interactions (Duchamp et al., 2019; Paluch et al., 2015) or gene expression at the single cell level (Kellogg et al., 2014). In addition, advanced "organ-on-chip" platforms were also reported, that allow cell culture in conditions that reproduce the *in vivo* conditions (Huh et al., 2010; Wan et al., 2022). Electrophysiological platforms also benefited from these technologies and arrays of microelectrodes allowed the access to intracellular electrical signals of electroactive cells (Angle et al., 2015; Desbiolles et al., 2020; Müller et al., 2015). Moreover, since 1990, microfluidics has contributed to many developments of chemical analysis techniques (Basova & Foret, 2015; Ha et al., 2021).

Moving away from chips, these technologies allowed the development of advanced neural interfaces to probe and stimulate the brain *in vivo*. Hence, the Utah Intracortical Electrodes Array was reported in 1997, that consisted of an implantable neural interface with an array of 100 needle electrodes. It allowed electrical recording from a population of neurons in the visual cortex of cats, by opposition to single electrode systems (Maynard et al., 1997). Neural interfaces have significantly evolved on many aspects since then (Im & Seo, 2016; Weltman et al., 2016); thus, fast CMOS chips were recently coupled to thin needles for faster electrical recording (Obaid et al., 2020). On the material side, conformal electrocorticography grids (Fallegger et al., 2021) and soft auditory brainstem implants were also reported (Vachicouras et al., 2019), for improved contact of the electrodes with the tissue. Moreover, developments also made it possible to combine electrical and drug delivery features on soft substrates (Kang et al., 2021; Minev et al., 2015). Finally, probes that include fluidic delivery and optical stimulation features were also developed, that allow neurostimulation and pharmacological studies in freely moving rodents (Canales et al., 2015; Jeong et al., 2015; McCall et al., 2017; H. Shin et al., 2021).

1.2.7 Methods for neurochemical monitoring in the brain

Technology is the key to study the brain and its chemicals. Thus, this subsection describes methods that allow monitoring neurochemicals *in vivo*. These include non-invasive methods that are the most suitable for human patients, and electrochemical methods, that are minimally invasive and benefit directly from microtechnologies. Optical-spectroscopy methods also exist, that benefit from micro- and nanofabrication techniques but they are not addressed here, because only limited *in vivo* studies were reported (Y. Zhang et al., 2021).

Non-invasive methods

Accessing the brain *in vivo* is delicate and needs a strong justification. Therefore, non-invasive techniques have been developed, to study brain activity and track molecules in the brain. Positron emission tomography (PET) is a functional imaging method that uses radiotracers that label molecules to monitor metabolic activity (Nasrallah & Dubroff, 2013). Alternatively,

functional magnetic resonance spectroscopy (fMRS) allows monitoring of neurochemicals without tracers, and uses a magnetic field to acquire magnetic resonance spectra of hydrogen. Since different metabolites produce different spectra, this allows the identification and the measurement of the molecules in the tissue. Due to its detection principle, PET is more sensitive than fMRS, with respective limits of detections in the pM-nM and μ M-mM ranges (Ngernsutivorakul, White, et al., 2018). Moreover, both methods have spatial resolutions in the range of millimeters, with temporal resolutions in the range of seconds to minutes. Therefore, the resolution might be too low to discriminate events in different brain compartments in mice, which is a key animal model to study the brain. Another disadvantage resides in the fact that the subjects need to be immobilized during the procedure.

Finally, genetically engineered sensors provide another solution for non-invasive measurement of molecules for research purposes. They consist of genetically modified cells that use regulator proteins that bind specific analytes and promote the transcription of genes encoding fluorescent probes (Ovechkina et al., 2021). Such constructs were reported for multiple neurotransmitters and neuromodulators, namely Glu, DA, and adenosine triphosphate (ATP). They provide the best performances in terms of sensitivity, selectivity, as well as of spatial and temporal resolution. However, to be truly non-invasive, the probes should be accessible to fluorescent microscopy techniques. For this reason and due to their principle, they are limited to small organisms that can be genetically modified (Z. Wu et al., 2022).

Electrochemical probes

In vivo, electrochemical methods mostly use electrodes to transduce chemical signals to electrical signals at a working electrode (Bard & Faulkner, 2001), but they can also use field effect transistors with specific recognition elements (Nakatsuka et al., 2018; C. Zhao et al., 2021). Different analytical methods exist (amperometry, cyclic voltammetry, differential pulse voltammetry, etc.), that rely on controlling the voltage applied to the working electrode with respect to a reference electrode, and on measuring the current between the working electrode and a counter electrode (Venton & Cao, 2020; Y. Zhang et al., 2021). Electrodes with a diameter in the millimeter range can be directly inserted in the brain for measurements (Béland-Millar et

al., 2017), but small electrodes can also be integrated in arrays, on neural interfaces (VanDersarl et al., 2015; Weltin & Kieninger, 2021), thus providing both high spatial and high temporal resolutions in the range of the millisecond. In addition to enabling fabrication on flexible substrates, microfabrication technologies allow customizable configuration of the electrodes for both stimulation and electrochemical sensing, as illustrated in Figure 1.3a.

Using electrodes, electrochemical methods also allow the analysis of the content of biological fluids (Chae et al., 2016; Frost & Meyerhoff, 2015; Rogers & Boutelle, 2017), and are suitable detectors after electrophoretic separation (Saylor & Lunte, 2015). However, electrochemical methods are only suitable for electroactive molecules (e.g., DA, serotonin, etc.), unless they are functionalized with membranes and recognition elements to transduce the analyte into an electroactive compound (Ribet et al., 2017). This makes their properties highly depend on the functionalization, size, topography, and materials of the electrodes (Evans & Murphy, 2008; Nakatsuka et al., 2018; Stieglitz, 2004). In fact, these methods are well suited for the measurement of DA, which is an electroactive molecule of high interest in the brain. Thus, DA has been intensively studied with different types of electrodes, that include specifically functionalized platinum electrodes (S. Zhang et al., 2018), and carbon fibers that require minimal fabrication (Schwerdt et al., 2017; Schwerdt et al., 2018). The latter ones are illustrated in Figure 1.3b, which shows the 8.5 μm diameter footprint of each fiber. In fact, this allows minimally invasive implantation and carbon is particularly suitable for the measurement of catecholamines (Trouillon & O'Hare, 2010; Trouillon et al., 2013). Finally, other novel electrical approaches were also recently reported with nanopipettes and aptamers on nanopores, for the measurement of serotonin, but their use was not yet reported *in vivo* (Nakatsuka, Heard, et al., 2021).

Based on these observations, it appears that electrochemical methods belong to the toolbox of analytical methods to probe the chemistry of the brain. They are particularly suited for monitoring fast changes of chemicals. However, their need for specific functionalization makes their multiplexing ability unfavorable and limits the palette of measurable molecules. Moreover, quantification requires accurate calibration since their surface properties are critical to their performances (Ngernsutivorakul, White, et al., 2018; Y. Zhang et al., 2021).

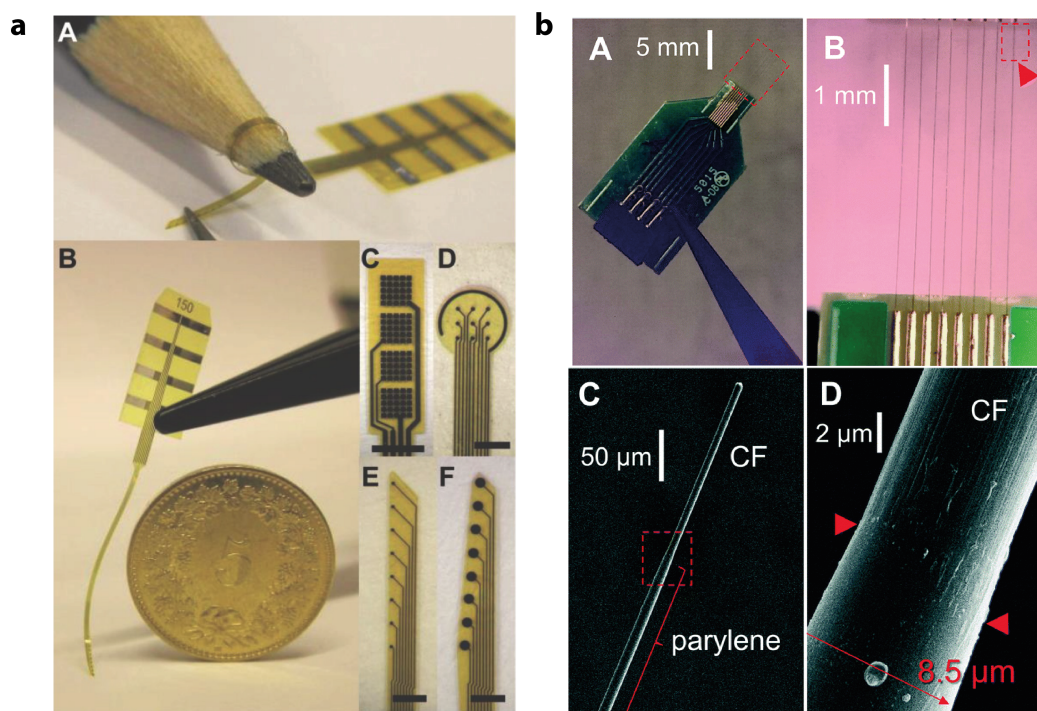


Figure 1.3: Electrochemical probes. **a** Flexible polyimide neuroelectronic interface with pyrolyzed carbon electrodes. Flexibility was demonstrated in (A), with retrieval of the initial shape was after flexing in (B). Moreover, different electrode configurations were allowed: for DBS in (C), for retinal stimulation in (D), and for electrochemical measurements at different locations with linear arrays in (E) and (F). Scale bars: C:2000 μm , D:800 μm , E-F:500 μm . *Reprinted from VanDersarl et al. (2015) with permission.* **b** Minimally invasive probe for neurochemical recording with carbon fibers. Array of 8 neurochemical probes integrated on a circuit board for electrical interfacing in (A). The outlined box indicates the zoomed region of the next panel. 8 parylene-coated carbon fiber probes are shown in (B) and a scanning electron microscope image shows the tip of a carbon fiber that protrudes out of the parylene insulation in (C). The fibers are very small and the arrowhead show the delineation between the exposed sensing fiber (diameter 7 μm) and the parylene insulation (diameter 8.5 μm) in (D). *Reprinted from Schwerdt et al. (2017) with permission.*

1.2.8 Summary

The brain is a complex organ that requires tightly controlled conditions to operate optimally and carry out signaling functions that spread throughout the entire body. However, its homeostasis can be perturbed by pathologies such as neurodegenerative diseases, which remain incurable for the moment. Thus, research is required to understand these pathologies and develop efficient treatments against them. Moreover, since these pathologies are linked with neurotransmitter imbalances, protein aggregation, and genetic mutations, the access to the

molecules in the brain could provide valuable insights on their mechanism to help develop cures. Non-invasive methods allow imaging of certain molecules and are ideal in human patients, but present a limited temporal resolution compared to electrochemical probes, that benefit from microfabrication techniques. Moreover, these techniques have provided researchers with versatile tools to stimulate nerves, record their activity and measure neurochemicals. However, a family of methods to measure the brain chemistry is still missing from this picture: the fluid sampling methods. They will be introduced and discussed in depth in the following.

1.3 State of the Art of brain fluid sampling probes

1.3.1 Sampling probes

Since the ECF contains many molecules, fluid sampling probes have been developed to collect these molecules in fluids. However, direct aspiration of brain fluid is limited to flow rates in the 1-2 nL/min range (Kennedy et al., 2002), because the brain is a dense tissue with a high hydraulic resistance. This is due to the short intercellular distances in the range of 10 to 100 nm (Syková & Nicholson, 2008), and to the small ECF volume fraction of 15-20%, that is defined as the volume of the extracellular space with respect to the total tissue volume. For these reasons, microdialysis probes and push-pull probes collect analytes from the ECF indirectly, by diffusion into a perfusate.

Microdialysis probes

Among the fluidic sampling probes, the microdialysis probe is the gold standard. Commercial probes are provided with guide cannulas to be cemented to the skull and to guide their insertion, as illustrated in Figure 1.4a. Moreover, homemade probes have also been reported (Lietsche et al., 2014). A typical microdialysis probe comprises two concentric capillaries surrounded by a semi-permeable membrane at the tip. To operate, the probe is continuously infused with a perfusion fluid (perfusate) from the inlet and common flow rates usually range

from $0.3 \mu\text{L}/\text{min}$ to $2 \mu\text{L}/\text{min}$ (Hammarlund-Udenaes, 2017a). When the perfusate reaches the tip, it wets the membrane and collects analytes from the tissue by diffusion through three compartments: the tissue, the membrane, and the perfusate inside the probe, as illustrated in Figure 1.4b. Thus, when the perfusate exits the probe, it is loaded with analytes from the extracellular space and is now called the dialysate.

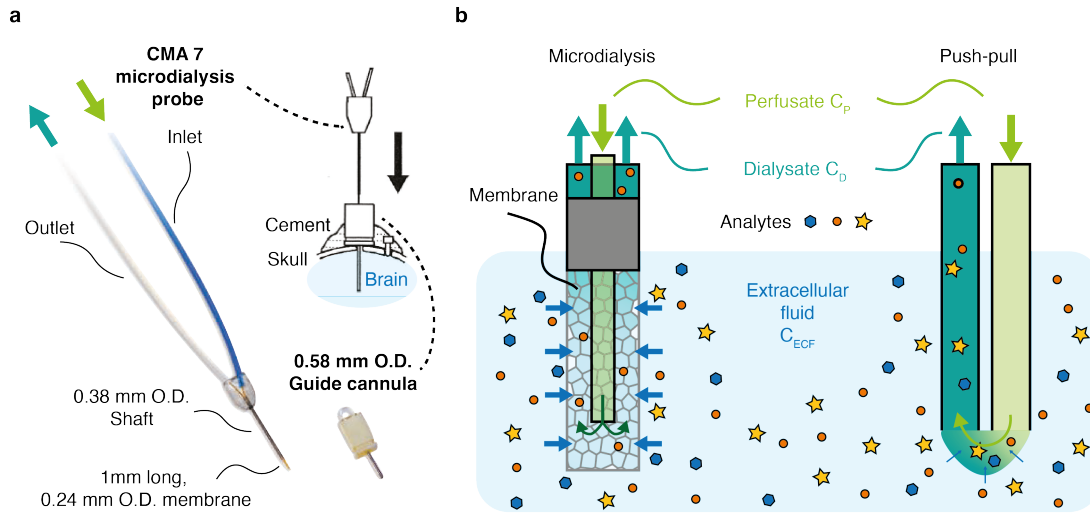


Figure 1.4: Microdialysis and push-pull sampling probes. **a** Pictures of the commercial microdialysis probe CMA 7 and its guide cannula. The inlet (blue) brings perfusate at the tip with the membrane, to collect analytes before exiting at the outlet. The probe can be inserted into the brain through a guide cannula. *Adapted from CMA Microdialysis AB.* **b** Schematic of the tip of microdialysis and push-pull probes in the ECF. The analytes in the ECF diffuse through the ECF itself, through the membrane and through the perfusate. In microdialysis, the perfusate interacts with the membrane while flowing from the tip to the outlet and it captures analytes of which the size is small enough to go through the membrane. In push-pull probes, the perfusate interacts with the tissue directly and is sampled back at the outlet.

The porous membrane is a key element of these probes since it confines the perfusate within the probe on one side and contacts the tissue on the other side. Thus, it defines the surface of interaction between the perfusate and the tissue. Its length is typically in the 1-4 mm range, which limits the spatial resolution but enhances the concentration of the dialysate (Ngernsutivorakul, White, et al., 2018). Moreover, the size of its pores determines the cut-off size of the analytes which can diffuse through the membrane. However, an inconvenient stands in the fact that its properties are likely to evolve over the course of experiments, due to biofouling and to clogging of the pores.

Push-pull sampling probes

Push-pull sampling probes are membrane-less alternatives to microdialysis probes. In fact, many customized push-pull probes were reported, with different geometrical implementations, but that share the same principles (Cepeda et al., 2015; Fisher & Shippy, 2022; Kennedy, 2013; Kottegoda et al., 2002; Slaney et al., 2013). Nevertheless, a typical probe can be considered as an assembly of two capillaries side-by-side or concentric, with one inlet and one outlet. This is shown in Figure 1.4b. The inlet delivers perfusate at the tip ("push") where it wets the tissue to collect analytes, prior to being sampled back at the outlet capillary ("pull"). As compared to microdialysis, the absence of membrane provides a higher spatial resolution and makes these probes better suited to collect large analytes, such as peptides (Raman et al., 2020; G. Wu et al., 2022) or extracellular vesicles (Bache et al., 2015). Nevertheless, this makes the fluid/tissue interface less defined and low flow rates are usually used to prevent perturbation of the tissue by the shear stress (Cepeda et al., 2015; Kennedy et al., 2002).

Characteristics of continuous sampling systems

Despite their different construction, microdialysis and push-pull sampling probes both rely on molecular diffusion in a dialysate to continuously collect analytes from the brain (Ngernsutivorakul, White, et al., 2018). Thus, due to the nature of the sampling, these methods form a family of continuous sampling methods, that share multiple characteristics and limitations. First, since diffusion is specific to each molecule, molecules with the same concentration in the ECF but different diffusion coefficients might have different concentrations in the dialysate. Therefore, the collection of the analytes needs to be calibrated. This is frequently done in a beaker under constant stirring (Tang et al., 2003) or in a gel of 0.6% agarose (Z.-J. Chen et al., 2004; Pomfret et al., 2013). Nevertheless, the accuracy of these *in vitro* methods is debated, and multiple *in vivo* calibration approaches exist, that are tedious to perform (Kho et al., 2017).

The second and third issues of these methods are related to their continuous sampling nature. In fact, they remove molecules from the tissue continuously and perturb their spatial distribution in the tissue. This progressively creates a depletion layer in the surroundings of the probe, that takes time to stabilize (Bungay et al., 2006). Therefore, the concentration recovered in

the dialysate is not immediately stable (transient regime) and the operators need to wait for this to stabilize prior to being able to collect molecules reliably. And when it becomes stable (steady-state regime), the concentration in the vicinity of the probe does not represent the real concentration of the ECF; thus, the concentration in the dialysate does not represent it either. This is the issue of the recovery fraction, that is defined as the concentration recovered in the dialysate with respect to the real concentration in the ECF (i.e., in unperturbed tissue), and that is lower than 1. Thus, the absolute quantification of the real concentration in the ECF is difficult with these methods. However, the monitoring of relative changes of concentration is possible in the steady-state regime.

Analytical methods

Unlike electrochemical methods that directly measure analytes in the brain, sampling methods only allow the collection of molecules, and a separate analytical system is used to process the dialysate. This is an advantage as it allows the selection of the most appropriate analytical system, according to the analytes to be studied: electrophoresis, liquid chromatography, mass spectrometry, fluorescent assays, etc. (Di Giovanni & Di Matteo, 2013; Kennedy, 2013; Wilson & Michael, 2017). These systems can be directly coupled to the outlet of the probes for online measurement, but the dialysate can also be preserved for offline analysis (Saylor & Lunte, 2015). On that matter, the properties of the analytical system have a significant impact on the temporal resolution of the sampling experiment as they determine the required volume of dialysate, thus the time during which analytes need to be sampled. For this reason, molecular measurements with sampling probes have suffered from a limited temporal resolution for years, in the range of 10-20 minutes. This resolution is too low to permit the detection of a single neurotransmission event, where a temporal resolution of milliseconds to seconds is needed. But this is sufficient to monitor slower events such as drug delivery or metabolic changes, for which a temporal resolution of minutes or hours is enough (Saylor et al., 2017). Nevertheless, thanks to this flexibility with respect to the analytical systems, the list of analytes that were successfully collected *in vivo* with these sampling methods, and later measured, is large (Chefer et al., 2009; Perry et al., 2009). Namely, it includes neurotransmitters (DA (Ungerstedt & Pycock, 1974), Glu (Ueda et al., 1992), acetylcholine (ACh) (Slaney et al., 2013)),

metabolites such as glucose (Fray et al., 1997; McNay & Gold, 1999; M. Wang et al., 2008), cytokines (Stenken & Elkins, 2015), neuropeptides (Wotjak et al., 2008) and drugs (Shannon et al., 2013). In summary, the broad panel of measurable molecules makes fluid sampling approaches very appealing to study the brain. Especially since these molecules can be of very different nature and can impact the homeostasis at different scales of time, and of concentration.

1.3.2 Microtechnologies for sampling probes

All brain fluid sampling systems are invasive and the footprint of microdialysis probes (frequently $>100\text{ }\mu\text{m}$ in diameter) is usually larger than the one of push-pull probes, that do not require a membrane and that could be produced from pulled capillaries (Cabay et al., 2018; Saha-Shah et al., 2016). Therefore, microfabrication technologies have allowed researchers to reduce the footprint of sampling probes in the last decade, thus allowing less invasive procedures, improved spatial resolution, and reduction of the flow rates down to 10-30 nL/min to improve analyte collection (Fisher & Shippy, 2022).

Scaling down microdialysis membranes was attempted in polyimide (Metz, Trautmann, et al., 2004), parylene (Kotake et al., 2008) and silicon devices (W. H. Lee et al., 2016; Zahn et al., 2005) that integrated fluidic channels under a porous membrane. A polyimide membrane and a silicon microdialysis probe are respectively shown in Figure 1.5a-b. In practice, only few microfabricated microdialysis probes were reported (Kotake et al., 2008; W. H. Lee et al., 2016; Zahn et al., 2005), probably due to difficult integration of the membrane for reliable *in vivo* sampling (Ngernsutivorakul, 2018). Alternatively, push-pull probes were also reported, that are easier to produce by pulling fused silica capillaries (Cabay et al., 2018; Fisher & Shippy, 2022), or with planar microfabrication technologies, since they only require two microchannels with openings close to each other. Examples of silicon push-pull probes are shown in Figure 1.5c-e, that integrate electrical recording features (d) or a frit to prevent clogging of the channels with debris of the extracellular matrix (e). Flexible probes were fabricated too, such as in Figure 1.5f, where polyimide and SU-8 technologies were used, to respectively integrate electrical and fluidic features. Moreover, probes were also made, that allow punctual collection of analytes.

Hence, a wireless system was recently reported, that uses microchannels within a soft PDMS needle for delivery and sampling of perfusate. This implementation is however limited to 4 samples of 500 nL each (G. Wu et al., 2022). As a last example, a microinvasive platform that integrates a nitinol-activated nanofluidic pump connected to a capillary was also recently reported. It proposed to infuse perfusate for 10 minutes at 95 nL/min, and to sample it back for 20 minutes at 65 nL/min. Thus, samples of 1.5 μ L were collected, that were later analyzed by LC-MS to demonstrate the successful collection of proteins and peptides (Raman et al., 2020).

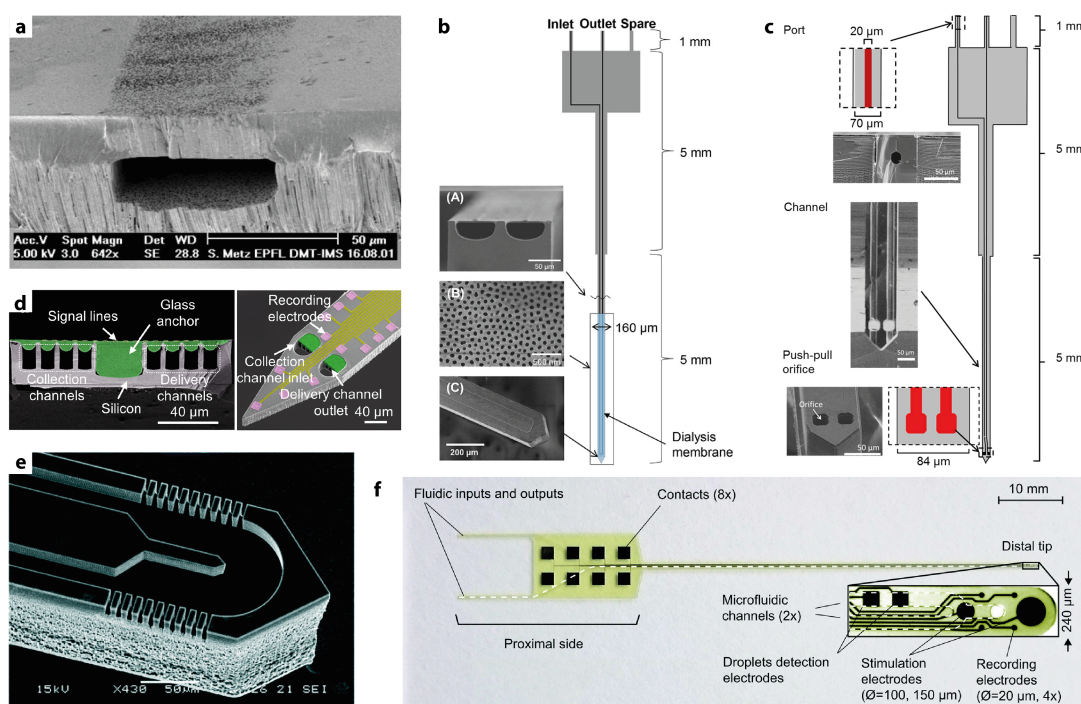


Figure 1.5: Microfabricated fluid sampling technologies. **a** SEM image of a nanoporous membrane integrated above a fluidic channel on chip. *Adapted with permission from Metz, Trautmann, et al. (2004).* **b** Silicon microdialysis probe with integrated silicon dialysis membrane. *Adapted with permission from W. H. Lee et al. (2016).* Copyright 2016 American Chemical Society. **c** Silicon push-pull probe with channels and fluidic openings at the tip. *Adapted with permission from W. H. Lee et al. (2013).* Copyright 2013 American Chemical Society. **d** Cross-section and tip of a silicon push-pull probe combining fluidic channels and electrodes. *Adapted with permission from Chae et al. (2021).* **e** Silicon-glass push-pull probe that integrates a frit to capture molecules while filtering the debris of the extracellular matrix. *Adapted with permission from van den Brink et al. (2019).* **f** Polyimide/SU-8 neural probe integrating microfluidic channels and electrodes for stimulation and recording of neural activity. The channels form a T-junction at the tip, that allows segmenting the sampled fluid into droplets within a carrier phase. *Reprinted with permission from Petit-Pierre et al. (2016).*

Droplet sampling approaches

With fluidic sampling approaches, temporal variations of the concentration of analytes during sampling are captured in bands of analytes at different locations in the dialysate. Thus, they must be kept spatially separated to maintain the temporal resolution of the sampling. However, Taylor dispersion occurs in the channels and in tubing, that causes broadening of the bands, thus a loss of temporal resolution (K. N. Schultz & Kennedy, 2008). A solution to this issue was first demonstrated in 2008 by the group of Prof. Robert Kennedy, that coupled the outlet of a microdialysis probe to a droplet generator in a PDMS chip. This allowed the segmentation of the dialysate into 6-28 nL plugs of samples within a phase of perfluorodecalin (M. Wang et al., 2008). Moreover, the detection of a step change in fluorescein concentration at the interface of the probe was reported with a temporal resolution of 15 s, as compared to 25 s to 160 s for unsegmented dialysate. Following on this, this group also reported a temporal resolution as high as 2 s with a microdialysis probe (M. Wang et al., 2010). Later, this strategy was also applied to microfabricated push-pull probes that were modified versions of the probe shown in Figure 1.5c, with an extra channel to deliver drugs in the push line. As a result, this implementation allowed monitoring Glu, ACh, GABA, and glutamine after chemical stimulation and with a temporal resolution of 6 s (Ngernsutivorakul, Steyer, et al., 2018).

Moreover, microfabricated push-pull probes that directly integrate the droplet segmentation feature were also reported. This includes a flexible polyimide/SU-8 neural interface that combines electronic and fluidic features (Petit-Pierre et al., 2016). The needle of the probe is illustrated in Figure 1.5f and it integrates a T-junction that makes it possible to sample droplets at the tip. This has allowed the sampling of 0.84 nL droplets at 6 Hz and the collection of droplets that accurately reflected a step change of concentration around the probe *in vitro*. This system was later augmented with a perfusion capillary and push-pull droplet sampling was reported in the brain of rats. Thus, 18 nL droplets were collected at the outlet capillary every 50 s. That allowed measurement of the physiological concentration of Cu and Zn by mass spectrometry (Petit-Pierre et al., 2017). In addition, direct push-pull sampling of droplets was also reported inside a silicon probe, that is shown in Figure 1.5e. The probe integrates a frit, as a microdialysis-like probe with an array of 3 μm x 20 μm lateral openings (van den Brink et al., 2019) to prevent clogging with debris during sampling. Using this approach, collection

of neurotransmitters was reported, with a temporal resolution of 3 to 6 s *in vitro*. Furthermore, with the implementation of a fluorescent assay at the outlet, the monitoring of Glu release was demonstrated in the brain of mice, with a temporal resolution of a few seconds to minutes.

Since its first demonstration in 2008, the droplet segmentation approach has gained popularity and a similar approach was also recently implemented in a wearable device to improve monitoring of glucose in dermal tissue (Nightingale et al., 2019). Furthermore, another probe also proposed segmentation by air at its outlet, instead of oil (Chae et al., 2021). However, this system did not use droplets to enhance the temporal resolution, but just to separate samples at the outlet. The needle of this probe is illustrated in Figure 1.5d. In fact, this probe also combines electrodes for recording of electrical activity, and fluidic channels for drug delivery and push-pull sampling. For sampling, fluid was continuously sampled at 100 nL/min and segmented by a plug of air at the outlet every 20 minutes, thus providing 2 μ L samples that could be processed by UPLC-MS/MS to measure Glu and GABA. In the brain of mice, this allowed monitoring the effects of stimulatory and inhibitory drugs, based on the electrical activity of the tissue and on the concentration of the neurotransmitters in the samples. Finally, the separation of samples by air was also recently reported at the tip of two capillaries with a porous head produced by Two-Photon Polymerization (Barbot et al., 2021), but this was not demonstrated for sampling *in vivo*.

1.4 Thesis positioning

Multiple methods exist to probe the neurochemicals in the brain and help scientists understand this organ better. This is critical to understand its pathologies and develop efficient treatments. Moreover, a wide variety of molecules exist, of which changes of concentration occur at different time scales. Therefore, they require different measurement methods and a comparative summary of four main families of methods to measure neurochemicals in the brain is reported in Table 1.1. On one hand, non-invasive functional imaging methods offer great performances but are limited in temporal and spatial resolutions, and in the molecules that can be monitored. On the other hand, fast variations are probably better monitored with electrochemical methods, but these methods are limited in the molecules that can be

measured. Finally, fluidic sampling approaches provide the most versatile solution in terms of molecules that can be addressed, since they collect many different molecules at a time and can be coupled to a wide palette of analytical methods. Therefore, these methods appear appropriate to study the brain and the development of its diseases.

Nonetheless, these methods would still benefit from further improvements. Although they have suffered from low spatial and temporal resolutions for a long time, because of the volume and mass requirements of analytical methods, this has changed with the improvements of analytical methods that require less material and can process smaller samples. In fact, this has allowed the processing of small droplets of dialysate and the droplet sampling approach introduced by M. Wang et al. (2008) has improved the temporal resolution of sampling methods by preventing dispersion of the analytes in the dialysate. This approach has sparked the interest of the microfluidics community and droplet sampling was adopted to improve the properties of fluidic sampling methods (W. H. Lee et al., 2013; Ngernsutivorakul, Steyer, et al., 2018; Nightingale et al., 2019; Petit-Pierre et al., 2016; van den Brink et al., 2019). Thus, microfabrication technologies have contributed to these advances, not only by allowing production of smaller probes with fluidic and electrical features, but also by providing microfluidic solutions to handle and analyze these biological droplet samples.

Nevertheless, there are limitations that these solutions did not address and which are inherent to the continuous sampling nature: the transient regime that causes an unstable recovery fraction at first and the limited recovery fraction that follows. Because of these effects, the concentration in the samples does not necessarily represent the actual concentration of the extracellular space accurately and sampling experiments can be long. Although these limitations can be addressed by low flow rate sampling methods, they offer a lower temporal resolution. Thus, they are not optimal to resolve short molecular events because they have a long sampling time (Cabay et al., 2018; Fisher & Shippy, 2022; Raman et al., 2020).

Therefore, developments should be performed that improve the stability of the recovery fraction and its level, while also providing a high temporal resolution. This would be a significant advancement of the field, as it would allow absolute quantification of baseline molecular concentrations and of concentration changes in the brain. This could also potentially allow

measurement of molecules that are depleted very fast with continuous methods and provide a better picture of the molecular content of the ECF. Moreover, the absence of transient regime would also allow faster sampling experiments. Finally, microfabrication technologies could also be exploited to develop a probe with further multimodal stimulation features, in addition to sampling features. This would allow chemical recording of the tissue response following different stimuli and improve the development of new therapies to treat brain disorders.

1.4.1 Thesis objectives

Droplets provided an efficient solution to increase the temporal resolution of fluid sampling probes, that offer powerful solutions to quantify molecules in the brain. Thus, multiple implementations of droplet sampling were reported that aimed for fast sampling and segmentation. However, the limitations related to the low recovery fraction and to the transient regime were not solved by droplets yet. In fact, droplets could also be used for that purpose. Thus, by adjusting the droplet generation approach and by sampling droplets on demand, instead of continuously, droplets could allow collection of highly concentrated samples at very precise moments, without transient regime, and within shorter sampling experiments. Moreover, droplets could also allow the collection of samples repeatedly, with a high temporal resolution, to quantify not only basal concentrations, but also concentration changes over time. Furthermore, microfabrication technologies could also enable the development of a probe that does not only allow chemical sampling, but chemical, electrical, and optical stimulation of the brain. Combined together, these properties would contribute to improving quantitative molecular studies in the brain. This would help unveil the physiology of the brain and help the development of new treatments against brain disorders on solid molecular bases.

Table 1.1: Summary of four main families of methods to measure neurochemicals in the brain

Properties	PET scan	Magnetic resonance methods - fMRS, fMRI, NMR	Electrochemical methods	Microdialysis & push-pull sampling
Footprint	Non-invasive. (Ngernsutivorakul, White, et al., 2018)	Non-invasive. (Alger, 2009; Ngernsutivorakul, White, et al., 2018)	Invasive: 5-100 μm (depends on probe size). (Ngernsutivorakul, White, et al., 2018; Z. Wu et al., 2022; Y. Zhang et al., 2021)	Invasive: <500 μm (microdialysis); <100 μm (microfabricated push-pull). (Kennedy, 2013; Stenken & Patton, 2017)
State of the subject	Mostly immobilized, freely moving possible. (Herfert et al., 2020; Miranda et al., 2019)	Immobilized. (Alger, 2009)	From anesthetized to freely moving. (C. Liu et al., 2020; Schwerdt et al., 2018)	From anesthetized to freely moving with/without tethering. (Al-Hasani et al., 2018; Chefer et al., 2009; Ungerstedt & Pycock, 1974; G. Wu et al., 2022)
Temporal resolution	From s to min. (Catana, 2019; G. Wang, 2019)	From few s to few min. (Rhodes, 2017)	From μs to s, depends on functionalization/method/responsiveness. (Frank et al., 2019; Ngernsutivorakul, White, et al., 2018; Z. Wu et al., 2022)	From 5-10 s (droplet push-pull sampling), to 10-30 min (traditional microdialysis and low flow push-pull sampling). (Fisher & Shippy, 2022; Ngernsutivorakul, White, et al., 2018; Raman et al., 2020; Song et al., 2012)
Spatial resolution	1.3-1.5 mm. (Herfert et al., 2020)	>1 mm. (Alger, 2009; Ngernsutivorakul, White, et al., 2018)	10-100 μm (depends on the size of electrodes). (Frank et al., 2019; Ngernsutivorakul, White, et al., 2018)	From 100 μm to 4 mm, depends on probe geometry, and analyte penetration depth. (Chefer et al., 2009; Ngernsutivorakul, White, et al., 2018; Y. Zhang et al., 2021)
Limit of detection (LoD)	LoD in pM to nM ranges, depends on tracers. (Ngernsutivorakul, White, et al., 2018)	LoD in μM to mM ranges. No tracers, limited sensitivity. (Alger, 2009; Ngernsutivorakul, White, et al., 2018)	LoD mostly in nM to μM ranges, depends on functionalization/method (amperometry, FSCV, field effect transistor). (Ngernsutivorakul, White, et al., 2018; C. Zhao et al., 2021)	LoD in pM to nM ranges, depends on analytical method. (Ngernsutivorakul, White, et al., 2018)
Absolute quantification	Possible. (Herfert et al., 2020)	Mostly relative, absolute possible with calibration. (Alger, 2009; Marjańska et al., 2012)	Possible. Mostly for differential signals, rather than baseline quantification. (Bucher & Wightman, 2015)	Possible, for basal concentration, depends on analytical method. (Kho et al., 2017; Y. Zhang et al., 2021)
Selectivity	High, depends on tracers. (Nasrallah & Dubroff, 2013)	High. (Alger, 2009; Gruetter et al., 2003)	Non-functionalized: low, determined by oxidation/reduction voltage. Functionalized: high, determined by recognition element. (Ngernsutivorakul, White, et al., 2018; Z. Wu et al., 2022)	High, depends on membrane and analytical method. (Ngernsutivorakul, White, et al., 2018; Perry et al., 2009; Y. Zhang et al., 2021)
Multiplexing	Limited, depends on the availability of tracers. (Herfert et al., 2020)	High. (Gruetter et al., 2003; Marjańska et al., 2012)	Non-functionalized: limited to electroactive species. Functionalized: limited by the availability of functionalization. (Ngernsutivorakul, White, et al., 2018; Y. Zhang et al., 2021)	High, depends on analytical method. (Ngernsutivorakul, White, et al., 2018)
Advantages	Non-invasive, for human studies.	Non-invasive, for human studies.	High spatial and temporal resolutions, limited invasiveness, live readout.	Versatility (collection of many molecules and coupling to the best suited analytical method), absolute baseline quantification.
Limitations	Availability of tracers, expensive. (K. N. Schultz & Kennedy, 2008)	Expensive equipment, whole tissue, low sensitivity.	Limited measurable analytes, challenges for baseline quantification, invasive.	Limited temporal and spatial resolutions, invasive, readout usually delayed.

Therefore, this thesis focuses on the development of a multimodal probe for acute experiments in the brain of mice, and of an alternative brain fluid sampling approach in droplets. This will allow to accurately collect and quantify the concentration of the molecules in the ECF, with a better temporal resolution than low flow rate methods. The new sampling approach is called Droplet on Demand (DoD) and it could be viewed as an intermittent sampling approach. It consists in a specific push-pull sampling sequence that operates in steps, and that is implemented in the probe. The sequential nature of the sampling will allow turning on and off the withdrawal of molecules from the brain, thus allowing on-demand sampling over narrow temporal windows. This will allow the tissue to equilibrate between samplings to avoid a transient regime and will also allow to sample molecules at specific times of interest, within shorter experiments than with continuous sampling approaches.

1.4.2 Thesis structure

This work describes the development of the DoD approach, from the design to the analysis of samples collected during *in vivo* experiments. It starts with an introduction to the theory of microdialysis sampling in chapter 2, to highlight the limitations of continuous sampling methods. This will guide the development of the DoD approach, to allow repeated samplings at high recovery fraction. Then, the principles of DoD will be illustrated in simulations. Next, chapter 3 reports the fabrication of the probe and the implementation of DoD sampling. Then, then performances of DoD sampling are verified in an *in vitro* model and in the brain in chapter 4. Following on this, the content of the droplets collected in the brain is measured by mass spectrometry in chapter 5. This will verify the properties of DoD for the collection of glucose in the brain of mice. In addition, the detection of neurotransmitters by mass spectrometry and the measurement of DA with a chip for chronoamperometry in droplets are presented in chapter 6. Finally, the work is summarized in chapter 7, and future directions are discussed.

Chapter 2

Theoretical bases of sampling systems

Part of this chapter is adapted with permission from Teixidor, J., Novello, S., Ortiz, D., Menin, L., Lashuel, H. A., Bertsch, A., & Renaud, P. (2022). On-Demand Nanoliter Sampling Probe for the Collection of Brain Fluid. Analytical Chemistry, 94(29), 10415–10426. Copyright 2022 American Chemical Society. This chapter discusses the theory of fluidic sampling methods. First the theoretical foundations of microdialysis sampling are introduced. Based on this, the DoD method is proposed to solve some limitations of continuous sampling methods. Finally, the concepts of DoD are studied within simulations.

2.1 Theory of continuous sampling by microdialysis

Microdialysis and push-pull probes allow the capture of analytes from the ECF in a dialysate. However, the concentration in the dialysate is lower than the concentration in the ECF, thus making the absolute quantification of the molecules in the ECF challenging. Theoretical developments and analytical models have been reported to study how the concentration of an analyte is recovered in the dialysate. These models allow studying how the system transitions from the start of the sampling to the steady-state sampling regime (Bungay et al., 1990; Bungay et al., 2006; Bungay et al., 2011; C.-F. Chen, 2017; K. C. Chen, 2006; Morrison et al., 1991; Morrison et al., 1999). This section aims to study the theory governing the sampling with

microdialysis probes and to identify how sampling can be improved to quantify molecules in the ECF more accurately. Thus, it reports the broad lines of the development proposed by Bungay et al. (2006). Moreover, although this development applies to a microdialysis probe, the same concepts apply to push-pull probes without membrane, since both methods sample analytes from the ECF, by diffusion into a continuous flow of dialysate.

2.1.1 Model of the system

A model is presented that considers the collection of a single analyte with microdialysis. It is illustrated in Figure 2.1.

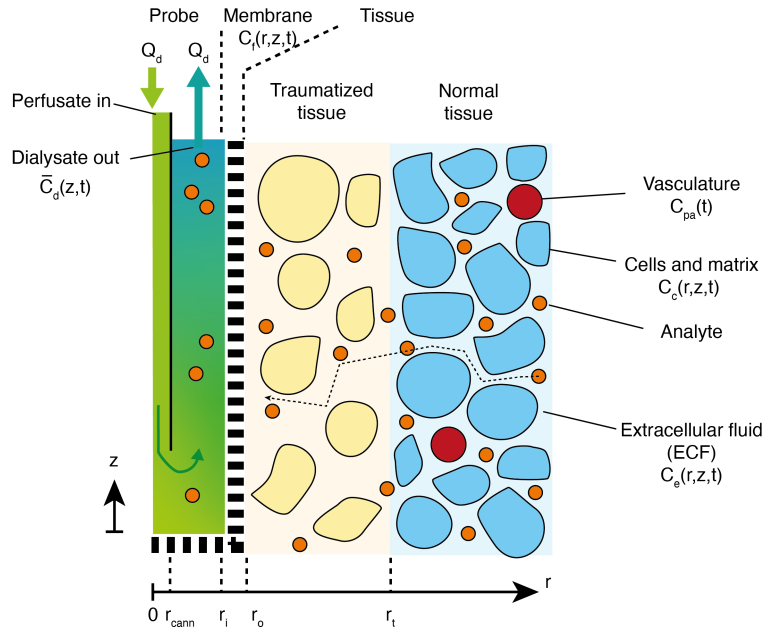


Figure 2.1: Schematic of the system with a cylindrical microdialysis probe. It consists of 3 domains: the annulus of perfusate/dialysate ($r_{cann} \leq r \leq r_i$) with a concentration C_d , the membrane ($r_i < r \leq r_o$) with a concentration C_m , and the tissue ($r > r_o$) with the extracellular concentration C_e . The analyte from the tissue reaches the perfusate by radial diffusion through the ECF and through the membrane. It gets collected in the dialysate, flowing along the z -axis, with a flow rate Q_d . Physiological interactions occur in the tissue, within the ECF, within the cells and with the vasculature. A traumatized tissue could be considered ($r_o < r \leq r_t$), with perturbed interactions with respect to the normal tissue ($r > r_t$), but the tissue is considered normal in this development, after a healing period. At $r = \infty$, the tissue has a concentration C_e^∞ , that should be reflected in the dialysate for a quantitative analysis.

During sampling with a microdialysis probe, 3 regions must be considered: the annulus of dialysate, the membrane, and the tissue. The tissue is an active region, where exchanges take place between the ECF, the intracellular space (the cells), and the vasculature, and where molecules are released and consumed. Due to the damages induced by the insertion and the potential reactions of the tissue to the probe, the tissue space can be further split into a traumatized tissue and a normal tissue (K. C. Chen, 2006). Since a healing period is usually allowed before sampling, the tissue will be considered uniform here. Initially, the concentration of the analyte is considered spatially uniform in the ECF, at concentration C_e^∞ . This level is the one that an experimenter would like to quantify by microdialysis. The membrane is a passive domain with a solid and a fluid phase and the analyte diffuses from the tissue to the dialysate through the membrane. Finally, the annulus of dialysate contains the perfusate/dialysate that flows inside the probe at rate Q_d .

After the insertion of the probe that is filled with perfusate, the collection of the analyte into the dialysate starts spontaneously, even in absence of flow inside the probe, since sampling is driven by diffusion. When the flow of perfusate Q_d starts, the dialysate exits the probe, with a concentration that depends on its interaction time with the membrane. Its concentration depends, in fact, on the concentration at the membrane, which depends on the spatial concentration in the ECF, which depends on the mass transport properties, and on the physiology of the analyte in the tissue.

In summary, from a mechanistic point of view, the tissue is initially in homeostatic conditions with a spatially homogeneous analyte concentration in the ECF, equal to C_e^∞ . In the tissue, physiological interactions behave as "sinks" that remove analytes from the ECF or as "sources" that release analytes into the ECF to maintain the homeostasis of the tissue. As soon as the microdialysis probe is inserted in the tissue, it starts removing analytes from the ECF. Thus, it acts as a "sink" that perturbs the equilibrium. Therefore, a new equilibrium (steady-state) needs to be reached. The rate at which this is reached depends on the mass transport of the analyte through the entire system, which is driven by diffusion, and it also depends on the physiological interactions of the analyte in the tissue. The analytical development in the next section will describe these processes mathematically, to illustrate their impact and their effect on the concentration of a single analyte collected in the dialysate.

2.1.2 Mathematical model of microdialysis

To model sampling and evaluate the concentration of the analyte that is collected in the dialysate, the concentration of the analyte $C[r, z, t]$ needs to be expressed in the whole system that is shown in Figure 2.1.

For the mathematical development, cylindrical coordinates are used, and the parameters r , z and t respectively stand for the radial distance, the axial distance, and the time. The axis of the microdialysis probe corresponds to the z axis and the length of the membrane is l_m . Diffusion is considered in all domains, but it is neglected in the azimuthal and axial directions. Convection only occurs in the dialysate, that has a flow rate Q_d along the z -axis. The variables C , Φ , b , D , k^x , k^r and G respectively represent concentrations, volume fractions, equilibrium binding ratios, diffusion coefficients, first order exchange rates, first order degradation rates, and zero-order generation rates. The subscripts t , e , pa , c , f and d respectively represent the tissue ($r > r_o$), the ECF (extracellular space), the plasma (vasculature), the cells (intracellular space), the fluid in the membrane ($r_i < r \leq r_o$), and the dialysate ($r_{cann} \leq r \leq r_i$). Domain-specific diffusion coefficients are also considered: D_d in the perfusate is the diffusion coefficient in water D_0 , D_m in the membrane, D_e in the ECF, D_c in the intracellular space, and D_t , an average diffusion coefficient in the tissue.

To begin with the analysis, mass balances must be written for the tissue and the probe.

Mass balances for the tissue

To obtain a mass balance for the tissue, mass balances must be found for the extracellular space (ECF) and for the intracellular space. The mass balance for the ECF illustrates all the physiological effects that need to be considered in the analysis. This mass balance for a chosen analyte is reported in Equation 2.1 and is described below with the extracellular concentration $C_e[r, z, t]$.

$$\begin{aligned}
\Phi_e b_e \frac{\partial C_e[r, z, t]}{\partial t} &= \Phi_e D_e \frac{1}{r} \frac{\partial}{\partial r} r \frac{\partial C_e[r, z, t]}{\partial r} \\
&\quad + \Phi_e (k_{pe}^x C_{pa}[t] - k_{ep}^x C_e[r, z, t]) \\
&\quad + (1 - \Phi_e) (k_{ce}^x C_c[r, z, t] - \Phi_e k_{ec}^x C_e[r, z, t]) \\
&\quad + \Phi_e (G_e - k_e^r C_e[r, z, t])
\end{aligned} \tag{2.1}$$

accumulation *diffusion* *blood – ECF exchanges* *cells – ECF exchanges* *synthesis and degradation*

The left side describes the accumulation of the analyte in the ECF over time, where b_e is an equilibrium binding ratio in the ECF. On the right, the first term stands for the diffusion of the analyte in the ECF, with an effective diffusion coefficient D_e . In fact, D_e is lower than D_0 , because of the tortuous path that the analyte needs to follow through the extracellular space and that is illustrated in Figure 2.1. The relationship between D_e and D_0 is expressed with a tortuosity factor $\lambda = \sqrt{D_0/D_e}$, described in Syková and Nicholson (2008). Blood-ECF exchanges consider the respective first-order exchange rates k_{pe}^x and k_{ep}^x , from the plasma to the ECF and reversely, with $C_{pa}[t]$ the analyte concentration in the plasma. Similarly, the cells-ECF exchanges consider an intracellular analyte concentration $C_c[r, z, t]$ and the respective first order analyte exchange rates k_{ce}^x and k_{ec}^x , from the cells to the ECF and reversely. Finally, the physiology in the ECF includes a zero-order analyte generation rate G_e and a first-order analyte degradation rate k_e^r .

Similarly, Equation A.1 is presented in Appendix A and describes the mass balance for the intracellular space. Under the assumption that the compartments are always in quasi-equilibrium, with rapid extracellular-to-intracellular exchanges, the mass balances in Equation 2.1 and in Equation A.1 provide a single mass balance for the tissue in Equation 2.2.

$$K_{te} \frac{\partial C_e[r, z, t]}{\partial t} = D_t \frac{1}{r} \frac{\partial}{\partial r} r \frac{\partial C_e[r, z, t]}{\partial r} + G_t + \Phi_e k_{pe}^x C_{pa}[t] - k_t C_e[r, z, t] \quad (2.2)$$

$$K_{te} = C_t / C_e = b_e \Phi_e + b_c (1 - \Phi_e) K_{ce} \quad (2.3)$$

$$G_t = \Phi_e G_e + (1 - \Phi_e) G_c \quad (2.4)$$

$$D_t = \Phi_e D_e + (1 - \Phi_e) D_c K_{ce} \quad (2.5)$$

$$k_t = \Phi_e k_{ep}^x + \Phi_e k_e^r + (1 - \Phi_e) k_c^r K_{ce} \quad (2.6)$$

In this expression, K_{te} is the equilibrium ratio of the total tissue concentration to the free extracellular concentration for the analyte (Equation 2.3), G_t is its total generation rate for the whole tissue (Equation 2.4), D_t is its effective diffusion coefficient through the whole tissue (Equation 2.5) and k_t is the analyte elimination rate constant for the whole tissue (Equation 2.6). They are expressed from the parameters for the extracellular and intracellular compartments, where b_c is the intracellular equilibrium binding ratio, G_c is the analyte generation rate, D_c is the intracellular analyte diffusion coefficient and k_c^r is the intracellular analyte reaction rate. The ratio of compartmental concentrations between the intracellular space and the extracellular space is defined as $K_{ce} = C_c / C_e$. It is assumed constant because of the linearity and reversibility of the binding and of the exchanges between the compartments and should be determined experimentally.

At this point, the model proposes to express the analyte concentration with respect to the concentration of the unperturbed ECF, $C_e^\infty[t]$, far away from the probe. In fact, this is the concentration of interest. Thus, since the spatial derivative far from the probe is null, the mass balance for the ECF far from the probe is obtained from Equation 2.2 and expressed in Equation 2.7.

$$K_{te} \frac{\partial C_e^\infty[t]}{\partial t} = G_t + \Phi_e k_{pe}^x C_{pa}[t] - k_t^r C_e^\infty[t] \quad (2.7)$$

Combining Equation 2.2 and Equation 2.7 gives Equation 2.8, a mass balance for the whole tissue, where the analyte concentration in the ECF is expressed relative to $C_e^\infty[t]$.

$$K_{te} \frac{\partial(C_e[r, z, t] - C_e^\infty[t])}{\partial t} = D_t \frac{1}{r} \frac{\partial}{\partial r} r \frac{\partial(C_e[r, z, t] - C_e^\infty[t])}{\partial r} - k_t(C_e[r, z, t] - C_e^\infty[t]) \quad (2.8)$$

Mass balance for the probe

A mass balance for the probe is also required. It can be obtained by finding mass balances for the membrane and for the annulus of dialysate. Thus, these mass balances can be coupled by using boundary conditions for the continuity of the concentration and for the continuity of the flux. These steps are reported in section A.2 of Appendix A. They provide the overall mass balance of the probe, expressed in Equation 2.9.

$$\frac{Q_d}{2\pi r_o} \frac{\partial \bar{C}_d[z, t]}{\partial z} = \mathcal{P}_{P_o} (C_e[r_o, z, t] - \bar{C}_d[z, t]) \quad (2.9)$$

This expression uses $\bar{C}_d[z, t]$, that is introduced as the radial-average of $C_d[r, z, t]$, the concentration in the dialysate. It also introduces the permeability of the probe \mathcal{P}_{P_o} , defined in Equation A.11 of Appendix A. \mathcal{P}_{P_o} represents the inverse of the resistance to the mass transport of the analyte, from the outer surface of the membrane to the dialysate, and it depends on the parameters of the probe and of the analyte.

From this point on, the mass balances found in Equation 2.8 and Equation 2.9 can be used to find solutions for the concentration in the entire system. And since the mass balance in Equation 2.8 presents a temporal derivative, there are two solutions to consider: one for the transient regime and one for the steady-state regime.

Transient regime

Finding a solution to the transient regime requires the consideration of the temporal derivative in Equation 2.8. The analytical development is long and complex; thus, simulations are frequently used to study this regime. Moreover, the samples from the transient regime are usually discarded by researchers, who are rather interested in the steady-state regime for per-

forming measurements. Therefore, the solution to the transient regime will not be discussed analytically here but interested readers will find the details of the development in (Bungay et al., 2006; Morrison et al., 1991). Nevertheless, the transient regime will be discussed later in this section because it is responsible for some of the limitations of continuous sampling methods.

Steady-state regime

In the steady-state, the time derivative in Equation 2.8 is null. This helps to find an analytical solution for the concentration in the whole system. This also allows defining the extraction fraction E_d , an expression that links the measurable concentrations of the perfusate C_d^{in} and of the dialysate C_d^{out} , with the unknown distant extracellular concentration C_e^∞ that a researcher would like to quantify. It is defined in Equation 2.10. In the case of pure sampling, when the perfusate is initially free of the analyte ($C_d^{in} = 0M$), it is called relative recovery or recovery fraction, and expressed in Equation 2.11. Since sampling is the focus of this work E_d will be called the recovery fraction and it will also be symbolized by η later in this work.

$$E_d = \frac{C_d^{in} - C_d^{out}}{C_d^{in} - C_e^\infty} \quad (2.10)$$

$$E_d \Big|_{C_d^{in}=0} = \frac{C_d^{out}}{C_e^\infty} = \eta \quad (2.11)$$

E_d can be expressed by the parameters of the probe and of the flow rate Q_d , as in Equation 2.12, where S_o is the total surface area of the membrane of length l_m .

$$E_d = 1 - \exp\left(-\frac{\mathcal{P}_o S_o}{Q_d}\right) \quad (2.12)$$

$$S_o = 2\pi r_o l_m \quad (2.13)$$

$$\mathcal{P}_o = \left(\frac{1}{\mathcal{P}_{P_o}} + \frac{1}{\mathcal{P}_{t_o}}\right)^{-1} \quad (2.14)$$

$$\mathcal{P}_{t_o} = \frac{D_t}{\Gamma} \left(\frac{K_1[r_o/\Gamma]}{K_0[r_o/\Gamma]} \right) \quad (2.15)$$

$$\Gamma = \sqrt{D_t/k_t} \quad (2.16)$$

In these equations, \mathcal{P}_o is the permeability of the whole system, defined in Equation 2.14. It is composed of the permeability of the probe \mathcal{P}_{p_o} , which is defined in Equation A.11, and which depends on the characteristics of the probe and on the diffusion of the analyte in all domains. \mathcal{P}_o is also composed of the permeability of the tissue \mathcal{P}_{t_o} , defined in Equation 2.15, and where K_0 and K_1 are modified Bessel functions of the second kind of zero and of first order, respectively. \mathcal{P}_{t_o} highly depends on the characteristics of the analyte, through the diffusion coefficient D_t and its elimination rate constant in the tissue k_t , respectively defined in Equation 2.5 and Equation 2.6. These parameters define the penetration depth Γ , which represents the radial distance from the probe over which the analyte concentration in the ECF is disturbed by the probe that removes analytes from the system.

The steady-state solution allows one to express the spatial concentration of the analyte in all domains: in the ECF of unperturbed tissue as C_e^∞ in Equation 2.17, in the ECF of depleted tissue as $C_e[r, z]$ in Equation 2.18, in the membrane as $C_f[r, z]$ in Equation 2.19, and in the dialysate as $\bar{C}_d[z]$ in Equation 2.20.

$$C_e^\infty = \frac{G_t + \Phi_e k_{pe}^x C_{pa}}{k_t} \quad (2.17)$$

$$\frac{C_e[r, z] - C_e^\infty}{\bar{C}_d[z] - C_e^\infty} = \frac{K_0[r/\Gamma] \mathcal{P}_o}{K_0[r_o/\Gamma] \mathcal{P}_{t_o}} \quad (2.18)$$

$$\frac{C_f[r, z] - C_e^\infty}{\bar{C}_d[z] - C_e^\infty} = \mathcal{P}_o \left[\frac{\ln[r/r_o]}{\ln[r_i/r_o]} \frac{1}{\mathcal{P}_{m_o}} + \frac{1}{\mathcal{P}_{t_o}} \right] \quad (2.19)$$

$$\frac{\bar{C}_d[z] - C_e^\infty}{C_d^{in} - C_e^\infty} = \exp\left(-\frac{\mathcal{P}_o S_o}{Q_d} \frac{z}{l_m}\right) \quad (2.20)$$

Averaging the solutions along the z-axis, over the length of the membrane l_m , allows easier analysis and graphical representation of the analyte concentration profiles with respect to the analyte concentration of unperturbed ECF. Moreover, in the case of sampling ($C_d^{in} = 0$), the solutions are provided by Equation 2.21, Equation 2.22, and Equation 2.23.

$$\frac{\langle C_e \rangle [r]}{C_e^\infty} = 1 - \frac{Q_d E_d}{\mathcal{P}_{t_o} S_o} \left(\frac{K_0 [r/\Gamma]}{K_0 [r_o/\Gamma]} \right) \quad (2.21)$$

$$\frac{\langle C_f \rangle [r]}{C_e^\infty} = 1 - \frac{Q_d E_d}{S_o} \left[\left(\frac{\ln[r/r_o]}{\ln[r_i/r_o]} \right) \frac{1}{\mathcal{P}_{m_o}} + \frac{1}{\mathcal{P}_{t_o}} \right] \quad (2.22)$$

$$\frac{\langle \bar{C}_d \rangle}{C_e^\infty} = 1 - \frac{Q_d E_d}{\mathcal{P}_o S_o} \quad (2.23)$$

From these equations, the r -dependency in Equation 2.21 suggests that the tissue is depleted by the sampling, while the Γ -dependency suggests that the extent of the depletion layer depends on the physiological interactions of the analyte in the tissue. In fact, the concept of the penetration depth Γ is critical for the steady-state and varies significantly among analytes with similar diffusion coefficients in the ECF.

To illustrate the concept of Γ , DA molecules and sucrose molecules can be considered. However, instead of the elimination rate constant k_t [1/h] in the equations of the model, this concept is usually provided as the clearance CL [mL/h], that represents the volume of ECF or of plasma that is eliminated of the analyte per unit of time. It can also be expressed by CL_m [mL/h/(g-tissue)], that is CL normalized by the mass of the tissue, and that is proportional to k_t . Thus, DA and sucrose have similar diffusion coefficients, respectively $D_{DA} = 2.38 \cdot 10^{-6} \text{ cm}^2/\text{s}$ and $D_{sucrose} = 3 \cdot 10^{-6} \text{ cm}^2/\text{s}$, but significantly different CL_m values, respectively $CL_{m,DA} = 10000 \text{ mL/h/(g-tissue)}$ and $CL_{m,sucrose} = 0.1 \text{ mL/h/(g-tissue)}$. Because if this, they have estimated penetration depths $\Gamma_{DA} = 0.01 \text{ mm}$ and $\Gamma_{sucrose} = 2 \text{ mm}$ (Stenken & Patton, 2017; Syková & Nicholson, 2008). This suggests that sampling depletes the tissue deeper in the case of analytes with slow tissue exchanges (low k_t , low CL_m), compared to rapidly exchanged analytes (high k_t , high CL_m), and that the spatial resolution of the sampling process depends on the analyte.

Furthermore, this also suggests that, for an analyte with a short Γ (high k_t), the permeability of the probe has a greater impact on the recovery fraction, relative to the permeability of the tissue. This is because this analyte does not travel over a long distance in the tissue before being eliminated. And this explains why the recovery fraction of rapidly exchanged analytes can be estimated by a calibration of the recovery fraction in a stirred beaker (Tang et al., 2003).

For other analytes with a long Γ , calibrations might require brain phantoms that mimic the hydraulic conditions of the tissue more accurately, such as agarose hydrogels (Bungay et al., 2011; Ngernsutivorakul, Steyer, et al., 2018; G. Wu et al., 2022). Nevertheless, these calibrations can be tedious to perform, and their reliability might be debated (Bungay et al., 2001; Kho et al., 2017).

Finally, Equation 2.12 suggest that E_d decreases with the flow rate of the perfusate Q_d . This is not surprising as this means that the contact time of the perfusate with the membrane is longer, thus the analyte has more time to diffuse in it. Therefore, reducing Q_d helps to collect a dialysate with a concentration that mirrors C_e^∞ better, but at the cost of a lower temporal resolution, which might not be appropriate for all studies.

2.1.3 Results of the microdialysis model

Bungay et al. (2006) applied the solutions for the transient and steady-state regimes to illustrate the spatial concentration in the tissue and the recovery fraction, as presented in Figure 2.2. The parameters that were used to plot the curves in this Figure are reported in Table A.1 of Appendix A and a uniform extracellular concentration of analyte was initially considered in the tissue at the beginning of the sampling process ($t = 0$ min).

Figure 2.2a reports the spatial concentration of the axially-averaged concentration profile in the system over time, for a single analyte. It shows that a depletion layer is progressively established in the tissue during the transient regime and that the recovery fraction decreases with time. It only stabilizes when the steady-state is reached.

Figure 2.2b reports the axially-averaged concentration profile for analytes with the same diffusion coefficient, but varying clearances per mass of tissue CL_m . Consistent with the discussion of penetration depth Γ , the curves show that analyte depletion is deeper into the tissue with low values of CL_m and that the recovery fraction E_d is lower.

Finally, Figure 2.2c shows the temporal evolution of E_d for three analytes with the same diffusion coefficients but different CL_m . This shows that analytes with high CL_m reach a stable E_d faster than analytes with low CL_m and that their recovery fraction is higher.

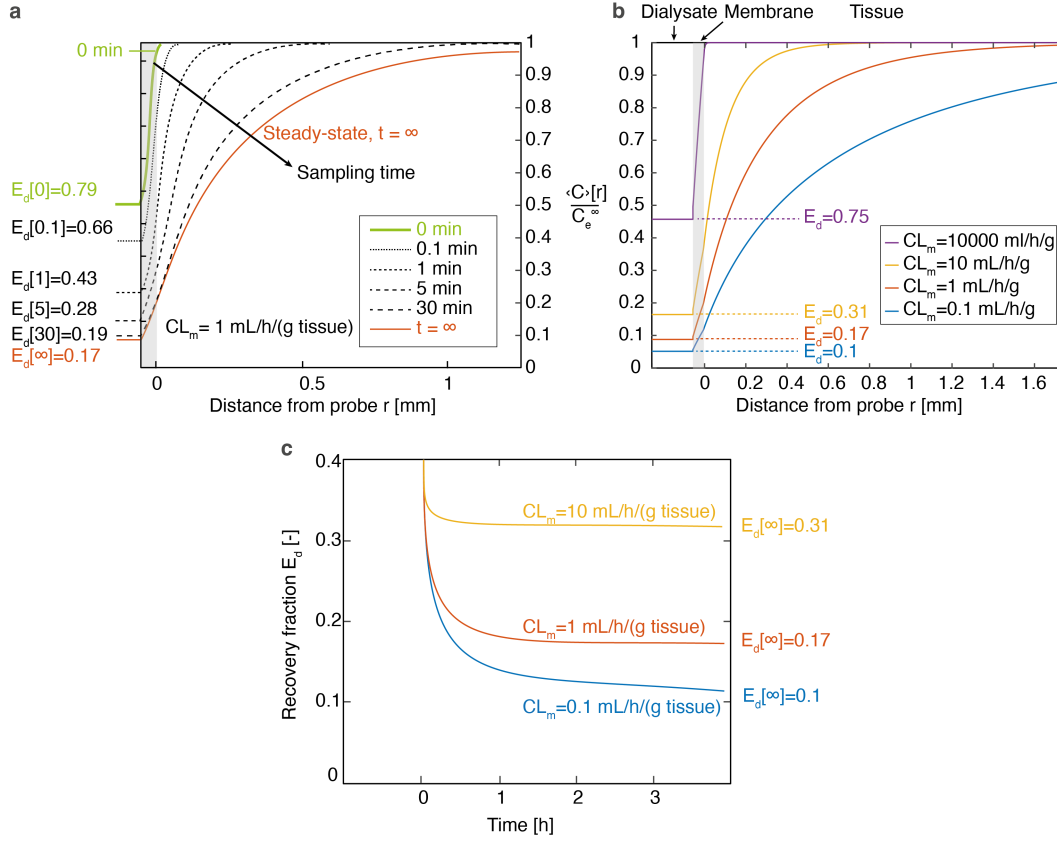


Figure 2.2: The concentration profiles and the recovery fraction predicted by the solutions of the microdialysis model. **a** Temporal evolution of the axially-averaged concentration profile $\langle C \rangle[r, t]$ relative to C_e^∞ , predicted by the solution for the transient regime. The recovery fraction E_d is added. **b** Concentration profile of $\langle C \rangle[r, t]$ relative to C_e^∞ in the entire system, for different CL_m , at steady-state. **c** Temporal evolution of the recovery fraction E_d , predicted by the solution for the transient regime, for different CL_m . Adapted with permissions from Bungay et al. (2006).

2.1.4 Extension to push-pull sampling

Push-pull probes do not possess a membrane that acts as a filter. Thus, only two domains would need to be considered for the modeling of the sampling effects in push-pull probes. Moreover, although their geometry differs from microdialysis probes (Chae et al., 2021; Ngernsativorakul, Steyer, et al., 2018; Petit-Pierre et al., 2016; van den Brink et al., 2019), they rely on the same principles to collect analytes from the ECF. Therefore, the same principles and limitations as the ones for microdialysis apply to push-pull probes that are operated continuously, because of their continuous sampling nature, only with different spatial properties.

2.1.5 Discussion

The model of microdialysis presented here, and that would also apply to push-pull sampling confirmed that during the transient regime, the recovery fraction in the dialysate E_d is unstable. Thus, the operators using such systems need to wait until the transient regime is over and the steady-state is reached to begin collecting reliably concentrated samples. This duration depends on the analyte considered. It can take as low as 10 minutes for certain analytes, or several hours for others (Bungay et al., 2001). Moreover, the recovery fraction at steady-state is linked to the clearance per mass of tissue CL_m , thus to the depth of the depletion layer. Together, these effects contribute to making the recovery fraction E_d lower than 1 and make it difficult to quantify the real ECF concentration C_e^∞ directly from the dialysate. In fact, the low recovery fraction provided by continuous sampling methods has been an issue for the researchers for decades (Kho et al., 2017). And although calibration methods exist to infer C_e^∞ based on the measured concentration in the samples, they can be tedious to apply, and there is no perfect solution yet. Among these methods, the zero-net-flux is frequently used. Despite this limitation, relative concentration changes in the ECF can still be reliably measured in the steady-state and computational models have been developed to predict the recovery fraction and infer C_e^∞ from the dialysate.

Limitations of continuous sampling methods

In summary, the transient regime and the low recovery fraction are two major limitations of continuous sampling methods. They are linked to the existence of a depletion layer due to the continuous withdrawal of analytes. Therefore, a transient regime is inevitable with continuous sampling methods, and it makes the experiments long, especially for analytes with low CL_m . Furthermore, when the steady-state regime is finally reached, the spatial concentration in the ECF is in fact influenced by previous sampling history. Thus, the samples are not truly independent of each other and a measurement at a specific time is influenced by the previous ones. Finally, the concentration of the analyte in the dialysate does not reflect the real concentration of the ECF because $E_d < 1$. Therefore, this prevents absolute quantification of C_e^∞ directly from the samples.

Solutions to the limitations

With continuous sampling methods, partial solutions to these limitations could be implemented. Thus, the recovery fraction can be increased by reducing the flow rate and allowing more time for the analytes to diffuse to the perfusate. However, this reduces the temporal resolution of the sampling unless smaller samples per unit of time are collected (Cabay et al., 2018; Fisher & Shippy, 2022). In addition, controlling low flow rates for an extended duration requires accurate equipment and can be challenging. Alternatively, the thickness of the dialysate domain can be reduced, hence the width of the annulus of dialysate, to reach a high concentration in the dialysate faster. Nevertheless, this leads to an increase of hydraulic resistance, which can make flow control more difficult (C.-F. Chen & Drew, 2008). To summarize, the solution means operating the probes slower and miniaturizing the volume of the perfusate/dialysate domain. Alternatively, to suppress the transient regime, the sampling conditions should be adapted such that the mass removal rate of the analyte by the probe is less than the rate of release of analytes into the ECF (Kennedy et al., 2002).

In addition, a novel approach could also adopt an intermittent sampling methodology, that optimizes the recovered concentration during punctual sampling events, and that allows the concentration to equilibrate in the tissue between sampling events. However, this would require the capability to turn the withdrawal of analytes on and off, which is not possible with traditional probes because diffusion cannot be stopped. Nevertheless, some solutions were still proposed in the literature, that use a perfusate separated by air, but they were never implemented *in vivo* (Barbot et al., 2021; C.-F. Chen, 2017; C.-F. Chen & Drew, 2008). Alternatively, the removal of analytes could be turned on and off with a push-pull approach that uses droplets and that works sequentially, as opposed to the droplet probes that operate continuously for fast sampling (Chae et al., 2021; Ngernsutivorakul, Steyer, et al., 2018; Petit-Pierre et al., 2017; van den Brink et al., 2019; M. Wang et al., 2010). This is the purpose of the Droplet on Demand approach that will be discussed next.

2.2 Definition of the Droplet on Demand approach

The DoD approach was inspired by the theory of microdialysis sampling to allow quantitative molecular studies with a sampling probe. Thus, DoD is presented as a sequential method that only removes analytes from the ECF at specific times and that lets the concentration of the analytes equilibrate in the tissue, without removal, between these times to prevent the creation of a depletion layer. This can be achieved by controlling the presence or the absence of perfusate in the tissue, with punctual infusion and punctual aspiration of the perfusate.

2.2.1 The objectives of the DoD

Based on this, the DoD method aims to collect samples with a high recovery fraction $E_d = \eta$ close to 1, to allow direct quantification of C_e^∞ from the samples, and without transient regime. This would allow on-demand punctual sampling events, or repeated sampling events with a stable recovery fraction at all times. Due to the absence of transient regime, this would also allow shorter sampling experiments for the animals and operators. These objectives are illustrated in terms of the recovery fraction in Figure 2.3a. To highlight them, a sketch of the temporal evolution of η for continuous sampling methods (with and without droplet segmentation) is shown, with a steady-state value η_{ss} , that is inspired from Figure 2.2c.

2.2.2 The steps of DoD sampling

To achieve these objectives, the DoD method proposes to collect molecules according to a specific sampling protocol in 4 phases. During the first phase, perfusate is infused in the tissue and creates a pocket of perfusate. During a second phase, analytes diffuse into the perfusate pocket, and the perfusate pocket gets aspirated in the probe during the third phase to form a droplet. This droplet represents the concentration of the ECF at a specific time. Past the sampling phase, the analyte concentration can equilibrate in absence of removal from the tissue, until a new sampling sequence is applied. This equilibration phase allows preventing the creation of a depletion layer. Overall, this is the method that allows turning on and off, the sampling and the removal of analytes from the tissue.

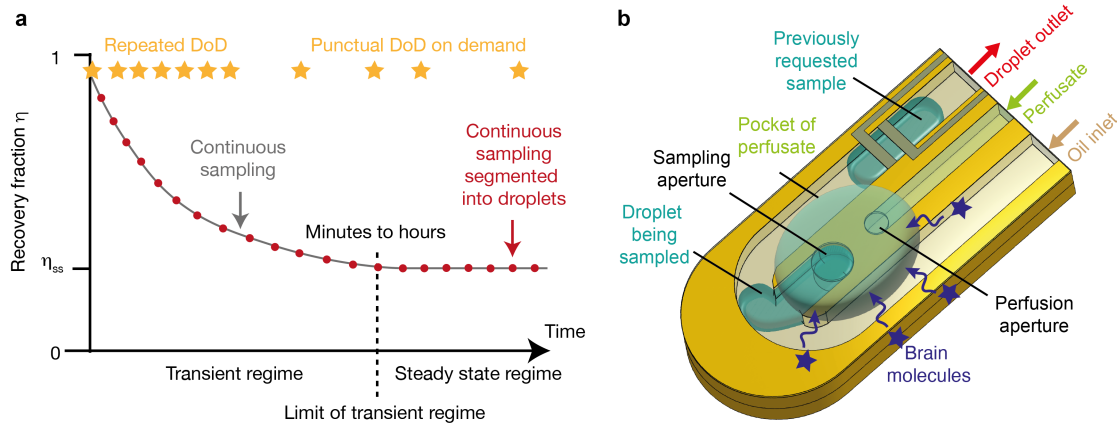


Figure 2.3: Concepts of DoD. **a** Objectives of DoD sampling in terms of recovery fraction. DoD aims to collect samples punctually or repeatedly while maintaining a high recovery fraction without transient regime. A sketch of the recovery fraction of continuous sampling methods (with and without droplet segmentation of the dialysate) is added for comparison and inspired by Figure 2.2c and η_{ss} is the steady-state level. **b** Overview of the tip of the 320 μm wide and 80 μm high probe that contains 3 microfluidic channels. The first one allows infusing perfusate in the tissue to create a pocket of perfusate. The second one is filled with oil and allows aspiration of the perfusate pocket loaded with molecules that diffused into it. The third one is filled with oil and allows segmenting the perfusate into droplets at the T-junction.

This method will be implemented in a specifically developed neural probe that will be described in detail in chapter 3. However, to describe the implementation of the concepts of DoD, the probe can be considered as a needle with three microchannels that are illustrated in Figure 2.3b. The perfusion channel allows delivery of perfusate in the tissue, the outlet channel allows aspiration of the perfusate into the probe and the last one, the inlet channel, allows the segmentation of the sampled fluid as droplet within the oil phase, perfluoro(methyldecalin) (PFD), at the T-junction.

To explain the DoD approach, the probe is considered inside the brain with its perfusion channel filled with perfusate and its outlet channel filled with PFD, as illustrated in Figure 2.4. The system is initially idle without any flow. In these conditions, no sampling occurs. Thus, the concentration of a single analyte is homogeneous in the whole ECF. At some point, the operator decides to collect a sample on-demand by starting a DoD cycle that will occur in five subsequent steps, that are described below.

1. **Perfusion step** A DoD cycle is started on-demand and the tissue is immediately infused with a controlled volume of perfusate $V_{\text{perfusion}}$, over the duration $t_{\text{perfusion}}$. Because of the density of the tissue, the hydraulic resistance opposes the penetration of the tissue by the fluid, and the perfusate forms a pocket of liquid at the probe-tissue interface, thus pushing the tissue away from the probe (Basser, 1992; Morrison et al., 1999).
2. **Diffusion step** The perfusate is initially free of analyte and a steep concentration gradient is created that causes fast diffusion of the analyte from the ECF to the pocket of perfusate. The duration of the diffusion step that is defined as $t_{\text{diffusion}}$ is controlled, and the concentration in the pocket increases over time. In fact, this defines the capture window of the analyte, thus the observation window.
3. **Sampling step** The pocket is aspirated inside the probe for a duration t_{sampling} , until the pocket is fully collected. Due to the hydraulic resistance of the brain, direct sampling of ECF is limited (Kennedy et al., 2002).
4. **Droplet move step** The oil is circulated within the probe to form a droplet with the sampled fluid, and the droplet is moved to the outlet over a duration t_{move} .
5. **Tissue recovery step** All flows are stopped, and a recovery time defined as t_{recovery} is observed. During this time, the analyte concentration equilibrates to the value present in the ECF. This step aims to retrieve the initial analyte concentration profile in the ECF before the next sampling event is triggered.

Based on these five steps, DoD can be applied to collect a single sample on-demand, but it also allows the collection of multiple samples by repetition. Therefore, the parameters and the interval between sampling events can be tuned depending on the needs. All DoD parameters are summarized in Table 2.1 and their importance will be described below in the case of single or repeated sampling.

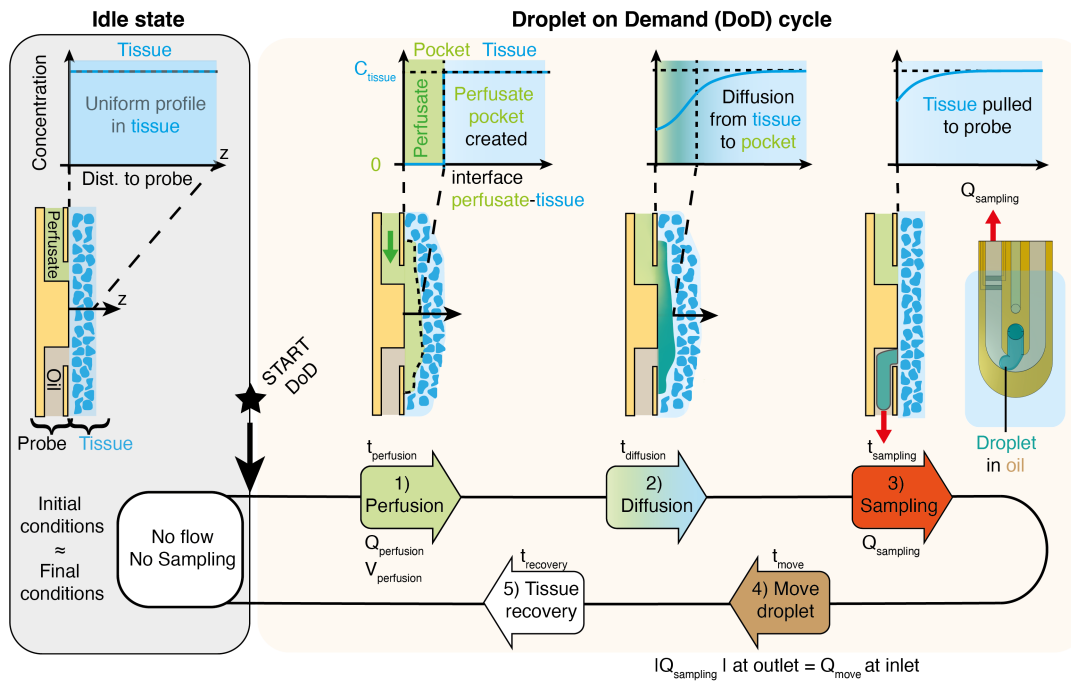


Figure 2.4: Concept of the DoD approach implemented at the tip of a probe. Only the perfusion and outlet lines are represented to illustrate the sampling of an analyte in the tissue. After insertion of the probe, the tissue and the probe are initially at rest, in the idle state (left). Thus, the tissue is unperturbed and a sketch of the spatially uniform concentration profile of the analyte in the ECF is shown at the top. 1) A cycle starts when desired by the operator with local infusion of perfusate. This creates a pocket of perfusate between the probe and the tissue, and a concentration gradient appears. 2) The analyte is progressively collected in the liquid pocket by diffusion. 3) The pocket is aspirated within the oil phase at the T-junction. 4) A droplet is formed and moved to the outlet. 5) No flow is applied in the recovery step and the analyte concentration equilibrates in the tissue only, by diffusion. The idle state resumes.

Table 2.1: Parameters of the DoD

Name	Symbol	Step
Perfusion volume	$V_{\text{perfusion}}$	Perfusion
Perfusion flow rate	$Q_{\text{perfusion}}$	Perfusion
Perfusion duration	$t_{\text{perfusion}}$	Perfusion
Diffusion time	$t_{\text{diffusion}}$	Diffusion
Sampling flow rate	Q_{sampling}	Sampling
Sampling pressure	P_{sampling}	Sampling
Sampling duration	t_{sampling}	Sampling
Oil volume	V_{move}	Move droplet
Oil flow rate	Q_{move}	Move droplet
Droplet move time	t_{move}	Move droplet
Recovery time	t_{recovery}	Recovery

Single DoD sequence

When DoD is applied to collect a single sample, a DoD *sequence* produces a unique droplet with a concentration that represents the concentration of the analyte in the ECF over the diffusion step. A *sequence* is defined through the steps 1-3 that are illustrated in Figure 2.4. Parameters $V_{\text{perfusion}}$ and $t_{\text{diffusion}}$ must be adjusted to maximize the recovery fraction η , defined as the sample concentration C_{sample} relative to the real concentration in the ECF C_{real} , in Equation 2.24. To allow quantification of C_{real} directly from the sample, η should be equal to 1. In practice, perfusion and sampling are not instantaneous, and their duration also contributes to the effective diffusion time.

$$\eta = \frac{C_{\text{sample}}}{C_{\text{real}}} = E_d \quad (2.24)$$

Repeated DoD cycles

A DoD *cycle* is defined by steps 1-5 in Figure 2.4, and the cycle time t_{cycle} is defined as the total time in Equation 2.25. The effects of the steps 1-3 are the same as for a DoD *sequence*. However, the steps 4-5 now define the equilibration period of duration $t_{\text{equilibration}}$ in Equation 2.26. The purpose of the equilibration period is to prevent the creation of a depletion layer in the tissue between sampling events, by allowing the concentration to equilibrate in the ECF, in absence of perfusate that would remove analytes from it. In other words, the objective of the equilibration period is to maintain the same initial concentration conditions in the ECF across subsequent sampling cycles. Therefore, its effect can be verified by following the recovery fraction η in subsequent samples.

$$t_{\text{cycle}} = t_{\text{perfusion}} + t_{\text{diffusion}} + t_{\text{sampling}} + t_{\text{equilibration}} \quad (2.25)$$

$$t_{\text{equilibration}} = t_{\text{move}} + t_{\text{recovery}} \quad (2.26)$$

2.3 Simulation of DoD sampling

To validate the concepts of DoD sampling, finite element analysis was performed with COM-SOL Multiphysics 5.6 to model the diffusion of an analyte within DoD sequences applied in a porous and passive medium.

2.3.1 Finite element analysis model

A model was built that considered a static 30 nL parallelepipedal pocket of perfusate that covered the tip of a flat 80 μm thick and 320 μm wide needle, that corresponds to the probe that will be described in chapter 3. The tip was at the center of a 126 mm^3 cube of porous medium with a concentration of 1 μM of glucose in the entire domain. Initially, the perfusate contained 0 μM of glucose. The free diffusion coefficient of glucose in the perfusate, D_0 , was 600 $\mu\text{m}^2/\text{s}$ at 20 °C. It was corrected with a tortuosity factor λ of 1.6 in the porous medium, to account for the tortuous path that molecules follow in the tissue (Syková & Nicholson, 2008). The porous medium was considered as a gel of 0.6% agarose with a porosity of 99.4%. The module "transport of diluted species in porous media" was used to simulate the diffusion of glucose in the medium and in the pocket. This considered mass transport by diffusion only, without convection. The governing equation in a single dimension is given in Equation 2.27, with the concentration c , the time t , the diffusion coefficient D and the spatial gradient ∇ . "No flow" conditions were set on the walls of the needle and on the sides of the cube. A progressive free quadrilateral mesh was set in the pocket of perfusate, with 2 μm thick features perpendicular to the surface of the needle. A progressive free tetrahedral mesh was used with features of maximum 50 μm in the 1 mm vicinity of the pocket and with coarse features further away in the rest of the medium. Steps of 0.5 s were used, with a relative tolerance of 0.005, and diffusion was the only mass transport mechanism.

$$\frac{\partial c}{\partial t} = D \nabla^2 c \quad (2.27)$$

The design of the model is shown in Figure 2.5a, that represents a 30 nL pocket of perfusate covering the probe, as a 40 μm thick layer between the probe and the medium. To illustrate the principle of the simulations, the temporal evolution of the glucose concentration on the cut surface is illustrated in Figure 2.5b, during a diffusion step of 60 s, in an 80 μm thick pocket of perfusate. It shows that the concentration is initially uniform in the whole medium (1 μM) and in the perfusate (0 μM). Over time, it shows that glucose diffuses from the medium to the perfusate.

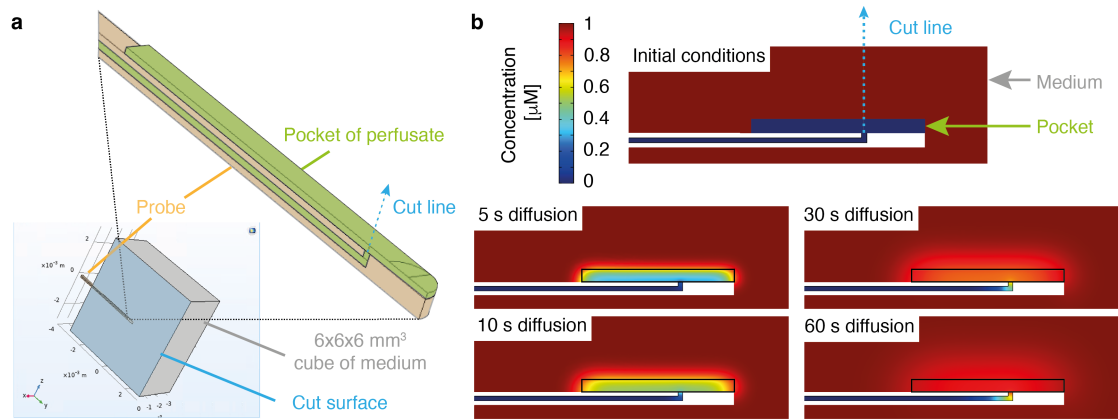


Figure 2.5: Finite element analysis model to study DoD. **a** The model considers glucose diffusing from the cube of medium (1 μM), into a perfusate pocket (0 μM) of 30 nL and with variable thickness (40 μm here) at the tip of the 320 μm wide probe. **b** Evolution of the glucose concentration in the system illustrated on the cut surface, during a diffusion step. The black rectangle shows the domain of an 80 μm thick pocket.

2.3.2 Effects of the parameters in a DoD sequence

The diffusion step and the recovery fraction

The effect of the diffusion time, $t_{\text{diffusion}}$, was studied with this model. The spatiotemporal evolution of the glucose concentration along the cut line is shown in Figure 2.6a. This line is perpendicular to the surface of the probe and goes from the interface probe-pocket to the tissue. It shows that, over time, the concentration progressively increases in the perfusate pocket, while it decreases in the medium. Given the different diffusion coefficients in both domains, the slope of the concentration profile is asymmetric and, as time passes, the tissue is depleted further away from the probe.

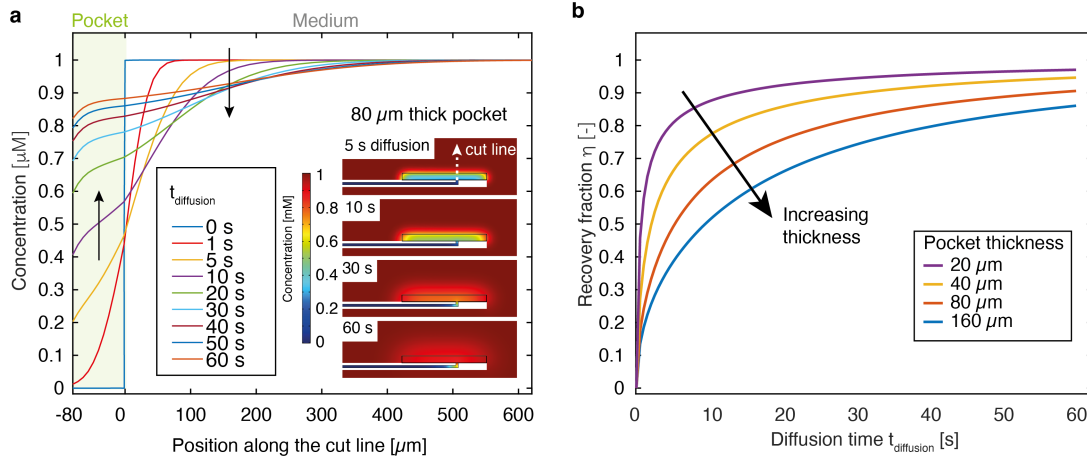


Figure 2.6: Simulations of glucose diffusion in the pocket and in the medium, during a 60 s diffusion step. **a** Spatiotemporal evolution of the glucose concentration along the cut line, in an 80 μm thick pocket. The insets show the concentration over the cut surface defined in Figure 2.5a. **b** Evolution of the recovery fraction against the DoD parameter $t_{\text{diffusion}}$ in 30 nL pockets of perfusate with a thickness varying from 20 to 160 μm .

Similarly, Figure 2.6b now shows the temporal evolution of the average concentration in the pocket, during a diffusion step, for 30 nL perfusate pockets of different thicknesses. As expected, the simulations confirm that the recovery fraction η increases with $t_{\text{diffusion}}$. They also show that, at a given time, the thinner the perfusate pocket, the higher the concentration. Moreover, at the early stage of diffusion, the rate of increase of the recovery fraction is much higher in thin pockets than in thick pockets. For all thicknesses, this rate is initially high and decays over time because of the steep concentration gradient with the medium. In all these conditions, the results also show that no pocket reached the condition $\eta = 1$ and to achieve a higher η , a longer $t_{\text{diffusion}}$ would be necessary. However, the decaying increase rate mitigates the interest in endlessly increasing $t_{\text{diffusion}}$, since η will ultimately be limited by local dilution with perfusate. Nonetheless, these results suggest using a small perfusion volume $V_{\text{perfusion}}$ to obtain a high η rapidly.

The equilibration phase and the concentration in the medium

The effect of the equilibration time was also studied, at the end of a diffusion step. Thus, a diffusion step of 10 s was simulated as in Figure 2.6 and a virtual sampling step was performed. This consisted of extracting the average concentration in the pocket, of setting the pocket concentration to 0 μM , and of applying impermeable barriers at the interfaces between the pocket and the medium. After this, the effect of the equilibration time $t_{\text{equilibration}}$ was studied, with diffusion occurring only in the medium. Moreover, the equilibration step used the spatial concentration in the medium at the end of the sampling step as its starting conditions.

Figure 2.7a shows the spatiotemporal evolution of the concentration in the medium during the equilibration step. It shows that the concentration gradient in the medium is attenuated over time because the analyte diffuses from the medium to the depleted region near the probe. After 60 s of equilibration, the homogeneity of the medium has improved with respect to the conditions at the end of the sampling. Nevertheless, the concentration did not return to the exact initial conditions. This was expected because sampling inevitably takes molecules away from the medium, and this medium is passive. Nonetheless, it shows that the introduction of an equilibration step contributes to recovering the initial conditions before sampling. Thus, this step contributes to preventing the creation of a depletion layer.

2.3.3 Repeated DoD cycles

Following on this, repeated DoD cycles were simulated, that implemented subsequent diffusion and equilibration steps repeatedly. Therefore, a first cycle was simulated as a diffusion step as previously described in Figure 2.6a, that was followed by an equilibration step as in Figure 2.7a. At the end of the equilibration step, the concentration of the pocket was set to 0 μM of glucose and the impermeable barrier between the pocket domain and the medium was removed. In fact, this corresponds to the virtual infusion of a new pocket of perfusate. Then, the simulation of the second cycle then proceeded like that of the first cycle, except with different starting conditions in the medium, that were given by the spatial concentration in the medium at the end of the equilibration step of the previously simulated cycle. This procedure was applied to simulate all cycles.

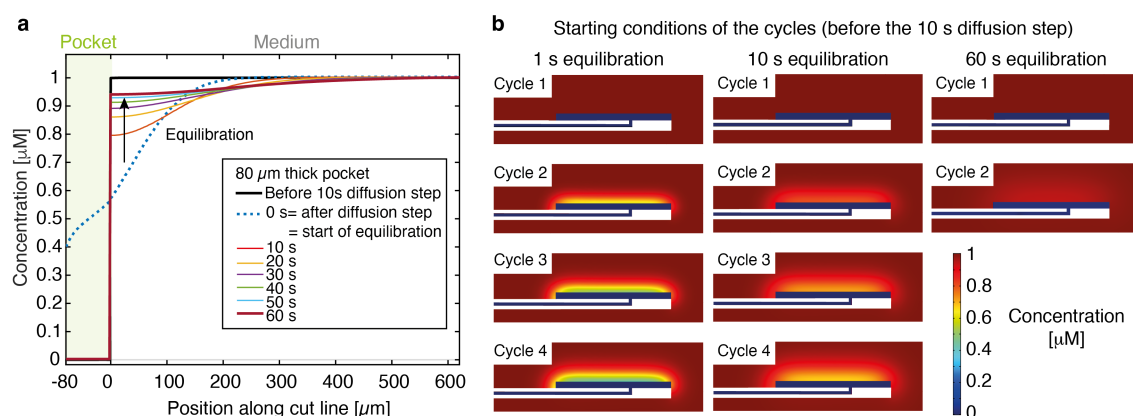


Figure 2.7: Simulations of glucose diffusion in the medium only, during equilibration steps that follow a 10 s diffusion step. **a** Spatiotemporal evolution of the concentration along the cut line, over a 60 s equilibration step. It starts with the concentration profile at the end of the diffusion step (dotted blue line). For comparison, the concentration profile before the diffusion step is also added (thick black line). **b** Starting conditions of the concentration in the medium, for subsequent sampling cycles, using 10 s of $t_{\text{diffusion}}$ and 1, 10 and 60 s of $t_{\text{equilibration}}$.

The starting conditions over repeated cycles

With the procedure described above, the effect of $t_{\text{equilibration}}$ on the starting conditions of subsequent cycles is illustrated in Figure 2.7b. Thus, sampling cycles with 10 s of diffusion were simulated repeatedly, in an 80 μm thick pocket, and with different equilibration times (1 s, 10 s and 60 s). The results illustrate the starting conditions of four subsequent cycles. Although they are identical at the beginning of cycle 1, the starting conditions become different at cycle 2, because of the different duration of the equilibration step, and the differences amplify over the cycles. These results show that the analyte should be given enough equilibration time to diffuse during this period, to reduce the concentration gradient in the medium and maintain similar starting conditions across repeated cycles. This is important for repeated sampling because this prevents the creation and the stabilization of a depletion layer, that would cause a transient regime and a decay of the concentration collected in the samples across the cycles. In addition, this would also lead to a steady-state regime with a reduced recovery fraction.

The stability of the recovery fraction across the cycles

Figure 2.8a further illustrates the principle of the simulation for repeated cycles, in 40 μm thick pockets, with diffusion and equilibration times of 10 s each. During the diffusion steps, diffusion of the analyte was simulated in the medium domain and in the pocket domain, whereas diffusion of the analyte was simulated in the medium domain only during the equilibration steps. The stars indicate the recovery fraction at sampling, at the end of the diffusion step, and before the equilibration step. Their decaying value indicates that the concentration decreased between the samples because of the too short equilibration time.

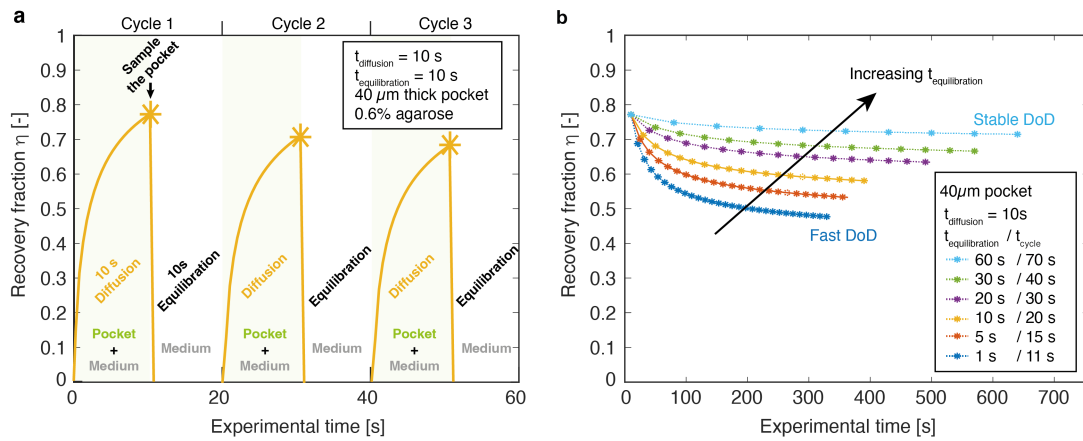


Figure 2.8: Simulations of the recovery fraction of glucose in a 40 μm thick perfusate pocket of 30 nL, over repeated DoD cycles. **a** Three cycles were simulated subsequently, by alternating steps of 10 s of diffusion in the pocket and in the medium, and steps of 10 s of equilibration in the medium only. The recovery fraction at sampling is represented by a star symbol between the diffusion and equilibration steps. **b** Evolution of the recovery fraction in subsequent samples. A steady diffusion time of 10 s was used, and the $t_{\text{equilibration}}$ was varied from 1 s (fast DoD) to 60 s (stable DoD).

This effect is even more pronounced in Figure 2.8b, that shows the recovery fraction at sampling for different sets of parameters and for repeated cycles. For all sets, a fixed diffusion time of 10 s was used, and the equilibration time ranged from 1 to 60 s. All sets of parameters provided the same recovery fraction in the first sample, since they shared the same diffusion time and initial starting conditions. However, the next samples provided different recovery fractions, because of their different equilibration times, that made the starting conditions change across subsequent cycles. Thus, with only 1 s of equilibration between subsequent cycles, samples from the "fast DoD" set were collected every 11 s, but their recovery fraction

was not steady. This set presents a fast transient that seemed to stabilize around 0.47 after about 300 s. This is significantly lower than the recovery fraction of 0.78 for the first sample. In contrast, when the equilibration time was increased to 60 s in the "stable DoD" set, samples were only collected every 70 s, but their recovery fraction was more stable between the first and the last samples, with values of 0.78 and 0.73 respectively.

In summary, "stable DoD" collected a small number of samples with a high and steady concentration, thus a high and steady η , while "fast DoD" collected samples more frequently, but with a decaying η . This highlights the importance of adjusting the DoD parameters according to the desired η and to the required temporal interval between the samples. Based on this, reaching a high and stable η for high frequency DoD protocols might require scaling down the volume of the perfusate pocket. Thus, for a same η , a shorter diffusion step would be required and since a smaller absolute amount of analyte would be removed at each cycle, the equilibration time could also be reduced. Moreover, it is interesting to note that due to its short equilibration time, the trend followed by "fast DoD" resembles the trend observed with continuous sampling methods, i.e., a transient regime followed by a steady-state regime. This is similar to the results in Figure 2.2c. In comparison, the transient regime does almost not exist with "stable DoD", or at least its time scale is longer than that of the experiment.

Optimization of the parameters

On one hand, Figure 2.6 showed that the recovery fraction in the pocket increases with $t_{\text{diffusion}}$, since the analyte has more time to diffuse into the pocket. This is the important timing of the DoD approach to reach a high recovery fraction for a single sampling event. On the other hand, Figure 2.8b showed that the stability of the recovery fraction between samples increases with $t_{\text{equilibration}}$. This is the important timing of the DoD to help the concentration equilibrate in the medium between repeated sampling events and to obtain a stable recovery fraction. In fact, both parameters should be optimized together to provide a stable and maximal recovery fraction when DoD is applied repeatedly. This is illustrated in Figure 2.9, that shows the evolution of the recovery fraction for different sets of diffusion time, equilibration time and pocket thickness.

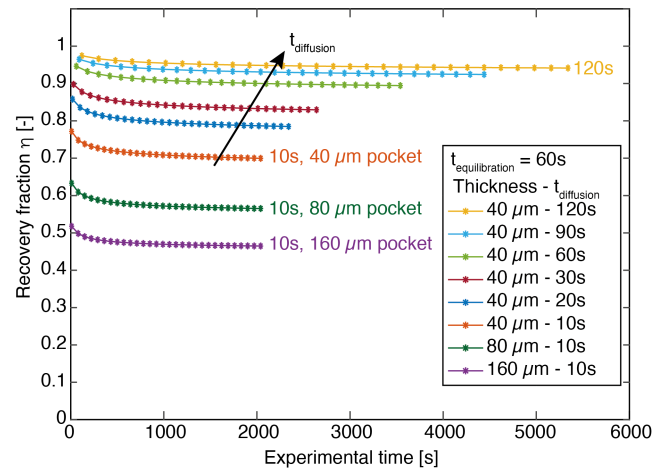


Figure 2.9: DoD for high and steady recovery fraction η for repetitive sampling cycles. $t_{\text{diffusion}}$ was varied from 10 s to 120 s, while the 60 s equilibration time was fixed. The thickness of the perfusate pocket was 40 μm for all sets of parameters, except for two sets with 80 μm and 160 μm respectively.

Thus, these results suggest that, for a 40 μm thick pocket, a diffusion time of 120 s and an equilibration time of 60 s provide a stable recovery fraction η around 0.95. In fact, even though achieving a η of 1 would be ideal, achieving a stable η of 0.95 would be significant and would allow quantitative molecular studies with repeated sampling events every 3 minutes. As a comparison, and although the recovery fraction for microdialysis depends on the sampling conditions (Kendrick, 1989), η is usually inferior to 0.40 at the usual flow rates of 1 $\mu\text{L}/\text{min}$ (Chefer et al., 2009). Alternatively, ultra-slow perfusate flow rates inferior to 100 nL/min reportedly provide recovery fractions close to 1 (Cabay et al., 2018; Menacherry et al., 1992). However, their drawback is that they usually require a longer collection time than the one proposed by DoD, typically 10 minutes. Moreover, their observation window of 10 minutes is larger than the one of DoD, that corresponds to $t_{\text{diffusion}}$, and that allows a more accurate capture of short and precisely defined molecular events.

Finally, Figure 2.9 shows again that the thickness of the pocket is also of major importance, since thicker pockets provide a lower recovery fraction for the same diffusion time. The thickness of the pocket can be influenced by the volume of perfusate infused in the tissue, but in practice, this is also influenced by external parameters such as the deformation of the tissue and probably even the insertion of the probe (Basser, 1992; Morrison et al., 1999). Nevertheless, this is difficult to control in real conditions and this was not investigated further.

2.3.4 Summary of the DoD simulations

The simulations confirmed the influence of $t_{\text{diffusion}}$ on the recovery fraction and the influence of $t_{\text{equilibration}}$ on its stability. They also showed the effect of the thickness of the pocket. Therefore, these results confirmed that with appropriate adjustment of the DoD parameters, the proposed method could fix some of the limitations of continuous sampling methods: the transient regime and the low recovery fraction. This was the objective of these simulations.

Nevertheless, some simplifications were made in this model, thus they cannot be used directly for the estimation of accurate operating parameters. In fact, the model considered a passive medium that would be accurate when sampling in a hydrogel but not in a tissue, except for analytes with a negligible elimination rate constant and no exchanges between the ECF and the tissue. Moreover, the model considered instantaneous perfusion and sampling, but in practice, their duration would also contribute to the effective diffusion time. Finally, it did not account for the growth and shrinkage of the perfusate pocket during perfusion and sampling. In fact, the thickness of the pocket would evolve during these steps and thus change the effective rate at which the recovery fraction increases.

Moreover, the simulation of cycles also showed that the sets of parameters that provided both a high and a steady recovery fraction had a higher cycle time than the sets with a transient regime. This suggests that a compromise should be made either on the height and on the stability of the recovery fraction, or on the temporal observation window and on the frequency of the sampling events. Moreover, due to the sequential nature of the DoD, monitoring fast molecular events with a recovery fraction might be challenging, such as for the release of neurotransmitters. However, there are many other molecules with slower dynamics, that would benefit more from accurate quantification than from high frequency measurements (Frank et al., 2019). This might be particularly interesting for the sampling of miRNAs encapsulated in extracellular vesicles (Bache et al., 2015) or to study protein aggregation of amyloid- β that occurs over years (Jagust & Landau, 2021). Alternatively, this could also allow the collection of molecules with low CL_m , that have a too low steady-state recovery fraction to be measurable with continuous sampling methods.

As a last comment, the model served to illustrate the concepts and mechanisms of DoD sampling, and simulations of molecular sampling in the brain were not attempted. Nevertheless, this could be performed by implementing the analyte elimination (k_t), exchange (k^x), and generation rates (G_t) in an active medium. The porosity of the medium might also need to be modified to reflect the density of the brain better. Finally, since all these parameters would need to be determined experimentally, the results of the simulations would need to be discussed carefully and verified.

2.4 Conclusion

This chapter discussed the theory of microdialysis and the concepts of transient regime, depletion layer, and recovery fraction were introduced. In fact, although the mathematical formulation for microdialysis was discussed, the observations and the results apply to all sampling methods that continuously collect analytes from the tissue. The theory allowed the identification of their limitations: the transient regime and the low recovery fraction η . They both result from the creation of a depletion layer when the rate of analyte removal is higher than the rate of analyte release in the ECF (Kennedy et al., 2002). These limitations make it difficult to collect samples that reflect the real concentration in the ECF and make sampling experiments long. Furthermore, because of the depletion layer, the concentration collected in the samples is influenced by the previous sampling history. Thus, they are not truly independent and do not only represent the concentration at an accurate point.

These limitations inspired the development of the DoD approach, as a sequential sampling method that alternates analyte collection and tissue equilibration. This approach aims to provide samples that accurately reflect the concentration in the ECF and that can be collected at any time, on-demand, without the need to wait for a transient regime to be over and for a steady-state to settle. This would allow the collection of samples that are truly independent and that reflect the ECF concentration over accurate temporal windows. Moreover, with droplets to segment the samples, it should be possible to collect multiple samples repeatedly. All this is proposed by the sequential sampling approach, that operates in perfusion, diffusion, sampling, and equilibration steps. And among the parameters of these steps, the diffusion time

and the volume of perfusate allow controlling the recovery fraction of the samples, whereas the equilibration time ensure a stable recovery fraction for repeated sampling events.

As a final note, although DoD aims to propose a solution to some major limitations of continuous sampling methods, it should not be perceived as a replacement of these methods. Instead, it is proposed as an independent alternative that could help researcher perform quantitative molecular studies with DoD or that could work in parallel to these methods to improve quantification and calibration. Moving away from the theory, the next chapter presents the fabrication of the probe dedicated to DoD sampling and the fluidic implementation of DoD.

Chapter 3

Implementation of DoD in a neural probe

This chapter reports the design and the fabrication of the neural probe for DoD. It also describes the fluidic interface and the implementation of DoD.

3.1 Presentation of the probe for DoD

The polyimide and SU-8 technologies were selected to fabricate the probe, as multilayer system and the fabrication process was inspired from prior technological developments (Mercanzini et al., 2009; Metz, Jiguet, et al., 2004; Petit-Pierre, 2017; Petit-Pierre et al., 2016; Petit-Pierre et al., 2017). Polyimide allows the integration of electrical features, while SU-8 allows the integration of microfluidic channels. Different types of polyimides were reported non-toxic in many life sciences studies and were also used in previously published neural probes (Constantin et al., 2019; Sim et al., 2017). SU-8 was also used in multiple *in vitro* and *in vivo* life sciences studies, and despite it does not satisfy all the requirements of the physiochemical biocompatibility test (Kotzar et al., 2002), SU-8 did not prove cytotoxic during short term implantation (Z. Chen & Lee, 2021). In addition, contact angles of 75° and 90° were respectively reported for pristine polyimide PI 2611 (HD Microsystems) and SU-8 (Joshi, 2018;

Martinez-Duarte & Madou, 2016), and could be modified by plasma treatment and grafting of functional molecules (Inagaki et al., 2001; Kumar & Sharma, 2015; Moresco et al., 2010; Tao et al., 2008). This is important to prevent biofouling of the surfaces and reduce the interactions between the droplets and the walls of the channels (Elvira et al., 2022).

An overview of the probe is illustrated in Figure 3.1a. It comprises a body and a needle with electrodes and microfluidic channels. All channels in the probe are interfaced to glass capillaries at the end of the body, with zero-dead-volume connections. The body also contains metallic pads for electrical interfacing, achieved with spring-loaded pins in a specifically designed holder. For electrical functions, a stack of titanium (Ti), platinum (Pt) and titanium was deposited on polyimide by sputtering (Mercanzini et al., 2008; Metz et al., 2001). Platinum is a noble metal frequently used for stimulation and recording electrodes because of its high conductivity, its resistance to corrosion, and its non-toxicity (Stieglitz, 2004). Ti was used to promote the adhesion of Pt and was etched in HF at the end of the fabrication process.

SU-8 and Polyimide have respective Young moduli of 4 GPa and 2.5 GPa (Sim et al., 2017) and they allowed producing a 12 mm long and flexible needle of 80-85 μm in thickness and 320 μm in width. This needle contains three channels. The perfusion channel has a cross-section of 40 μm x 40 μm , and allows the infusion of perfusate at the tip. Opposite, the inlet and outlet channels are filled with PFD and are 70 μm in width and 40 μm in thickness. They intersect at the T-junction at the tip, and they allow sampling of fluid from the brain, that they later segment in droplets. PFD was selected as the carrier phase for droplets since it was previously used *in vivo* (Petit-Pierre et al., 2017) and a similar fluorinated oil, perfluorodecalin, was also reported chemically and biologically inert (Badv et al., 2017; Saha-Shah et al., 2016).

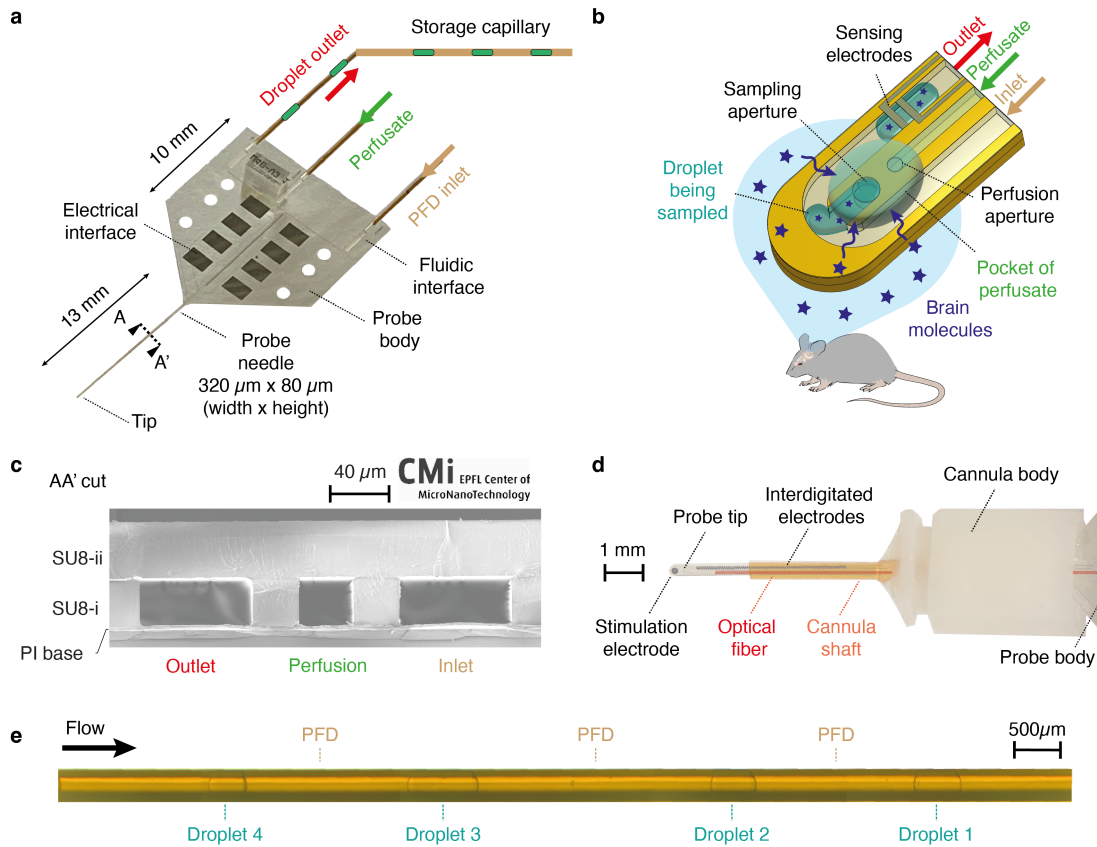


Figure 3.1: Overview of the features of the polyimide/SU-8 probe for DoD sampling. **a** Picture of the probe. The body allows fluidic and electrical interfacing, and all channels lead to the tip of the flexible needle, where droplets are collected and later moved to a storage capillary at the outlet. **b** Schematic of a sampling cycle at the tip of the probe. The perfusion channel is filled with perfusate, while the inlet and outlet channels are filled with PFD and intersect at the T-junction. During the perfusion step, a pocket of perfusate is created at the tip. Molecules diffuse into the pocket during the diffusion step, and the pocket is aspirated within the PFD phases during the sampling step. This forms a droplet at the T-junction, that is moved towards the outlet in the move step and detected by the electrodes. **c** SEM picture of the AA' cross section of the needle, showing the channels defined between the polyimide base (PI-i, ELEC, PI-ii) and two SU-8 layers (SU8-i and SU8-ii). **d** Picture of the probe with an optical fiber (false colored in red) inserted through a microdialysis cannula CMA7. **e** Picture of the storage capillary that keeps the droplets separated by PFD until analysis.

The needle is barely rigid enough to be inserted into the brain, thus it can be strengthened with an optical fiber of 125 μm in diameter glued on top of it. This permits insertion into the brain through a small hole in the skull and accurate targeting of the desired brain region. Moreover, it also adds a local light delivery feature that could be useful for PBM studies with chemical recording (Oueslati et al., 2015). The assembly is compact enough to fit a microdialysis cannula CMA7 (CMA Microdialysis AB) that is shown in Figure 3.1d. This system has an inner diameter of 400 μm and a total body length of 8 mm. Thus, the probe can protrude by up to 4 mm from the tip of the shaft of the cannula.

Single pairs of electrodes and interdigitated electrodes were integrated for droplet-sensing in the outlet channel, based on the conductivity of the liquid. A stimulation electrode was also integrated at the tip of the needle for dual studies with electrical stimulation and chemical monitoring. In addition, interdigitated electrodes passivated below the polyimide at the bottom of the channel were also integrated, to produce a capacitive sensor for droplet size and velocity measurement. This sensor was only used to characterize fast generation of small droplets *in vitro* but not for DoD sampling. Its development is reported in Appendix C.

Finally, the outlet channel is connected to a storage capillary that collects the samples and preserves their generation order. It can be disconnected from the probe and stored until analysis with the suitable analytical method for the target analytes. A storage capillary with 4 droplets separated by PFD is shown in Figure 3.1e.

3.2 Fabrication of the probe

The probe was fabricated at the EPFL Center of MicroNanoTechnology CMi, according to the process illustrated in Figure 3.2. It consisted in deposition and patterning of five different layers: 3 μm of polyimide (PI-i), 500 nm of Ti-Pt-Ti (ELEC), 1 μm of polyimide (PI-ii), 40 μm of SU-8 (SU8-i), and 40 μm of SU-8 (SU8-ii). This section briefly reports the main steps of the fabrication, whereas the details of the equipment and recipes are reported in Appendix B.

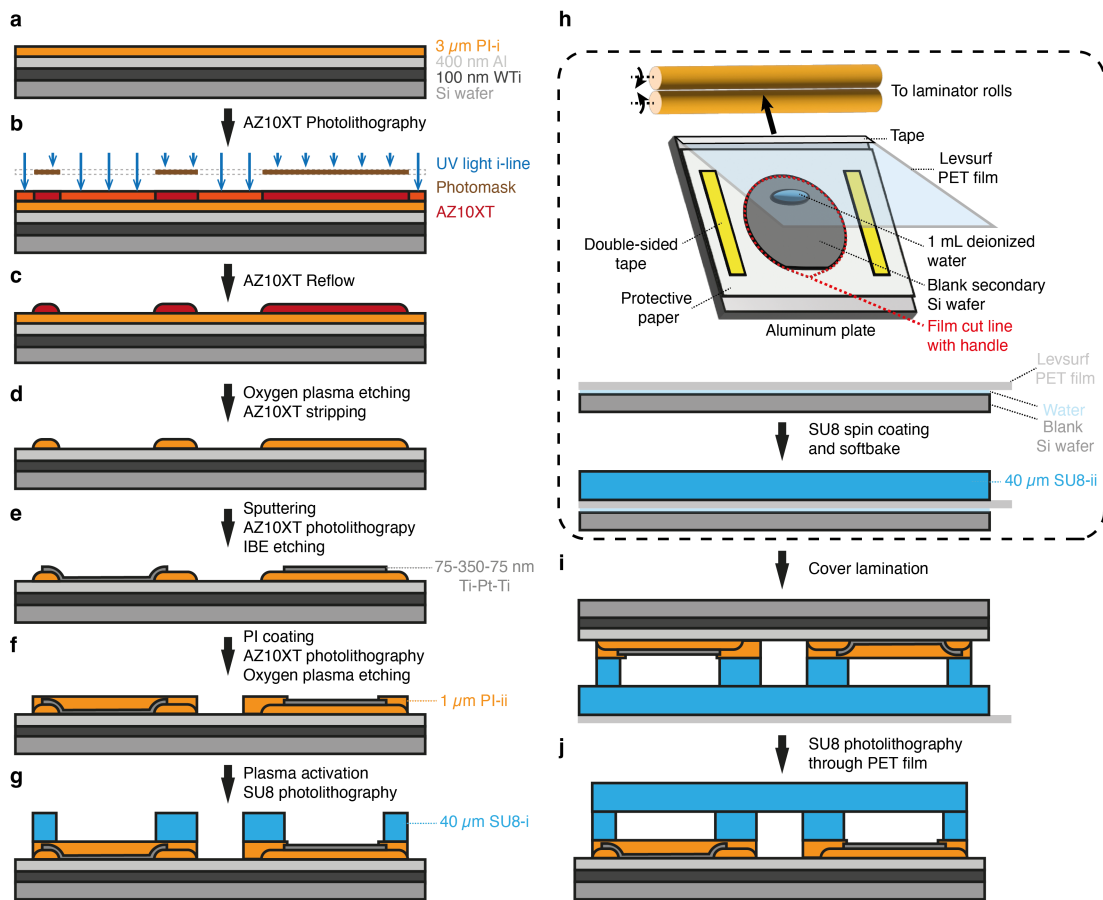


Figure 3.2: Probe fabrication process. **a** Deposition of the metallic sacrificial layers by sputtering and spin coating of the 3 μm thick polyimide base layer (PI-i) on the main wafer. **b** Coating and exposure of the positive PR AZ10XT on a mask aligner. **c** Reflow of the PR. **d** O_2 plasma etching of the unprotected PI-i and transfer of pattern and profile of the PR. **e** Deposition of the 500 nm thick Ti-Pt-Ti metallic layer for the electrodes by sputtering, photolithography, and patterning by ion beam etching. **f** Spin coating of the 1 μm thick polyimide passivation layer (PI-ii), photolithography, and patterning of PI-ii by O_2 plasma etching. **g** Spin coating and photolithography of SU-8 to pattern the channels (SU8-i). **h** Preparation of the SU-8 cover layer (SU8-ii) on a flexible film. The flexible PET film is laminated to a secondary wafer and held by capillary force by water. It allows production of a dry SU-8 film (SU8-ii) on a flexible PET substrate. **i** The flexible carrier is peeled off the secondary wafer and the main wafer is laminated to the SU-8 dry film. **j** The cover is patterned through the flexible PET film by photolithography.

3.2.1 Polyimide layer - PI-i

Production started on a silicon wafer, with the deposition of a thin film of 100 nm of tungsten-titanium (WTi) and of 400 nm of aluminum (Al) by sputtering. This would be the sacrificial layer to release the probes at the end. Next, a 3 μm thick layer of polyimide (PI2611, Dupont) was spin coated, baked, and patterned by photolithography with the positive photoresist (PR) AZ10XT (Figure 3.2a-b). A reflow of the PR AZ10XT was performed to produce a slanted profile that was transferred to the PI-i layer during etching (Figure 3.2c). Etching was performed in oxygen plasma with the pyralin process, and the PR was later stripped away (Figure 3.2d).

At the center of the wafer, PI-i was measured between 2.75 – 2.85 μm in thickness. Because of the PR reflow, the etching produced slanted edges that are shown in Figure 3.3. The angle of the edge was measured between 31-34° with the aluminum base layer. This angle allowed smooth transition of the subsequent electrical layer between two heights, thus improving their robustness.

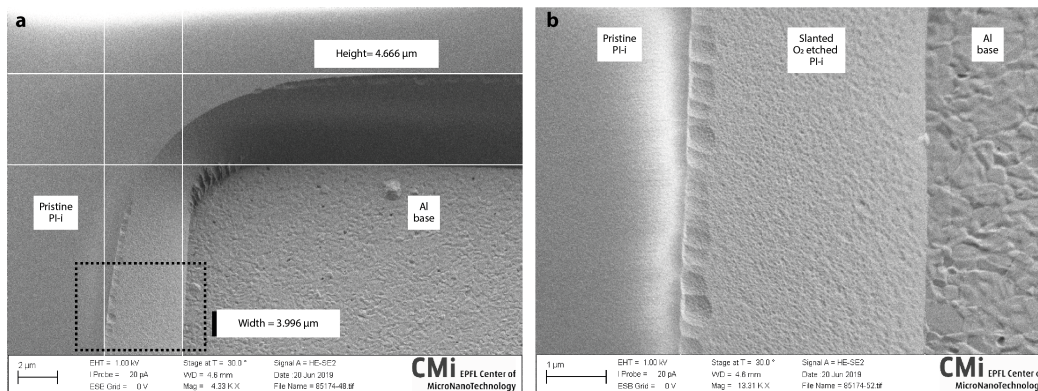


Figure 3.3: Probe fabrication process at CMi - slanted polyimide base layer. **a** At the location of the electrical contact pads, the slanted edges ensure a smooth transition of the metallic layer between two levels. The rectangular area is shown in the next frame. **b** The pristine PI-i layer is smooth, whereas the slanted edged is rough due to partial etching during PR profile transfer and the grains of the aluminum base layer are visible.

3.2.2 Metallic layer - ELEC

Then, a stack of 75 nm of titanium, 350 nm of platinum, and 75 nm of titanium (Ti-Pt-Ti) was deposited on PI-i by sputtering. This served to produce metallic electrodes by photolithography and ion beam etching (Figure 3.2e). An example of interdigitated electrodes integrated in the outlet channel is reported in Figure 3.4a.

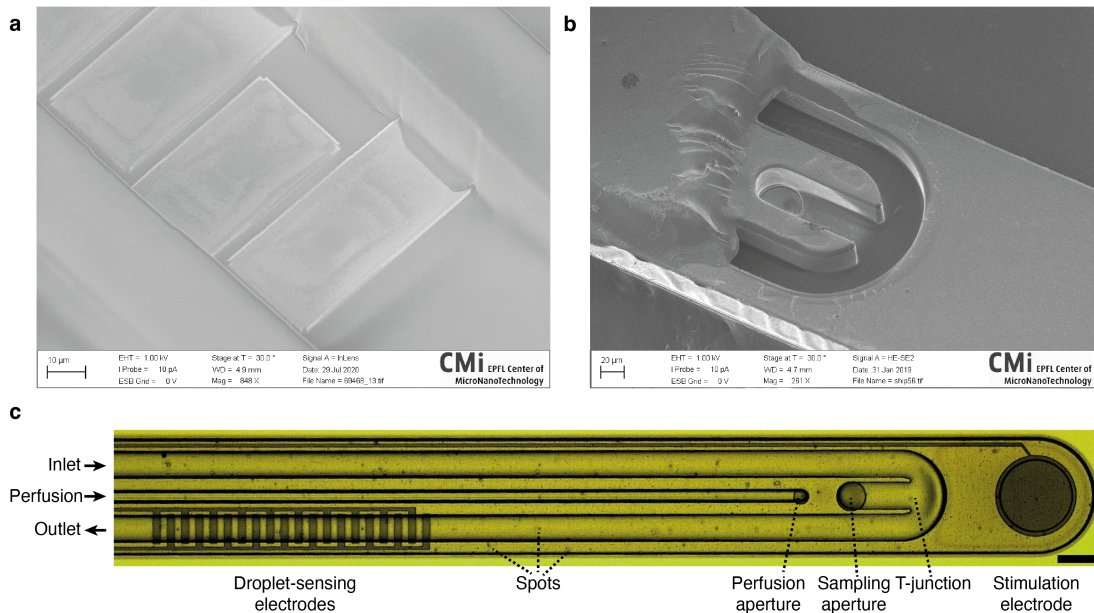


Figure 3.4: Probe fabrication process at CMi - electrodes and fluidic channels. **a** The Ti-Pt-Ti electrodes deposited on PI-i access the fluidic channel defined by SU8-i through an opening in PI-ii. **b** The T-junction at the tip of the probe is formed by the SU8-i layer. **c** Finalized probe after SU8-ii development. The inlet, perfusion and outlet channels patterned in SU8-i are integrated in the needle. The perfusion aperture allows perfusate delivery into the tissue with the perfusion channel. The inlet and outlet channels intersect at the T-junction that leads to the sampling aperture through PI-i and PI-ii. Interdigitated droplet-sensing electrodes in the outlet channel allow droplet detection directly after sampling. A stimulation electrode is also available at the tip, which contacts the tissue on the PI-i side. The scale bar is 100 μm.

3.2.3 Polyimide layer - PI-ii

Another polyimide layer, of 1 μm , was spin coated and patterned with a process similar to PI-i, without the reflow of PR for the slanted edges. This allowed the encapsulation of the electrical tracks and the passivation of the electrodes for capacitive droplet detection (Figure 3.2f). In fact, this layer was the bottom of the fluidic channels and openings through it permitted the electrodes to access the content of the channel for resistive sensing. Due to the topography during the spin coating process, the PI-ii thickness was not homogeneous and was measured between 1.1 μm and 1.9 μm over the wafer. This did not perturb the operation of the probe, but influenced the sensitivity of the capacitive sensor described in Appendix C.

3.2.4 SU-8 channels - SU8-i

Fluidic channels were patterned by photolithography of a 40 μm thick SU-8 layer (SU-8 3025, MicroChem) that was spin coated over the PI-ii layer (Figure 3.2g). Temperature ramps of 5°C/min were introduced in the baking steps to limit the stress between the materials in the system. This allowed the production of straight needles. Moreover, the development time in Propylene Glycol Monomethyl Ether Acetate (PGMEA) was critical to ensure full SU-8 development in the channels and avoid overetching that would cause leakages. The thickness of the SU8-i layer was measured between 36 μm and 40 μm over the wafer.

3.2.5 SU-8 cover - SU8-ii

A 40 μm thick SU-8 dry film was produced on a flexible PET substrate (Levsurf LS100, Kimoto) laminated on a secondary wafer (Figure 3.2h). After oxygen plasma activation of the SU8-i layer, the dry film of SU8-ii was laminated on top of SU8-i to close the channels (Figure 3.2i). This film was selected for its high transmittance, low haze, and low surface roughness. Thus, it allowed accurate photopatterning of the SU8-ii layer through it. Moreover, due to the low affinity of PET with crosslinked SU-8, the PET film could be easily peeled off the wafer after the post-exposure bake (Figure 3.2j).

Figure 3.4b shows the tip of a probe with a partially polymerized SU8-ii cover layer. The T-junction formed by SU8-i is visible, that intersects the inlet, the outlet and the sampling channels that leads to the sampling aperture through the polyimide layers. The tip of a finalized probe on the wafer is illustrated in Figure 3.4c, with the fluidic channels, their apertures to access the brain and interdigitated droplet-sensing electrodes for resistive sensing in the outlet channel. The spots that can be seen all over the probe, are due to the roughness of the PET film that was transferred to the outer part of SU8-ii. Nevertheless, this did not cause any issue and exposure through the PET film allowed accurate photolithography of SU8-ii. Moreover, a cross-section of the needle can be seen in Figure 3.1, and it shows that channels with sharp edges were obtained with this process.

3.2.6 Anodic release and titanium etching

At this point, the probes were all attached to the main wafer, as illustrated in Figure 3.5a. Furthermore, the SU8-i layer was designed such that the fluidic channels would be sealed during the development of the SU8-ii layer step, to prevent PGMEA and dissolved SU-8 to redeposit in the channels. Therefore, the end of the fluidic connection ports on the probe body had to be cut open with a laser (OPTEC LSV3, EXCIMER Laser 193 nm). Next, an anodic release process was carried out to detach the implants from the wafer in a NaCl bath. This was achieved by applying 0.7 V to the wafer, with respect to a platinum counter electrode in the bath (Mercanzini et al., 2008; Metz, Trautmann, et al., 2004). This dissolved the aluminum layer and released the probes in the bath overnight. Following this, the probes were rinsed in deionized water and isopropanol and the titanium layer on the outer side of the exposed electrodes was etched away in 1% HF to expose platinum. Finally, the probes were cleaned with deionized water, isopropanol, and ethanol, and stored flat between two plates covered by clean room paper to maintain the needle straight.

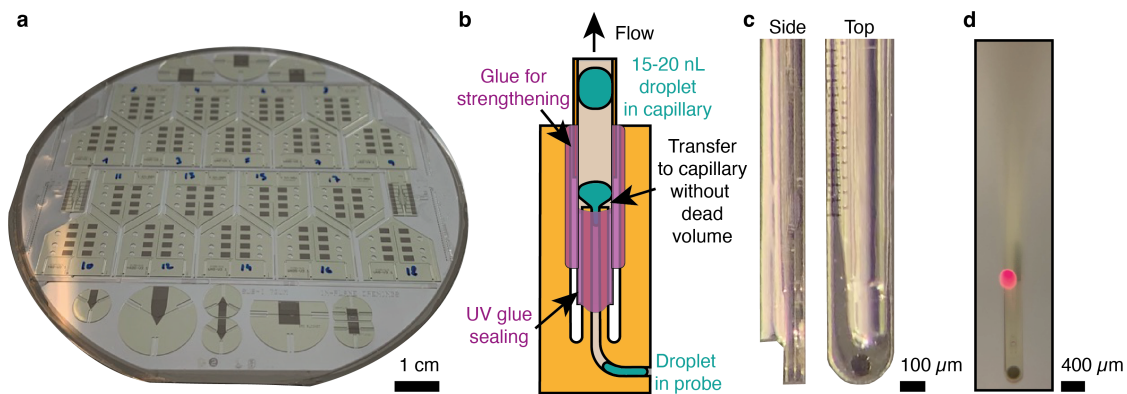


Figure 3.5: Post-fabrication of the probes. **a** Before release, a wafer contains 18 probes surrounded by characterization devices on the sides. **b** Schematic of the fluidic interface to transfer droplets from the probe to the storage capillary with no dead volume. **c** Top and side views of the probe after gluing of the optical fiber at the tip of the probe, on the SU-8 side. **d** Picture of the tip of the probe, for local delivery of light through the fiber.

3.2.7 Interfacing

The fluidic channels were interfaced to fused silica capillaries (TSP-250350, 250 μm Inner diameter (ID), 350 μm Outer diameter (OD), BGB Analytik AG) with UV-sensitive epoxy. This allowed connections with no dead volume between the channels of the probe and the glass capillaries, as is illustrated in Figure 3.5b. To ease insertion in the brain and allow light delivery, the probes were also augmented with an optical fiber that was glued on the needle. To that end, a polished optical fiber with a cladding outer diameter of 125 μm (FG-105LCA, Thorlabs) was used and glued with the same UV-sensitive epoxy. The assembly is shown in Figure 3.5c-d.

3.2.8 Surface treatments

Polyimide and SU-8 are natively hydrophobic materials (Khomiakova et al., 2020; Kumar & Sharma, 2015). However, since the bottom and the walls of the channels were exposed to oxygen plasma during fabrication (Figure 3.2i), their hydrophilicity increased. Although, partial hydrophobic recovery usually occurs for SU-8 over time, the contact angle with water remains below 90° even after months (Jokinen et al., 2012; Walther et al., 2007). Therefore, the affinity of the aqueous phase with the surfaces of the channels and of the capillaries was high,

as reported by the concave interfaces of the droplets in Figure 3.6a-b. Thus, the aqueous phase interacted with the surfaces more than PFD, which could induce crosstalk between droplets and pinning of aqueous phase on the walls. Moreover, in these conditions, small droplets in the capillary were prone to splitting on the glass surfaces.

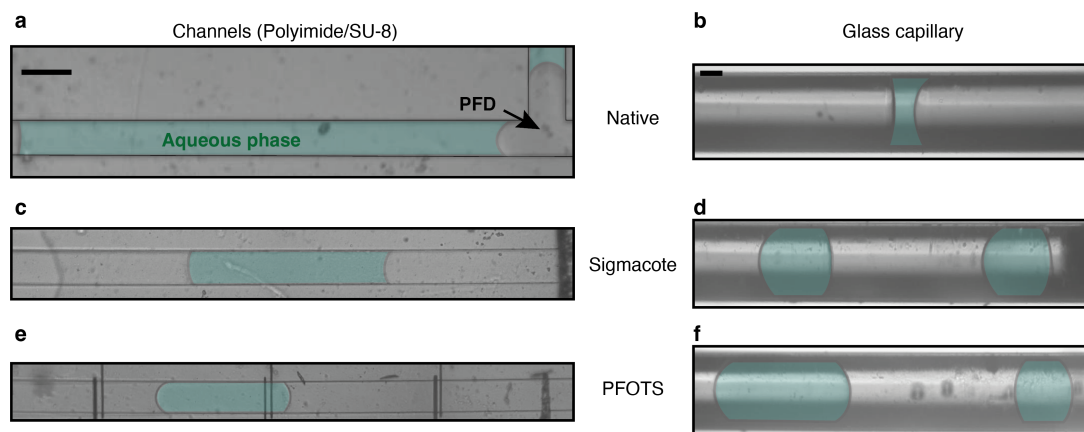


Figure 3.6: Wetting of the surfaces by the aqueous phase and the PFD, for different treatments, in *in vitro* conditions. A microfluidic channel with polyimide and SU-8 surfaces is shown in the left column, with flowing droplets. The glass surface of the outlet capillary is in the right column with static droplets. In both columns, the scale bars represent 100 μm . **a-b** Pristine surfaces. **c-d** Surfaces after plasma treatment and Sigmacote functionalization. **e-f** Surfaces after plasma treatment and PFOTS functionalization.

Thus, two surface treatments were applied to the probes and to the capillaries. The first one consisted of trichloro(1h,1h,2h,2h-perfluorooctyl)silane (PFOTS), which is fluorinated silane that was tested as an omniphobic treatment for catheter surfaces (Badv et al., 2017). The second one consisted of Sigmacote, an antifouling treatment with 5% 1,7-dichlorooctamethyltetrasiloxane in heptane, and that presents CH_3 groups for hydrophobic surfaces. To apply these treatments, the probes and the capillaries were exposed to O_2 plasma for 60 s at 100 W and 0.4 mbar in a benchtop plasma asher (FEMTO, Diener Electronics), for surface activation. Following this, a solution of 2% PFOTS (448931-10G, Merck) in PFD (372439-100G, Merck) or a solution of Sigmacote (SL-2, Merck) was infused in the channels and capillaries. For PFOTS treatment, an incubation time of 20 minutes at 75°C was observed. Then, the channels were rinsed with PFD and dried out with air. For Sigmacote treatment, an incubation time of 20 minutes at 20°C was observed. Then, the channels were dried out with air and incubated for 20 minutes at 100°C. After each treatment, the elements were rinsed with deionized water and dried out with air.

With Sigmacote, improvements in the surface hydrophobicity were obtained in the channels and mainly in the capillaries, as shown in Figure 3.6c-d. With PFOTS, improvements were obtained in both conditions and were even better in the channels, as shown by the two convex interfaces of the droplets in Figure 3.6e-f. In fact, both treatments improved the affinity of the surfaces with PFD and reduced the affinity with the aqueous phase. Nevertheless, PFOTS proved more efficient than Sigmacote in *in vitro* conditions, especially inside the channels, while Sigmacote reduced the wetting of the aqueous phase in the capillaries better than PFOTS in *in vivo* conditions. This was probably because of the proteins and other biomolecules that induced biofouling of the surfaces with real samples. Therefore, PFOTS treatment was preferentially applied to the probes and Sigmacote treatment was preferentially applied to the capillaries.

3.3 Characterization of the fluidic system

The fluidic system to operate the probes is described in this section. It was designed for DoD and continuous push-pull sampling, that are the main operation modes.

3.3.1 Materials

The fluidic setup to operate the probe is shown in Figure 3.7. It was designed to respond fast, since DoD relies on accurate flow and timing control with multiple changes that are illustrated in Figure 3.8. Therefore, it used rigid tubing and glass syringes only and the inlet and outlet lines were filled with PFD, while the perfusion line was filled with perfusate. Reagents were also degassed under vacuum for 20 minutes prior to use, to prevent air bubble generation in the outlet channel.

A syringe-pump (NeMESYS low-pressure module, Cetoni) drove the perfusion line to deliver accurate volumes of perfusate. Similarly, another syringe-pump drove the inlet line. Thus, 25 μ L glass syringes with cemented needles (1702N, Hamilton) were used, that were interfaced end-to-end to 45 cm long rigid glass capillaries (TSP-250350, 250 μ m ID, 360 μ m OD, BGB Analytik AG), through press-fit connectors LMT-55 tubing (070534-02L-ND, VWR).

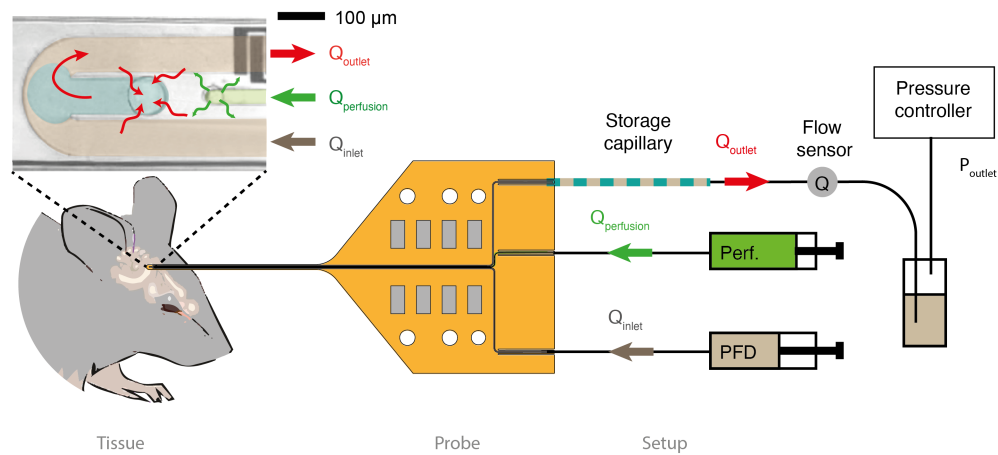


Figure 3.7: Fluidic setup. The perfusion and inlet lines are driven by syringe-pumps, while the outlet line is controlled with pressure and uses a flow sensor. All three lines reach the tip of the probe and access the tissue. The perfusate is delivered to the brain at the perfusion aperture. The inlet and outlet lines form a T-junction with the sampling channel that accesses the brain through the sampling aperture and from which droplets are collected. After sampling, the droplets are moved and stored in the storage capillary at the outlet.

Pressure control (Elveflow AF1 Dual, -700 mbar to 1000 mbar, Elvexsys) was used at the outlet line, together with a flow rate sensor (MFS 2, Elvexsys). This allowed control of the pressure applied to the tissue when sampling, to avoid sampling by ultrafiltration. This also reduced the generation of air bubbles, compared to actuation with syringe pumps.

The operation of the system was controlled with a custom LabVIEW interface combining all fluidic equipment. Its modularity also allowed communication with other equipment (Fluigent systems, Arduino, solenoid valves, etc.). The software also created logs of the operations and allowed programming of flow sequences for DoD.

3.3.2 Implementation of DoD

The DoD method was proposed in subsection 2.2.2 and was implemented in the probe. It works in cycles of 5 steps that were illustrated in Figure 2.4 and that can be implemented in the probe as in Figure 3.8. The inlet and perfusion lines are controlled in volume, with syringe pumps, while the outlet line is controlled in pressure, with a pressure controller.

In idle state, the probe is in contact with the tissue and all flows are stopped. A cycle starts with a *perfusion* step, during which the perfusion channel infuses a chosen and accurately controlled volume of perfusate, thus creating a perfusate pocket at the probe-tissue interface. All flows are stopped during the *diffusion* step and diffusion of the analytes occurs from the tissue to the pocket. The *sampling* step takes place after the desired diffusion time. Thus, the pocket is sampled by applying a negative pressure to the outlet $P_{sampling}$, that induces a flow Q_{outlet} in the outlet line, which depends on the hydraulic resistance of the system. This forms a droplet within the PFD phase at the T-junction, that moves towards the outlet, and is detected by the droplet-sensing electrodes. After sampling comes the *move* step, during which the flow rates of the inlet and outlet lines are matched ($Q_{outlet} = -Q_{inlet}$) to circulate the PFD and the droplet within the probe and towards the outlet. This occurs without any flow to or from the tissue and the droplet is transferred to the storage capillary at the outlet. During the *recovery* step, all flows are set to zero and the tissue equilibrates until the next cycle.

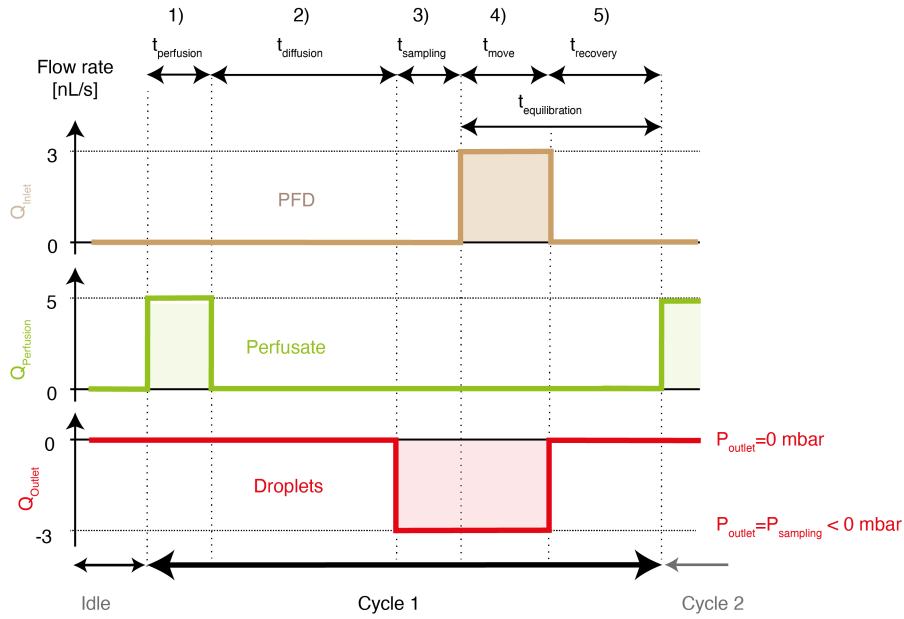


Figure 3.8: Implementation of the flow rate in the DoD steps in the inlet, perfusion, and outlet lines, that respectively contain PFD, perfusate and droplets within PFD. The inlet and perfusion lines are controlled in volume, while the outlet line is controlled in pressure. Positive flow rates go from the setup to the tip.

3.3.3 Implementation of continuous sampling

Continuous sampling can be achieved in a single phase of dialysate or in dialysate segmented in droplets. For single phase sampling, perfusate is infused at the flow rate $Q_{\text{perfusion}}$ and the outlet flow rate is adjusted so that $Q_{\text{outlet}} = -Q_{\text{perfusion}}$, whereas Q_{inlet} is set to zero. Alternatively, the dialysate can also be segmented within droplets. Thus, perfusate is infused at $Q_{\text{perfusion}}$, PFD is circulated at Q_{inlet} and the outlet flow rate is set to $Q_{\text{outlet}} = -(Q_{\text{perfusion}} + Q_{\text{inlet}})$, to collect the dialysate segmented by PFD. In both cases the fluidic lines operate continuously, and analytes are collected continuously.

3.3.4 Model of the fluidic system

The system was designed to operate in laminar flow conditions and therefore, the fluidic-electric analogy (Bruus, 2008; Oh et al., 2012) was used to model the fluidic system as in Figure 3.9. Since all components of the probe and the fluidic setup were rigid, they were modeled by hydraulic resistances R_h of which the values are reported in Table B.1 of section B.1. However, deformable elements should be modeled as capacitances. Since brain tissue is porous and deformable, flow in this medium is complex. The flow in the tissue is governed by Darcy's law and the deformability of the tissue also needs to be considered (Basser, 1992; Ehlers & Wagner, 2015). Thus, the brain was viewed as a hydraulic impedance \bar{Z}_b with real and imaginary parts $Re(\bar{Z}_b)$ and $Im(\bar{Z}_b)$, respectively. Despite an expression for the hydraulic resistivity in brain tissue was given by Morrison et al. (1999), estimation of the tissue resistance was not attempted as it would vary according to specific infusion conditions. Instead, the effects of tissue were only considered qualitatively to estimate the flow rate allowed for perfusion.

Flow during the *perfusion* step

A model of the perfusion line is shown in Figure 3.9a. During perfusion, the perfusion flow rate $Q_{perfusion}$ is controlled by a syringe pump and aims to create a pocket of perfusate at the tissue-probe interface. Thus, during a step infusion of perfusate, and because of the high density of the tissue, a little part of the perfusate is expected to penetrate the brain (Q_{brain}) while most of the flow is expected to contribute to the deformation of the tissue and the creation of a pocket at the tip of the probe (Q_{pocket}). Moreover, a deformable gap also needs to be considered between the tissue and the probe, that was modeled by a variable impedance \bar{Z}_g . Depending on the pressure in the pocket, deformation of brain tissue could enlarge the gap up to the surface of the brain, thus causing the perfusate to leak out of the tissue (Q_{leak}). This should be avoided. In fact, \bar{Z}_g would rather correspond to the behavior of a transistor, that would start conducting current above a high enough bias.

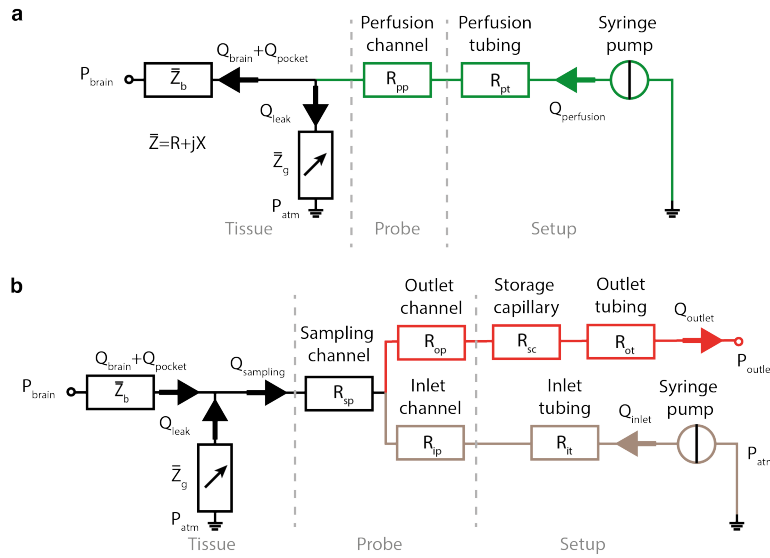


Figure 3.9: Hydraulic model of the fluidic setup. **a** Hydraulic model of the perfusion line driven by a syringe pump to infuse perfusate in the tissue. **b** Hydraulic model of the inlet and outlet lines connected to the sampling channel via the T-junction. The inlet line is driven by a syringe pump, whereas the outlet line is controlled in pressure.

To prevent leakage through this gap, the flow rate $Q_{perfusion}$ should be kept low enough to prevent backflow of perfusate up to the brain surface. Thus, for infusion in gray matter in the rat brain, Morrison et al. (1999) proposed an estimation of the backflow distance x_b (in cm) along a catheter of radius r_c (in cm), with the infusion rate $Q_{perfusion}$ (in $\mu\text{L}/\text{min}$). This is expressed in Equation 3.1.

$$x_b = 11.414 \cdot r_c^{0.8} \cdot Q_{perfusion}^{0.6} \quad (3.1)$$

Assuming the mouse striatum as a sphere of 20-38 mm³ (Rosen & Williams, 2001), this suggested that the backflow distance should not exceed the radius of the sphere, thus $x_b = 1.68$ mm. Moreover, if the probe were considered as a cylinder of radius $r_c = 160 \mu\text{m}$, the maximal allowed flow rate to avoid a backflow beyond 1.68 mm would be 3.5 nL/s. Therefore, the perfusion flow rate was set to 3 nL/s to avoid significant backflow coming out of the striatum *in vivo*.

Flow during the *sampling* step

During sampling, the flow occurs from the brain and through the outlet line only, as is illustrated in Figure 3.9b and with $Q_{outlet} = 0$ nL/s. Therefore, for an applied negative pressure P_{outlet} at the outlet, the flow rate $Q_{sampling} = Q_{outlet}$ depends on the total resistance of the outlet line and of the resistance in the tissue. Thus, the flow goes from the tissue through the short sampling channel from the sampling aperture to the T-junction (R_{sp}), the probe outlet (R_{op}), the storage capillary (R_{sc}) and to the outlet tubing that also includes the flow sensor (R_{ot}). Moreover, the impedance in the tissue space that is seen by the system should also be considered. In fact, this impedance changes over a sampling step. Thus, at the beginning of the sampling step, the flow comes from the pocket (Q_{pocket}) and the overall resistance seen by the system is low. However, after the pocket is fully sampled, the probe is in direct contact with the dense tissue and the resistance seen by the system is high; thus, the flow is minimal (Q_{brain}). Moreover, during sampling, Q_{leak} should not contribute because negative pressure that would rather tend to close the gap.

Flow during the *move* step

After sampling, the droplet in the outlet line is moved to the storage capillary. This is achieved by circulating PFD from the inlet line to the outlet line, while adjusting P_{outlet} so that $Q_{outlet} = -Q_{inlet}$. Therefore, the inlet and the outlet lines are concerned by this step, that are illustrated in Figure 3.9b.

3.3.5 Calibration of the outlet flow rate

Sampling and circulating flow rates in the range of 1 – 10 nL/s were targeted, within the stable operation conditions of the pressure controller. Therefore, the resistance of the outlet line was designed to operate at 10 nL/s at -200 mbar, thus 600 nL/min. This ensured a -500 mbar margin of maneuver for *in vivo* experiments, where the unknown impedance of the tissue would be involved. Omitting the impedance of the tissue, the total outlet resistance R_o was given by Equation 3.2, with the resistances in the probe R_{sp} and R_{op} , the resistance of the storage capillary R_{sc} , and the resistance of the outlet tubing R_{ot} , that included a flow sensor and a flow resistor. Their values are reported in Table B.1.

$$R_o = R_{sp} + R_{op} + R_{sc} + R_{ot} \quad (3.2)$$

Since R_{sp} , R_{op} and R_{sc} would change with the number of droplets in the system, the system was designed to operate at 10 nL/s at -200 mbar in the conditions of maximal resistance $R_{o,max}$. Modeling the pressure drop across a droplet in flow depends on many parameters: the difference in viscosity between the phases, the capillary number, the distance between the droplets, the size of the droplet and the channel geometry (Baroud et al., 2010; Labrot et al., 2009; Vanapalli et al., 2009). Thus, droplets were assumed as aqueous plugs of 20 nL ($\mu_{water} = 10^{-3} \text{ Pa} \cdot \text{s} = 10^{-3} \text{ kg/m/s}^2$) separated by 140 nL of PFD ($\mu_{PFD} = 6.41 \cdot 10^{-3} \text{ Pa} \cdot \text{s} = 6.41 \cdot 10^{-3} \text{ kg/m/s}^2$), in a storage capillary that was long enough to collect 100 droplets. Therefore, given the large droplets with respect to the dimensions of the channels and given the large separation distances in the capillary, the resistance of R_{op} and R_{sc} were computed as sums of resistances for 20 nL of water and resistances for 140 nL of PFD (Glawdel, 2012).

Based on this, R_{ot} was adjusted to limit the variation of R_o below 10%, namely to -8% over an experiment. Therefore, the resistance of the outlet was maximal when the system was entirely filled by PFD ($R_{o,max} = 1.99E + 15 \text{ kg}/(\text{m}^4\cdot\text{s})$) and minimal when the system was filled with 100 aqueous droplets of 20 nL separated by PFD ($R_{o,min} = 1.82E + 15 \text{ kg}/(\text{m}^4\cdot\text{s})$).

The estimated $R_{o,max}$ was equivalent to a hydraulic conductance of 3.01 nL/min/mbar or 0.0502 nL/s/mbar, which would provide a flow rate of 602 nL/min for -200 mbar applied to the outlet. This was verified experimentally by measuring the flow rate for different values of the outlet pressure when the probe was aspirating PFD from a beaker. The results are illustrated in Figure 3.10, and they confirmed a hydraulic conductance of 3.00 nL/min/mbar.

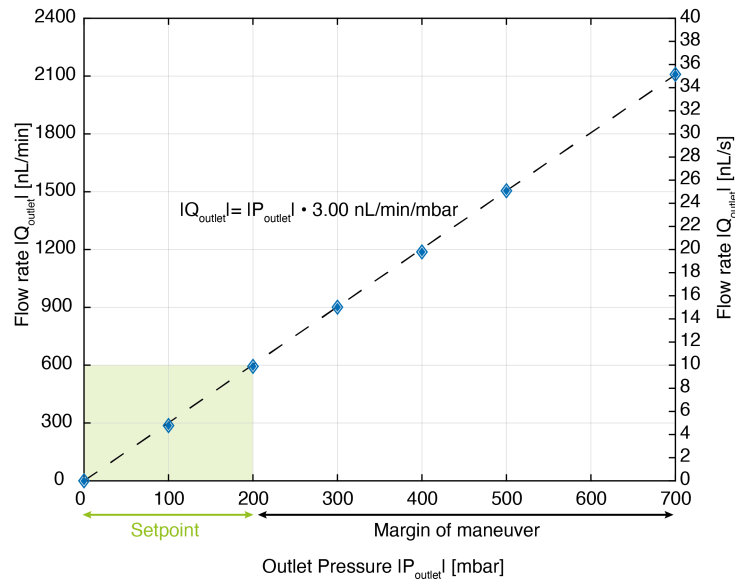


Figure 3.10: Calibration of the pressure-flow rate relationship at the outlet of the probe, for PFD sampling from a beaker.

3.4 Conclusion

The probe was fabricated in clean room and interfaced to a fluidic setup to implement the DoD sampling approach, but also continuous sampling with and without dialysate segmentation. The model of the fluidic system was discussed and the relation between the pressure at the outlet and the flow rate was characterized. Next, DoD will be applied to sample droplets in *in vitro* and *in vivo* models in chapter 4.

Chapter 4

Sampling models

*Part of this chapter is adapted with permission from Teixidor, J., Novello, S., Ortiz, D., Menin, L., Lashuel, H. A., Bertsch, A., & Renaud, P. (2022). On-Demand Nanoliter Sampling Probe for the Collection of Brain Fluid. Analytical Chemistry, 94(29), 10415–10426. Copyright 2022 American Chemical Society. This chapter reports the application of DoD sampling in *in vitro* and *in vivo* models.*

4.1 *In vitro* model - agarose brain phantom

First, the system was optimized and tested *in vitro* in a brain phantom of 0.6% agarose. With the tip of the probe inserted in the gel, this model allowed characterization of the performances of the DoD method, based on the recovery of NaCl and fluorescein from the gel. This passive model was used to emulate *in vivo* sampling better than free fluid in a beaker (Z.-J. Chen et al., 2004; Nicholson, 2001; Pomfret et al., 2013). Although it is less dense than the brain and does not integrate the exchanges and the metabolism, this model was also previously used by others (Ngernsutivorakul, Steyer, et al., 2018; Raman et al., 2020). Thus, it was deemed a valid model to validate the implementation of DoD sampling.

4.1.1 Materials

The gel was prepared from agarose (A9539-10G, Merck) dissolved in a Tris-Borate-EDTA buffer 1X (T4415, Merck), according to the process described by (Z.-J. Chen et al., 2004). The gel was cut into cubes of 1 cm^3 that were later soaked in an aqueous solution of 150 mM NaCl (S9888, CAS 7647-14-5, Merck) and 100 μM fluorescein (46955, CAS 2321-07-5, Merck). The cubes served as passive brain tissue models for the sampling of fluorescein and NaCl with the probe. For this purpose, a solution of 300 mM of sucrose (S0389, CAS 57-50-1, Merck) in deionized water was used as perfusate. After sampling, the recovery of these molecules was respectively measured by fluorescence and electrically. Fluorescence reported the fluorescein concentration in the droplets and was measured with an inverted microscope Leica DMIL (H3 filter set, objective 506075 - C Plan 10X/0.22 or objective 506151 - C Plan L20X/0.3, Leica Microsystems Wetzlar GmbH). Movies were acquired with a CMOS camera (UI-3060CP-C-HQ R2, IDS Imaging Development Systems GmbH) and analyzed with Fiji (ImageJ2) and MATLAB R2020b (MathWorks). The signal of the fluorescence varied linearly with the fluorescein concentration and was calibrated before each experiment.

For electrical measurements, a pair of coplanar Pt electrodes separated by 20 μm was used to measure the current across droplets moving over the electrodes, which reflected their conductivity, thus their NaCl concentration. Each electrode was 70 μm long and 20 μm wide and perpendicular to the outlet channel. They were similar to the interdigitated electrodes illustrated in Figure 3.4c, except that there were only 2 fingers. An impedance analysis system allowed the characterization of the electrodes (Agilent 4294A, Agilent technologies), with a sinusoidal excitation voltage of 100 mV in amplitude and a frequency ranging from 40 Hz to 10 MHz. This is reported in section D.1 of Appendix D. To measure the conductivity of fast-moving droplets, the current was measured with a HF2LI Lock-in amplifier and an HF2TA transimpedance current amplifier (Zurich Instruments), with a sinusoidal excitation signal of 100 mV at 1 MHz. The conductivity of 0 mM NaCl in 300 mM sucrose and 150 mM NaCl in 300 mM sucrose was measured at 5.99 $\mu\text{S}/\text{cm}$ and 11.02 mS/cm, respectively. In the following, the NaCl concentration in the solutions is reported as the fraction of 150 mM NaCl in 300 mM sucrose. Thus, 0 mM NaCl in 300 mM sucrose is 0% NaCl, 75 mM NaCl in 300 mM sucrose is 50% NaCl and 150 mM NaCl in 300 mM sucrose is 100% NaCl.

4.1.2 Electrical measurement of the NaCl in droplets

Based on the impedance results in section D.1, the HF2LI Lock-in amplifier was used to record the current $i(t) = I_i \sin(\omega t + \phi_i)$ across droplets moving in the channel, where $i(t)$ was the instantaneous current, I_i was the amplitude of the current, and ϕ_i was the phase, with respect to the excitation signal from the equipment. Therefore, a calibration was performed in droplets to evaluate the linearity of the signal at 1 MHz and in presence of PFD that could create a thin film over the electrodes. Hence, the tip of the probe was inserted in a tubing that was infused with solutions of different NaCl concentration and droplets were directly generated from it. Following their generation, the electrodes in the outlet channel measured the signal across them. The amplitude of the current I_i and the absolute value of the phase $|\phi_i|$ are reported for different NaCl concentrations in Figure 4.1a. In these conditions, a high linearity between the measured current and the concentration was obtained at 1 MHz.

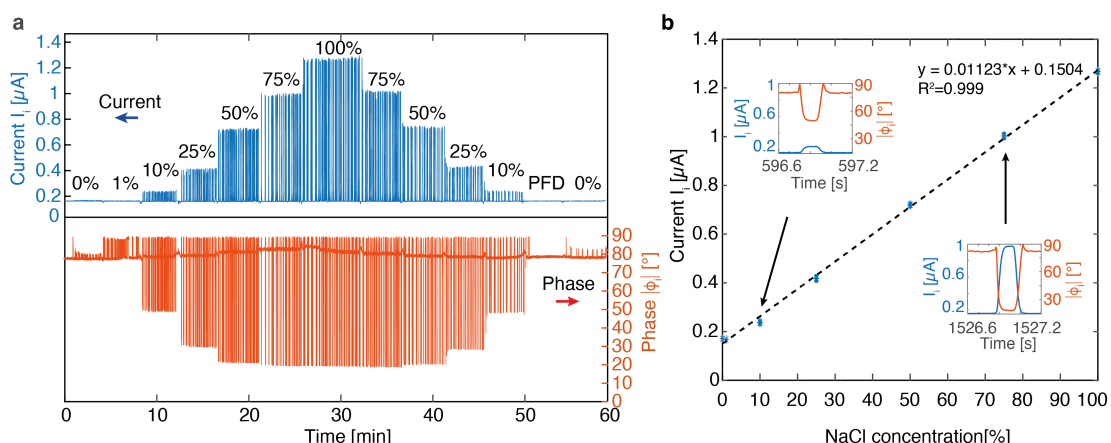


Figure 4.1: Electrical measurement of the NaCl concentration in the droplets. **a** Current I_i and phase $|\phi_i|$ measured through droplets flowing over the electrodes in the probe and containing between 0 mM (0%) and 150 mM NaCl (100%). **b** Calibration curve of the peak current I_i through the droplets against their NaCl concentration. The insets show the current and phase signals of two droplets, with the variation of $|\phi_i|$ to 90° at the arrival and departure of the droplets from the electrodes.

When the electrodes were covered by PFD, $|\phi_i|$ and I_i were approximately 80° and 0.15 μ A, respectively. However, when an aqueous droplet moved over the electrodes, an increase of I_i and a reduction of $|\phi_i|$ were observed, thus reflecting a change to a more resistive behavior of the system. Moreover, Figure 4.1b shows that the peak of I_i varied linearly and reversibly

with the NaCl concentration over the whole range of concentrations. Thus, the current I_i provided an estimation of the NaCl concentration in the sample with a linear function β such as $C_{\text{sample, NaCl}} = \beta(I_i)$. $|\phi_i|$ also varied with the NaCl concentration but did not scale linearly with it. Nonetheless, since $|\phi_i|$ varied abruptly to 90° at the arrival and departure of a droplet, it allowed discrimination of a PFD phase from an aqueous phase at low NaCl concentration, where the variation of I_i was low.

4.1.3 Droplet generation by DoD

The fluidic setup described in chapter 3 was used to implement DoD during *in vitro* experiments and verify its properties. For this purpose, the tip of the probe was inserted at the center of a cube of gel to emulate sampling in the brain, as illustrated in Figure 4.2a. A solution of 300 mM of sucrose served as perfusate with low conductivity in the perfusion line, to collect NaCl and fluorescein from the gel, while the rest was filled with PFD. With this system, the DoD sampling parameters were adjusted to allow droplet generation according to the flow sequence in Figure 3.8. During this process, multiple perfusion volumes, flow rates and timings were optimized to produce droplets of various sizes and Figure 4.2b shows an example of droplet generation at the T-junction. This shows a small droplet being aspirated through the sampling aperture during a 1 s *sampling* step, followed by a *move* step that started circulating PFD from the inlet to the outlet to displace the droplet. An additional droplet generation movie in agarose is available as supporting information of Teixidor et al. (2022).

4.1.4 Effect of the diffusion time on the recovery fraction

DoD cycles were applied, that used the parameters in Table 4.1. Briefly, a cycle started by infusing perfusate at 5 nL/s to create a 30 nL pocket of perfusate in the gel $V_{\text{perfusion}}$. Then, the diffusion time $t_{\text{diffusion}}$ was varied from 1 to 60 s and the pocket was aspirated over 10 s at -3 nL/s by adjusting P_{outlet} . After aspiration, the droplet was moved to the outlet by the circulating PFD within the probe at 3 nL/s, for 40 s. All flows were then stopped, and a recovery time of 20 s was observed, resulting in an equilibration time $t_{\text{equilibration}}$ of 60 s before the next cycle. The long equilibration time allowed the gel to equilibrate between two sampling events

and therefore the samples be considered as from punctual and independent sampling events. Thus, the effect of $t_{\text{diffusion}}$ could be studied without influence of depletion layer in the gel. This allowed the characterization of the effect of $t_{\text{diffusion}}$ over the collected concentration.

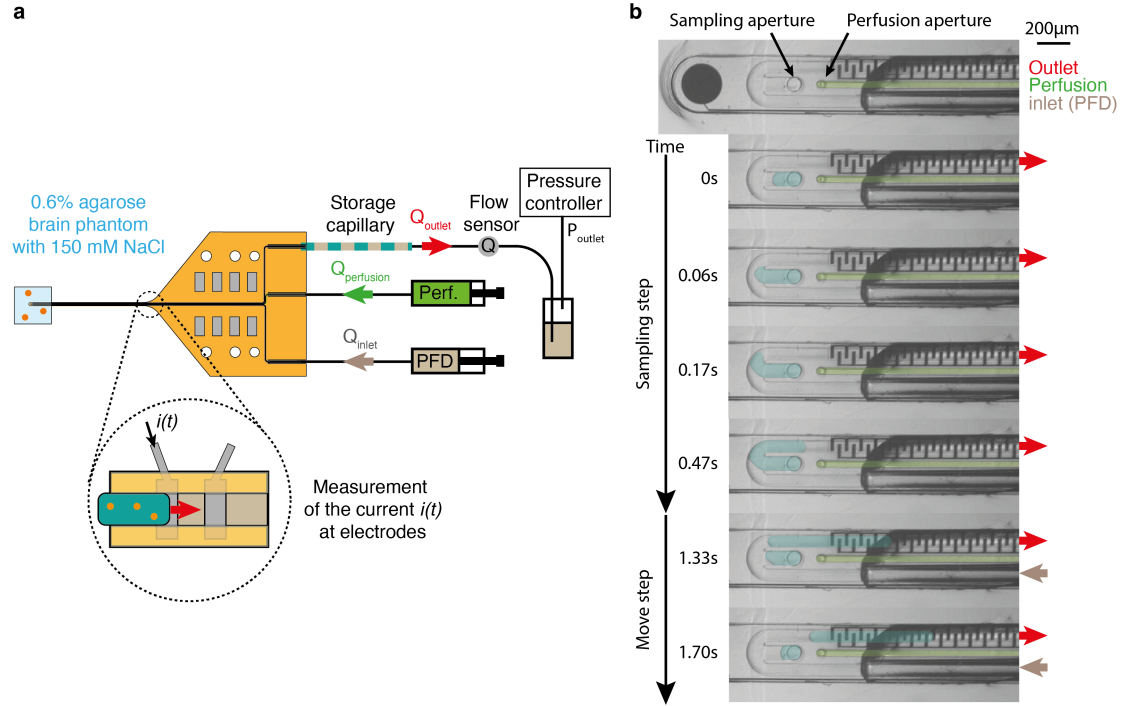


Figure 4.2: In vitro experiments of DoD in an agarose gel phantom. **a** The tip of the probe was inserted in a cube of 0.6% agarose. The inlet and perfusion flow rates were controlled by syringe-pumps whereas the outlet line was controlled by a pressure controller, connected to a flow sensor. Electrodes in the outlet channel measured the current through the droplets. **b** In idle state, the full probe is loaded with PFD, except the perfusion line filled with perfusate. Example of a 1.8 nL droplet generated during a *sampling* step from 0 s to 1 s and followed by a *move* step that started circulating the droplet at 1 s.

Using the characterization of the electrodes presented in Figure 4.1, the amplitude of the current $I_i = I_{\text{sample, NaCl}}$ was measured across the electrodes during sampling. The trace of the signal confirmed that the generation worked correctly and allowed measuring the concentration of NaCl in the droplets with the linear calibration curve presented in Figure 4.1b. Reference signals for the real concentrations in the gel were also acquired. This permitted to express the concentration in the samples in terms of recovery fraction η as in Equation 2.24.

Table 4.1: DoD parameters used for the *in vitro* experiments.

Perfusion ¹ volume [nL]	Perfusion time [s]	Diffusion time [s]	Sampling ² time [s]	Equilibration ^{3,4} time [s]	Number of samples [-]
30	6	1	10	60	17
30	6	3	10	60	22
30	6	5	10	60	28
30	6	10	10	60	35
30	6	30	10	60	17
30	6	60	10	60	13

¹ $Q_{\text{perfusion}} = 10 \text{ nL/s}$.

² P_{outlet} was adjusted to obtain $Q_{\text{outlet}} = -3 \text{ nL/s}$.

³ $t_{\text{equilibration}} = t_{\text{move}} + t_{\text{recovery}} = 20 \text{ s} + 40 \text{ s} = 60 \text{ s}$.

⁴ $Q_{\text{inlet}} = 3 \text{ nL/s}$ during t_{move} .

As an example, the trace of the current is expressed in terms of recovery fraction and reported in Figure 4.3a, for 3 different sets of parameters that produced 3 subsequent droplets. From these signals, the recovery fraction of the samples was extracted as the peak recovery fraction in the signal. The summary of the recovery fractions obtained with different values of $t_{\text{diffusion}}$ is reported in Figure 4.3b.

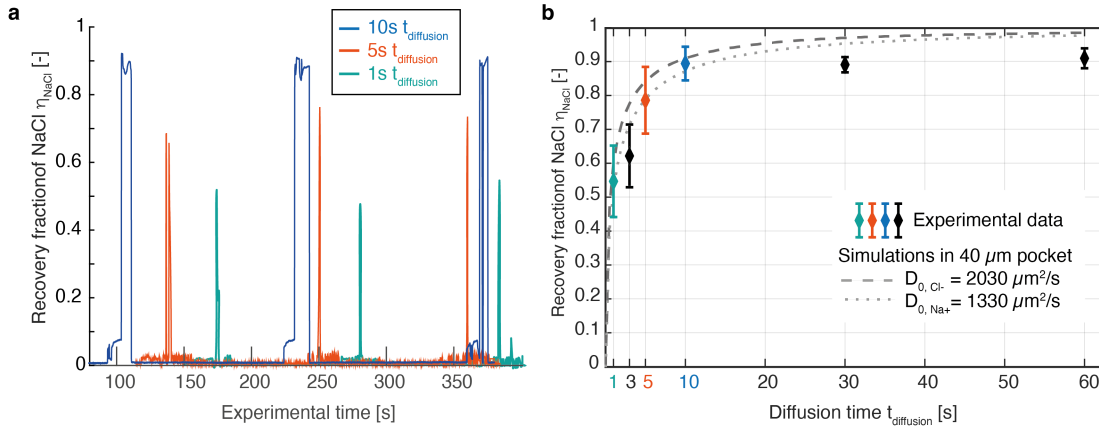


Figure 4.3: Effect of $t_{\text{diffusion}}$ measured *in vitro*. **a** The trace of the current, converted into the recovery fraction of NaCl, shows the recovery fraction of NaCl from the gel in 3 droplets generated by DoD with $t_{\text{diffusion}}$ values of 1 s, 5 s and 10 s. **b** Summary of the recovery fraction measured in the droplets against $t_{\text{diffusion}}$. The simulated recovery fraction of Na^+ and Cl^- is added for qualitative comparison.

Figure 4.3b shows that the recovery fraction, thus the collected concentration, increased with $t_{\text{diffusion}}$ until 10 s and remained stable for longer diffusion times. The large error bars from 1 s to 10 s illustrate the high sensitivity of the measurement to the diffusion time, since a strong concentration gradient initially exists between the pocket and the medium. The error bars are also enhanced by the fact that perfusion and sampling are not instantaneous, unlike in the simulations. Thus, collection of NaCl also depends on the creation and shrinking of the perfusate pocket. For longer diffusion times, the recovery fraction reached a plateau at 0.89 ± 0.04 with reduced error bars. However, the recovery did not increase further by increasing $t_{\text{diffusion}}$. This was probably because of the local dilution by the perfusate in this passive model.

Furthermore, predictions for the recovery fraction of Na^+ and Cl^- were made with the finite element analysis model introduced in chapter 2. Despite the real thickness of the pocket was unknown, it was expected to be within tens of microns and up to the thickness of the probe. Therefore, a 40 μm thick pocket was considered, and the simulations were added in overlay of Figure 4.3b for qualitative comparison. Little difference in η was predicted for the diffusion coefficients of Na^+ and Cl^- , that were respectively taken as $D_{0,\text{Na}^+} = 1330 \mu\text{m}^2/\text{s}$ and $D_{0,\text{Cl}^-} = 2030 \mu\text{m}^2/\text{s}$. This was probably due to the thinness of the pocket with respect to the scale of $t_{\text{diffusion}}$. Nevertheless, the uncertainty on the shape of the pocket and its non-instantaneous creation and sampling prevented strict comparison between the experimental data and the estimations by the simulations. This uncertainty could be clarified by measuring the shape of the pocket in the gel, for example with confocal imaging of a fluorescent dye in the perfusate. However, this was not done because the shape of the pocket in the gel would probably differ from the shape in the brain. Despite this, the similar trends followed by η with respect to $t_{\text{diffusion}}$ confirmed the principle and the effect of the diffusion step in the DoD sequence.

In parallel, the concentration of fluorescein $C_{\text{sample, fluo}}$ was measured by fluorescence through the probe for verification purposes. Similar results were obtained with fluorescein in the same droplets, although a larger standard deviation was obtained. These results are reported in section D.2 of Appendix D.

4.1.5 Effect of the equilibration time on the recovery fraction

The effect of $t_{\text{equilibration}}$ was also investigated. As indicated by the simulations in section 2.3.2, this parameter was supposed to suppress the transient regime typical of continuous sampling methods, by preventing the creation of a depletion layer in the gel. The principle relied on letting the concentration of the analyte in the medium equilibrate between two sampling events to provide similar starting conditions at the beginning of each cycle. This would permit to collect samples repeatedly and with a stable η . Therefore, the effect of $t_{\text{equilibration}}$ was evaluated by monitoring η across subsequent samples.

In the experiments in subsection 4.1.4, $t_{\text{equilibration}}$ was set to 60 s and η was steady. This is illustrated in Figure 4.4a, that reports the recovery fraction of the first sampled droplets with different DoD settings. In such conditions, each DoD cycle could be considered as a punctual sampling event and the samples were truly independent of each other. In addition, $t_{\text{equilibration}}$ was reduced to 21 s and 1 s to make a transient regime appear, that would be reflected by a decaying η across the droplets. However, this did not occur and the effect of $t_{\text{equilibration}}$ could not be illustrated directly with this model. With this implementation of DoD, this could be because of the small size of the perfusate pocket, thus the low quantity of removed analyte, but it could also be because of the high diffusion coefficients of Na^+ and Cl^- in water. Therefore, it was hypothesized that the absence of transient regime was characteristic of the sequential approach of DoD.

4.1.6 DoD and continuous sampling

To verify if the absence of transient regime was specific to DoD, an indirect approach was selected, by comparison with the performances of continuous push-pull sampling. Thus, the probe was used in continuous sampling mode to verify the existence of the transient and steady-state regimes. This was implemented as described in subsection 3.3.3, to collect dialysate in a single phase, but also dialysate segmented in droplets. A similar procedure as for DoD sampling was used, with the tip of the probe at the center of the gel. The perfusion flow rate $Q_{\text{perfusion}}$ and the instantaneous recovery fraction $\eta(t)$ was measured over time, based on the current across the electrodes.

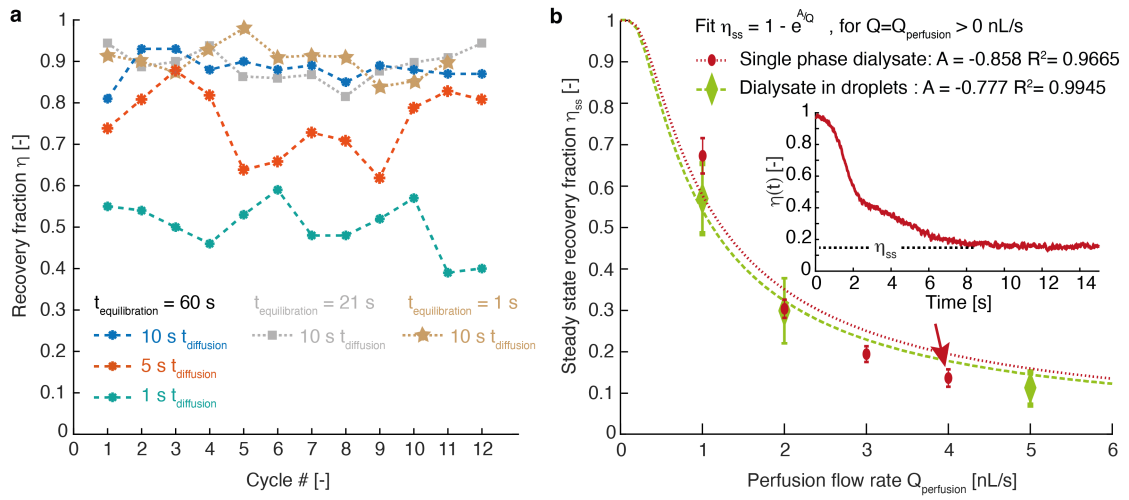


Figure 4.4: Recovery fraction and transient regime in DoD and continuous sampling conditions *in vitro*. **a** The recovery fraction η of subsequently sampled droplets with DoD cycles using $t_{\text{diffusion}}$ values of 1 s, 5 s and 10 s and $t_{\text{equilibration}}$ of 60 s. Two sets with $t_{\text{diffusion}}$ of 10 s and $t_{\text{equilibration}}$ of 21 s and 1 s are also reported. **b** The steady-state recovery fraction η_{ss} obtained for continuous push-pull sampling without and with segmentation into droplets. The perfusion flow rate $Q_{\text{perfusion}}$ was varied, and the outlet flow rate was adjusted accordingly. The inset shows the instantaneous evolution of $\eta(t)$, with a short transient regime and the steady-state η_{ss} .

The results are reported in Figure 4.4b. The inset shows the instantaneous recovery fraction in the dialysate for single phase push-pull sampling. It reports that a short transient regime existed, during which $\eta(t)$ decayed until a steady-state recovery fraction η_{ss} was reached, that depended on $Q_{\text{perfusion}}$. With this model, the timescale of the transient regime was short, and the transient regime was followed by a steady-state regime within several seconds only. Still, these two regimes appeared in all conditions, whereas this was not the case with DoD. As expected, similar results were obtained when the dialysate was segmented in droplets.

The relation between η_{ss} and $Q_{\text{perfusion}}$ was fitted with the prototype of the function in Equation 2.12, that expressed the steady-state recovery fraction E_d in microdialysis, as a function of the parameters of the system and of the flow rate of dialysate. The fit agreed well with the experimental data. Thus, it confirmed that the dynamics and the phenomena involved in microdialysis sampling and in push-pull sampling are similar, and that they could be observed with this model. Thus, despite the limitations of the model, the model was still valid to confirm the properties of DoD and would allow comparison of DoD to continuous sampling methods.

Among the differences between DoD sampling and continuous sampling, the results showed that DoD permitted collection of samples without transient regime. Opposite, a transient regime and a steady-state regime existed with continuous sampling methods. Moreover, the recovery fraction η of DoD is influenced by the diffusion time, while η_{ss} is influenced by the perfusion flow rate $Q_{\text{perfusion}}$ in continuous sampling methods.

The fitted curve for continuous sampling suggested that comparable performances with DoD could be obtained if $Q_{\text{perfusion}}$ were significantly reduced to approximately 0.25 nL/min. However, control of low flow rates for an extended period could prove difficult, especially in *in vivo* conditions. This would also reduce the interest of continuous sampling in terms of temporal resolution unless droplets were generated immediately after sampling, inside the probe. This would be feasible within this probe, but this was not investigated because this would also produce very small droplets of which the analysis might be challenging.

4.1.7 Discussion

The sampling experiments in this model verified the implementation DoD. On one hand, the effect of $t_{\text{diffusion}}$ was investigated and the results agreed with the simulations, since the recovery fraction could be tuned by adjusting the duration of the *diffusion* step. On the other hand, the effect of $t_{\text{equilibration}}$ could not be directly studied because no transient regime appeared in any of the conditions. Because direct study of $t_{\text{equilibration}}$ was not possible with DoD, the stability of the recovery fraction in the samples was hypothesized as specific to DoD and its sequential approach. This was verified indirectly, by comparison of the recovery fraction with to continuous sampling approaches that presented a transient regime and a steady-state regime. In fact, this confirmed that DoD is suitable for analyte sampling at high recovery fraction and without transient regime.

Nevertheless, the study and the confirmation of the real performances of DoD *in vivo* would require an active model with the same mechanical and hydraulic properties as brain tissue. This is not available yet. Moreover, in addition to the uncertainty on the shape of the pocket of perfusate, this prevented extraction of exact sampling parameters that could be directly used *in vivo*. For these reasons, DoD was next applied in a real brain.

4.2 *In vivo* model - mouse striatum

To demonstrate the potential of the sampling approach in a complex *in vivo* setting, DoD was applied in the striatum of anesthetized mice. This allowed to establish a procedure to collect droplets reliably, with the support of the sensors in the system.

4.2.1 Surgical procedure

All experimental procedures were performed in accordance with the local animal care authorities, under the cantonal license VD3492. Acute sampling experiments were performed with C57BL6/J mice and narcosis was induced by intra-peritoneal injection (10 μ L/g) of a cocktail of ketamine (100 mg/kg) and xylazine (10 mg/kg). The head of the animal was shaved, the skin was cleaned with betadine and the animal was placed on a stereotaxic frame to which the probe holder was secured. A lubricant eye ointment was applied to prevent dry eyes during anesthesia. A heating pad or an infrared lamp was used to maintain the temperature of the body during the procedure. Stereotactic coordinates were set to +0.6 mm anteroposterior, 2.0 mm mediolateral and -2.60 mm dorsoventrally from bregma, to target the dorsal striatum. A hole just big enough for the probe to access the brain was drilled into the skull without injuring the brain. During experiments, blood glucose measurements were carried out by collecting 0.6 μ L of blood from the tail vein on FreeStyle Precision test strips, with a glucometer (FreeStyle Precision Neo, Abbott).

4.2.2 Experimental procedure

The setup and methods were identical to the ones used *in vitro*, except the perfusion line was filled with Perfusion Fluid CNS (P000151, CMA Microdialysis) as perfusate. The probe was secured on a holder mounted on a stereotactic frame as in Figure 4.5b and inserted into the brain of the animal, with a small hole in its skull. Moreover, a digital endoscope (Andonstar) permitted to observe the outlet capillary to ensure that clean and blood-free samples were obtained and to size them.

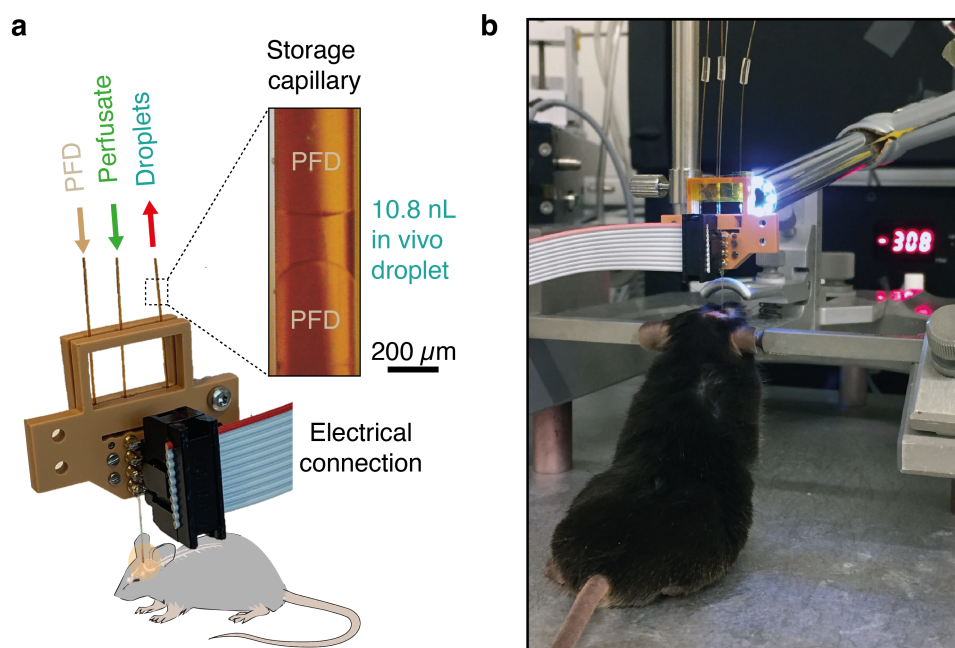


Figure 4.5: *In vivo* sampling in the brain of a mouse. **a** Fluidic and electrical interfacing of the probe, for the collection of the droplets in the storage capillary. **b** Real sampling conditions, with the endoscope in the background that monitors the droplets in the storage capillary. In these experiments, no cannula was used, and the needle was directly inserted in the brain through a small hole in the skull. The infrared lamp to maintain the body temperature is not shown.

During insertion of the probe, all lines dispensed fluid at 3 nL/s and the flows were stopped once in position. The total dispensed volumes were approximately 15 nL of perfusate and 30 nL of PFD and channel clogging never occurred with this procedure. Next, two cleaning cycles were performed to remove the dispensed fluids and potential debris, until clean samples were seen at the outlet. A cleaning cycle consisted of infusing 300 nL of perfusate into the tissue at 3 nL/s and sampling it back at the outlet at 3 nL/s. After two cleaning cycles, the system was left idle for 10 minutes, for the tissue to equilibrate, prior to starting the sampling session.

The end of an experiment was dictated by the end of the anesthesia. Thus, when the first signs of awakening were observed, the probe was removed from the brain and the animal was sutured back and allowed to recover. This usually occurred 90 to 120 minutes following the beginning of the anesthesia. Finally, the samples were stored in the outlet storage capillary at -20 °C, thus preserving their sampling order until analysis. The procedure did not induce any noticeable impairment in the animal.

4.2.3 Application of DoD *in vivo*

The implementation of DoD in the brain required some adjustments of the parameters with respect to the parameters used *in vitro*. This was supported by the signals of the electrodes in the probe and of the flow sensor at the outlet, that are reported in the following. They allowed reliable sampling over experiments of up to 120 minutes in complex *in vivo* settings.

Electrical droplet detection

The electrodes in the outlet channel that were previously used for NaCl concentration measurements *in vitro* allowed the identification of the changes of phases in the channel *in vivo*. Thus, they confirmed the successful operation of the system, by ensuring that an aqueous phase was collected with the right timing and allowed estimation of the sampling yield with different DoD settings. The sampling yield was defined as the rate of DoD sequences that successfully generated a droplet, with respect to the total number of DoD sequences applied. Figure 4.6 provides an example of this. Thus, 15 DoD cycles were applied, that infused 30 nL of $V_{\text{perfusion}}$ over 10 s and used $t_{\text{diffusion}}$ of 10 s, t_{sampling} of 10 s, t_{move} of 20 s and t_{recovery} of 1 s, for a total equilibration time $t_{\text{equilibration}}$ of 21 s. The width of the peaks is related to the volume and to the velocity of the droplets, that varies with the hydraulic resistance. Moreover, small peaks between the samples peaks correspond to residuals of aqueous phase pinned to the electrodes, because of biofouling. They are negligible compared to the samples and do not cause perturbations, and their signals are distinct from the signal of the samples.

Figure 4.6 reports that the 14 first cycles successfully generated a droplet, while the 15th cycle missed. This provided a sampling yield of 93% and suggested that the parameters needed to be adjusted for the next sampling events. This would be supported by monitor the signal of the flow rate sensor. Missed cycles are frequently due to the appearance of air bubbles in the outlet line or to the mismatch of the inlet and outlet flow rates, that cause an outflow of a few nanoliters of PFD at the tip. However, since PFD is inert, it can simply be aspirated back inside the probe to restore correct DoD operation for the next cycles. Moreover, air bubbles can be avoided by limiting the amplitude of the vacuum applied to the outlet and by degassing the solutions before the experiments.

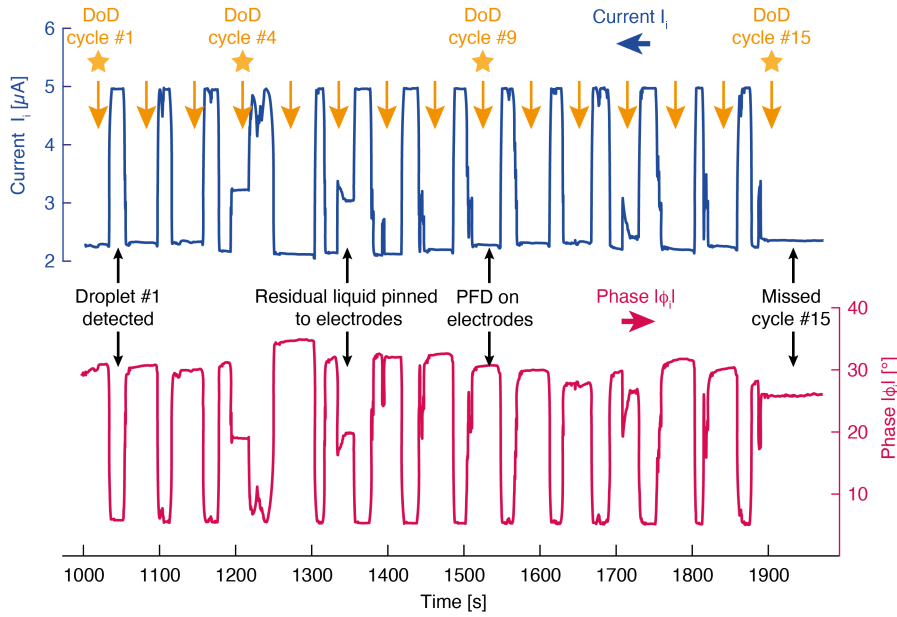


Figure 4.6: Electrical signal recorded by the droplet-sensing electrodes in the outlet channel during 15 DoD cycles *in vivo*. The amplitude of the current I_i increased when a droplet moved over the electrodes, whereas the absolute value of the phase ϕ_i reduced. In this example, 14 out of 15 cycles successfully produced a droplet.

Flow rate monitoring

During sampling, the hydraulic resistances reported in Figure 3.9b of chapter 3 could change and induce missed sampling events such as in Figure 4.6. These variations occurred in the tissue after full aspiration of the perfusate pocket, but also in the probe and in the storage capillary where droplets accumulated over time. These effects were also enhanced by the interactions between the droplets and the surfaces of the capillary because of biofouling, by the air bubbles extracted from the PFD over time and by the increase of hydraulic resistance caused by the viscous samples. However, these changes could be monitored by the flow sensor in the outlet line, that measured Q_{outlet} and allowed the adjustment of the sampling parameters. This is illustrated in Figure 4.7 during two DoD cycles in the brain.

Figure 4.7a reports a fast sampling cycle at the beginning of an experiment. The *perfusion* step started in (i), and no flow was expected in the outlet line, according to the implementation of DoD presented in Figure 3.8. In fact, the variation of Q_{outlet} was an artifact from the pressure

change at the end of the *move* step from the previous cycle, because of the compliances in the system, probably caused by air bubbles. However, this artifact disappeared fast, and the outlet flow rate correctly read 0 nL/min until the end of the *perfusion* and *diffusion* steps (ii). *Sampling* started by applying -300 mbar to the outlet and another artifact of the compliances appeared (iii) until the desired sampling flow rate of -300 nL/min was reached (iv). When the aspiration of the pocket finished (v), Q_{outlet} progressively reduced and stabilized to 0 nL/min (vi). At the beginning of the *move* step (vii), PFD was infused at the inlet at 300 nL/min and started moving the droplet towards the outlet. Thus, Q_{outlet} went back to -300 nL/min until the end of the step (viii). Finally, P_{outlet} was set back to 0 mbar for the *recovery* step and another effect of the compliances appeared before the next cycle (ix).

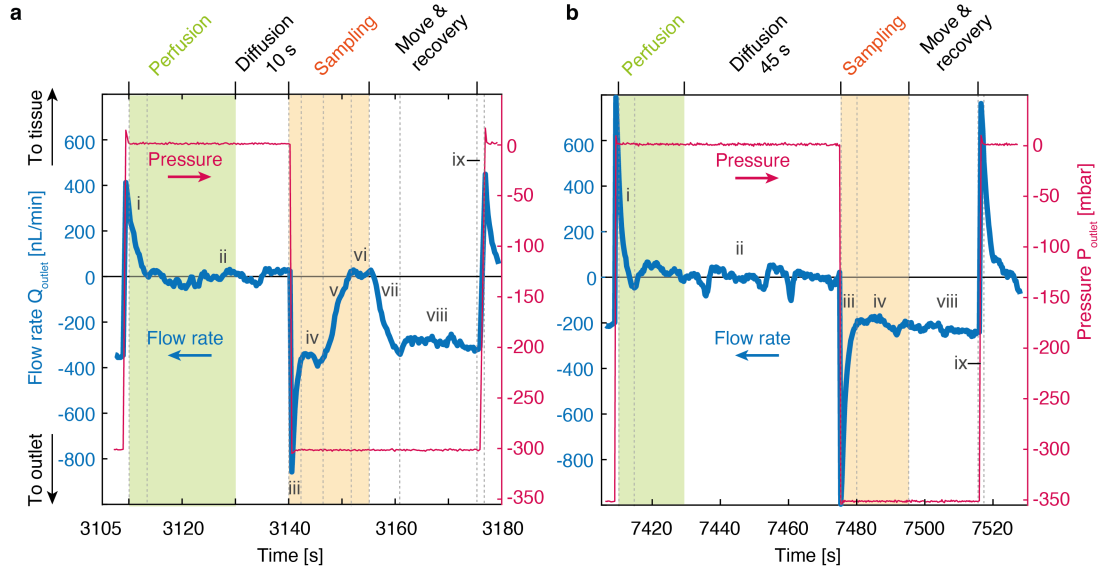


Figure 4.7: Outlet flow rate Q_{outlet} (left axis) and pressure P_{outlet} applied to the outlet line (right axis) for two DoD cycles executed *in vivo* at different stages of a sampling experiment. **a** Behavior of the flow rate during a cycle at the beginning of an experiment. Fast droplet aspiration occurred during the *sampling* step (iv), and Q_{outlet} reduced to 0 nL/min when the probe became in direct contact with the tissue (vi). This illustrated the high hydraulic resistance of the tissue and the need to adjust the parameters of DoD to prevent this. The parameters were $V_{\text{perfusion}} = 60$ nL at 3 nL/s, $t_{\text{diffusion}} = 10$ s, $P_{\text{outlet}} = -300$ mbar during $t_{\text{sampling}} = 15$ s, $Q_{\text{inlet}} = 300$ nL/min during $t_{\text{move}} = 20$ s, and $t_{\text{recovery}} = 1$ s. **b** A cycle was applied later in the same experiment, with modified sampling parameters to compensate for the changes of hydraulic resistance in the outlet line and to allow a smooth transition between the end of the *sampling* step and the *move* step. The parameters were $V_{\text{perfusion}} = 60$ nL at 3 nL/s over 20 s, $t_{\text{diffusion}} = 45$ s, $P_{\text{outlet}} = -350$ mbar during $t_{\text{sampling}} = 20$ s, $Q_{\text{inlet}} = 200$ nL/min during $t_{\text{move}} = 20$ s, and $t_{\text{recovery}} = 1$ s.

The trace of Q_{outlet} in Figure 4.7a showed that sampling occurred fast and that the parameters of the *sampling* step needed to be adjusted to prevent the application of P_{outlet} directly to the tissue (vi). This adjustment would prevent direct sampling by ultrafiltration and potential tissue perturbations. In fact, the change of Q_{outlet} from (iv) to (vi) also confirmed that a change occurred in the hydraulic system when the aspiration of the pocket finished. As discussed in the section 3.3.4, this probably reflected the high hydraulic resistance of the brain that makes it difficult to extract fluid directly from the brain. This also suggested that no flow came from the gap between the probe and the tissue.

In addition, the settings also required some adjustments to compensate for the changes of hydraulic resistance in the outlet line over the duration of long experiments. This is illustrated in Figure 4.7b that reports Q_{outlet} and P_{outlet} during another cycle, later in the same experiment. In this case, despite P_{outlet} was reduced to -350 mbar instead of -300 mbar in Figure 4.7a, Q_{outlet} read -200 nL/min only, instead of -300 nL/min (iv). Figure 4.7b also shows that in these conditions, with t_{sampling} extended by 5 s, and with Q_{inlet} reduced to 200 nL/min, it was possible adjust the sampling so that the aspiration of the pocket did not finish before the end of the *sampling* step. Thus, the states (v), (vi) and (vii) did not appear and a seamless transition occurred between the two steps. Except the effect of the compliances, the trace of Q_{outlet} was the one expected by the implementation presented in Figure 3.8. In practice, P_{outlet} was frequently adjusted to allow only the early phase of (v) to appear before the *move* step, to ensure no dispense of PFD to the brain.

Collection of samples *in vivo*

The readout of the two sensors described in the previous section allowed the adjustment of the settings for reliable sampling in a complex environment. Moreover, the size of the collected samples in the storage capillary also required characterization. Thus, perfusion volumes of 30 nL and 60 nL were infused at 3 nL/s, to limit the backflow along the needle and prevent perfusate leakage out of the brain, as discussed in section 3.3.4. Moreover, the collected droplets were imaged in the capillary at the exit of the probe with an endoscope. This allowed measuring their size and determining the optimal perfusion volume $V_{\text{perfusion}}$.

The characteristics of the droplets are reported in Table 4.2 for the two different perfusion volumes. Additionally, a movie of droplet sampling *in vivo* available as supporting information of Teixidor et al. (2022).

Table 4.2: Properties of the droplets collected *in vivo*

Perfusion volume [nL]	Average droplet size [nL]	Standard deviation [nL]	Median droplet size [nL]	1st quartile [nL]	3rd quartile [nL]	Number of droplets [-]	Sampling yield [%]
30	9.9	4.1	9.6	7.2	11.4	88	85
60	24.4	15.7	21	12.2	30.7	115	91

Unsurprisingly, smaller droplets were obtained with 30 nL of perfusate than with 60 nL, with average volumes of 9.9 nL and 24.4 nL, respectively. This means that only 33% and 40% of $V_{\text{perfusion}}$ was sampled back, respectively. The fate of the volume difference was not investigated but the missing volume could have penetrated the dense tissue or flowed back along the probe. However, the surface of the brain was monitored during the experiments and did not show any liquid leaking out of the brain. This is also supported by the limited backflow propagation length x_b that was expected with a perfusion flow rate of 3 nL/s, as discussed in section 3.3.4. This should be verified, but it appears likely that tissue penetration had occurred along the needle.

Moreover, despite the large variability in size, both volumes of perfusate allowed droplet sampling with comparable sampling yields, respectively 85% and 91%. However, in practice, droplets smaller than 12 nL were prone to collapsing on the surfaces of the capillary. After collapsing, the aqueous phase would wait for the next droplet and merge with it, thus inducing a loss of temporal resolution from 1 to 2 t_{cycle} . This especially occurred when the affinity of the aqueous phase with the glass was high because of biofouling. This is illustrated by the small contact angle between the droplet and the walls of the capillary in Figure 4.5a. Although functional treatment of the capillary with Sigmacote prevented this by reducing biofouling, the effect faded over time.

4.2.4 Discussion

The results confirmed the successful implementation of the DoD approach *in vivo*. With the developed procedure that includes cleaning cycles and 10 minutes of rest, DoD cycles could be applied already 20 minutes after the insertion of the probe and the sampling experiments usually lasted for 60 to 90 minutes and were limited by the duration of the anesthesia, not by the sampling system. In fact, the droplet-sensing electrodes and the flow sensor were key features to ensure the correct operation of the system for punctual and repeated sampling and to adjust the sampling parameters over the duration of the experiments. Despite the number of samples collected over a sampling experiment varied according to the number of cycles applied and to their settings, between 30 and 70 samples were usually collected in the storage capillary, every 1 to 2 minutes. But this could be changed based on the requirements of the study and faster sampling settings could prove interesting to monitor concentration changes with temporal dynamics in the range of a few minutes. Anecdotally, the fastest DoD cycles that were successfully tested had a cycle time t_{cycle} as short as 32 s and used 30 nL of perfusate. Moreover, continuous sampling with dialysate segmented in droplets was also successfully tested, but these conditions were not characterized.

The tests of the perfusion volumes suggested that both 30 nL and 60 nL could be used to collect droplets, but that 60 nL provided a higher reliability because the droplets were larger and collapsed less frequently in the capillary. The issue of the collapse could be reduced by using a narrower storage capillary, but this would increase the hydraulic resistance of the outlet line, or by using a more efficient antifouling treatment. A surfactant could also improve the stability of the droplets and prevent merging, but it could perturb sample analysis and it should be biocompatible. Moreover, the shape and the fate of the perfusate pocket in the tissue should be investigated in further studies to understand the mismatch between the perfused volume and the collected volume. This would benefit the optimization of $V_{\text{perfusion}}$ but also the development of more realistic simulations and more realistic brain models. In the meantime, a major question that remains concerns the ability of the method to collect molecules in the samples. This will be discussed in the next chapter.

4.3 Conclusion

The DoD approach was studied in two models. The first model consisted of a passive 0.6% agarose brain phantom (*in vitro* model) and the second one was the striatum of an anesthetized mouse (*in vivo* model). In addition to confirming the ability of sampling droplets by DoD, the experiments in agarose confirmed the effect of $t_{\text{diffusion}}$ over the recovery fraction of NaCl in the gel. On the other hand, the effect of $t_{\text{equilibration}}$ could not be investigated directly since no transient regime appeared with DoD. However, the results suggested that the absence of transient regime is characteristic of DoD, by comparison with continuous sampling applied to this same model. Despite the limitations of the passive model, this still permitted to confirm that the DoD approach was suitable to collect samples punctually or repeatedly, with a high recovery fraction of NaCl. Overall, experiments with this model allowed the confirmation that this implementation met the objectives that were described in subsection 2.2.1.

Finally, the implementation of DoD was confirmed *in vivo*. Reliable surgical and sampling protocols were developed with the help of the electrodes in the probe and of the flow sensor in the outlet line. Using these protocols, droplets with a median size of 9.6 nL and 21 nL could be reliably collected with perfusion volumes of 30 nL and 60 nL, respectively. These samples were frozen in the storage capillary at the end of the experiments and their analysis will be described in chapter 5. This will permit to verify the collection of brain molecules in the samples collected with the DoD method.

Chapter 5

Glucose collection with the DoD approach

Part of this chapter is adapted with permission from Teixidor, J., Novello, S., Ortiz, D., Menin, L., Lashuel, H. A., Bertsch, A., & Renaud, P. (2022). On-Demand Nanoliter Sampling Probe for the Collection of Brain Fluid. Analytical Chemistry, 94(29), 10415–10426. Copyright 2022 American Chemical Society.

This chapter reports the analysis of the *in vivo* samples collected with the DoD approach presented in the previous chapter. The analytical method selected for this purpose was nanoelectrospray ionization Fourier transform mass spectrometry (nanoESI-FTMS). It allowed quantification of glucose in the samples to confirm the sampling properties of DoD.

5.1 Analytical methods for droplet samples

To evaluate the potential of DoD sampling for the capture molecules in the brain, appropriate analytical methods for 20 nL samples were needed to quantify the extracted molecules. Given the conditions of the samples (size, salts, concentrations, interfering molecules, etc.), the choice of an analytical method for this purpose was a major challenge. In fact, this was a challenge that sampling studies with microdialysis or push-pull sampling face as well, and

which makes it required to consider the properties of both the sampling method and the analytical method in the study design. Thus, with these sampling methods, trade-offs need to be made between the flow rate of dialysate, the time to collect a sample, the desired recovery fraction, and the analytical system (Hammarlund-Udenaes, 2017b). They influence the volume and the concentration of the samples, that need to be compatible with the properties of the analytical method. Therefore, the selection of an analytical method to measure the molecules in the droplets was based on the library of droplet-compatible solutions that had been reported. Thus, extensive reviews were published on the analytics of droplets and small volumes of samples, that benefited from many advances in microfluidics (Basova & Foret, 2015; Feng et al., 2019; Ha et al., 2021; W.-w. Liu & Zhu, 2020; Perry et al., 2009; Shang et al., 2017; Y. Zhu & Fang, 2013). This includes fluorescence (Nightingale et al., 2019; van den Brink et al., 2019; M. Wang et al., 2008), electrochemistry (Abadie et al., 2021; Chae et al., 2016; Delahaye et al., 2021; Suea-Ngam et al., 2015), electrophoresis (Niu et al., 2013; M. Wang et al., 2011; M. Wang et al., 2009), chromatography (Piendl et al., 2021), and mass spectrometry (Bell et al., 2021; N. Bergman et al., 2014; R. Chen et al., 2012; Ngernsutivorakul, Steyer, et al., 2018; Pereira et al., 2013; Persike et al., 2010; Petit-Pierre et al., 2017; Song et al., 2012).

Among these methods, nanoelectrospray ionization mass spectrometry (nanoESI-MS) is a soft ionization method that has been frequently used to analyze droplets of dialysate. With this method, the samples are infused into an emitter located in front of a mass spectrometer and a high voltage is applied to it, to generate an electrospray. This consists of a spray of liquid droplets that become increasingly charged as the solvent evaporates and release ions that can be detected by the mass spectrometer. Its relative tolerance to ion-suppression is a significant advantage for the analysis of dialysate (Ngernsutivorakul, Steyer, et al., 2018; Schmidt et al., 2003), since the ECF and the perfusate contain a high concentration of salts (e.g., 147 mM of Na^+ and 153.8 mM of Cl^- in CNS Perfusion fluid from CMA Microdialysis). In addition, low flow rates can be used, and the method is sensitive to the concentration, not to the total mass of an analyte. Thus, this method was suitable for the measurement and the quantification of small molecules in individual droplets. In fact, this method had been reported for the analysis of ACh, Glu, GABA, and glutamine in droplets of dialysate by direct infusion (Ngernsutivorakul, Steyer, et al., 2018; Song et al., 2012). In addition, the method was

also reported robust to fluorinated oils that separated the droplets, and it could be combined with custom emitters and advanced MS features for ion accumulation, ion fragmentation and ion mobility separation (Beulig et al., 2017; Hartner et al., 2021; Peretzki et al., 2020; Y. Zhang et al., 2022). Based on this, this method was deemed appropriate to measure the concentration of the molecules captured in the samples collected by DoD. Thus, it would permit to verify the properties of the method in a complex *in vivo* setting. Moreover, since the samples were complex and since performing a separation of the analytes in small samples would be challenging, nanoESI-FTMS was selected because it provided a higher resolution compared to nanoESI-MS.

5.2 Development of the nanoESI-FTMS method

Among the wide range of molecules in the striatum of mice that can be measured by nanoESI-FTMS, quantification of neurotransmitters and glucose is of particular interest. In fact, their study could illustrate the molecular imbalances that occur in the brain and that are caused by neurodegenerative diseases (Allaman et al., 2010; Han et al., 2021). As a reference, the basal extracellular concentrations of DA, ACh, Glu and GABA were respectively reported as 1.7 ± 0.2 nM, 42 ± 10 nM, 1100 ± 200 nM, and 39 ± 4 nM, in the striatum of rats (Slaney et al., 2013). Alternatively, the basal extracellular concentration of glucose was reported at 1.4 ± 0.59 mM in the motor cortex of mice (Béland-Millar et al., 2017), but values in the 0.3 to 3.3 mM range were also reported (Fray et al., 1997; McNay & Gold, 1999; Routh, 2002; Valenta et al., 2021). Because of its higher concentration, and because its concentration was not supposed to spontaneously vary significantly over the timescale of the sampling experiments, glucose was selected as the molecule of choice to verify the collection properties of DoD *in vivo*. This will be developed and reported in this section.

Despite the analysis of droplets by nanoESI-MS had been reported in the literature, the method with nanoESI-FTMS needed to be developed at EPFL to analyze the content of the *in vivo* droplets collected in the storage capillary. This was performed at the Mass Spectrometry and Elemental Analysis Platform (SB-ISIC-MSEAP), with technical support from Laure Menin and Daniel Ortiz.

5.2.1 Materials and methods

A schematic of the setup that was used is described in Figure 5.1a. The capillary with the samples (TSP 250350, 250 μm ID, 360 μm OD, BGB Analytik AG) was interfaced to the stainless steel nanoemitters PSSE-3 (30 mm in length, 30 μm ID, 150 μm OD, PepSep) through a custom transparent press-fit connector for seamless droplet transfer. This connector was made of two pieces of 190 μm ID Tygon LMT-55 tubing (ISM05502-10, Ismatec) and 130 μm ID Tygon LMT-55 tubing (ISM05502-10, Ismatec), connected by a piece of fused silica capillary (TSP-100245, 100 μm ID, 238 μm OD, BGB Analytik AG). The actual dead-volume of this connector was measured from 0.5 to 3 nL, depending on the adjustment and was deemed negligible compared to the volume of the samples. The flow rate was driven by a NeMESYS low-pressure syringe pump (Cetoni), with a 10 μL glass syringe (1701N, Hamilton) at 120 nL/min, through LMT-55 tubing (97618-09, VWR). Finally, the samples were electrosprayed at the emitter, to which a spray voltage of 2.6 kV was applied, with respect to the mass spectrometer (LTQ Orbitrap ELITE ETD, Thermo Scientific). The system was equipped with the nanoSpray Flex Ion source (Thermo Scientific) and Figure 5.1b shows a close view of the front of the mass spectrometer. This shows that an ABIRD system (ESI Source Solutions) blew filtered air over the MS inlet to remove polysiloxanes in ambient air, and that a short fluorinated tubing (250 μm ID, BGB Analytik AG or BIOGENERAL) was used as a drain for PFD and placed around the emitter to prevent PFD accumulation at the tip (Beulig et al., 2017). This was important, because even if a clean electrospray could be obtained without it, as shown in Figure 5.1c, it could also be perturbed by the accumulation of PFD in Figure 5.1d, which produced a signal of poor quality.

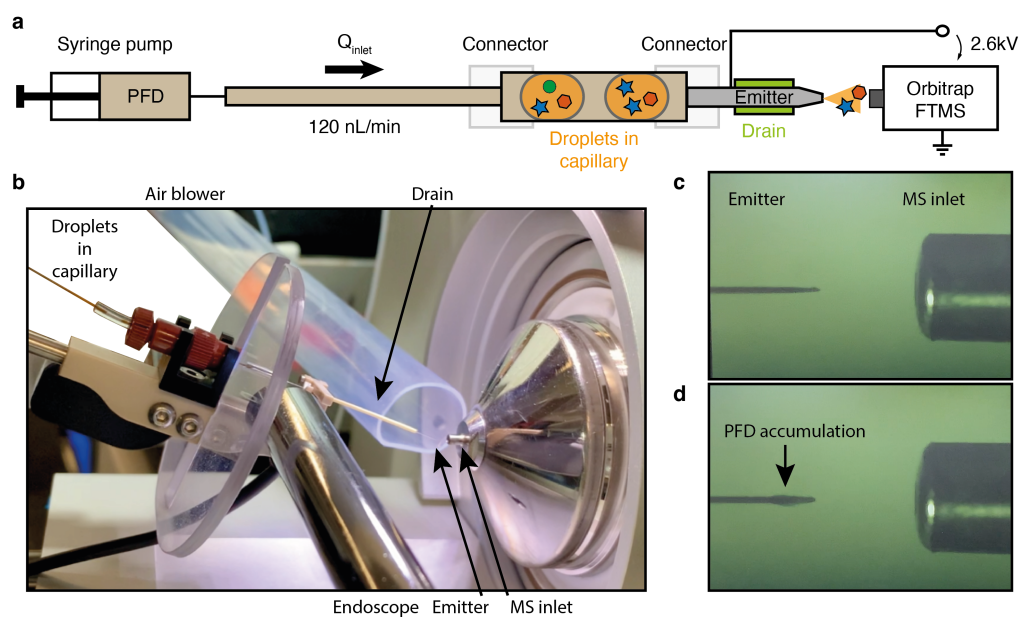


Figure 5.1: Setup for nanoESI-FTMS measurements. **a** Schematic of the setup. A syringe-pump drives the flow of PFD that infuses the droplets into the emitter at high voltage, at the inlet of the mass spectrometer. The drain helps remove the PFD that accumulates at the tip. **b** Picture of the experimental setup. The endoscope verifies seamless droplet transfer from the capillary to the emitter. The air blower blows filtered air at the emitter tip. **c** Close up on the emitter tip (130 μm OD) during droplet spraying. **d** Close up on the emitter tip during a long phase of PFD during two droplets, with PFD accumulation at the tip in absence of drain.

D-(+)-Glucose (G8270, CAS 50-99-7, Merck) in Perfusion Fluid CNS (CMA Microdialysis) was used to prepare *in vitro* calibration and reference samples. To help ionization and provide a reference for quantitative analysis, an additive was prepared, that was mixed with the calibration samples and that would need to be added to the real samples later. The additive was prepared by dissolving an isotope of glucose, D-Glucose-13C6 (389374, CAS 110187-42-3, Merck) in 67% deionized water and 33% acetonitrile (ACN) (900667, CAS 75-05-8, Merck). This isotope was referred to as the Internal standard (IS). Glucose and IS were detected in Selected Ion Monitoring (SIM) mode using a 20 m/z wide window centered on 206 m/z . Moreover, the signals of both molecules were respectively extracted at 203.05 m/z and 209.07 m/z , with a mass extraction window of 100 ppm. FT-MS spectra were recorded in the reduced profile mode at a resolution set to 30000. Moreover, 1 microscan was used with a maximum injection time of 1000 ms and the automatic gain control (AGC) was set to 5E5. Data analysis was performed on Xcalibur (Thermo Scientific) and MATLAB (R2020b, MathWorks).

5.2.2 Characterization of the signals

The preliminary experiments with glucose in CNS perfusion fluid are reported in section E.1 of Appendix E. They confirmed the seamless transfer of droplets to the emitter and concluded that an additive was required to enhance the ionization of glucose. Thus, the results in this section were all obtained with glucose in CNS Perfusion fluid and the additive. The additive contained ACN to enhance the ionization and the IS served as a reference to compensate for the variations of the signal of glucose and to quantify the glucose. In the final samples, the ACN content was always adjusted to 30%, whereas the IS concentration required some optimization.

The detection of 50 μM of glucose and 100 μM of IS in SIM mode is shown in the ion chromatogram in Figure 5.2a. Moreover, their identities were also confirmed by accurate mass measurements, following fragmentation by collision induced dissociation (CID), with energies of 28 eV and 35 eV respectively, followed by the assignment of their main fragment ions. Consequently, glucose produced a main fragment at 164.93 m/z in Figure 5.2b, while the main fragment of the IS was at 190.88 m/z in Figure 5.2c. However, the fragmentation efficiency of the IS was much lower than the one of glucose and the signal of the IS fragment did not reflect the IS concentration reliably. Therefore, both molecules were measured in SIM mode as in Figure 5.2a.

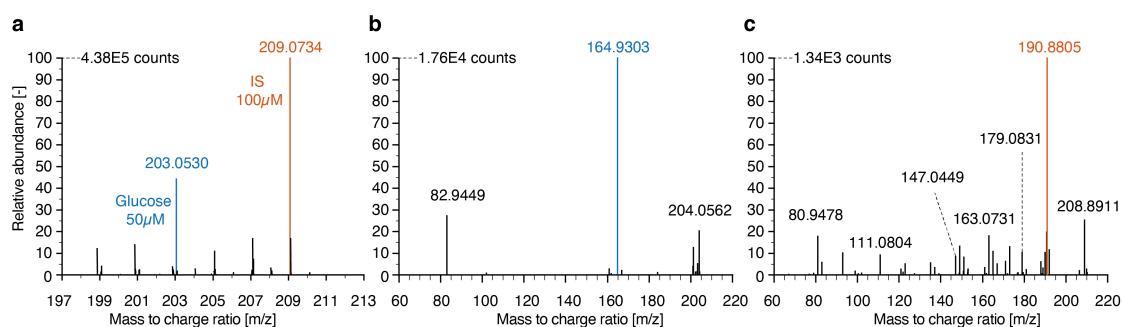


Figure 5.2: Glucose and internal standard measured in calibration solutions. **a** Ion chromatogram of a solution of 50 μM of glucose (203.05 m/z) and 100 μM of IS (209.07 m/z) in CNS Perfusion fluid and additive. **b** Ion chromatogram after fragmentation of the glucose (CID energy 28 eV at 203.05 m/z). **c** Ion chromatogram after fragmentation of the IS (CID energy 35 eV at 209.07 m/z).

Next, the relative abundance of glucose and IS was characterized in reference droplets in CNS Perfusion fluid mixed with additive, with a fixed concentration of IS at 250 μM and glucose concentrations varying from 0 μM to 1500 μM , as in Figure 5.3. The signals of glucose, IS and their ratio over the analysis of three droplets of 20 to 30 nL are shown in Figure 5.3a. Because the two molecules are similar, their signals varied identically in response of the perturbations of the electrospray and the computation of their ratio allowed more a reliable quantification of the glucose. This was also shown in section E.2 of Appendix E.

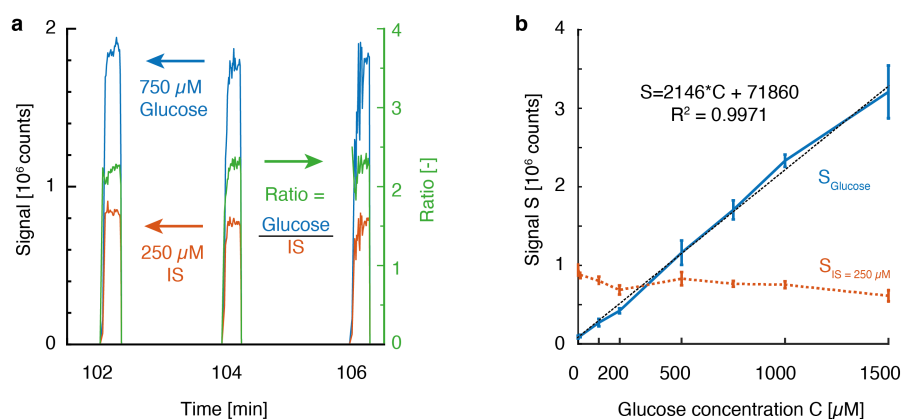


Figure 5.3: Calibration of the signals of glucose and IS with reference droplets. **a** Raw signals and their ratio, for three droplets containing 750 μM of glucose and 250 μM of IS. **b** Calibration of the signals for glucose concentrations of 0, 10, 100, 200, 500, 750, 1000 and 1500 μM , with 250 μM of IS in reference droplets.

The stability of the IS signal was investigated in droplets of different glucose concentrations to confirm the reliable use of IS as a reference for glucose quantification. This is shown in Figure 5.3b. Thus, the signal of glucose varied linearly with the concentration, while the signal of 250 μM of IS did not vary significantly within the 200-1000 μM glucose range. This suggested that the IS was a suitable reference for absolute quantification of glucose in this range of concentrations. However, the results also showed that when the difference in concentration between the two molecules was large ($C_{\text{glucose}} \ll C_{\text{IS}}$ or $C_{\text{glucose}} \gg C_{\text{IS}}$), the most concentrated molecule induced ion-suppression on the other molecule, probably due to competitive effects. Moreover, this suggested to use a concentration of IS close to the concentration of the glucose in the *in vivo* samples and this required to find an accurate dilution factor.

5.2.3 Quantification of glucose

To determine the right concentration of IS to be added to the samples, direct infusion of raw *in vivo* samples was performed and the signal of glucose over 4 droplets is shown in Figure 5.4a.

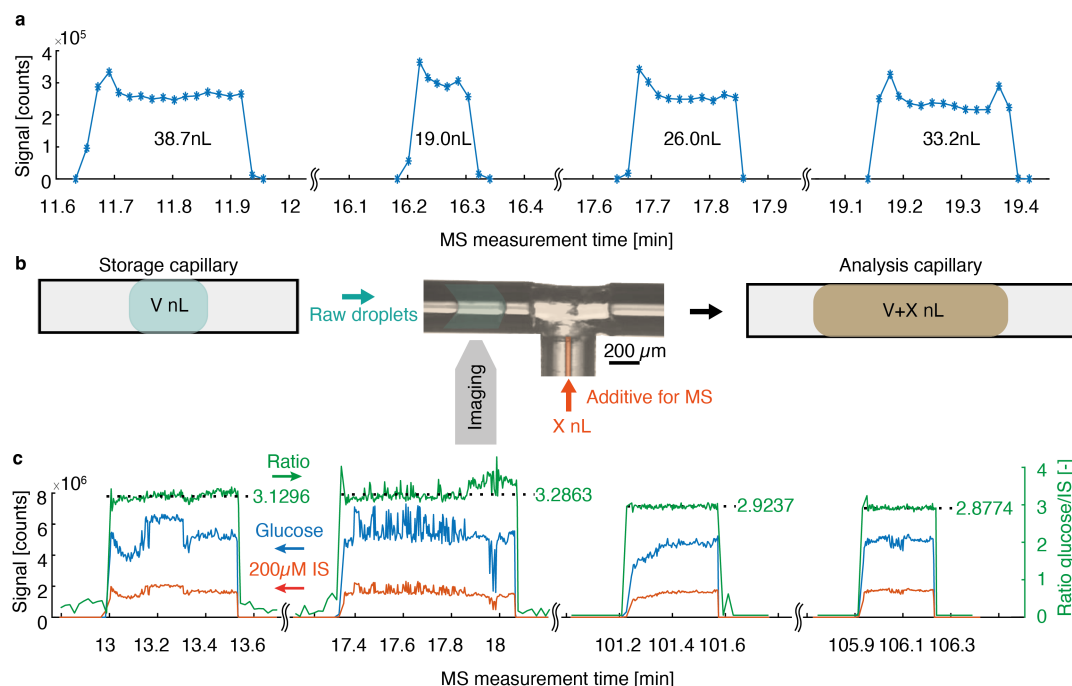


Figure 5.4: Signals of glucose and IS with *in vivo* sampled droplets. **a** Glucose signal of raw droplets, directly infused at 120 nL/min. **b** Picoinjection of additive is done with a custom T-junction. A raw droplet of volume V is moved to the junction and measured optically. Then, the appropriate volume of additive is injected to form a diluted droplet of volume $V+X$. **c** Signals of droplets diluted with additive (1:4 ratio). Final ACN and IS concentrations of 30% and 200 μ M. The ratio of the signals and its median are added with respect to the right axis.

Although relatively sharp rectangular signals were obtained, variations at the beginning and at the end of the droplets made the extraction of the concentration questionable, even with a calibration. Moreover, only a few points could be acquired over the duration of each droplet, because ionization was not optimal and because the samples were small. Based on this, and with the help of calibration curves without additive, the glucose concentration was estimated between 2 mM and 3 mM, in droplets sampled *in vivo* with a perfusion volume of 60 nL and a diffusion time of 10 s. Thus, dilution factors of 5 and 10 were tested for the dilution of *in vivo* droplets with the additive. With these dilution factors, final IS concentrations of 250 μ M and 200 μ M were targeted, respectively. In both cases, the final fraction of ACN was set to 30%.

A picoinjection procedure was performed to inject the additive in the samples. This was done with a custom T-junction, that is illustrated in Figure 5.4b. It was made of a 10 mm-long piece of Tygon LMT-55 tubing (SC0026T, 250 μm OD, Ismatec) with a hole of 250 μm in diameter drilled on the side and perpendicular to its lumen. This hole was fitted with a glass capillary with an inner diameter of 50 μm (TSP-050375, 360 μm OD, BGB Analytik AG) and the assembly was glued with epoxy and treated with Sigmacote to prevent biofouling. To perform picoinjection, the storage capillary with the raw droplets was connected to a syringe pump and inserted at one end of this junction, while a new capillary called the analysis capillary was inserted at the opposite end. Finally, the middle capillary was connected to a syringe filled with the additive. During operation, the raw droplets were subsequently moved close to the T-junction and their size was measured optically on a microscope. Then, they were moved to the junction, where the injection of additive occurred, with an accurate volume to reach the desired dilution factor. Mixing occurred spontaneously because no surfactant was present, and the final volume of the diluted droplet was measured to ensure the accuracy of the addition. After the addition, the diluted droplet was transferred to the analysis capillary and the same procedure was applied to the next raw droplet. Additionally, a movie of the picoinjection procedure is available as supporting information of Teixidor et al. (2022).

Thus, this picoinjection procedure permitted to inject the right amount of additive to the raw droplets that were of different sizes and the signals of the glucose and the IS in diluted droplets are reported in Figure 5.4c. Interestingly, a stronger glucose signal was obtained compared to Figure 5.4a, despite the dilution. It shows that the ACN enhanced the ionization and that this permitted a more frequent acquisition of measurement points by the mass spectrometer. The larger volume also allowed a longer acquisition time per sample. In addition, this was also probably induced by the reduced ion-suppression caused by the salts that were also diluted. Similar to the observations with reference *in vitro* samples in Figure 5.3a, the computation of the ratio of the glucose signal to the IS signal allowed the compensation of the signal variations. This improved the reliability of the measurements and allowed absolute quantification of the glucose in the samples. To that end, a calibration curve between the measured ratio and the real glucose concentration that was initially in the raw droplet was established after each experiment and a typical calibration curve is reported in section E.3 of Appendix E.

5.3 Properties of DoD for the collection of glucose

The method developed in section 5.2 allowed the quantification of the glucose collected *in vivo* with the DoD approach.

5.3.1 The stability of the concentration

First, the stability of the recovery fraction over successive sampling events was verified. This is illustrated in Figure 5.5, with the first 10 sampled droplets from 3 sets of repeated sampling events, of which the parameters are reported in the first 3 rows of Table 5.1. The sampling events respectively used 1 s, 5 s, and 10 s of diffusion time, while all sets used 30 nL of perfusate infused over 10 s, 20 s of sampling time and 30 s of equilibration time.

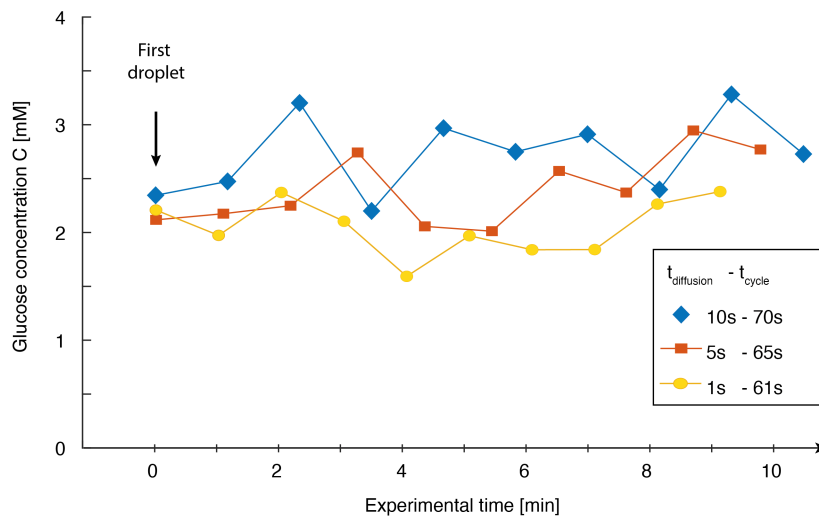


Figure 5.5: Glucose measured in 3 sets of DoD sampling parameters with respective diffusion times of 10 s, 5 s, and 1 s, in the same animal. The 10 first subsequently sampled droplets of each set are reported. All sets used 30 nL of perfusion over 10 s, 20 s of sampling time and 30 s of equilibration time.

Table 5.1: DoD parameters for glucose quantification *in vivo*

Perfusion volume [nL]	Perfusion time [s]	Diffusion time [s]	Sampling time [s]	Equilibration time [s]	Number of samples [-]
30	10	1	20	30	45
30	10	5	20	30	26
30	10	10	20	30	17
60	20	1	20	30	13
60	20	10	20	30	11
60	20	30	20	30	11
60	20	60	20	30	6

Based on these results, DoD did not appear to cause any transient regime since the measured concentration did not decay across the subsequent samples. Consequently, all samples could be considered independent. This also means that in these conditions, a reliable sample could be obtained from the first sampling event. In fact, this absence of transient regime, when sampling was applied repeatedly, was already observed *in vitro* in Figure 4.4a. Thus, this seemed to confirm that DoD sampling prevented the appearance of a transient regime *in vivo*, at least for the collection of glucose, and there is no need to wait for a steady-state regime to be installed before obtaining a steady recovery fraction. Furthermore, with the developed sampling procedure that included two cleaning cycles followed by 10 minutes of rest before starting the samplings, this allowed the collection of a first sample within approximately 20 minutes. Sampling could probably be performed earlier, but this was not investigated. Finally, the fact that no transient regime occurred with DoD is a significant advantage compared to the continuous sampling methods that need to stabilize the recovery fraction first.

Moreover, all measured samples provided a concentration of glucose within the range reported in the literature, from 0.3 to 3.3 mM, according to Routh (2002). Furthermore, these results also agreed with the initial estimations of the glucose concentration in early experiments without IS and that were reported in Figure 5.4.

Recalling Equation 2.12 from chapter 2 and the effects of the perfusion flow rate on the recovery fraction of NaCl in the gel, that were presented in Figure 4.4b, an equivalent average flow rate of perfusate can be considered to explain the high concentration measured in the samples. Since the sets used 30 nL of perfusate over cycle times from 61 s to 70 s, this provides

equivalent continuous flow rates from 29.5 nL/min to 25.7 nL/min, respectively. These flow rates were much lower than the flow rates frequently used in microdialysis but close to the very low flow rate of 25 nL/min that was recently used with push-pull micropipettes to sample neurotransmitters from tissue sections *ex vivo* (Cabay et al., 2018) and from the brain of flies *in vivo* (Fisher & Shippy, 2022). With this push-pull flow rate, samples were collected every 10 minutes and high recovery fractions of neurotransmitters were claimed because of the low flow rate. Although it is still difficult to draw a parallel between these reports and the results obtained here since the models and molecules were different, the high concentrations obtained in this work appear consistent with the theory and with the literature. As a last note, despite these articles did not discuss the existence of a transient regime, a slow decay of the sampled concentration was reported over hours of continuous sampling (Cabay et al., 2018). Therefore, it cannot be excluded that DoD still induced a very slow transient regime, which is simply not visible within the timescale of the experiments. However, even if this were the case, this transient regime would probably not induce a significant reduction of the recovery fraction in the DoD samples to be an issue within the acute sampling experiments in this work.

5.3.2 The diffusion time and the concentration

In Figure 4.3 of subsection 4.1.4, longer diffusion times increased the recovery fraction of NaCl in the samples in *in vitro* conditions. This effect was also studied *in vivo* by the quantification of glucose in the samples collected with 7 different sets of DoD parameters, that are summarized in Table 5.1. One animal was used with 30 nL of perfusion volume and some of the measured samples were presented in Figure 5.5. Another animal was used with 60 nL of perfusion volume. All the other parameters were kept identical and the results are reported in Figure 5.6, with the numerical data in Table 5.2.

Regardless of the perfusion volume that was used, the results indicate that the collected concentration of glucose increased with the diffusion time. Moreover the dependence of the concentration with respect to the diffusion time seemed to follow a trend similar to the one observed in simulations in Figure 2.6 and *in vitro* in Figure 4.3. The reason for the high

concentration that was obtained already after 1 s of diffusion probably comes from the non-instantaneous creation of the perfusate pocket in the brain. In fact, the infusion of 30 nL and 60 nL of perfusate at 3 nL/s takes respectively 10 s and 20 s. During this time, not only does the pocket grow, but it already starts to collect samples. It is also interesting to observe that the error bars reduced when the diffusion time increased, similar to the observations *in vitro*.

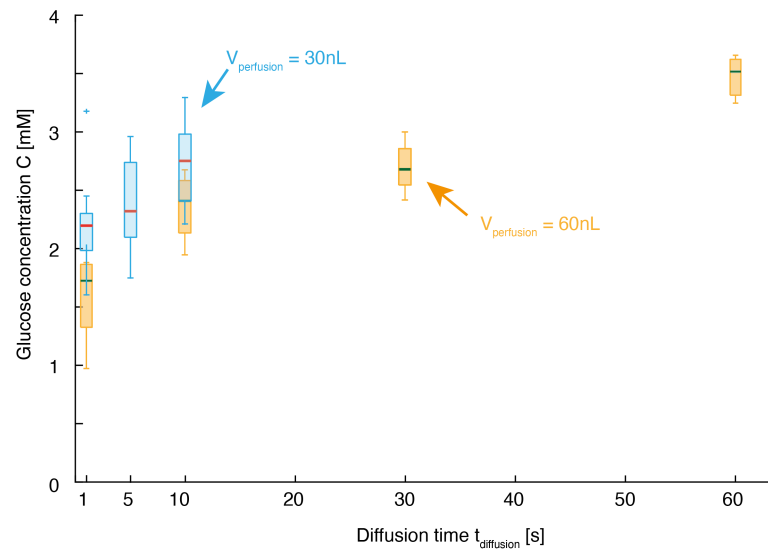


Figure 5.6: Glucose quantified in droplets sampled *in vivo*, with sets of DoD parameters that varied the perfusion volume between 30 nL and 70 nL and the diffusion time from 1 s to 60 s.

Table 5.2: Summary of the glucose measurements presented in Figure 5.6

$V_{\text{perfusion}}$ $t_{\text{diffusion}}$	30 nL			60 nL			
	1 s	5 s	10 s	1 s	10 s	30 s	60 s
Average concentration [μM]	2177	2381	2735	1596	2369	2702	3477
Standard deviation [μM]	312	372	368	360	265	191	170
Median [μM]	2194	2320	2748	1737	2418	2687	3520
Number of DoD samples	45	26	17	13	11	11	6

The question of the effect of the perfused volume is also of interest and for diffusion times of 1 s and 10 s, the concentration was lower with a perfusion volume of 60 nL than with 30 nL. It is legitimate to wonder to which extent the extra volume contributes to increasing the thickness of the pocket and to which extent it rather elongates it along the probe. Based on these results, it is not possible to answer this question, especially since the samplings were performed in different animals. Because of that, these differences could come from differences in glucose in the brains or from slightly different conditions of the pocket between the probe and the tissue and that influenced the pocket shape. Since a perfusate volume of 60 nL allowed the collection of samples with concentrations close to the ones measured in the samples with a perfusate volume of 30 nL, but with a higher sample stability in the capillary, an in-depth study of the formation and shrinking of the perfusate pocket would be needed in the case of a perfusate volume of 60 nL. This would allow to optimize an optimal *perfusion* step and to limit the loss of perfusate that was reported in section 4.2.3.

On that matter, it is also interesting to recall the question of the lost perfusate volume, that was discussed in section 4.2.3. In fact, despite the loss of perfusate, the concentration measured in the samples did not decay over time. This was surprising because one could have expected that this would induce a progressive dilution of the concentration over time. A hypothesis to explain the absence of this effect could be that the perfusion rate is low enough and that the pocket shape is distributed over a long distance. Thus, the brain could accommodate the full perfusion volume without significant dilution of the analytes in the ECF. At the time of writing, the answers to this question are not known, but the fact that this did not perturb the concentration in the samples is a positive property. However, further studies on the pocket shape and on the fate of the perfusate should also focus on this aspect.

5.3.3 The recovery fraction of glucose in the brain

Sampling at a high recovery fraction is one of the objectives of the DoD and based on the data in Table 5.2, 3.48 ± 0.17 mM was the highest average concentration of glucose measured in the samples, with 60 nL of perfusate and 60 s of diffusion time. This provides an equivalent flow rate of 36 nL/min, close to the low flow rates used for high recovery fraction and limited

transient regime in the literature (Cabay et al., 2018; Fisher & Shippy, 2022). In contrast to *in vitro* conditions where the concentration of the medium was known, defining the true glucose concentration in the ECF is a delicate question, but the literature could provide estimates.

According to the literature, the extracellular glucose concentration measured with microdialysis was reported in the range of $350 \pm 20 \mu\text{M}$ (Fray et al., 1997) and $530 \mu\text{M}$ in the striatum of awake rats (Valenta et al., 2021), and at $1.3 \pm 0.03 \text{ mM}$ in the hippocampus of awake rats (McNay et al., 2000). In fact, large variations were reported for the extracellular glucose concentration in the brain of rats, in the 0.3 to 3.3 mM range, according to McNay and Gold (1999), Ronne-Engström et al. (1995), and Routh (2002). This value seemed to vary according to the brain compartment and according to the measurement procedure. For example, a basal concentration of $1.4 \pm 0.59 \text{ mM}$ was reported in the motor cortex of awake mice with an electrochemical probe (Béland-Millar et al., 2017). In another study, a concentration of 3.3 mM was quantified with microdialysis in the brain of anaesthetized rats (Ronne-Engström et al., 1995). In this study, the concentration was measured with the no-net-flux method, which is one of the main methods to quantify the concentration of an analyte in the ECF with microdialysis (Kho et al., 2017). Furthermore, this concentration of 3.3 mM was close to the concentration of $3.48 \pm 0.17 \text{ mM}$ measured in this work by DoD and reported in Figure 5.6.

To verify if the conditions reported by Ronne-Engström et al. (1995) were close to the conditions in this work, a literature review was conducted. This provided that an anesthesia with ketamine/xylazine could induce a hyperglycemia in mice (Brown et al., 2005). In this work, a fast increase of blood glucose concentration was reported in mice 15 minutes after the anesthesia with ketamine/xylazine. Thus, hyperglycemia levels of approximately 268% of the baseline concentration were reported after 60 minutes and even reached up to 460% in some cases. Although this study did not mention the possible increase in extracellular glucose concentration in the brain, it was hypothesized that this effect could explain the high concentration of glucose that was measured in the DoD samples.

Therefore, blood glucose measurements were performed from the tail vein of an animal to verify if a hyperglycemia followed the anesthesia. Thus, small drops of blood were analyzed with a glucometer (FreeStyle Precision Neo, Abbott) and a glycemia of 8.1 mM was measured

5 minutes after the anesthesia. This served as the reference, although this value might have already been above the real baseline. In fact, the animal license did not permit to do measurements earlier. Measurements were repeated 20 minutes after the anesthesia and until the end of sampling session. After 20 minutes, a significant hyperglycemia was observed, that remained steady for the rest of the experiment, with an average concentration of 23.8 ± 3.2 mM. Considering the baseline glycemia of 8.1 mM, these measurements suggested that blood glucose levels increased to at least $294 \pm 40\%$ of the baseline level. This confirmed the induction of a hyperglycemia by the anesthesia, as reported by Brown et al. (2005).

In addition, and although variable ratios from 2 to 10 were reported between the blood glucose concentration and the extracellular glucose concentration in the brain (Routh, 2002), it seemed likely that this hyperglycemia could be reflected in the striatum. For these reasons, except the fact that the concentration of 3.3 mM was measured in rats (Ronne-Engström et al., 1995), this value appeared an acceptable reference to estimate the recovery fraction of the samples collected by DoD. Thus, this would provide a recovery fraction between 99% and 112%. Since the recovery fraction has a superior bound at 100%, by definition in Equation 2.12, a value above 100% does not make sense. However, this still suggests that the recovery fraction in the samples was high, which was one of the objectives of the development of the DoD approach. Nonetheless, the estimation of the recovery fraction is only as accurate as the accuracy of the value considered as the true concentration, 3.3 mM here. This value was measured in rats and assumed to be similar in the brain of mice, because these are two rodent models that share many properties. However, although no report of different glucose concentration in the brain of mice and rats was found in the literature, differences could still exist between these models (Ellenbroek & Youn, 2016).

5.4 Conclusion

The nanoESI-FTMS method proved appropriate to quantify glucose in droplets sampled by DoD. This permitted to confirm the absence of transient regime when sampling was applied in the brain repeatedly with DoD. This was consistent with the measurements *in vitro*, for the collection of NaCl from a passive gel model. Furthermore, this absence of transient regime confirmed that this method is suited for punctual sampling events at specific times of interest for the study and within short experiments, since there is no need to wait for a steady-state regime to be installed. These are significant advantages of DoD in comparison to continuous sampling methods. However, DoD should not be perceived as a replacement of microdialysis and push-pull sampling method. Instead, it should be considered as an alternative method to improve quantitative molecular studies in the brain. It could be used either as a standalone method, or in parallel of continuous sampling methods, to help calibrate them.

Moreover, the measurements also confirmed the effect of the diffusion time on the recovery fraction in the samples collected in the brain. Nonetheless, the estimation of the recovery fraction in the DoD samples was challenging because of the choice of the reference for the extracellular glucose concentration. In practice, it would be interesting to perform more experiments and to see if the concentration keeps increasing beyond 60 s of diffusion time. This would also allow an estimation of the maximal concentration that can possibly be collected and help determine the real glucose concentration in the ECF. In the meantime, the concentration of 3.3 mM that was reported in the brain of anesthetized rats appeared to be a good estimation of the real glucose concentration in the ECF in the conditions of this work. This value was very close to the maximal concentration of 3.48 ± 0.17 mM that was measured in the DoD samples but claiming a reliable value of the recovery fraction would be delicate. However, it still seems reasonable to affirm that a high recovery fraction was obtained with the DoD approach.

Finally, these experiments showed the potential of the method for the collection of glucose, which served as a proof-of-concept molecule. In practice, if a study targeting other analytes were conducted with DoD, the properties of the approach should also be characterized for each analyte, since its transport and its physiological interactions in the tissue might influence the

recovery fraction. Since the development of analytical methods for such samples is complex and since each study would have different goals, this was not performed for other molecules. Nevertheless, this work with glucose paved the way for the design of new studies to detect and quantify molecules in the brain and the next chapter will briefly report the measurement of neurotransmitters in droplets to show that DoD sampling is not limited to the collection and measurement of glucose.

Chapter 6

Measurement of neurotransmitters in droplets

Part of this chapter is adapted from Leroy, A., Teixidor, J., Bertsch, A., & Renaud, P. (2021). In-flow electrochemical detection of chemicals in droplets with pyrolysed photoresist electrodes: application as a module for quantification of microsampled dopamine. Lab on a Chip, 21(17), 3328–3337, with permission from the Royal Society of Chemistry. Equal authorship was awarded to A. Leroy and J. Teixidor. Specific contributions from J. Teixidor included design of the study and of the system, discussion of the results, experiments with the probe, and revision of the manuscript to answer the questions of the reviewers.

Among the molecules in the extracellular fluid, neurotransmitters are key indicators of signaling events. The main ones include DA, ACh, Glu, and GABA, of which basal extracellular concentrations of 1.7 ± 0.2 nM, 42 ± 10 nM, 1100 ± 200 nM, and 39 ± 4 nM were respectively reported in the striatum of rats (Slaney et al., 2013). Their concentration and their release can be perturbed by brain pathologies and their measurement *in vivo* is of high interest. Similar to glucose, these are small molecules, but their physiology is different, and their basal concentration is much lower. They can be measured by different methods and this section reports their detection by nanoESI-FTMS, and the development of an electrochemical chip for in-flow measurement of DA in droplets.

6.1 Measurement of neurotransmitters by nanoESI-FTMS

The nanoESI-FTMS method was developed for the quantification of glucose, but its properties are also suitable for the measurement of neurotransmitters. Thus, detection of DA, ACh, Glu and GABA was attempted as a proof of concept.

6.1.1 Materials and methods

Dopamine hydrochloride (H8502-5G, Merck), L-glutamic acid monosodium salt monohydrate (49621-250G, Merck), Acetylcholine chloride (A6625-25G, Merck) and γ -Aminobutyric acid, (A2129-10G, Merck) were dissolved in deionized water. The other materials were identical to the ones described in chapter 5. Moreover, an electrospray ionization (ESI) buffer was made of 0.2% formic acid and ACN, that was used for the identification of the peaks and for the fragmentation of the neurotransmitters.

6.1.2 Detection and fragmentation

A test sample was prepared, that consisted of 1 μ M of each neurotransmitter in 50% deionized water and 50% ESI buffer. Using the same setup as described in section 5.2, all neurotransmitters were detected in SIM mode, as reported in Figure 6.1. Although they had the same concentration, their relative abundance was different and this suggested differences in ionization efficiency. Moreover, another large peak was identified at 137.06 m/z, that was produced by acetonitrile. This illustrated the potential interferences that can perturb the measurement of small molecules by direct infusion and SIM mode, especially in complex matrices such as the one of the *in vivo* samples. For this reason, the measurement of the neurotransmitters was found more reliable after fragmentation in Parallel Reaction Monitoring (PRM) mode. Moreover, the fragmentation by CID helped to ensure that the signal came from the expected molecules. Thus, all neurotransmitters except DA could be fragmented in these conditions, and the location of their main fragment is reported in Table 6.1.

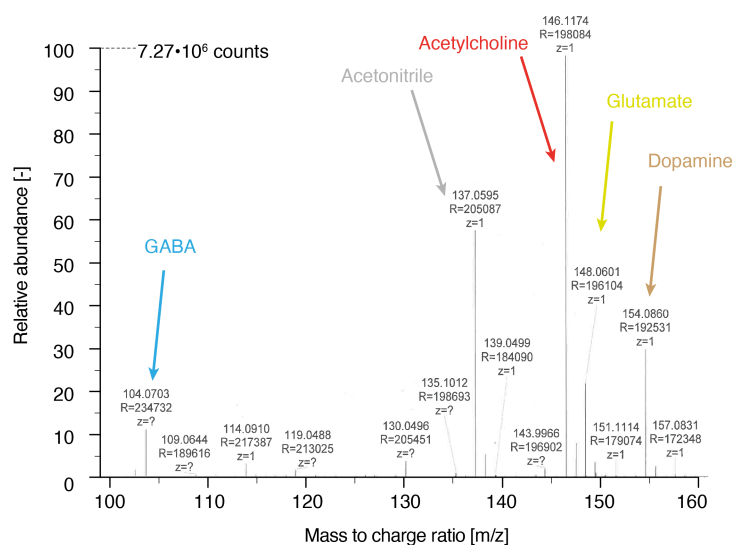


Figure 6.1: Ion chromatogram of GABA, ACh, Glu and DA at 1 μ M in 50% deionized water and 50% ESI buffer.

Table 6.1: Main peaks and fragments of the neurotransmitters

Neurotransmitter	Main peak [m/z]	Main fragment [m/z]	Collision energy eV	Fragmentation window width [m/z]
DA	154.08	-	-	-
Glu	148.06	130.05	30	4
Ach	146.12	87.04	30	4
GABA	104.07	87.04	23	4

6.1.3 Measurement in complex matrices

Next, the neurotransmitters were diluted in pure CNS perfusion fluid to reflect the matrix of raw samples obtained by DoD. In these conditions, the salts induced significant ion-suppression and reduced the signal of all neurotransmitters by 3 to 4 orders of magnitude, even in PRM mode. This suggested that ionization should be enhanced to quantify them reliably, especially to detect their respective baseline concentrations. This would require further investments in method development and the selection of appropriate internal standards. Despite this, ACh and Glu appeared to be the most likely neurotransmitters to be quantifiable because of the high ionization efficiency of ACh and because of the high basal concentration of Glu in the striatum. Therefore, their detection was attempted as a proof of concept, in *in vivo* samples collected by DoD and that were prepared for glucose quantification, as described

in chapter 5. Thus, the raw samples were diluted 10 times with the additive introduced in section 5.2 and were infused at 120 nL/min into the emitter. The signals of glucose, ACh, and Glu were subsequently measured over the spray of a sample, and they are reported in Figure 6.2a.

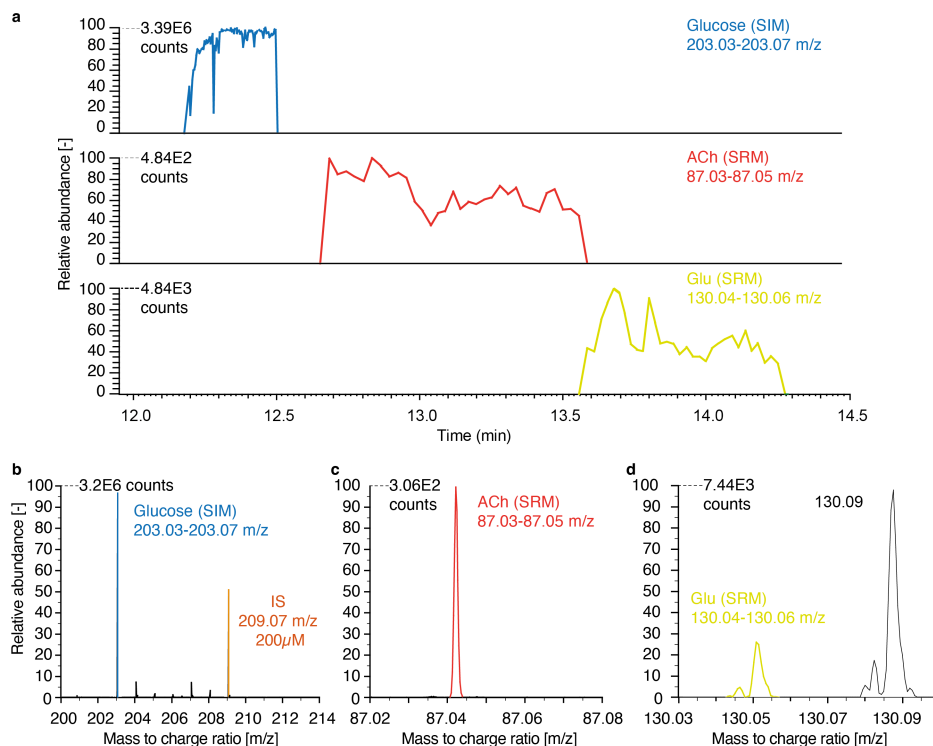


Figure 6.2: Detection of glucose, ACh and Glu in an *in vivo* sample diluted 10 times in the additive for glucose quantification. **a** Signals of glucose at 203.05 m/z in SIM mode, ACh in PRM at 87.04 m/z (30eV CID at 146.12 m/z) and Glu in PRM at 130.05 m/z (30eV CID at 148.06 m/z). **b** Ion chromatogram of glucose and IS in SIM mode. **c** Ion chromatogram of the main fragment of ACh in PRM. **d** Ion chromatogram of the main fragment of Glu in PRM, with an interferent at 130.09 m/z.

As before, glucose and IS were measured in SIM mode at 203.05 m/z and 209.07 m/z respectively and their ion chromatogram is shown in Figure 6.2b. Alternatively, ACh and Glu were fragmented in PRM mode with the parameters in Table 6.1 and their main fragments were extracted at 87.04 m/z and 130.05 m/z respectively. Their respective ion chromatograms are reported in Figure 6.2c and Figure 6.2d. Interestingly, the ion chromatogram of Glu contains not only the fragment at 130.05 m/z, but also an interfering molecule.

Over their corresponding measurement period, the PRM signals of the main fragments of ACh and Glu provided average intensities of 306 and 1970 counts, respectively. In these conditions, the intensities were too low to allow the reliable absolute quantification of these molecules. Nonetheless, an order of magnitude of signal improvement might be reachable by adjusting the dilution factor, and with the appropriate isotopes as internal standards in the additive. This measurement also illustrated the multiplexing ability of the nanoESI-FTMS method and the importance of having internal standards to stabilize the signals for quantitative analysis.

6.1.4 Conclusion

The results in Figure 6.2 showed that ACh and Glu could be measured with the nanoESI-FTMS, without triggering their release with excitatory drugs nor with electrical stimulation. The measurement of DA and GABA would require more developments, but the results suggest that quantitative molecular studies of these molecules could be performed in samples collected by DoD, with only little optimization. In fact, the electrodes and the optical fiber could even allow dual studies of these neurotransmitters, with electrical and optical stimulation, and chemical recording. Moreover, chemical stimulation could also be achieved, by the infusion of drugs through the perfusion channel, or by introduction of droplets of drugs within PFD in the inlet channel.

6.2 Electrochemical measurement of dopamine in droplets

The collection of DA with sampling methods is possible (K. C. Chen, 2005; Ungerstedt & Pycock, 1974) and many analytical methods have been developed to measure this neurotransmitter (Niyonambaza et al., 2019; Syslová et al., 2012; Y. Zhang et al., 2021). This includes not only fluorescent assays (X. Liu et al., 2016; X. Liu et al., 2019) and mass spectrometry (H.-M. Bergman, 2018; Fernandes et al., 2016; Gill et al., 2017), but also aptamer-mediated field effect transistors (Nakatsuka, Abendroth, et al., 2021; Nakatsuka et al., 2018), Raman spectroscopy (Cao et al., 2018) and much more. Although ESI-MS reportedly allowed dopamine measurement (Gill et al., 2017), measurement of DA in droplets by nanoESI-FTMS proved difficult. This was

probably due to the high salinity of the perfusion fluid with respect to the concentration of DA. In fact, many methods are sensitive to the conditions of the matrix and require larger samples. Thus, many methods might not be applicable to the droplets collected by DoD, unless significant method development were achieved.

Despite these considerations, electrochemical probes are frequently used to measure DA directly in the brain, namely with Fast Scan Cyclic Voltammetry (FSCV) (Schwerdt et al., 2018; M. Shin & Venton, 2018; Suzuki et al., 2007; Wassum, 2017; Yoshimi et al., 2011). To that end, carbon is a material of choice (Martinez-Duarte et al., 2010; Robinson et al., 2003; Venton & Cao, 2020) and integration of pyrolyzed carbon electrodes in the probe would be possible (VanDersarl et al., 2015), to allow live readout of DA release in the tissue. However, quantitative electrochemistry is challenging, especially in a complex biological setting, where biofouling can occur (Trouillon & O'Hare, 2010).

Alternatively, an electrochemical system for DA quantification in the droplets would also be of interest as it would allow the study of relative concentration changes in the droplets, between DA and the molecules measured by nanoESI-FTMS. In fact, chronoamperometry in flowing droplets has been studied in the literature (Abadie et al., 2017; Abadie et al., 2021; H. Liu & Crooks, 2013), but the quantitative measurement of the content of droplets has remained challenging with this approach. This is because of the film of oil over the electrodes, that needs to be perforated to allow the contact with the aqueous phase (Delahaye et al., 2021). Nonetheless, one study was found, that reported the measurement of dopamine in droplets (Suea-Ngam et al., 2015). This approach used chronoamperometry with carbon paste electrodes and a limit of detection (LoD) of 20 μM was reported. This LoD was significantly higher than the LoD reported with other approaches that used chronoamperometry and carbon electrodes. Thus, a LoD of 65 nM was obtained with pyrolyzed SU-8 by VanDersarl et al. (2015), a LoD of 11 nM was obtained with carbon fibers by Suzuki et al. (2007), and a LoD of 5 nM was obtained with boron doped diamond by Yoshimi et al. (2011). However, none of these studies was performed in droplets.

Because of the potential of pyrolyzed carbon electrodes that was reported by VanDersarl et al. (2015) and because of the possibility to pattern these electrodes by photolithography, a module with pyrolyzed carbon microelectrodes in a microfluidic channel was developed for chronoamperometric measurement of DA. The module was designed to be connected to the outlet of the probe in a plug-and-play fashion to measure DA in droplets directly after sampling, while leaving them intact for further analysis downstream. This work was accomplished and published in collaboration with A. Leroy (Leroy et al., 2021). The main results are partially reproduced in this section.

6.2.1 Fabrication of the electrochemical module

The chips consisted of a bottom layer with pyrolyzed carbon electrodes on a fused silica substrate, and of a top PDMS layer with microfluidic channels. The fabrication process of the bottom layer is reported in Figure 6.3a-c. Thus, a 4" fused silica wafer was used as the substrate for the electrodes. First, it was rinsed in a piranha bath (30% H_2O_2 in 96% concentrated H_2SO_4) and treated with HMDS (Hexamethyldisilazane) in vapor phase at 125°C in an atmosphere-controlled oven (YES, USA). Then, a 2.6 μm -thick layer of the positive PR (AZ-1512 HS, Microchemicals, USA) was coated on the wafer, exposed with an i-line MaskLess Aligner 150 writing tool (Heidelberg Instruments, Germany), and developed in AZ 726 MIF (Microchemicals, USA) to structure the PR. Consequently, the wafer was baked at 120°C for 30 minutes to enhance the cross-linking of the PR and the adhesion to the substrate. Then, the entire wafer was pyrolyzed in forming gas atmosphere (3% H_2 in N_2). Using ramps of 5°C/min, the wafer was brought to 180°C and kept at this temperature for 30 minutes. Then, it was brought and kept to 900°C for 60 minutes to carbonize the PR before ramping down the temperature to 20°C. Finally, a 30 s O_2 plasma cleaning step (500 W, TePla 300) was achieved to remove the carbon smithereens around the electrodes, that resulted from the pyrolysis, and the wafer was diced into chips presenting carbon microelectrodes.

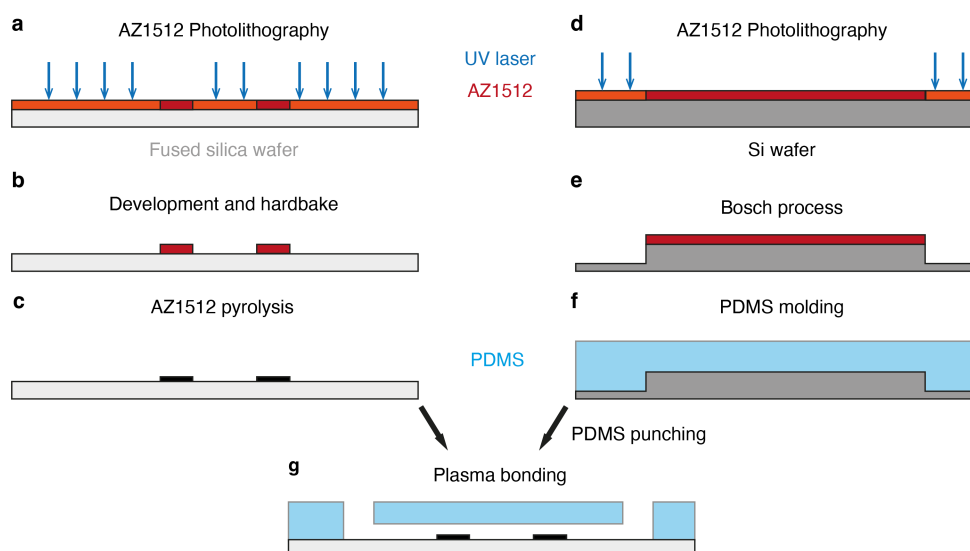


Figure 6.3: Fabrication of the electrochemical module. The fabrication of the bottom layer with pyrolyzed carbon electrodes is shown in the panels a-c, whereas the fabrication of the top PDMS layer is shown in the panels d-f. **a** Photolithography of a 2.6 μm thick layer of AZ1512-HS on a fused silica wafer. **b** Development and hardbake of the PR. **c** Pyrolysis at 180°C and 900°C. **d** Photolithography of a 2.6 μm thick layer of AZ1512-HS on a silicon wafer. **e** Etching of the unprotected silicon over a depth of 16 μm by Bosch process. **f** After cleaning and silanization of the mold, PDMS was cast over the mold and cured. **g** After cutting, punching, and cleaning of the PDMS layer, oxygen plasma bonding of the top and bottom layers was achieved.

The fabrication process of the top PDMS layer is reported in Figure 6.3d-f. A 4" silicon wafer was used as a mold for PDMS. It was cleaned in a piranha bath and a photolithography step with a 2.6 μm thick layer of AZ-1512 HS was performed, similar to the one described on the fused silica wafer. This allowed the transfer of the design of the 100 μm wide microfluidic channels to the PR. Next, anisotropic etching was performed over a depth of 16 μm by Bosch process (AMS200 DRIE, Deep Reactive Ion Etching, Alcatel) and the PR was stripped in O_2 plasma (500 W, TePla 300). Following another O_2 plasma treatment for 7 minutes at 500 W, the wafer was silanized with PFOTS in gas phase overnight. To prepare the PDMS microfluidic chips, silicone elastomer and curing agent (Sylgard 184) were used, at a 10:1 ratio. After weighting, they were mixed, degassed under vacuum, and cast on the silicon wafer. After a second degassing step under vacuum, the PDMS was cured at 80°C for 3 hours in an oven. Then, the PDMS was peeled off the wafer and cut into chips, that were punched to create cylindrical apertures with 330 μm or 500 μm in diameter.

Finally, the chips were assembled by bonding the top and bottom layers together, as illustrated in Figure 6.3g. Both parts were exposed to O_2 plasma at 29 W for 45 s (Harrick Scientific, USA) and bonded together permanently with the carbon electrodes inside the microchannel. Then, the assembly was placed in an oven at 80°C for 10 minutes under a weight, to enhance the adhesion and produce a chip as in Figure 6.4. All the chips contained electrodes in a straight microfluidic channel for electrochemical measurement and some chips also included a microfluidic T-junction to generate droplets before the electrodes.

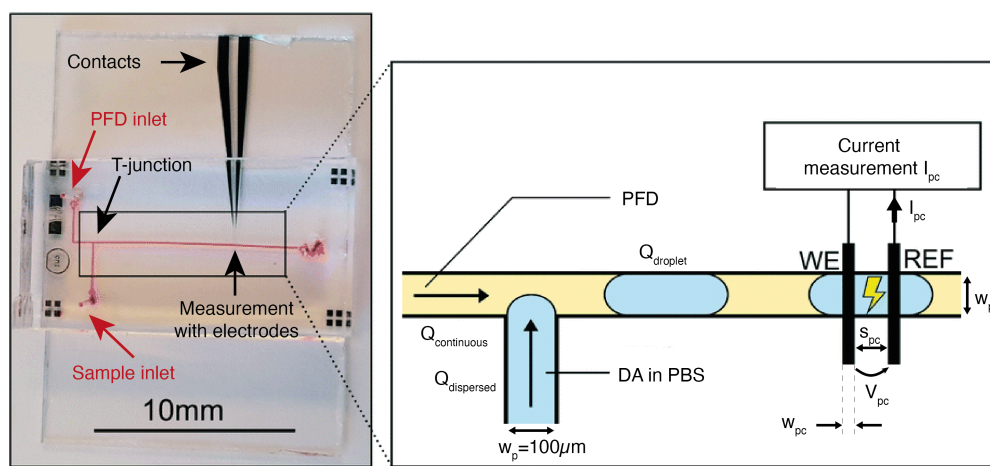


Figure 6.4: Chip with T-junction for droplet generation and electrochemical measurement in droplets. The PFD inlet is used to flow the continuous phase into the chip, whereas the sample inlet allows infusion of the dispersed phase (FcMeOH or DA in PBS). Droplets are formed at the T-junction and the current I_{pc} is measured at the electrodes by potentiostatic chronoamperometry, with a voltage V_{pc} applied to WE with respect to REF. The channels are 100 μm wide (w_p) and 16 μm high (h_p). The electrodes are 5 μm wide (w_{pc}) and separated by 75 μm (s_{pc}).

6.2.2 Materials and methods

Pairs of 5 μm wide pyrolyzed carbon electrodes (w_{pc}) separated by 75 μm (s_{pc}) were used, that presented contact pads for electrical interfacing with spring contact connectors. Both electrodes were identical and accessed the fluid in the channel. Along the direction of the flow in the channel, the first electrode was called the working electrode (WE), whereas the second one was the pseudo-reference electrode (REF) electrode. Chronoamperometric measurements were performed by applying a DC voltage V_{pc} across the electrodes with a function

generator (Agilent 33220A) and by measuring the current I_{pc} with a current preamplifier (SR750, Stanford Research System). This was connected to an acquisition card (PowerLab 4/25, AD Instruments) that transmitted the data to the Chart5 software (AD Instruments). Aqueous sample solutions were prepared by dissolving ferrocenemethanol 97% (FcMeOH, 335061, Merck) and dopamine hydrochloride (DA, H8502, Merck) in Phosphate Buffered Saline (PBS) (P4417, Merck). Droplets of these solutions were produced by segmentation with PFD.

Fluidic setup

Syringe pumps (Harvard Apparatus PHD200) and glass syringes (Hamilton SR4 25 μ L 702N) were used to infuse the sample and PFD phases independently, respectively at $Q_{dispersed}$ and $Q_{continuous}$, to tune the droplet generation and the droplet flow rate $Q_{droplet}$ over the sensor. Rigid PEEK tubing (250 μ m ID, 792 μ m OD, 1301020004-5F, SGE) and fused silica tubing (250 μ m ID, 360 μ m OD, TSP-250350, BGB) were used for fluidic interfacing with Tygon LMT-55 connectors (SC0026T, Ismatec). Optical monitoring of the droplets was done with an inverted microscope (Axiovert 100, Zeiss) and image analysis was carried out with Fiji (ImageJ2).

Electrochemical procedure

Before each measurement, the electrodes were activated electrochemically by applying 0.8 V to WE with respect to REF for 15 to 30 minutes while continuously flowing a solution of 500 nM of DA in the channel, until a stable current was obtained. Finally, the channels were rinsed with PBS. Potentiostatic chronoamperometry was the selected analytical method for current measurement across the electrodes. Thus, a DC voltage V_{pc} of 0.5 V was applied to WE with respect to REF for the measurement of FcMeOH, whereas 0.8 V was applied for the measurement of DA.

6.2.3 Measurement of FcMeOH in droplets

FcMeOH was used in early experiments to confirm the working principles of the chip with respect to the literature. Thus, a typical signal measured by the electrodes during the passage of a droplet with 1 mM of FcMeOH is reported in Figure 6.5a.

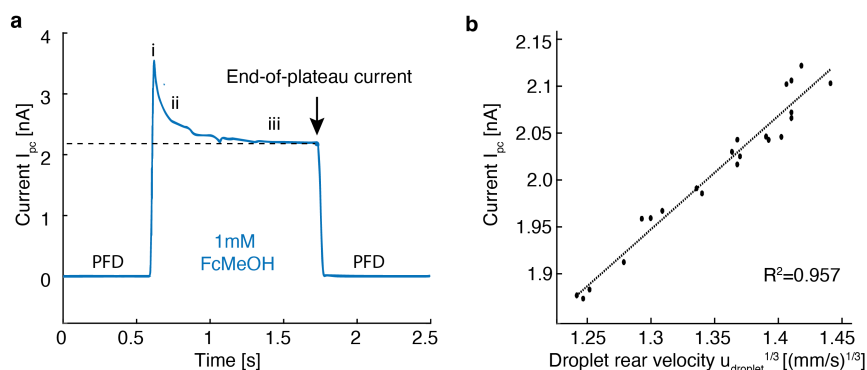


Figure 6.5: Chronoamperometric measurement of FcMeOH in droplets. **a** Typical signal of the current I_{pc} across a droplet of 1 mM FcMeOH, with three distinct phases: a rapid rise of capacitive current (*i*), a decay due to the growth of the depletion layer (*ii*), and a quasi-steady-state plateau until the end of the droplet (*iii*). **b** Verification of the Levich law with FcMeOH in droplets. For a constant concentration, the current I_{pc} varies linearly with $u_{droplet}^{1/3}$.

The shape of the signal I_{pc} agreed with the signals reported in other articles that studied chronoamperometry in droplets (Abadie et al., 2017; H. Liu & Crooks, 2013; Suea-Ngam et al., 2015). Thus, when the electrodes were covered by PFD, the baseline current was close to 0 pA. However, as soon as a droplet reached the electrodes, a peak of capacitive current was observed that reflected the formation of a capacitive double layer in the solution over the electrodes (*i*). This initial peak was followed by a decay of current that reflected the growth of a depletion layer of the analyte in the vicinity of WE (*ii*). If the passage of the droplet over the electrodes lasted long enough, the current reached a quasi-steady-state plateau (*iii*) because of the internal recirculating convection inside the droplet, that stabilized the depletion layer (Abadie et al., 2017). As the droplet left the electrodes, the current decayed back to the baseline level almost immediately.

Amatore et al. (2007) reported that, in such settings, the operation regimes of WE could be categorized into zones. An interesting zone is the one of the Levich regime, where the thickness of the diffusion layer is limited by convection. In this regime, the current of the plateau, I_{Levich} , scales linearly with the cubic root of the average droplet velocity $u_{droplet}^{1/3}$ and with the bulk concentration of the analyte C_{FcMeOH} . This is expressed in Equation 6.1, where F is the Faraday constant, n_q is the number of electrons exchanged per molecule, w_p is the width of the channel, h_p is its height, w_{pc} is the width of the electrode along the flow, and D_{FcMeOH} is the diffusion coefficient of the FcMeOH that is the analyte. A criterion for this regime is given in Equation 6.2, where W_{WE} is the normalized electrode length in the channel and Pe is the Peclet number.

$$I_{Levich} = 0.925 n_q F w_p C_{FcMeOH} (w_{pc} D_{FcMeOH})^{2/3} \left(\frac{4 u_{droplet}}{h_p} \right)^{1/3} \quad (6.1)$$

$$\frac{W_{WE}}{Pe} < 0.04 \quad (6.2)$$

$$Pe = \frac{u_{droplet} h_p}{D_{FcMeOH}} \quad (6.3)$$

$$W_{WE} = \frac{w_{pc}}{h_p} \quad (6.4)$$

With a droplet flow rate $Q_{droplet}$ of 250 nL/min in the channel of cross section $1600 \mu\text{m}^2$, and with a free diffusion coefficient D_{FcMeOH} of $610 \mu\text{m}^2/\text{s}$ for FcMeOH (Liljeroth et al., 2002), the criterion in Equation 6.2 provided $0.0046 < 0.04$ and confirmed the theoretical application of the Levich regime in these conditions. To confirm the Levich regime experimentally, the linear dependence of the current to the cubic root of the droplet velocity $u_{droplet}^{1/3}$ was verified with droplets of 1 mM of FcMeOH. Thus, the current at the end of the plateau was extracted against $u_{droplet}$ that was measured optically from 1.25^3 mm/s to 1.45^3 mm/s , thus giving a flow rate $Q_{droplet}$ from 188 nL/min to 293 nL/min. This is reported in Figure 6.5b and the linear relationship between the current and $u_{droplet}^{1/3}$ confirmed that the Levich regime applied in the conditions of the chip. Therefore, this confirmed that the value of the plateau of current could reflect the concentration in the droplet C_{FcMeOH} .

6.2.4 Measurement of dopamine in droplets

Next, FcMeOH was replaced with DA in the sample solution and the measurement of DA was characterized. The peak oxidation potential of DA was reported at 600 mV applied to a WE against a reference electrode of Ag|AgCl (Robinson et al., 2003). However, since REF in the chip was a pseudo-reference carbon electrode, the voltage corresponding to the oxidation peak needed to be evaluated experimentally. Moreover, the presence of a film of PFD over the electrodes could also impact the required voltage to oxidize DA. The determination of this voltage was achieved by measuring the end-of-plateau current with different voltages V_{pc} , and with droplets of 100 μM of DA separated by PFD that were flowed over the electrodes. This was repeated for droplets of PBS and the results are reported in Figure 6.6a. For each voltage, between 16 and 31 chronoamperometric signals of droplets were recorded to extract the average end-of-plateau current for droplets of DA and PBS, respectively I_{DA} and I_{PBS} .

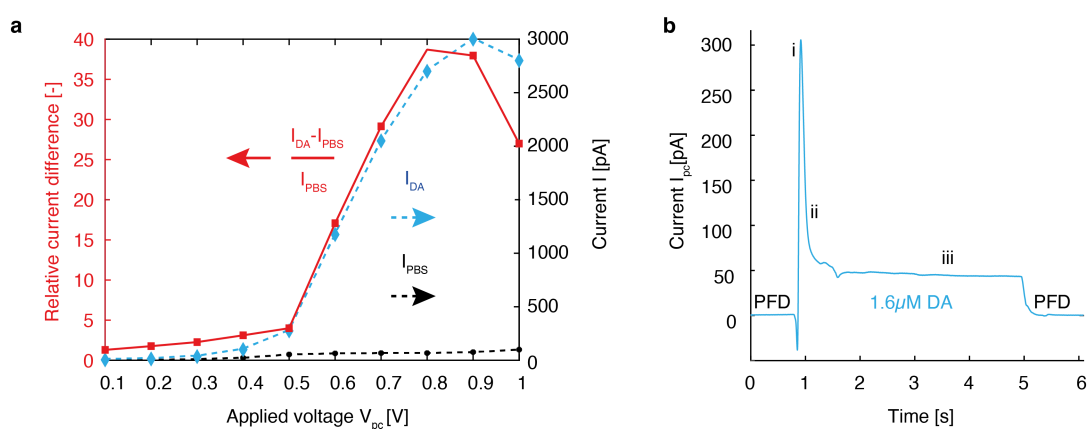


Figure 6.6: Electrochemical measurements of DA in droplets. **a** Evaluation of the voltage V_{pc} to maximize the faradaic current from the oxidation of DA, I_{DA} , with respect to the current from PBS, I_{PBS} . The curves report the average end-of-plateau current for droplets of 100 μM of DA and droplets of PBS at different values of V_{pc} . The relative difference in current is also reported. **b** A typical signal of current I_{pc} obtained from the passage of a 21 nL droplet with 1.6 μM of DA and with V_{pc} of 0.8 V. The three phases *i*, *ii*, and *iii* are the same as for FcMeOH.

The relative difference between I_{DA} and I_{PBS} was maximal with a voltage V_{pc} of 0.8 V. Thus, 0.8 V was selected for the measurement of the concentration of DA. Using this voltage, the typical signal of current across a droplet with 1.6 μM of DA is shown in Figure 6.6b. This signal was similar to the signal recorded for droplets of FcMeOH and illustrated in Figure 6.5a and it presented the same distinct phases *i*, *ii*, and *iii*.

Calibration

Next, the measurement method was evaluated with respect to the concentration of DA in the droplets. Thus, calibration curves were established for the concentration C_{DA} that varied from 0 nM to 20 μM . 2 nL to 4 nL droplets of DA separated by PFD were used in one chip, while continuous sample phases of DA without PFD were used in another one. In the former case, the end-of-plateau current was extracted from I_{DA} , while the average current was extracted after current stabilization in the latter case. In both cases, the flow rate over the electrodes $Q_{droplet}$ was set to 250 nL/min. The respective calibration curves are reported in Figure 6.7a and Figure 6.7b.

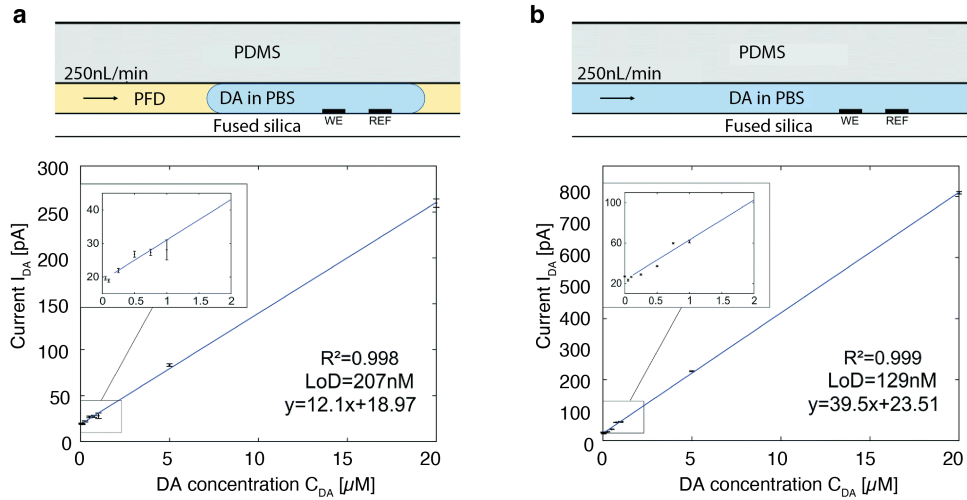


Figure 6.7: Calibration curves of the end-of-plateau current I_{DA} against the concentration of DA, C_{DA} , varied from 0 μM to 20 μM . The flow rate $Q_{droplet}$ was set to 250 nL/min. The insets show the measurement points in the 0 μM to 2 μM range. **a** Calibration in 2 nL to 4 nL droplets separated by PFD. **b** Calibration in continuous sample phase without PFD.

The measurement in droplets is reported in Figure 6.7a and the I_{DA} scaled linearly with respect to C_{DA} , with a sensitivity of 12.1 pA/ μ M. Moreover, a similar linearity with a sensitivity of 12.6 pA/ μ M was obtained with the same procedure in another chip that is not presented here. In fact, the linearity was expected by the law of Levich in Equation 6.1 and a LoD of 207 nM was estimated using the method described by Armbruster and Pry (2008). However, because of the large standard deviation at 1 μ M, the estimation of the limit of quantification was not trivial. It would probably be close to 1-2 μ M, which would be approximately three orders of magnitude higher than the basal concentration of DA in the striatum, thus 1.7 ± 0.2 nM (Slaney et al., 2013).

The properties observed with another chip and in absence of PFD are illustrated in Figure 6.7b. Although similar properties were obtained compared to the case of droplets, the sensitivity of 39.5 pA/ μ M was higher than in droplets. Moreover, a LoD of 129 nM was obtained which was lower than the LoD of 207 nM in droplets. The lower sensitivity obtained in the droplets could be because of the presence of a thin film of PFD that reduced the effective surface of the electrodes, but this was not investigated. Alternatively, it could also be because of the chip-to-chip variability. The reasons for this variability were not investigated neither, but since electrochemical processes occur at the interface of the electrodes, local variations of the thickness of the pyrolyzed electrodes, of the topography, of the activity, of the hybridization ratio sp^2/sp^3 after pyrolysis, and of the cleanliness could affect the performances (Rezaei et al., 2020). This showed that the properties of the electrochemical measurement were not dramatically perturbed by the presence of PFD, which is chemically and biologically inert (Tamimi et al., 2013), although the sensitivity was reduced. This also showed that all chips should be calibrated with droplets before use. This is a disadvantage but would allow the identification of the best chips independently of the probe used for sampling.

Proof of concept with the probe

As a final proof of concept experiment, the probe for DoD was used to directly sample DA from a beaker, in continuous sampling mode but without perfusion of buffer. Instead, PFD was continuously infused into the probe at $Q_{inlet} = 5$ nL/s at the inlet and Q_{outlet} was adjusted between -5 nL/s and -10 nL/s at the outlet. This permitted to sample droplets from the beaker within the PFD from the inlet and to circulate the liquids towards the electrochemical chip for the measurement of I_{DA} in the droplets. The principle of the experiment is illustrated in Figure 6.8a.

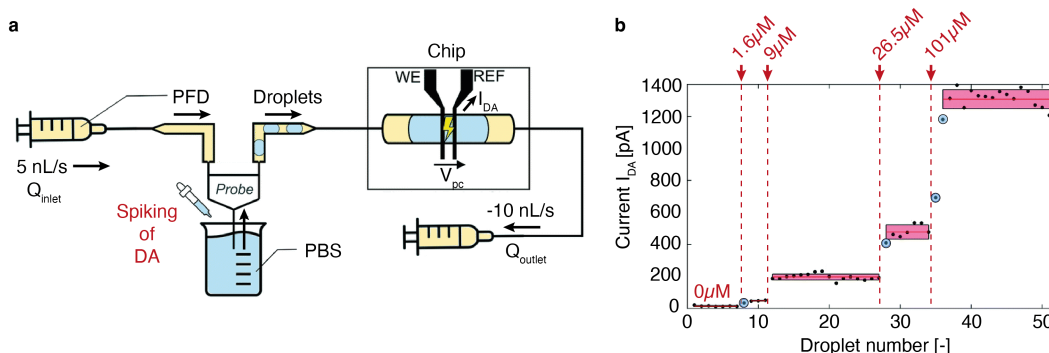


Figure 6.8: Proof of concept experiment where the electrochemical chip was coupled to the outlet of the sampling probe. **a** The tip of the probe was inserted in a beaker of PBS spiked with DA. Droplets were generated by adjusting the flow rates Q_{inlet} and Q_{outlet} with syringe pumps. After generation, the droplets were transferred to the electrochemical chip for online measurement of I_{DA} in the droplets. **b** The current I_{DA} is reported for the analyzed droplets (black dots) over five step changes of the concentration C_{DA} in the beaker, from 0 μM to 101 μM. The blue circled dots represent the current obtained from droplets of different concentrations that merged in the interconnects. The center of the pink rectangles represents the average current for each step of C_{DA} , whereas the top and bottom boundaries represent the standard deviation.

The beaker initially contained PBS only ($C_{DA}=0$ μM) and was spiked with DA punctually, while constant stirring rapidly homogenized the concentration in the beaker. Thus, steps concentration changes of C_{DA} were produced, of 0 μM, 1.6 μM, 9 μM, 26.5 μM and 101 μM of DA. With this approach, droplets of volumes ranging from 30 nL to 70 nL were collected at the outlet and transferred to the chip for chronoamperometric analysis. This is reported in Figure 6.8b.

Because of the interconnects to transfer the droplets to the chip and because of the absence of surfactant, some droplets merged, thus causing different numbers of droplets analyzed for each concentration. When merging occurred between droplets of different concentrations, an intermediate current was measured, as reported by the blue circled dots. This issue could be solved easily with little fluidic adjustments for seamless droplet transfer to the chip.

This simple experiment proved that this module could be coupled to the probe to allow online measurement of C_{DA} in droplets. Although integration of these electrodes in the probe would be feasible, this would increase the complexity of the fabrication process. Instead, this solution provides an analytical system which is independent and that could even be coupled to other probes that sample neurochemicals in droplets (Ngernsutivorakul, Steyer, et al., 2018; Petit-Pierre et al., 2017; van den Brink et al., 2019).

6.2.5 Discussion and conclusion

An electrochemical module for the quantification of DA in nanoliter-sized droplets was investigated, that used pyrolyzed carbon electrodes. The module used a simple fabrication process and could be interfaced to the outlet of the probe presented in chapter 3. The signal of the current measured by potentiostatic chronoamperometry agreed with the literature and the law of Levich applied in these conditions. Thus, the concentration of DA was directly reflected by the plateau of the current measured across a droplet in flow and a linear relationship between the current I_{DA} and the concentration C_{DA} was obtained.

With this approach, a LoD of 207 nM of DA was obtained in droplets, whereas a LoD of 129 nM was obtained in a continuous phase of sample without PFD. These properties compared well to the literature, especially to the only report of the measurement of DA in droplets, that claimed a LoD of 20 μ M with carbon paste electrodes (Suea-Ngam et al., 2015). Although other works that used chronoamperometric measurement of DA reported lower LoDs, they used electrodes with larger surfaces and did not measure DA in droplets (Suzuki et al., 2007; VanDersarl et al., 2015; Yoshimi et al., 2011).

With the current properties of the system, the quantification of the basal concentration of DA in the striatum would not be possible, but the detection of a relative concentration change following a stimulation could be possible (W. Schultz, 2007; Slaney et al., 2013). Nevertheless, a few future improvements might benefit the properties and the reliability of the system for quantitative measurement of DA. Thus, larger electrodes or of a different configuration of the electrochemical cell with 3 electrodes could improve the properties of the system (Abadie et al., 2021; Delahaye et al., 2021). In addition, the use of a microfabricated reference electrode of Ag|AgCl could also be considered (Bard & Faulkner, 2001; Huang et al., 2007), but the investigations with Ag|AgCl and 3 electrodes, that are not reported here, did not provide improvements that would justify a more complicated fabrication process. This was probably because of the stability of pyrolyzed carbon electrodes that was reported in the literature (Rezaei et al., 2020). However, the use of 3 electrodes would be worth considering to apply other electrochemical methods that require a better control of the applied potential and that could prove more sensitive. Thus, FSCV and redox-cycling could also be investigated, especially if multiple scans could be performed during the passage of droplets. Moreover, this could also permit to discriminate the current from DA from the current from molecules, thus provide a higher selectivity of the measurement (Su et al., 2020; Venton & Cao, 2020).

Alternatively, further work could also focus on the functionalization of the electrodes to improve the sensitivity to DA and ensure the selectivity of the signal. This would be critical to analyze DA in *in vivo* samples with a complex matrix, that contains other catecholamines, interfering molecules, and probably biofouling compounds (Trouillon & O'Hare, 2010; Zanetti et al., 2021). Alternatively, other functionalizations could be investigated to measure other compounds with these pyrolyzed carbon electrodes (Nakatsuka, Heard, et al., 2021; Ribet et al., 2017; Su et al., 2020).

6.3 Conclusion

This chapter discussed two approaches to measure neurotransmitters in droplets. The nanoESI-FTMS method, that was developed for the quantification of glucose in the droplets, was applied to the measurement of DA, ACh, Glu and GABA. The ion-suppression caused by the salts in the matrix only allowed the detection of ACh and Glu in the *in vivo* samples that were initially prepared for the quantification of glucose. Although the intensity of the signal was low, the adjustment of the dilution and the use of appropriate internal standards could probably allow quantitative measurements of these neurotransmitters. Alternatively, an electrochemical chip that can be coupled to the outlet of the probe was developed and it allowed the measurement of DA in droplets by chronoamperometry. The current scaled linearly with the concentration and a LoD of 207 nM was obtained in droplets. Nevertheless, some improvements might still be required to allow the reliable quantification of DA in *in vivo* samples.

These two approaches would be particularly interesting to study neurotransmission with the probe since neurological processes involve these neurotransmitters. Moreover, these studies would benefit from the electrical, optical, and chemical stimulation features permitted by the probe. These three features could stimulate the release of these neurotransmitters, while DoD sampling would allow droplet collection to monitor their temporal changes of concentration absolutely, but also relative to each other.

Chapter 7

Conclusion and future perspectives

7.1 Conclusion

This work reported the efforts to improve the study of molecules and processes in the brain with fluidic sampling approaches. Such studies are critical to understand the homeostasis of the brain, but also molecular signaling and neurotransmission, that involve electrical and chemical signals (Kandel et al., 2014). Moreover, they are necessary to understand the development of brain pathologies and develop efficient treatments. A wide range of molecules are involved at different stages of these processes (ions, neurotransmitters, metabolites, proteins, neuropeptides, RNAs, etc.); they have different physiological activity, and their concentrations change over different time scales and amplitudes. Because of this, obtaining a full picture of all the processes is complex (Frank et al., 2019). Push-pull sampling probes probably provide the most versatile invasive solution to probe neurochemicals in the brain since they allow non-selective collection of all sorts of biomarkers (Chefer et al., 2009; Ngernsutivorakul, White, et al., 2018; Perry et al., 2009; Y. Zhang et al., 2021). With fluid sampling probes, sampling is only the first step towards measurement of the concentration of neurochemicals and the second step is sample analysis, that depends on the characteristics and the quality of the samples. Therefore, the objective of this work was improving analyte collection to provide samples that mirror the molecules in the ECF better, for quantitative molecular studies. These concepts were covered in this work and are summarized in the following.

- **Theory of fluid sampling probes**

At first, the theory of sampling by microdialysis was reviewed to understand the limitations of continuous sampling methods that collect molecules by diffusion in a perfusate (Bungay et al., 2006; Morrison et al., 1991). This highlighted the creation and the stabilization of a depletion layer in the surroundings of a probe, that extends in the tissue. The recovery fraction was introduced, that reports the collected concentration in the dialysate with respect to the real concentration in the ECF, that quantitative studies aim to measure. The concepts of transient and steady-state regimes were also introduced. During the transient regime a depletion layer grows in the tissue and the recovery fraction decays over time. Alternatively, the steady-state regime appears once the depletion layer is stable and presents a temporally stable recovery fraction. As a major consequence, reliable measurements can only be performed after reaching the steady-state regime and the concentration in the samples does not represent the real concentration in the ECF. This prevents direct quantification of the content in the ECF. In fact, this applies to all sampling methods that continuously deplete the tissue, when the rate of analyte extraction is higher than the rate of analyte supply in the tissue (Kennedy et al., 2002).

- **The DoD sampling approach**

The Droplet on Demand approach was proposed to solve the limitations of continuous sampling methods. It consists of an intermittent sampling approach, that alternates periods of analyte removal and tissue equilibration without analyte removal. Thus, the method proceeds in sequential steps: creation of a pocket of perfusate in the tissue (*perfusion*); collection of analytes in the tissue by *diffusion*; *sampling* of the pocket loaded with analytes; and *equilibration* of the concentration in the ECF by diffusion, and in absence of analyte extraction. This method was illustrated in simulations and showed that it would allow sample collection with a high recovery fraction by adjustment of the *diffusion* time. Moreover, adjustment of the *equilibration* time for repeated sampling events would prevent the growth of a depletion layer, thus a transient regime. Therefore, the samples would be truly independent. Finally, this would allow punctual sampling of analytes on-demand and within a defined temporal window that corresponds to the duration of the *diffusion* step. The duration of the sampling cycle affects the frequency

at which samples can be collected, thus the temporal resolution. The spatial resolution of the method depends on the interface between the perfusate pocket and the tissue, but also on the travel length of the analytes, that is determined by the diffusion and the physiology of the analytes in the tissue.

- **Fabrication of the probe**

A microfabricated probe was developed to implement the DoD approach for acute sampling in the brain of mice. It was produced with polyimide and SU-8 technologies, and integrated microfluidic channels for fluidic delivery and sampling, a T-junction for droplet generation, and electrical features for brain stimulation and droplet detection in the channels. The fluidic features allowed infusion of perfusate, collection of the perfusate pocket and circulation of oil to produce droplet samples, that could be stored in a glass capillary for offline analysis. All features were embedded in a 320 μm wide and 80 μm high flexible needle that was augmented with an optical fiber for light delivery and for improved insertion in brain tissue. Moreover, the surfaces were rendered hydrophobic to prevent biofouling and a sampling setup was built for DoD sampling and continuous push-pull sampling in droplets.

- **Sampling in an *in vitro* model**

Sampling was demonstrated for the collection of NaCl from a gel of agarose as an *in vitro* model of the brain. This allowed confirmation of the sampling properties predicted by the simulations in chapter 2. Thus, tuning of the *diffusion* time allowed adjustment of the recovery fraction in the samples and no transient regime was observed, even with short *equilibration* times. Opposite, continuous push-pull sampling presented a transient regime. By comparison, the absence of transient regime was deemed characteristic of DoD sampling. This also drew a parallel between the effects of the *diffusion* time with DoD and of the perfusion flow rate with continuous push-pull sampling, to adjust the recovery fraction.

- **Sampling in the striatum of mice**

Sampling was also illustrated *in vivo* during acute experiments in the brain of anaesthetized mice. The droplet-sensing electrodes and the readout of the flow rate sensor ensured correct operation of the system and permitted adjustment of the sampling pressure. Thus, they prevented partial pocket sampling, PFD delivery to the brain and sampling by ultrafiltration. In this real model, *perfusion* volumes of 30 nL and 60 nL allowed collection of droplets of 9.9 ± 4.1 nL and 24.4 ± 15.7 nL and with sampling yields of 85% and 91%, respectively. Nevertheless, a perfusion volume of 60 nL allowed collection of more stable droplets. However, the question of the shape of the perfusate pocket and of the missing volume of perfusate remain open.

- **Quantification of glucose in *in vivo* samples**

An analytical method was developed to quantify the glucose in the samples collected *in vivo*, that was nanoESI-FTMS. Quantification of glucose was possible after dilution of the samples with an additive that contained an internal standard as a reference, acetonitrile to enhance ionization, and deionized water to reduce ion-suppression by the salts in the matrix. This allowed confirmation of the influence of the *diffusion* time over the concentration of glucose collected from the brain and confirmed the absence of transient regime when samples were collected repeatedly every 61 s to 130 s. Evaluation of the exact recovery fraction was complex due to the lack of consensus on the real concentration of glucose in the ECF (Routh, 2002). However, the maximal collected concentration was 3.48 ± 0.17 mM, which was close to the concentration of 3.3 mM that was reported by Ronne-Engström et al. (1995) in similar conditions, but with microdialysis in rats. Nevertheless, this suggested that a high recovery fraction was obtained with DoD. Overall, these results confirmed the goals of DoD as a new sampling approach.

- **Measurement of neurotransmitters**

Measurement of neurotransmitters was also investigated. Thus, the nanoESI-FTMS method allowed measurement of ACh and Glu in *in vivo* samples that were prepared for glucose quantification. In fact, an optimization of the dilution with an appropriate additive could probably even allow their quantification. In addition, an electrochemical module for in-flow chronoamperometric measurement of DA concentration in droplets was developed. This was tested with *in vitro* samples and a LoD of 207 nM was obtained. This could probably allow the detection of tonic DA release after stimulation, but could probably be further improved to allow the measurement of the baseline concentration of DA. Finally, a proof of concept experiment showed that this module could be coupled to the outlet of the probe to measure the concentration of DA in the droplets. In fact, this could also be used by other droplet sampling probes (Ngernsutivorakul, Steyer, et al., 2018; Petit-Pierre et al., 2017; van den Brink et al., 2019).

In summary, the main contribution of this work was the development of a novel sampling paradigm called DoD, that alternates phases of analyte collection in small volumes and phases of tissue equilibration. The *diffusion* time determines the concentration of a sample but also the observation window. Thus, an increase of the diffusion time increases the recovery fraction, but its reduction allows refinement of the capture window for neurochemicals, to monitor precisely defined events. Moreover, because of the absence of transient regime, this allows not only punctual sampling, but also repeated collection of independent samples. The implementation in a multimodal probe for stimulation and chemical recording was demonstrated and the sampling concepts that were proposed in simulations were confirmed *in vitro* and *in vivo*. Nevertheless, the properties of the method depend on the analytes that are considered by a study, and they should be characterized to ensure correct analyte collection at high and stable recovery fraction.

Finally, the properties of the DoD approach are synthesized in Table 7.1. This table also reports the characteristics of other sampling methods published in the literature for comparison purposes. Based on this, it appears that DoD provides droplet samples of similar size to the droplets obtained in the works of Ngernsutivorakul, Steyer, et al. (2018) and van den Brink et al. (2019). Whereas it does not offer a temporal resolution as high as in these works, it ensures a high and steady recovery fraction across the samples; which these works do not. In fact, samples with a high recovery fraction and a limited transient regime can also be collected with other methods called low flow rate methods, that were described by Cabay et al. (2018), Fisher and Shippy (2022), Raman et al. (2020), and G. Wu et al. (2022). On this matter, the flow rates of these methods are comparable to the equivalent flow rates used by DoD. However, their sampling frequency, hence their temporal resolution, is lower than the one possible with DoD. Moreover, thanks to the use of droplets, DoD allows to collect multiple samples without perturbation of the sampling system, unlike in these methods. Because of these properties, DoD might be more suited to track and quantify concentration changes that occur over a few minutes. Despite these differences, it is important to note that the performances of the different methods depend on the analytical methods that determine the size of the required samples, and on the target analytes. Therefore, their properties should be discussed carefully and strict comparisons should be avoided, unless the methods are applied in the same conditions.

In addition, the probe for DoD embeds features to ensure correct fluidic operation during sampling and deliver multiple stimuli to the brain. In fact, these features are also available in the works of Chae et al. (2021) and Petit-Pierre et al. (2017), except optical stimulation. Thus, the probe for DoD is more versatile in terms of multimodal stimulation and recording aspects. On the footprint aspect, the dimensions of the DoD probe are usually comparable or larger than the ones of other microfabricated probes. This is to limit the hydraulic resistance of small channels and to ensure leak-free channels. However, the reduced footprint is still an improvement compared traditional microdialysis probes and the other properties of the DoD probe compare positively to microdialysis systems.

Table 7.1: Synthesis of the sampling methods in the literature

Reference	This work	Petit-Pierre <i>et al.</i> (2017)	Ngernsutvorakul <i>et al.</i> (2018)	Chae <i>et al.</i> (2021)	van den Brink <i>et al.</i> (2019)	Cabay <i>et al.</i> (2018) & Fisher <i>et al.</i> (2022)	Raman <i>et al.</i> (2020)	Wu <i>et al.</i> (2022)	Fray <i>et al.</i> (1997)
Description	Droplet on Demand	Probe for direct droplet sampling	Push-pull Si probe	Push-pull multimodal probe	Push-pull Si-SiO ₂ probe	Pulled fused silica probes	Micro-invasive platform	Wireless PDMS probe	Traditional microdialysis
Materials contacting the tissue	Polyimide, SU-8, Pt	Polyimide, SU-8, Pt	Silicon	Silicon, SiO ₂ , Pt electrodes	Silicon, SiO ₂	Fused silica	Fused silica	PDMS	Polyacrylonitrile
Footprint	80 x 320 μm^2	(80 + 196) x 240 μm^2	84 x 70 μm^2	144 x 40 μm^2	140 x 140 μm^2	30.8 μm OD	80 μm OD	350 μm x 150 μm	300 μm OD
Channel size (number)	70 x 40 μm^2 (3)	80 x 40 μm^2 (2+1)	20 x 20 μm^2 (3)	36 x 12 μm^2 (2)	Openings of 3 x 20 μm^2 (20)	\approx 5 μm diameter (2)	50 μm diameter (1)	10 x 10 μm^2 (4)	N.A. (2)
Spatial resolution	7000 μm^2	>5000 μm^2	1200 μm^2	\approx 3000 μm^2	1200 μm^2	\approx 745 μm^2	\approx 2000 μm^2	100 μm^2	3'769'000 μm^2
Temporal resolution	>30 s, depends on perfusion volume and target recovery fraction	50 s	> 6-15 s	20 min	Few s to min	10 min	30 min	2 min	2.5 min
Flow rate	25.7-36 nL/min	N.A.	100 nL/min	100 nL/min	\approx 50-100 nL/min	25 nL/min	65-95 nL/min	500 nL/min	2 $\mu\text{L}/\text{min}$
Sample size	9.9-24.4 nL (tunable)	17.9 nL	4.5 nL	\geq 2000 nL	\approx 4.5 nL (estimated)	250 nL	<1500 nL	500 nL	5 μL
Droplet segmentation	PFD	PFD	Perfluorodecalin and PFO	Air	Decane	No	No	No	No
Droplet detection	Electrical (at tip), optical (probe body and outlet)	Optical, at probe body and outlet	Optical, at external generator	Optical, at outlet	Optical (probe body and external generator)	-	-	-	-
Multiple samples	Yes, in storage capillary (>100 samples)	Yes, in storage capillary	Yes, in storage capillary	Yes, in storage capillary	Yes, in storage capillary	Yes, cut capillary	Yes, change collection tube	Yes, maximum 4, possible to extract with a syringe	Yes, change collection tube
Recovery fraction	High and tunable, trade-off with temporal resolution: \approx 89% in agarose (NaCl and fluorescein) No, or avoidable by tuning the timing of the sequence.	N.A.	Tunable by flow rate, but affects droplet generation: <20% in agarose at 100nL/min (fluorescein)	93% in steady liquid at 100 nL/min (glutamate)	61% in stirred liquid at 50 nL/min, (glutamate)	\approx 90% in steady liquid at 20 nL/min (arginine, methionine, fluorescein)	67.4% in steady fluid (myelin basic protein, 13-21 kDa)	90% in agarose (dopamine); >80% in agarose (neuropeptide Y)	Limited, 39.2% <i>in vivo</i> (glucose)
Transient regime	N.A.	N.A.	N.A.	N.A.	N.A.	No, or limited.	N.A.	N.A.	Yes.
Chemical stimulation	Possible (perfusion or inlet channel)	Possible (perfusion capillary)	Possible (drug delivery channel)	Possible (inlet channel)	Possible	Possible	Possible	Possible	Yes (zero-net-flux-method)
Optical stimulation	Possible (optical fiber, waveguide integration possible)	-	-	-	-	-	-	-	-
Electrical stimulation	Possible (electrodes)	Possible (electrodes)	-	Possible (electrodes)	-	-	-	-	-
Electrical recording	Possible (electrodes)	Possible (electrodes)	-	Possible (electrodes)	-	-	-	-	-
Advantages	Sampling on demand, narrow sampling window, no transient, high recovery fraction, droplet log, flexible.	Droplet segmentation directly at tip, electrical features, flexible.	High temporal resolution combined with chemical delivery.	Multimodal probe.	Droplet generation close to the tip (probe 1), frit to reduce clogging.	Simple fabrication, limited invasiveness, high recovery fraction, limited transient regime.	Limited invasiveness.	Wireless probe for push-pull sampling, soft needle for long-term experiments.	Simple flow control.
Limitations	Fluidic control, temporal resolution limited by volume of perfusate.	Fluidic control, needs perfusion capillary.	Technological complexity, continuous sampling.	Technological complexity, continuous sampling.	Technological complexity, fluidic control in the probe, continuous sampling.	Limited features, manual operation required to collect multiple samples.	Low temporal resolution, manual operation required to collect > 4 samples.	Manual operation required to collect > 4 samples.	Transient regime, limited recovery fraction, large footprint.

Legend: N.A. = information not available; PFO = 1H,1H,2H,2H-perfluoro-1-octanol.

7.2 Future perspectives

Studying neurochemicals in the brain with sampling probes is a complex matter because of the physical and physiological characteristics of the target analytes. Therefore, future work should be planned with a priority defined by the objectives of the studies to be conducted. Nevertheless, improvements of the DoD sampling approach could already be envisioned.

A first question to answer would be related to the shape and to the fate of the pocket of perfusate in the tissue. In fact, it was assumed as a flat and thin film in simulations, but it probably presents a complex and non-homogeneous shape, that spreads along the needle (Basser, 1992; Morrison et al., 1999). Moreover, the final shape probably depends on the insertion in the tissue and on the debris produced by the probe. This should be investigated to optimize the perfusion volume and the flow rate. In the current implementation, the volume of the collected samples was in average only 33% and 40% of the respectively perfused volumes of 30 nL and 60 nL. Thus, the missing volume might have penetrated the tissue at the tip or flowed back to the surface and penetrated the tissue along the probe. It is also possible that the missing volume has simply gone too far away to be collected back into the probe. Fortunately, this did not induce a reduction of the concentration in the samples, but this should be investigated to ensure a reliable pocket shape at every insertion of the probe. This question contrasts with microdialysis where the flow is confined within the probe by the membrane, and with continuous push-pull probes where perfusate is almost immediately sampled back. Patterning grooves at the tip of the probe and reducing the volume of perfusate to a few nanoliters might help control the shape of the pocket better, but this would still be difficult in a complex setting such as in the brain.

The stimulation features that are included in the probe were not used in the present thesis. However, they would be available for DBS studies with electrostimulation (Mercanzini et al., 2017), for PBM studies with light delivery (Johnstone et al., 2016) and even for studies of the effects of locally delivered drugs (Chae et al., 2021). This could be achieved by loading drugs in the perfusion channel, or in the inlet channel, as drug droplets. Furthermore, studies combining all stimulation approaches could also be performed, for example to study reinforcement of DBS effects by near-infrared light delivery (Salehpour & Hamblin, 2020). In fact, such dual

stimulation/chemical recording studies are a main advantage of the probe that was developed.

A limitation of the current probe comes from its design for acute studies in anesthetized animals. Therefore, the measurements might mirror the ECF of a traumatized tissue instead of the ECF of a normal tissue. Thus, development of more compact probes that could be secured to a microdialysis cannula to perform measurements after a healing period could be investigated. This would also allow measurements in freely moving, but still tethered animals. Integration of waveguides would also reduce its footprint and limit the damages to the tissue. In addition, wireless implants have been recently reported, that integrate optical, fluidic, and electronic features (Burton et al., 2021; Gutruf & Rogers, 2018; Jeong et al., 2015; McCall et al., 2017; Sim et al., 2017). This could be a next improvement, but handling of the fluids and recovery of the samples would require adjustments and integration of highly reliable pumps over extended periods (Raman et al., 2020; G. Wu et al., 2022).

New developments and new studies will also benefit from advanced analytical methods, with improved sensitivity, selectivity, and robustness to interfering molecules (Ha et al., 2021; Payne et al., 2020; Steyer & Kennedy, 2019; Y. Zhang et al., 2022). Improvements in the last 15 years have already allowed splitting the dialysate into nanoliter volumes (Ngernsutivorakul, Steyer, et al., 2018; Petit-Pierre et al., 2017; van den Brink et al., 2019). The next ones could allow the analysis of smaller samples. Thus, reduced perfusion volumes could be used, that would allow faster sampling and a reduction of the quantity of analytes removed from the tissue. This would contribute to increasing the temporal resolution for DoD but also to reducing the extent of the depletion layer for continuous sampling probes. Thus, it would allow to sample analytes at high recovery fraction without any compromise on the temporal resolution. In addition, adaptation of the tubing size and improvement of the anti-fouling treatment might be required to collect smaller samples. Nevertheless, this method might still remain too slow to resolve a single event of neurotransmitter release, especially compared to electrochemical methods. For this reason, in addition to quantifying baseline levels of neurochemicals DoD would probably allow to resolve concentration changes related to volume transmission, hormonal fluctuations, protein accumulation, pharmacokinetics and gene expression changes (Frank et al., 2019; K. N. Schultz & Kennedy, 2008). The same is true for all sampling methods, of which analyte collection in a perfusate is limited by the diffusion of analytes.

In addition, the development of online analytical systems that could be placed at the outlet of the probe, or integrated in it, could also allow real-time monitoring of concentration changes. An example of such a solution could be the electrochemical chip reported in chapter 6. Moreover, they would also allow to adjust the DoD sequence during sampling experiments to obtain a recovery fraction of 1. In fact, another interesting development would consist of an adaptation of the zero-net-flux method for microdialysis (Kho et al., 2017). Thus, a perfusate with a known concentration of an analyte could be used and infused in the brain, and its concentration change in the collected sample could be measured at the outlet. The sign of this change would help evaluate the actual concentration in the ECF. Moreover, it would also be possible to load small volumes of perfusate with different known concentrations, as droplets in the perfusion line, or in the inlet line for this purpose.

Similar to push-pull probes, the current implementation could allow the collection of larger molecules than neurotransmitters, such as extracellular α -synuclein (H.-J. Lee et al., 2014) and extracellular vesicles/exosomes (Saugstad et al., 2017). These biomarkers that are released in the ECF are rich in many molecules; this includes proteins, but also DNA and RNAs (Bache et al., 2015; Mousavi et al., 2022). Opposite to many neurochemicals for which the low concentration is an important challenge in terms of analytics, RNAs (messenger RNAs (mRNAs), miRNAs, etc.) could benefit from amplification technologies such as quantitative real-time PCR (qPCR) and digital PCR to provide valuable information on gene regulation in the brain (Keller et al., 2022). This could shine light on the effects of new therapies such as PBM (Kushibiki et al., 2013) and even contribute to developing the diagnostic of neurodegenerative diseases (Goh et al., 2019; Roser et al., 2018). Nevertheless, extracellular vesicles and extracellular RNAs still remain challenging to collect, to extract, and to quantify (Dave et al., 2019; Kopkova et al., 2018). Their abundance is also the subject of multiple studies in different biological fluids, but it is possible that they are present at very low concentrations in the ECF. Moreover, they probably present low clearance rates and low diffusion coefficients (Bache et al., 2015; Saugstad et al., 2017). Consequently, DoD sampling might prove particularly suitable for collection of these biomarkers, that would probably be depleted from the tissue very rapidly with continuous sampling methods. On this matter, preliminary experiments were designed that target multiple miRNAs from the brain in DoD samples. Their list and the

protocols are reported in Appendix F. They will verify the ability to extract miRNAs with the current implementation and could later be used to study the effects of PBM in animal models of the PD (Oueslati et al., 2015).

Appendix A

Supplementary information related to Chapter 2

The appendix contains the details of the equations and of the development that are complementary to the equations described in chapter 2, and which is based on the developments by Bungay et al. (2006) and Morrison et al. (1991).

A.1 Mass balance in the intracellular space

The mass balance for the intracellular space is reported in Equation A.1, where $C_c[r, z, t]$, D_c and b_c respectively represent the concentration, the effective diffusion coefficient and an equilibrium binding ratio in the cellular compartment.

$$\begin{aligned} (1 - \phi_e) b_c \frac{\partial C_c[r, z, t]}{\partial t} = & (1 - \phi_e) D_c \frac{1}{r} \frac{\partial}{\partial r} r \frac{\partial C_c[r, z, t]}{\partial r} \\ & - \left((1 - \phi_e) k_{ce}^x C_c[r, z, t] - \phi_e k_{ec}^x C_e[r, z, t] \right) \\ & + (1 - \phi_e) (G_c - k_c^r C_c[r, z, t]) \end{aligned} \quad (\text{A.1})$$

A.2 Quasi-steady-state mass balances for the probe

To find the concentration in the dialysate, the concentrations in the membrane and in the dialysate must be expressed.

A.2.1 Mass balance in the membrane

The membrane is treated as a uniform passive medium, with an aqueous fluid phase and a solid matrix phase, with respective volume fractions ϕ_f and ϕ_s . The mass balance for the fluid phase of the membrane is expressed in Equation A.2, $C_f[r, z, t]$ is the concentration of the analyte in the fluid phase, where K_{mf} , in Equation A.3, is a membrane-to-fluid equilibrium partition coefficient and where D_m is a diffusion coefficient for the whole membrane expressed in Equation A.4. The diffusion coefficients D_f and D_s respectively stand for the diffusion in the fluid phase and in the solid phase, whereas K_{sf} is the solid-to-fluid partition coefficient. D_f might be lower than the diffusion coefficient in the dialysate D_0 due to the tortuous path through the porous membrane. If the solid phase was totally impermeable to the analyte and no adsorption occurred, then the concentration in the membrane would correspond to the concentration in its fluidic phase, thus $K_{mf} = 1$ and $D_s = 0$. In practice, ϕ_f , ϕ_s , D_m , D_f , D_s and K_{sf} depend on the characteristics of the membrane and should be measured.

$$K_{mf} \frac{\partial C_f[r, z, t]}{\partial t} = D_m \frac{1}{r} \frac{\partial}{\partial r} r \frac{\partial C_f[r, z, t]}{\partial r} \quad (\text{A.2})$$

$$K_{mf} = \frac{C_m}{C_f} = \phi_f + \phi_s K_{sf} \quad (\text{A.3})$$

$$D_m = \phi_f D_f + \phi_s D_s K_{sf} \quad (\text{A.4})$$

A.2.2 Boundary conditions

Boundary conditions for the continuity of the concentration (Equation A.5) and for the continuity of the flux (Equation A.6) at the tissue-membrane interface ($r = r_o$) can be used to link this equation to the mass balance for the tissue in Equation 2.8.

$$C_f[r_o, z, t] = C_e[r_o, z, t] \quad (\text{A.5})$$

$$D_m \left(\frac{\partial C_f}{\partial r} \right)_{r=r_o} = D_t \left(\frac{\partial C_e}{\partial r} \right)_{r=r_o} \quad (\text{A.6})$$

Boundary conditions for the continuity of the concentration (Equation A.7) and for the continuity of the flux (Equation A.8), can be set again at the dialysate-membrane interface ($r = r_i$), to connect Equation A.2 to the concentration in the dialysate. At this interface, the analyte enters the dialysate, where it diffuses radially and where the flow Q_d runs along the z-axis. As a result of the flow of the dialysate, convection and diffusion contribute to the flux. Therefore, a coefficient is introduced for the permeability of the annulus of dialysate, \mathcal{P}_{d_i} . It represents the overall mass transport in the dialysate and is the inverse to the resistance to mass transport. \mathcal{P}_{d_i} is expressed in Equation A.9, as a function of the diffusion coefficient in the dialysate D_d and the geometry of the probe. The concept is explained in details in Bungay et al. (1990). $\bar{C}_d[z, t]$ is also introduced, as the radial-average of $C_d[r, z, t]$.

$$C_d[r_i, z, t] = C_f[r_i, z, t] \quad (\text{A.7})$$

$$\mathcal{P}_{d_i}(C_d[r_i, z, t] - \bar{C}_d[z, t]) = D_m \left(\frac{\partial C_f}{\partial r} \right)_{r=r_i} \quad (\text{A.8})$$

$$\mathcal{P}_{d_i} = \frac{35D_d}{13(r_i - r_{cann})} \quad (\text{A.9})$$

A quasi-steady-state assumption is then proposed, that sets the time derivatives to zero in the dialysate and in the membrane. This allows integrating Equation A.2 twice, and, by using the boundary conditions in Equation A.5, Equation A.6, Equation A.7 and Equation A.8, it provides a relationship between $\bar{C}_d[z, t]$ and the concentration in the tissue at the membrane $C_e[r_o, z, t]$. This relation is expressed in Equation A.10.

$$\mathcal{P}_{P_o}(C_e[r_o, z, t] - \bar{C}_d[z, t]) = D_t \left(\frac{\partial C_e[r, z, t]}{\partial r} \right)_{r=r_o} \quad (\text{A.10})$$

$$\mathcal{P}_{P_o} = \left(\frac{1}{\mathcal{P}_{d_o}} + \frac{1}{\mathcal{P}_{m_o}} \right)^{-1} \quad (\text{A.11})$$

$$\mathcal{P}_{m_o} = \frac{D_m}{r_o \ln(r_o/r_i)} \quad (\text{A.12})$$

$$\mathcal{P}_{d_o} = \frac{35r_i D_d}{13r_o(r_i - r_{cann})} \quad (\text{A.13})$$

This introduces the permeability of the probe \mathcal{P}_{P_o} , defined in Equation A.11. It represents the inverse of the resistance to the diffusion of the analyte, from the outer surface of the membrane to the dialysate. It is based on the permeabilities of the membrane \mathcal{P}_{m_o} (Equation A.12) and of the dialysate \mathcal{P}_{d_o} (Equation A.13). They depend on the geometry of the probe and on the diffusion coefficients of the analyte in the membrane D_m and in the dialysate D_d .

A.2.3 Mass balance for the dialysate

A last mass balance is required for the annulus of dialysate, which is provided in Equation A.14, where A is the area of the annulus. This is explained by Morrison et al. (1991). The left-hand-side represents the rate of change of concentration in an annular element of thickness dz at an axial location z . In the right-hand-side, the first term represents the net gain of material due to the flow in and out of the element. The second term stands for the material that enters the element due to the flux across the inner wall of the membrane. Using the quasi-steady-state assumption again, the time derivative is zero.

$$\frac{\partial \bar{C}_d[z, t]}{\partial t} = -\frac{Q_d}{A} \frac{\partial \bar{C}_d[z, t]}{\partial z} + \frac{2\pi r_i}{A} D_m \left(\frac{\partial C_f[r, z, t]}{\partial r} \right)_{r=r_i} = 0 \quad (\text{A.14})$$

$$A = \pi(r_i^2 - r_{cann}^2) \quad (\text{A.15})$$

Equation A.14 can be rewritten with the help of the boundary conditions, as Equation A.16.

$$Q_d \frac{\partial \bar{C}_d[z, t]}{\partial z} = 2\pi r_o D_m \left(\frac{\partial C_e[r, z, t]}{\partial r} \right)_{r=r_o} \quad (\text{A.16})$$

Finally, Equation A.16 can be combined with Equation A.10 to provide the overall mass balance of the probe in Equation 2.9.

A.3 Parameters for the simulations

The parameters used for the simulations illustrated in Figure 2.2 are reported in Table A.1.

Table A.1: Parameters for the simulations of microdialysis in Bungay et al. (2006)

Parameter	Symbol	Value	Units	Parameter	Symbol	Value	Units
Inner cannula radius	r_{cann}	120	μm	Diffusion coeff. in dialysate	D_d	750	$\mu m^2/s$
Inner membrane radius	r_i	200	μm	Diffusion coeff. in membrane	D_m	100	$\mu m^2/s$
Outer membrane radius	r_o	250	μm	Diffusion coeff. in tissue	D_t	60	$\mu m^2/s$
Membrane length	l_m	1	cm	Clearance per mass of tissue	CL_m	0.1, 1, 10, 10000	mL/h/g tissue
Dialysate flow rate	Q_d	$1.667 \cdot 10^{-11}$	m^3/s	Equilibrium ratio tissue-ECF	K_{te}	1	-
Tissue density	ρ	1	g/mL				

Appendix B

Supplementary information related to Chapter 3

This appendix reports supplementary information regarding chapter 3. Namely, it reports the hydraulic resistances of the microfluidic system and the runcard for the details of the fabrication process with the equipment and recipes at CMi.

B.1 Hydraulic resistances

The computation of the hydraulic resistances of the microfluidic system is based on the hydraulic-electric analogy (Bruus, 2008; Oh et al., 2012). The resistances of circular and rectangular cross-sections, $R_{h,circ}$ and $R_{h,rect}$, were computed with Equation B.1 and Equation B.2, respectively. They were used to link the applied pressure different ΔP across a fluidic circuit to the flow rate Q with the law of Poiseuille, as in Equation B.3.

$$R_{h,circ} = \frac{128\mu L}{\pi d^4} \quad (B.1)$$

$$R_{h,rect} = \frac{12\mu L}{wh^3(1 - 0.63\frac{h}{w})} \quad (B.2)$$

$$\Delta P = Q \cdot R_h \quad (B.3)$$

In these equations, μ was the viscosity, L the length of the circuit, d the diameter of a circular channel, h the height of a rectangular channel and w the width of a rectangular channel ($h < w$). Table B.1 reports the parameters of the hydraulic circuit described in Figure 3.7. However, it does not contain the elements in the tissue.

Table B.1: Parameters of the hydraulic circuit

Index	System ⁰	Name	Symbol	Phase	Length [cm]	Section	Dimensions W,H or D [μm]	Volume [μL]	Resistance R_h [$\text{kg}/(\text{m}^4 \cdot \text{s})$]
\$1	Perfusion Probe	Perfusion	R_{pp}	Water ¹	2.80	□	40,40	0.045	3.11E+14
\$2	Perfusion Setup	Tubing perf	R_{pt}	Water	40	○	250	19.635	4.17E+12
\$3	TOTAL PERFUSION							19.680	3.15E+14
\$4	Inlet Probe	Inlet	R_{ip}	PFD ²	3.40	□	70,40	0.095	9.12E+14
\$5	Inlet Setup	Tubing inlet	R_{it}	PFD	40	○		19.635	4.17E+12
\$6	TOTAL INLET							19.730	9.39E+14
\$7	Sampling probe	Sampling PFD	$R_{sp,max}$	PFD	0.01	□	70,40	0.00028	2.68E+12
\$8	Outlet probe	Outlet PFD	$R_{op,max}$	PFD	3.40	□	70,40	0.095	9.12E+14
\$9	OUTLET PROBE MAX							0.09528	9.15E+14
\$10	Sampling probe	Sampling water	$R_{sp,min}$	Water	0.01	□	70,40	0.00028	4.19E+11
\$11	Outlet probe	Outlet with 20/75 nL	$R_{op,min}$	Water/PFD	3.40	□	70,40	0.095	7.50E+14
\$12	OUTLET PROBE MIN							0.09528	7.50E+14
\$13	OUTLET STORAGE MAX	Storage capillary	$R_{sc,max}$	PFD	40	○	250	19.635	2.67E+13
\$14	OUTLET STORAGE MIN	Storage capillary 100 x 20 nL	$R_{sc,min}$	Water/PFD	40	○	250	19.635	2.45E+13
\$15	Outlet Tubing	Sensor S	R_{se}	Water	3	○	150	0.530	2.41E+12
\$16	Outlet Tubing	1cm Resistor	R_r	Water	1	○	25	0.005	1.04E+15
\$17	Outlet Tubing	Outlet capillary	R_{oc}	Water	40	○	250	19.635	4.17E+12
\$18	OUTLET TUBING		R_{ot}					20.170	1.05E+15
\$19	TOTAL OUTLET MAX ³	Total outlet	$R_{o,max}$					39.900	1.99E+15
\$20	TOTAL OUTLET MIN ⁴	Total outlet	$R_{o,min}$					39.900	1.82E+15

⁰ The row in capital letters stands for the sum of all the elements in lower case letters above it, and between the horizontal lines of the table.

For example, \$3 is the sum of \$1 and \$2, while \$6 is the sum of \$4 and \$5.

¹ $\mu_{\text{water}} = 10^{-3} \text{Pa} \cdot \text{s} = 10^{-3} \text{kg}/\text{m} \cdot \text{s}^2$, the viscosity of water.

² $\mu_{\text{PFD}} = 6.41 \cdot 10^{-3} \text{Pa} \cdot \text{s} = 6.41 \cdot 10^{-3} \text{kg}/\text{m} \cdot \text{s}^2$, the viscosity of PFD

³ $R_{o,max} = \$9 + R_{sc,max} + R_{ot}$: only PFD inside the probe (95 nL) and the storage capillary.

⁴ $R_{o,min} = \$12 + R_{sc,min} + R_{ot}$: 20 nL aqueous droplet and 75 nL of PFD inside the probe and 100x20 nL droplets within PFD in the storage capillary.

B.2 Details of the fabrication

The details of the fabrication process at CMi is reported in the next 3 pages.

STEP N°	DESCRIPTION	EQUIPMENT @ CMI	PROGRAM/PARAMETERS/RECIPE	COMMENTS/INSTRUCTIONS
0	WAFER PREPARATION			
0.1	Stock out			
0.2	Check			
1	SACRIFICIAL LAYER DEPOSITION			
1.1	Sacrificial layer deposition	Z4/SPIDER600	Recipe W-Al with 41s (100nm WTi10% PM3) and 120s (400nm Al PM4)	
2	POLYIMIDE LAYER PI-i			
2.1	Get PI bottle out of the freezer	Z1/Freezer	Take bottle out 1h in advance	
2.2	Dehydration	Z1/Suss hot plate	125°C for 10min on tissue	
2.3	PI 2611 spin coating Target 3µm	Z1/Sawatec LMS 200	5s from 0 to 500rpm 5s @ 500rpm 39.3s from 500 to 4430rpm 40s @ 4430rpm 1s from 4430 to 5430rpm 1s from 5430 to 4430rpm 5s @ 4430rpm 44.3s from 4430 to 0rpm	
2.4	Softbake	Z1/Suss hot plates	3' @ 75°C on tissue on hotplate 1 3' @ 105°C on tissue on hotplate 2	
2.5	Hard bake	Z2/Heraeus T6060 oven	45min from 20°C to 200°C Turn ON N2 @ 200°C. 1h @ 200°C. 25min to 300°C 2h @ 300°C. Cooldown to 20°C	
2.6	PR coating AZ 10XT 5µm for PI-i	Z6/EVG150	Dehydrate, no EBR, standard C4_D_10XT_5_EC	
2.7	PR exposure	Z1/MA6Gen3	360mJ/cm² i-line, mask PI-i	
2.8	PR development	Z6/EVG150	5um D4_10Xt_5_PUD Rinse + dry in SRD	
2.9	PR reflow	Z1/Süss Hotplate	2' @ 125°C on hotplate	For smooth PI-i edges
2.10	Backside cleaning + rinse + SRD dry	Z1/Plade solvent	Clean backside with an acetone wipe, dip in DIW, SRD dry	DIW = deionized water.
2.11	PI-i etch	Z2/STS	Pyralin recipe, add 30s once etching interferences produce a flat signal instead of sinus (277nm/period for polyimide) => approx 11 periods = 3'24" + 30"	Extra 30s for PR shape transfer to PI-i
2.12	PR strip (preparation)	Z2/Tepla Gigabatch	High power 600W 30s	
2.13	PR strip (wet)	Z2/UFT Resist R1165	5' in Remover 1 70°C - 5' in Remover 2 70°C - QDR - Cascade	
2.14	PR strip (finish)	Z2/Tepla Gigabatch	Low power 200W 30s	
3	TI-PT-TI ELECTRODES			
3.1	Surface preparation	Z2/Tepla gigabatch	Low power 200W for 30s	
3.2	Ti(r) Pt Ti(r) deposition	Z4/SPIDER 600	75nm Ti, 350 nm Pt, 75 nm Ti Recipe Ti-1_Pt-3_Ti-1_Etch_O2 (RF bias)	
3.3	Surface cleaning	Z2/Tepla gigabatch	High power 600W 30s	
3.4	PR coating AZ10XT 2µm for Electrodes	Z1/RiteTrack	C4_N_10XT_2_EC	
3.5	PR exposure	Z1/MA6Gen3	230mJ/cm² i-line, mask Elec, with alignment on 1.	
3.6	PR development	Z1/RiteTrack	D4_N_10XT_2_B Rinse + dry in SRD	
3.7	Backside cleaning + rinse + SRD dry	Z1/Plade solvent	Clean backside with an acetone wipe, dip in DIW, SRD dry	
3.8	Reflow	Z1/Süss Hotplate	2' @ 125°C on hotplate	To prevent fences.
3.9	Ti-Pt-Ti etch	Z11/IBE350	Etch 75nm Ti, 350nm Pt, 75nm Ti IBE_MEDIUM, -10°, approx 10'	
3.10	PR strip (preparation)	Z2/Tepla Gigabatch	High power 600W 30s	To remove PR crust from IBE etching.
3.11	PR strip (wet)	Z2/UFT Resist R1165	5' in Remover 1 70°C - 5' in Remover 2 70°C - QDR - Cascade	
3.12	PR strip (finish)	Z2/Tepla Gigabatch	Low power 200W 30s	
4	POLYIMIDE LAYER PI-ii			
4.1	Get PI bottle out of the freezer	Z1/Freezer	Take bottle out 1h in advance	
4.2	Dehydration	Z1/Suss hot plate	125°C for 20min on tissue	
4.3	Adhesion promoter	Z6/Plade solvents	Spin coat VM652 primer + dry with N2	
4.4	PI 2610 spin coating	Z1/Sawatec LMS 200	5s from 0 to 500rpm 5s @ 500rpm 35s from 500 to 4000rpm 40s @ 4000rpm 1s from 4000 to 5000rpm 1s from 5000 to 4000rpm 5s @ 4000rpm 40s from 4000 to 0rpm	
4.5	Softbake	Z1/Suss hot plates	3' @ 75°C on tissue on hotplate 1 3' @ 105°C on tissue on hotplate 2	
4.6	Hard bake	Z2/Heraeus T6060 oven	45min from 20°C to 200°C Turn ON N2 @ 200°C. 1h @ 200°C. 25min to 300°C 2h @ 300°C. Cooldown to 20°C	
4.7	PR coating AZ 10XT 5µm for PI-ii	Z6/EVG150	Dehydrate, no EBR, standard C4_D_10XT_5_EC	
4.8	PR exposure	Z1/MA6Gen3	360mJ/cm² i-line, mask PI-ii, alignment 3 on 2	
4.9	PR development	Z6/EVG150	5um D4_10Xt_5_PUD Rinse + dry in SRD	
4.10	Backside cleaning + rinse + SRD dry	Z1/Plade solvent	Clean backside with an acetone wipe, dip in DIW, SRD dry	
4.11	PI-ii etch	Z2/STS	Pyralin recipe, add 15s once etching interferences produce a flat signal instead of sinus (277nm/period for polyimide) => approx 1'40"	
4.12	PR strip (preparation)	Z2/Tepla Gigabatch	High power 600W 30s	

5				
SU-8 LAYER SU8-i (CHANNELS)				
5.1	Polyimide dehydration	Z1/Suss hotplate	125°C for 20min on tissue	
5.2	Surface activation	Z2/ Tepla Gigabatch	Low power, 200W, 30s	
5.3	Spin Coating MC3025 - SU8-i	Z1/Sawatec Coater	Recipe for MC3025 Segment 1: Time: 5s / Speed: 500rpm Segment 2: Time: 5s / Speed: 500rpm Segment 3: Time: 13.8s / Speed: 1875 rpm Segment 4: Time: 40s / Speed: 1875 rpm Segment 5: Time: 1s / Speed: 2875 rpm Segment 6: Time: 1s / Speed: 1875 rpm Segment 7: Time: 5s / Speed: 1875 rpm Segment 8: Time: 18.5s / Speed: 0rpm	
5.4	Soft bake. Ramps reduce the stress.	Z1/Sawatec Hotplate	Recipe for MC3025 ramp Segment 1: Time: 10s / Temp.: 30° Base Temp.: 30° / Vacuum : ON / N2: ON / Pin: Down Segment 2: Time: 1800s / Temp.: 95° Vacuum : OFF / N2: ON / Pin: Down Segment 3: Time: 780s / Temp.: 95° End segment: OFF / Vacuum : OFF / N2: ON / Pin: Down Segment 4: Time: 1800s / Temp.: 30° Vacuum : OFF / N2: ON / Pin: Down	
5.5	Exposure	Z1/MA6Gen3	MC3025 325mJ /cm², mask SU8-i, alignment 4 on 3.	
5.6	Post-exposure bake Ramps reduce the stress.	Z1/Sawatec Hotplate	Segment 1: Time: 10s / Temp.: 30° Base Temp.: 30° / Vacuum : OFF / N2: ON / Pin: Down Segment 2: Time: 900s / Temp.: 65° Segment 3: Time: 120s / Temp.: 65° Segment 3: Time: 900s / Temp.: 95° Segment 3: Time: 270s / Temp.: 95° Segment 4: Time: 1800s / Temp.: 30°	
5.7	Development	Z1/WetBench	Use PGMEA only, use spider in baths to put wafer upside down, agitate manually and gently. bath #1: start timer 30s P1: take out and dispense PGMEA on top surface for 10s above bath #1 bath #1: until timer at 60s P2: take out and dispense PGMEA on top + bottom for 10s above bath #1 bath #2 : for 30s, until timer at 90s P3: take out and dispense PGMEA on top surface for 10s above bath #2 bath #2 : for 30s, until timer at for 120s P4: take out and dispense PGMEA on top for 5s + 5s on bottom + 10s top surface again above bath #2, insist on channels and tips. Dry out thoroughly with N2 Check on microscope.	The development is VERY critical! Make it as short as possible. Do no use isopropanol.
6				
SU-8 LAYER SU8-ii (COVER) - DRY FILM ON FLEXIBLE PET FILM				
6.0	Stock out		Take clean Si wafer	
6.1	Surface cleaning	Z2/ Tepla Gigabatch	High power 600W 7 minutes	
6.2	Lamination of PET film. Possible to omit water, but it would limit the spin coating speed later.	Z1/photoPro33	Line a plate with clean room paper. Place double-sided tape on the left and right sides. Tape a 15x15cm piece of Levsurf film (=PET) on the top, primer layer on towards the Si wafer. Hold the sheet up and remove the protective film of the double sided tape. Place the clean wafer at center. Apply 1mL of DI water at the top of the wafer, while holding the sheet up. Insert into laminator, while keeping the film in tension. Parameters : Speed 2/ Temperature 20°C Cut the film around the wafer and leave a handle. Keep the film on the wafer for spin coating.	
6.3	Spin Coating MC3025 - SU8-ii	Z1/Sawatec Coater	Same as SU8-i.	
6.4	Soft bake. Ramps reduce the stress.	Z1Sawatec HP401Z	Same as SU8-i. At the end, you have a SU8-ii dry film on a flexible PET film. Store it on the wafer until use.	
7				
SU-8 LAYER SU8-ii (COVER) - LAMINATION OF SU8-ii TO SU8-i				
7.1	Prepare plate		Prepare lamination plate, cover it with clean room paper and tape a 15x15cm piece of mylar/PET foil at the top. Already turn on the RLM419 and let it reach the target setpoint (Temperature setpoint SP =48°C). Get the SU8 dry film on the PET film ready.	
7.2	SU8-i surface activation	Z2/ Tepla Gigabatch	High power, 600W, 30s	Proceed to lamination directly after plasma.
7.3	Lamination.	Z1/RLM419	Lift the Mylar foil. Carefully peel off the PET film with the su8-ii layer from the wafer and place it on the lamination plate with the su8-ii layer facing up. Place the wafer with su8-i layer upside down on the su8-ii layer (visual alignment). Bring them in contact at once. Put the mylar sheet down to close the assembly. Proceed to lamination on RLM419, twice. Leave the wafer, the cover, and the mylar protection unmoved for the second time. Speed 0.2m/min, 32kg, SP 48°C for MC3025	Monitor the temperature to prevent melting of SU8-ii inside channels.

8	SU-8 LAYER SU8-ii (COVER) - PHOTOLITHOGRAPHY			
8.1	Exposure of SU8-ii though the PET film.	Z1/MA6Gen3	Hard Contact, 200 mJ/cm ² . Mask SU8-ii, alignment on 4.	Set large alignment distance and proceed carefully. This is a challenging alignment because of the long distance between the mask and the alignment marks on the wafer.
8.2	Post-exposure bake	Z1/Accu Plate	Place a Mylar sheet on hotplate, with wafer upside down to crosslink the SU8-ii layer. 40 min from 20°C to 100°C, 4min at 100°C, 20 min to 50°C; remove wafer at 65°C and carefully peel off the levsurf layer. Put back the wafer with the Si side on the protective Mylar sheet on the hotplate and turn heating off. Let cool down to 30°C.	The unexposed SU8-ii is viscous and sticks to levsurf, but not the exposed SU8-ii.
8.3	Development	Z1/WetBench	Same as SU8-i.	
8.4	Plasma cleaning	Z2/ Tepla Gigabatch	Descum recipe for 30s or 60s to clean the residuals on the surface.	
9	INLET OPENING AND FINISHING			
9.1	Inlets opening	Z18/OPTec Excimer Laser	Cut the inlets open with the laser.	
9.3	Optional flood exposure	Z1/Ma6Gen3	Optional, perform a flood exposure at 325 mJ/cm ² on the entire wafer, before a hardbake.	
9.4	Optional hardbake	Z1/Accuplate	Optional, depending on crosslinking and need to reduce thermal stress.	
10	ANODIC RELEASE			
10.1	Anodic release	Lab	Put wafer in 2M NaCl. Use Ti-Pt coated wafer as counter electrode (=GND). Apply 0.7V to wafer with probes. It takes about 6h, depending on the cleanliness of the Al surface and on the design.	
10.2	Cleaning in DIW	Lab	Put the probes in DIW beakers to remove the salts. Use 3 baths, 1h in each.	Optional: Check the conductivity of the solution
10.5	Cleaning in IPA	Lab	Dip the probes in 50% IPA 50% DIW and place between plates covered with clean room paper for drying out.	Be carefull about the use of IPA, can replace with Ethanol. Dilute in water if needed.
11	TI ETCHING			
11.1	HF dip to etch the Ti outer layer on the electrodes	Z14/ Arias Acid	Dip the probes in 1%HF for 2 minutes. Rinse in DIW for 5 min + in another DIW beaker for 10 minutes. Dry out in appropriate equipment with exhaust.	

Appendix C

Characterization of the capacitive sensor

A capacitive sensor was integrated in the probe, to measure the size and the velocity of droplets. It consisted of two electrodes with interdigitated fingers below the outlet channel, that measured the capacitance in the channel. When a droplet of ECF arrives over the sensing area, the change of permittivity between PFD and ECF causes a variation of capacitance measured by the electrodes. Longer droplets cover more electrodes, thus produce a larger variation. This allows measuring the size of the droplet, but also its velocity.

C.1 Definition of the model

The fingers were located between the 3 μm thick PI-i layer (h_{PI-i}) and the PI-ii layer (h_{PI-ii}). Two fingers were considered to design the sensor and a model was used, that was inspired from the work of J. Z. Chen et al. (2004) and Elbuken et al. (2011). The model considered the equivalent capacitance between the fingers, in function of the capacitances encountered by the field lines between these fingers. The equivalent field lines and capacitances are illustrated in Figure C.1, with a side-view of the outlet channel that contains a droplet of ECF surrounded by PFD.

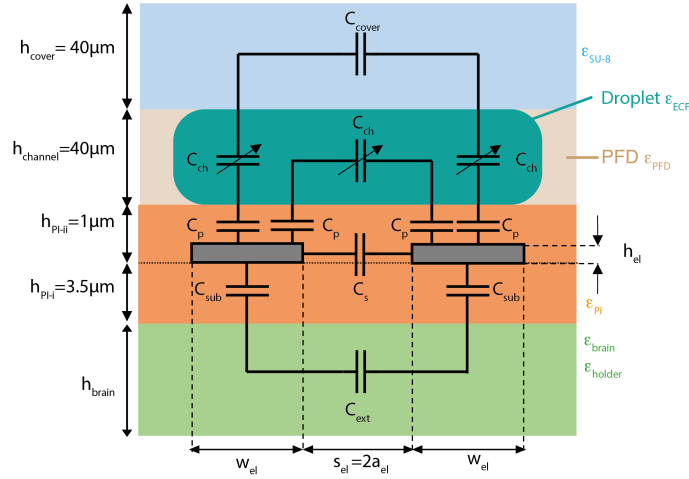


Figure C.1: Side-view of the channel with a droplet of ECF in PFD. The equivalent capacitances encountered by the field lines between the two fingers are shown.

The channel was considered $40 \mu\text{m}$ high (h_{channel}) and $80 \mu\text{m}$ wide (w_{outlet}). (At the time of the design, the channels were $80 \mu\text{m}$ wide instead of $70 \mu\text{m}$ wide in the final versions of the probe.) The fingers were considered 500 nm thick (h_{el}) and with a length $L_{\text{el}} = w_{\text{outlet}}$. Their width w_{el} and their spacing $s_{\text{el}} = 2a_{\text{el}}$ needed to be optimized, where a_{el} is half the spacing. The vacuum permittivity was $\epsilon_0 = 8.854 \cdot 10^{-12} \text{ Fm}^{-1}$, whereas the relative permittivity of polyimide, SU-8, PFD, the brain and of ECF were respectively expressed as $\epsilon_{\text{Pi}} = 2.9$, $\epsilon_{\text{SU-8}} = 3.2$, $\epsilon_{\text{PFD}} = 1.86$, $\epsilon_{\text{brain}} \approx \epsilon_{\text{ECF}} = 80$. The capacitances considered in the model were the capacitances of the passivation layer PI-ii C_p , of the substrate layer PI-i C_{sub} and $C_{\text{sub},2}$, of the PFD-filled channel $C_{\text{Ch,PFD}}$, of the ECF-filled channel $C_{\text{Ch,ECF}}$, of the SU8-ii cover layer C_{cover} and of the external medium C_{ext} . Their analytical expressions are reported from Equation C.1 to Equation C.7.

$$C_p = \frac{\epsilon_0 \epsilon_{\text{Pi}} w_{\text{el}} L_{\text{el}}}{h_{\text{PI-ii}} - h_{\text{el}}} \quad (\text{C.1})$$

$$C_{\text{sub}} = \frac{\epsilon_0 \epsilon_{\text{Pi}} w_{\text{el}} L_{\text{el}}}{h_{\text{PI-i}}} \quad (\text{C.2})$$

$$C_{\text{sub},2} = \frac{\epsilon_0 \epsilon_{\text{Pi}} h_{\text{el}} L_{\text{el}}}{2a} \quad (\text{C.3})$$

$$C_{\text{Ch,PFD}} = \frac{2\epsilon_0 \epsilon_{\text{PFD}} L_{\text{el}}}{\pi} \ln \left[1 + \frac{w_{\text{el}}}{a_{\text{el}}} + \sqrt{\left(1 + \frac{w_{\text{el}}}{a_{\text{el}}}\right)^2 - 1} \right] \quad (\text{C.4})$$

$$C_{\text{Ch,ECF}} = \frac{2\epsilon_0 \epsilon_{\text{ECF}} L_{\text{el}}}{\pi} \ln \left[1 + \frac{w_{\text{el}}}{a_{\text{el}}} + \sqrt{\left(1 + \frac{w_{\text{el}}}{a_{\text{el}}}\right)^2 - 1} \right] \quad (\text{C.5})$$

$$C_{cover} = \frac{2\epsilon_0\epsilon_{SU8}L_{el}}{\pi} \ln \left[1 + \frac{w_{el}}{a_{el}} + \sqrt{\left(1 + \frac{w_{el}}{a_{el}}\right)^2 - 1} \right] \quad (C.6)$$

$$C_{ext} = \frac{2\epsilon_0\epsilon_{ext}L_{el}}{\pi} \ln \left[1 + \frac{w_{el}}{a_{el}} + \sqrt{\left(1 + \frac{w_{el}}{a_{el}}\right)^2 - 1} \right] \quad (C.7)$$

C.2 Optimization of the design

Considering $h_{PI-ii} = 1 \mu\text{m}$, optimization was performed by varying the width w_{el} and the spacing $s_{el} = 2a_{el}$ of the fingers. Optimization consisted of maximizing the difference of capacitance between an ECF-filled channel and a PFD-filled channel $C_{tot,ECF} - C_{tot,PFD}$, that is produced when a droplet of ECF covers the electrodes. The only constrain was set by the required resolution of the sensor and a resolution of 0.1 nL was targeted. Considering a channel cross-section of $w_{outlet} \cdot h_{channel} = 80 \cdot 40 \mu\text{m}^2$, the maximal distance between the center of two fingers was given by $w_{el} + s_{el} \leq 31.25 \mu\text{m}$.

C.3 Analytical computations

The total capacitance sensed by the electrodes, C_{tot} , is expressed by 4 capacitances in parallel C_1 , C_2 , C_3 and C_4 , that are respectively expressed from Equation C.8 to Equation C.12.

$$\frac{1}{C_1} = \frac{1}{C_p} + \frac{1}{C_{Ch}} + \frac{1}{C_{top}} + \frac{1}{C_{Ch}} + \frac{1}{C_p} \quad (C.8)$$

$$\frac{1}{C_2} = \frac{1}{C_p} + \frac{1}{C_{Ch}} + \frac{1}{C_p} \quad C_2 = \frac{C_p C_{Ch}}{C_p + 2C_{Ch}} \quad (C.9)$$

$$C_3 = C_{sub,2} \quad (C.10)$$

$$\frac{1}{C_4} = \frac{1}{C_{sub}} + \frac{1}{C_{brain}} + \frac{1}{C_{sub}} \quad C_4 = \frac{C_{sub} C_{brain}}{C_{sub} + 2C_{brain}} \quad (C.11)$$

$$C_{tot} = C_1 + C_2 + C_3 + C_4 \quad (C.12)$$

C_1 stands for the capacitance of the field lines going through the channel and the cover. Moreover, the penetration depth of the electrodes T_{el} corresponds to the maximum vertical distance of the field line emanating from the outermost edge of the electrode pair. It is expressed in Equation C.13 and allows to determine if C_1 contributes to C_{tot} . Thus, given the condition $w_{el} + s_{el} \leq 31.25 \mu\text{m}$, T_{el} is always inferior to h_{channel} and C_1 does not contribute to the effective capacitance C_{eff} .

$$T_{el} = a_{el} \sqrt{\left(1 + \frac{w_{el}}{a_{el}}\right)^2 - 1} < h_{\text{channel}} = 40 \mu\text{m} \quad (\text{C.13})$$

C_2 stands for the capacitance of the field lines through the channel and is the capacitance of interest. It varies with the content of the channel ($\Delta C_2 \neq 0$). C_3 stands for the capacitance of the field lines through the polyimide between the fingers and it does not vary. Thus, it contributes to the baseline only ($\Delta C_3 = 0$). Finally, C_4 stands for the capacitance of the field lines through the external medium. It is not sensitive to the content of the channel and therefore $\Delta C_4 = 0$. However, since it probes the surroundings, it could be affected by external variations. These variations can be prevented by placing the sensor on the probe body, where it is surrounded by the holder that has a permittivity $\epsilon_{\text{holder}} \approx \epsilon_{\text{SU-8}}$. Therefore, the effective capacitance C_{eff} is given by Equation C.14 and the variation ΔC_{eff} is given by Equation C.15. This equation suggests that it only depends on the capacitance of the polyimide passivation layer C_p and on the capacitance of the channel C_{Ch} .

$$C_{eff} = C_2 + C_3 + C_4 \quad (\text{C.14})$$

$$\Delta C_{eff} = \Delta C_2 = \frac{C_p C_{Ch,ECF}}{C_p + 2C_{Ch,ECF}} - \frac{C_p C_{Ch,PFD}}{C_p + 2C_{Ch,PFD}} \quad (\text{C.15})$$

This equation was implemented on MATLAB to find the values of w_{el} and s_{el} that provided the maximal variation ΔC_{eff} , under the condition $w_{el} + s_{el} \leq 31.25 \mu\text{m}$. Using steps that are realistic in terms of microfabrication, of $1 \mu\text{m}$, the maximal ΔC_{eff} was found for $s_{el} = 10 \mu\text{m}$, $w_{el} = 20 \mu\text{m}$.

C.4 Simulations

Simulations with COMSOL Multiphysics 5.6 were performed to verify these results. The geometry in Figure C.1 was implemented, with 14 pairs of fingers. The system was considered surrounded by air. A "Boundary layers" mesh was used, with "General physics" and "Extra fine" settings in the entire system. The maximal and minimum element sizes were respectively $20\text{ }\mu\text{m}$ and $0.1\text{ }\mu\text{m}$, with a maximum element growth rate of 1.3, a curvature factor of 0.2 and a resolution of narrow regions of 1. The relative tolerance was 0.01.

Figure C.2a represents the ΔC_{eff} normalized by the baseline capacitance when the channel is filled with PFD only C_{PFD} , and where the dashed black line represents the condition $w_{el} + s_{el} = 31.25\text{ }\mu\text{m}$. The red star represents the simulated value for $s_{el} = 10\text{ }\mu\text{m}$, $w_{el} = 20\text{ }\mu\text{m}$ and confirms the results obtained with the analytical model.

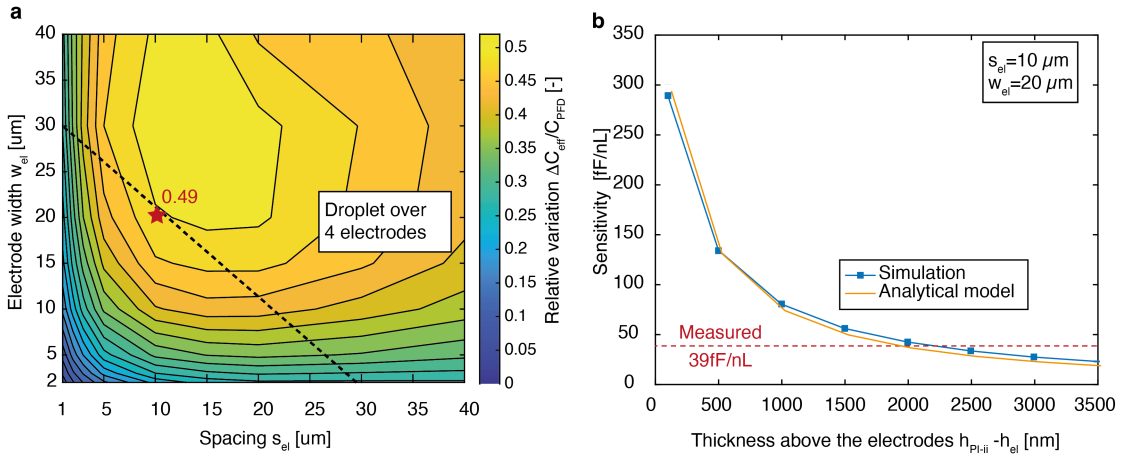


Figure C.2: Simulations and analytical estimations of the capacitive sensor. **a** Map of the relative variation of the capacitance relative to the baseline capacitance with PFD, for different combinations of s_{el} and w_{el} . The simulation considered the capacitance over 4 electrodes. The red star represents the estimation for a sensor with $s_{el} = 10\text{ }\mu\text{m}$ and $w_{el} = 20\text{ }\mu\text{m}$. The dashed black line represents the condition $w_{el} + s_{el} = 31.25\text{ }\mu\text{m}$. **b** Sensitivity of the signal to the droplet size as a function of thickness of the polyimide layer over the electrodes. The experimentally measured sensitivity with a probe is added for comparison.

Moreover, the analytical model and the simulations also investigated the effect of the thickness of the polyimide passivation layer PI-ii h_{PI-ii} on the sensitivity of the signal variation to the droplet size. The sensitivity was defined as the variation ΔC_{eff} with respect to the volume of ECF over the sensor. Thus, h_{PI-ii} was varied between $h_{el} + 100\text{ nm}$ and $h_{el} + 3500\text{ nm}$ and

ΔC_{eff} was evaluated for a fixed droplet volume of 2.6 nL. Both approaches provide similar results that are illustrated in Figure C.2b. The results suggested to use the thinnest possible PI-ii layer to maximize the sensitivity, but in practice, the topography of the wafer (3 μm of PI-i and 0.5 μm of electrodes) made it challenging to obtain a homogeneous PI-ii layer of 1 μm .

C.5 Results

The sensor was implemented in a probe with a 40 μm high and a 80 μm wide channel. It contained 105 fingers of width $w_{el} = 20 \mu\text{m}$ and length $L_{el} = 80 \mu\text{m}$, spaced by $s_{el} = 10 \mu\text{m}$. The total length of the sensor was 3170 μm , thus corresponded to a maximal detectable droplet size of 10.1 nL. A thickness h_{PI-ii} of 1 μm was targeted for the of polyimide passivation layer PI-ii. In practice, it was measured between 1.1 – 1.9 μm at different places over the wafer. The capacitance was measured with a capacitance-to-digital converter board (EVAL-AD7746EB, Analog Devices). This inexpensive component was selected for its compactness in surgery room settings. It used an excitation signal at 32kHz and a sampling frequency of 90Hz. The tip of the probe was placed in a beaker of PBS and droplets were observed in the channels on an inverted microscope Leica DMIL in brightfield. Their size was later measured with Fiji (ImageJ). PFD was flowed from the inlet line to the tip at Q_{inlet} and negative pressure was applied at the outlet to obtain $|Q_{outlet}| > Q_{inlet}$ and generate droplets at the T-junction.

Treating the surfaces of the channels with PFOTS was necessary to obtain clean signals. Without this treatment, the affinity of the surfaces was higher with PBS than with PFD and small PBS droplets remained pinned to the corners of the channels, thus producing chaotic signals, that are reported in Figure C.3a. Opposite, the signal obtained in a PFOTS treated probe allowed clear identification and measurement of the droplets, as shown in Figure C.3b.

The signal of a single droplet is shown in Figure C.3c. When the droplet enters the sensing area, the signal increases linearly over time with sensor coverage, and reaches a plateau when the full droplet is over the sensor. The signal reverses when the droplet leaves. Therefore, the temporal signal of the droplet has a trapezoidal shape, of which the height depends on the droplet size, while the rising and falling slopes reflect the entrance and exit velocities.

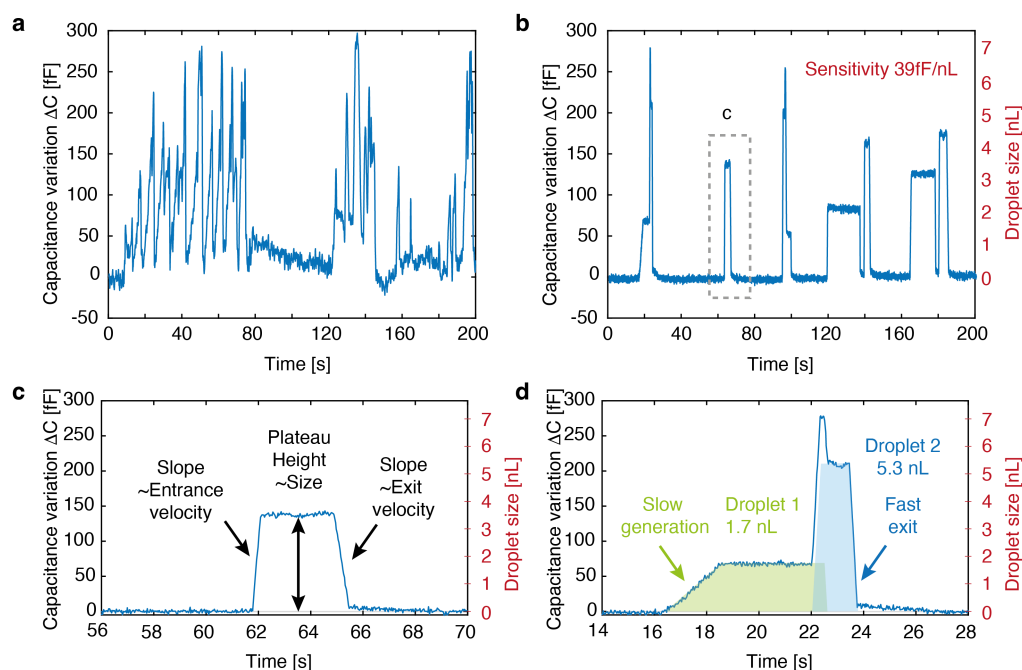


Figure C.3: Droplet characterization by capacitive sensing electrodes. **a** With untreated probes, the signal does not allow accurate detection, nor characterization of the droplets. **b** With PFOTS-treated probes, the signal allows clear identification and characterization of the droplets. The capacitance variation can be translated into the droplet size using the 39 fF/nL sensibility obtained after calibration. **c** A droplet produces a signal with a trapezoidal shape. The slopes allow velocity measurement while the height of the plateau reflects the size of the droplet. **d** Two subsequent droplets on the sensor can be discriminated and measured since they produce superposed trapezoidal signals.

Assuming a 1 μm thick conformal polyimide layer covering the electrodes, sensitivities of 73.9 fF/nL and 79.7 fF/nL were respectively expected by the analytical model and the simulations. The sensitivity of the sensor was evaluated by extracting the height of the plateau of the capacitive signal and by measuring the droplet size optically. A linear calibration was obtained with a linear fit $y = 39x$ ($R^2 = 0.9995$) was obtained between the volume x and the capacitance y , thus providing a sensitivity of 39 fF/nL. This measured sensitivity was respectively 47% and 51% lower than expected by the analytical model and the simulations. This difference could be explained by the difference in effective thickness of PI-ii over the electrodes. As observed in Figure C.2b, the sensitivity is highly sensitive to the thickness. Moreover, the models would rather predict a thickness between 1.80 μm and 2.15 μm for this sensitivity.

Furthermore, the presence of multiple droplets over the electrodes can be detected as a superposition of their respective trapezoidal signal. This is illustrated in Figure C.3d, where the signal reports a first 1.7 nL droplet, followed by another droplet of 5.3 nL. The second droplet entered just before the first one left, which caused a superposition of their respective signals. Moreover, the entrance and exit slopes of the signals reflect the velocity of the droplets. In this example, the entrance flow rate was slow, whereas the exit was very fast. This was probably caused by a change of hydraulic resistance in the outlet line.

C.6 Discussion and conclusion

The predictions of the analytical model and of the simulations agreed and allowed designing a sensor for optimal performances. The sensor was produced and tested, and it provided the expected signals when the surfaces of the channel were treated with PFOTS. The sensitivity to the droplet volume was measured as 39 fF/nL, thus 47% and 51% lower than expected by the analytical model and the simulations. This is probably due to the inhomogeneous thickness of the PI-ii film over the wafer (measured between 1.1 – 1.9 μm). Consequently, this thickness variability required each probe to be calibrated before use.

Despite this, the system was able to detect the droplets and measure them reliably. Moreover, to the knowledge of the author, such a feature has not been reported in brain fluid sampling probes yet. It could allow smarter sampling systems that accurately log each sampled droplet in time and in volume, and that automate droplet generation with optimal operational setpoints. Within this work, the sensor proved useful to characterize droplet generation and optimize the setup when small droplets were generated at high frequency, namely in continuous sampling mode. With DoD sampling, larger droplets were collected and enlarging the sensor would have been required to avoid saturation of the signal. The sensor was also tested in mice brains *ex vivo* and although it allowed droplet detection, biofouling of the surfaces with biological fluid made droplet sizing less reliable. An improved surface functionalization would probably allow all features to operate correctly in these settings, but this was not investigated further.

Appendix D

Supplementary information related to Chapter 4

This chapter reports the characterization of the pair of electrodes in the outlet channel of the probe, that was used to measure the NaCl concentration in droplets which were collected in a gel, in section D.1. It also reports data on the collection of fluorescein in droplets by application of DoD in the gel, in section D.2.

D.1 Characterization of the electrodes for conductivity measurements

The interface of two coplanar electrodes in an electrolyte was modeled with a complex electrical impedance \bar{Z}_0 as in Figure D.1a and expressed in Equation D.1, with a module Z_{el} and a phase ϕ_{el} . The model comprises a resistance to charge transfer R_{Ct} at the surface of the electrode, in parallel with a complex constant phase element \bar{Z}_{CPE} , that stands for the double layer capacitance. These elements are in series with the bulk electrolyte resistance R_{bulk} (Franks et al., 2005). Finally, all these elements are in parallel with the capacitance C_d that stands for the polyimide dielectric insulation that surrounds the electrodes (Mercanzini et al., 2009).

Impedance spectra were acquired to determine the optimal measurement frequency, that would provide a linear relationship between the current and the NaCl concentration in the samples. The parameter of interest was R_{bulk} , which is the inverse of the conductance of the solution, that depends on the NaCl concentration. Thus, Z_{el} and ϕ_{el} were acquired when the electrodes were exposed to aqueous solutions of different NaCl concentration, from 0 mM (0%) to 150 mM (100%). The Bode plots of the spectra are reported in Figure D.1b.

$$\bar{Z}_0 = Z_{el} e^{j\phi_{el}} \quad (\text{D.1})$$

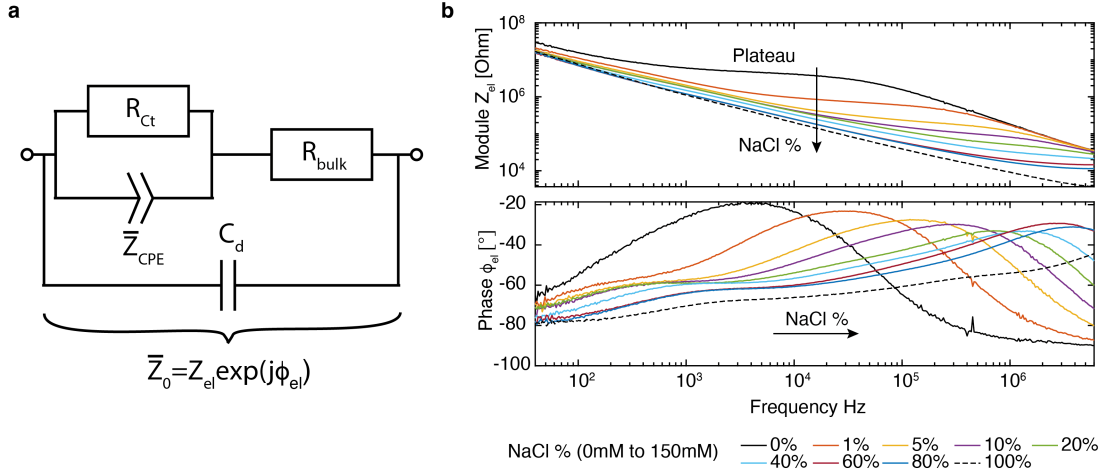


Figure D.1: Complex impedance \bar{Z}_0 of a pair of $20 \mu\text{m} \times 70 \mu\text{m}$ electrodes, separated by $20 \mu\text{m}$, and exposed to an electrolyte. **a** Electrical model of the impedance, with the resistance to charge transfer R_{Ct} of the electrode, the constant phase element \bar{Z}_{CPE} for the double layer capacitance, the resistance of the bulk electrolyte R_{bulk} , and the capacitance of the dielectric insulation C_d . **b** Bode diagram of the impedance spectra for electrolytes with a NaCl concentration ranging from 0 mM (0%) to 150 mM (100%) NaCl.

The plot of Z_{el} presents three domains: a decaying slope at low frequencies, a plateau, and another decaying slope at high frequencies. The slope at low frequency is related to the interface, that is modeled by a constant phase element \bar{Z}_{CPE} expressed in Equation D.2. In this expression, M_0 is a measure of the magnitude of \bar{Z}_{CPE} and $\omega = 2\pi f$ is the pulsation, with the frequency f . The parameter n represents the state of the surface and varies between 0 and 1 (Franks et al., 2005; Mercanzini et al., 2009). When $n = 0$, \bar{Z}_{CPE} is a pure resistance, while it is a pure capacitance when $n = 1$.

$$\overline{Z}_{CPE}(\omega) = \frac{1}{M_0(j\omega)^n} \quad (D.2)$$

\overline{Z}_{CPE} can be modeled by the Gouy-Chapman-Stern model. In this model (Equation D.3), \overline{Z}_{CPE} is assumed as a capacitance C_I that is given by two capacitances in series: a Helmholtz capacitance C_H that stands for the charges held within the outer Helmholtz plane (OHP), and a Gouy-Chapman capacitance C_G that stands for the diffuse charges (Bard & Faulkner, 2001).

$$\frac{1}{C_I} = \frac{1}{C_H} + \frac{1}{C_G} \quad (D.3)$$

$$C_H = \frac{\epsilon_0 \epsilon_r A_{el}}{d_{OHP}} \quad (D.4)$$

$$C_G = \frac{\epsilon_0 \epsilon_r A_{el} \cosh(\frac{z_0 V_0}{2U_{th}})}{L_D} \quad (D.5)$$

$$L_D = \sqrt{\frac{\epsilon_0 \epsilon_r U_r}{2C_0 z_0^2 q_e}} \quad (D.6)$$

Here, d_{OHP} is the thickness of the double-layer, A_{el} is the surface area of an electrode, ϵ_0 is the permittivity of free space, ϵ_r is the relative permittivity of the double layer, z_0 is the charge of the ions, U_{th} is the thermal voltage and V_0 is the voltage applied to the electrode. The Debye length L_D is expressed in Equation D.6, where C_0 is the concentration of the bulk electrolyte and q_e is the elementary charge (Bard & Faulkner, 2001; Franks et al., 2005). These elements suggest that the NaCl concentration impacts \overline{Z}_{CPE} , thus they explain why the plateau of Z_{el} appears at different frequencies in Figure D.1b.

Moreover, Figure D.1b shows that the phase ϕ_{el} had a maximum at the frequency that corresponded to the location of the plateau. Therefore, Mercanzini et al. (2009) proposed the peak resistance frequency (PRF) method to extract an approximation of R_{bulk} . This method consists of extracting the value of Z_{el} when ϕ_{el} is closest to 0° , thus when the system is the most resistive. This method was applied for all concentrations that presented a local maximum within the probed frequencies in Figure D.1b. This provided a linear relationship between the concentration of NaCl and $1/Z_{el}$, that approximates the conductance of the solution given by $1/R_{bulk}$. This is illustrated in Figure D.2.

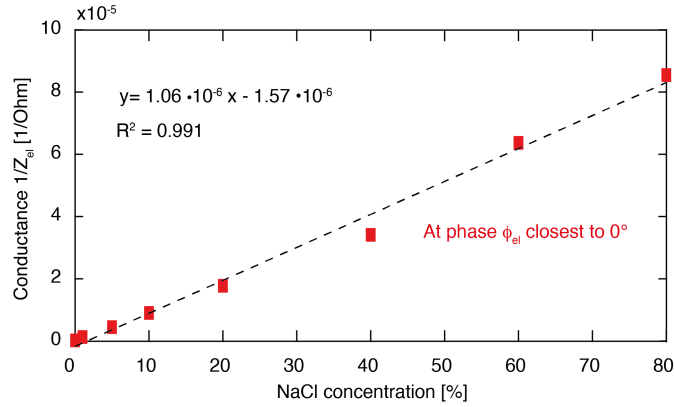


Figure D.2: Plot of $1/Z_{el}$ against the concentration of NaCl. Z_{el} was extracted with the PRF method at different frequencies determined by the frequency where the phase was closest to 0° .

As shown in Figure D.1b, the frequency at which ϕ_{el} was closest to 0° changed with the concentration: from 26 kHz at 1% to 3.8 MHz at 80%. Since scanning the frequencies proved not optimal in short and fast-moving droplets, a frequency that optimized the linearity of $1/Z_{el}$ with respect to the NaCl concentration was found at 1.005 MHz on this equipment and in absence of PFD. Thus, a frequency of 1 MHz was selected for further measurements in droplets, that are presented in subsection 4.1.2.

D.2 Recovery of fluorescein from a gel with DoD sampling

The sampling procedure was identical to the one described for NaCl in subsection 4.1.4. A linear calibration curve was established between the intensity of the fluorescence in the droplets and the concentration of fluorescein to measure the recovery fraction of fluorescein. The effect of $t_{\text{diffusion}}$ over the recovery fraction of fluorescein that was sampled from a gel of agarose by DoD is shown in Figure D.3. The simulated recovery fractions of Na^+ , Cl^- and fluorescein with are added for qualitative comparison. The diffusion coefficient of fluorescein in water at 20°C , $D_{0,fluor}$, was taken as $425 \mu\text{m}^2/\text{s}$.

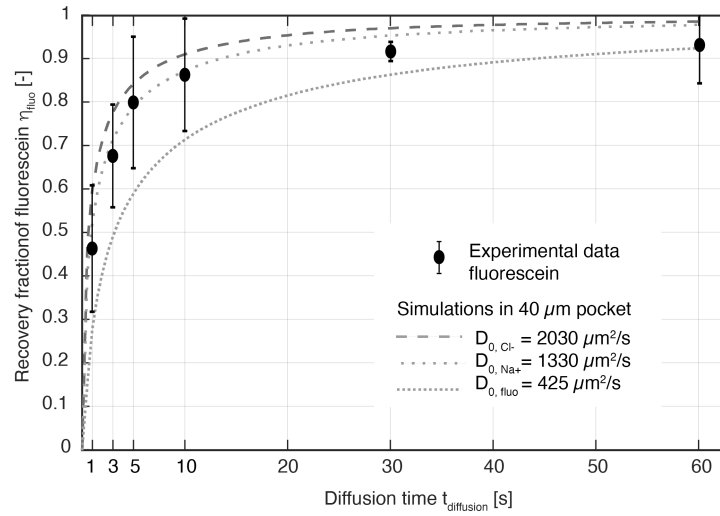


Figure D.3: Effect of $t_{\text{diffusion}}$ measured *in vitro*. Summary of the recovery fraction measured by the fluorescence of fluorescein recovered in the droplets against $t_{\text{diffusion}}$.

D.3 Tissue sections

Tissue sections were obtained, after probe insertion, dispensing of 60 nL of ink at 3 nL/s, waiting for 60 s, aspiration of the liquid, and probe removal. These sections are illustrated in Figure D.4. The insertion tract is barely visible and only a small spot of ink is visible at a location that corresponds to the tip of the probe.

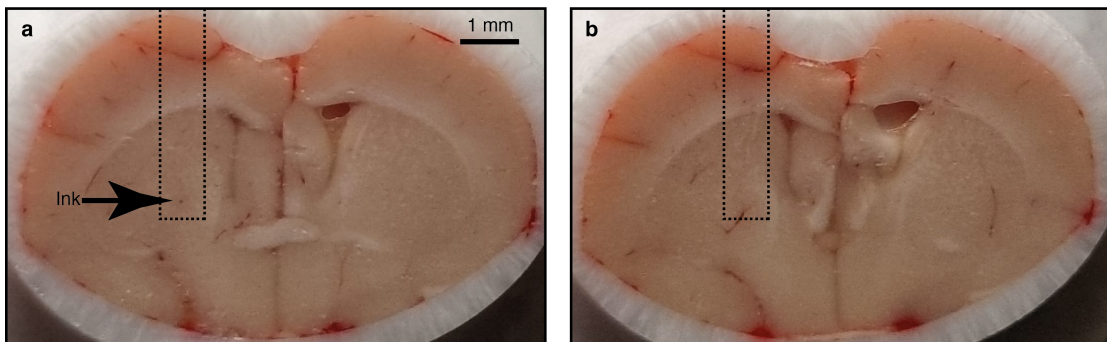


Figure D.4: Pictures of the medial striatum (a) and of the caudal striatum (b), after probe insertion, ink infusion, ink aspiration, and probe removal. The arrow shows the ink spot and the rectangular zone highlights the area where the tract should be visible.

Appendix E

Supplementary information related to Chapter 5

This appendix reports supplementary results regarding the development of the nanoESI-FTMS method for quantification of glucose in the droplets.

E.1 Droplets of glucose

Droplets of 20 nL to 30 nL were prepared in a capillary. They contained glucose in CNS perfusion fluid and were directly infused into the emitter at 120 nL/min. First, the transfer of droplets to the emitter was evaluated and a sharp step change of glucose concentration was obtained, without any mixing. This is shown in Figure E.1a.

This confirmed the good transfer of droplets at the connector. However, perturbations of the signal between the droplets were observed. They were caused by the accumulation of PFD at the emitter in absence of drain around the emitter. Moreover, the signal glucose was sensitive to variations of the quality of the electrospray and varied even for a constant concentration of glucose. This was solved by mixing the glucose solution in perfusion fluid with the additive that contained ACN and 200 μ M of IS, to enhance the ionization and provide a reference for glucose quantification. Their detection is reported in subsection 5.2.2.

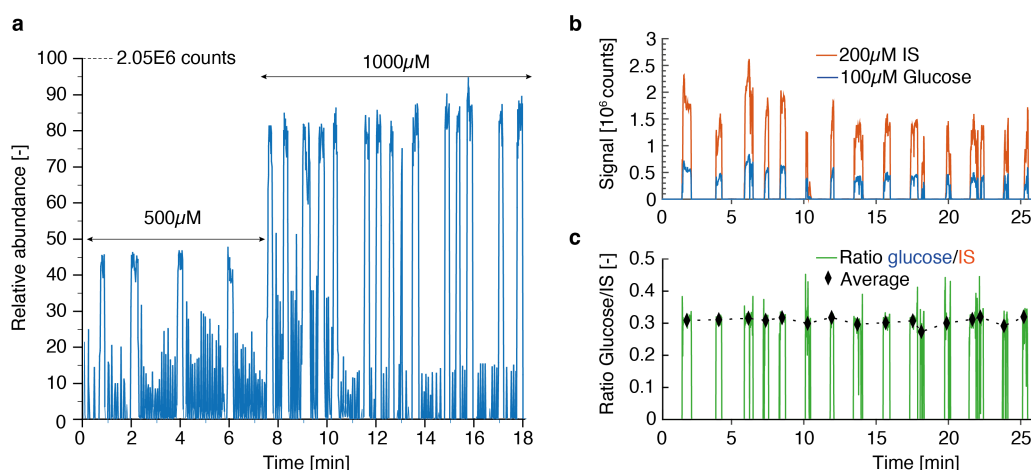


Figure E.1: Analysis of glucose and IS signals in 30 nL *in vitro* droplets. **a** Step concentration change of glucose in droplets, from 500 μM to 1000 μM . **b** Raw signals of 200 μM IS and 100 μM glucose. **c** Ratio of glucose and IS signals, with the median ratio over the duration of each droplet displayed as a black diamond \diamond .

E.2 Droplets of glucose and additive

Cleaner signals were obtained when the glucose solutions were mixed with the additive and when a drain for PFD was used. The IS also improved the reliability of the measurement. This is shown in Figure E.1b. These results show that, when considered alone, a constant glucose concentration of 100 μM produced an average signal of $3.55 \cdot 10^5$ counts, with a standard deviation of $1.58 \cdot 10^5$ counts, thus a variation of 44% around the average. With the help of the IS, the ratio between the signals was computed over the full passage of droplets. This ratio is reported in Figure E.1c and the results show that the stability of the signal was improved. In fact, for a mean ratio of glucose to IS equal to 0.317, the variation was reduced to 7.85%. Nevertheless, the measured ratio was different from the expected one of 0.5, for 100 μM of glucose and 200 μM of IS. Therefore, a calibration curve would be required for accurate quantification.

E.3 Calibration curve for *in vivo* samples

Since the real ratio of glucose and IS signals did not perfectly match the real ratio in the reference samples, a calibration curve for the ratio was performed after analysis of *in vivo* samples. Such a calibration curve is reported in Figure E.2. In this example the IS concentration was set to 200 μM and the dilution factor was 10. Thus, an initial glucose concentration of 2 mM was diluted to 200 μM and was supposed to provide a ratio of 1 with respect to the IS signal (perfect ratio). In practice the ratio was slightly lower, and the calibration curve allowed to extract the initial glucose concentration from the ratio.

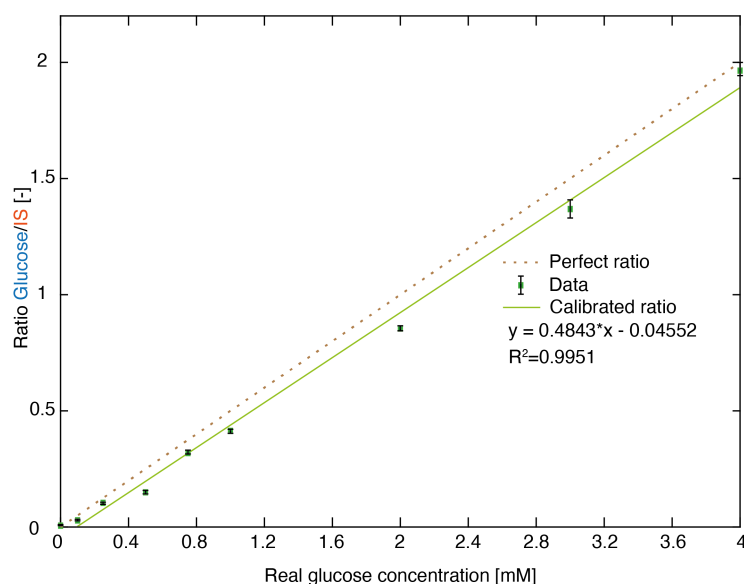


Figure E.2: Calibration curve obtained at the end the measurement of *in vivo* samples, that links the measured ratio to the real glucose concentration that was initially in the reference samples. The IS concentration was 200 μM and the dilution factor was 10. The data represents the median of the ratio, and the error bars represent the quantiles 0.25 and 0.75.

Appendix F

Measurement of miRNAs

Experiments were planned to verify the potential for studying gene regulation in a mouse model of PD, in response to PBM treatment (Oueslati et al., 2015), with the probe presented in this work.

F.1 Selection of the miRNAs

Thus, miRNAs were selected, based on their expression in the mouse brain, according to the miRNATissueAtlas2 (Keller et al., 2022). Among these miRNAs, some were reportedly involved in α -synuclein regulation (L. Zhao & Wang, 2019), whereas others were reportedly involved in PD (Goh et al., 2019). They are reported in Table F.1, with their mean expression in the brain and the total of their mean expression in all tested tissues (bone, bowel (small intestine), brain, heart, limb muscle, lung, marrow adipose tissue) (Keller et al., 2022).

F.2 Objectives and materials of the study

The objective of the preliminary experiments is to evaluate the possibility to measure the 11 first miRNAs reported in Table F.1 in DoD samples by qPCR. Thus, TaqMan Advanced miRNA assays (A25576, Applied Biosystems) for these miRNAs will be used. Because of the low volumes of the samples and of the probably low expression of some selected miRNAs, not all sequences are expected to be detected but mmu-miR-133a-3p and mmu-miR-208a-5p could serve as negative controls. Selection of negative controls would need to be rigorously discussed for further studies. Since the miRNAs are expected to be in extracellular vesicles, a lysis step will be performed with the TaqMan Fast Advanced Cells-to-CT Kit (A35374, Invitrogen). Moreover, an exogenous control sequence from *C. elegans* will be used (5' phosphorylated sequence UAUCACAGCCAGCUUUGAUGUGC (from 5' to 3'), 10620310, Thermo Fisher Scientific), together with the corresponding TaqMan Advanced miRNA assay (A25576, cel-miR-2, 478291_mir, Applied Biosystems).

Table F.1: Selection of miRNAs for experiments in DoD samples

miRNAs	Characteristics			Expression levels (Keller et al., 2022)		
	α -synuclein (L. Zhao & Wang, 2019)	PD (Goh et al., 2019)	Brain specific	Brain [Reads]	All tissues [Reads]	Ratio Brain/Total [-]
mmu-miR-124-3p			X	122383.6943	130874.2054	0.935124641
mmu-miR-29b-3p		X		83886.34162	245863.4199	0.341190819
mmu-miR-9-5p			X	28786.47576	30765.97231	0.935659549
mmu-miR-26a-5p		X		19972.44499	107961.61	0.184995805
mmu-miR-136-5p			X	18548.03337	22728.37374	0.816073934
mmu-miR-181a-5p				17697.25603	40352.26033	0.438569138
mmu-miR-29a-3p		X		12657.53264	50661.53967	0.249845005
mmu-miR-127-3p			X	10245.31729	12617.97269	0.811962233
mmu-miR-138-5p			X	9763.389805	11021.84802	0.885821487
mmu-miR-22-3p				9523.542353	170536.3718	0.05584464
mmu-let-7f-5p	X	X		8900.724985	55388.47675	0.160696331
mmu-miR-133a-3p				233.194969	209237.9096	0.001114497
mmu-miR-208a-5p				0	44.8047402	0

F.3 Experimental protocol

The experimental protocol will be based on the assays provided by Thermo Fisher Scientific for analysis with the thermal cycler QuantStudio 7 (Applied Biosystems) at the Gene Expression Core Facility from EPFL. The protocol will be optimized progressively and will aim quantification of miRNAs in single droplets collected by DoD. However, for preliminary experiments, droplets collected during a complete sampling session *in vivo* will be merged as a single large raw sample of approximately 1 μL . After lysis, the exogenous control sequence will be spiked at a concentration of 1 pM. The rest will be performed according to the proposed TaqMan workflow illustrated in Figure F.1, with the TaqMan Fast Advanced Master Mix (4444557, Applied Biosystems) and the TaqMan Advanced miRNA cDNA Synthesis Kit (A28007, Applied Biosystems).

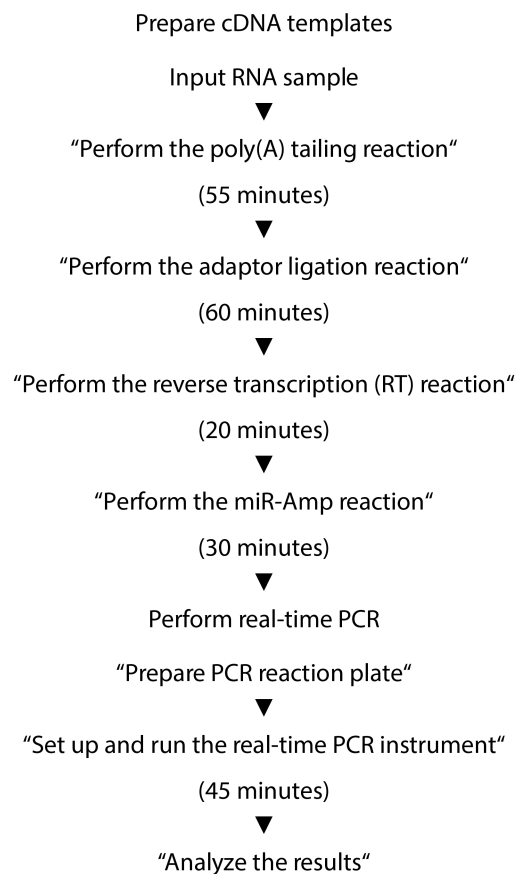


Figure F.1: Initial workflow of the TaqMan Advanced Assay for quantification of the selected miRNAs in the DoD samples.

Bibliography

- Abadie, T., Sella, C., & Thouin, L. (2017). Electrochemical detection of droplet content in microfluidic devices: Evidence of internal recirculating convection within droplets. *Electrochemistry Communications*, 80, 55–59.
- Abadie, T., Souprayan, C., Sella, C., & Thouin, L. (2021). Quantitative Electrolysis of Droplet Contents in Microfluidic Channels. Concept and Experimental Validation. *Electrochimica Acta*, 139017.
- Alberts, B., Bray, D., Hopkin, K., Johnson, A., Lewis, J., Raff, M., Roberts, K., & Walter, P. (2009). *Essential Cell Biology* (Vol. 3). Garland Science.
- Alger, J. (2009). Magnetic Resonance Spectroscopy. *Encyclopedia of neuroscience* (pp. 601–607). Elsevier.
- Al-Hasani, R., Wong, J.-M. T., Mabrouk, O. S., McCall, J. G., Schmitz, G. P., Porter-Stransky, K. A., Aragona, B. J., Kennedy, R. T., & Bruchas, M. R. (2018). In vivo detection of optically-evoked opioid peptide release. *eLife*, 7, 1–13.
- Allaman, I., Gavillet, M., Belanger, M., Laroche, T., Viertl, D., Lashuel, H. A., & Magistretti, P. J. (2010). Amyloid-beta Aggregates Cause Alterations of Astrocytic Metabolic Phenotype: Impact on Neuronal Viability. *Journal of Neuroscience*, 30(9), 3326–3338.
- Amatore, C., Da Mota, N., Sella, C., & Thouin, L. (2007). Theory and Experiments of Transport at Channel Microband Electrodes under Laminar Flows. 1. Steady-State Regimes at a Single Electrode. *Analytical Chemistry*, 79(22), 8502–8510.
- Amirifar, L., Besanjideh, M., Nasiri, R., Shamloo, A., Nasrollahi, F., de Barros, N. R., Davoodi, E., Erdem, A., Mahmoodi, M., Hosseini, V., Montazerian, H., Jahangiry, J., Darabi, M. A.,

- Haghniaz, R., Dokmeci, M. R., Annabi, N., Ahadian, S., & Khademhosseini, A. (2022). Droplet-based microfluidics in biomedical applications. *Biofabrication*, 14(2), 022001.
- Angle, M. R., Cui, B., & Melosh, N. A. (2015). Nanotechnology and neurophysiology. *Current Opinion in Neurobiology*, 32, 132–140.
- Armbruster, D. A., & Pry, T. (2008). Limit of blank, limit of detection and limit of quantitation. *The Clinical biochemist. Reviews*, 29 Suppl 1, 49–52.
- Azevedo, F. A., Carvalho, L. R., Grinberg, L. T., Farfel, J. M., Ferretti, R. E., Leite, R. E., Filho, W. J., Lent, R., & Herculano-Houzel, S. (2009). Equal numbers of neuronal and nonneuronal cells make the human brain an isometrically scaled-up primate brain. *The Journal of Comparative Neurology*, 513(5), 532–541.
- Bache, S., Rasmussen, R., Rossing, M., Hammer, N. R., Juhler, M., Friis-Hansen, L., Nielsen, F. C., & Møller, K. (2015). Detection and quantification of microRNA in cerebral microdialysate. *Journal of Translational Medicine*, 13(149).
- Badv, M., Jaffer, I. H., Weitz, J. I., & Didar, T. F. (2017). An omniphobic lubricant-infused coating produced by chemical vapor deposition of hydrophobic organosilanes attenuates clotting on catheter surfaces. *Scientific Reports*, 7(1), 11639.
- Bai, Y., Weibull, E., Joensson, H. N., & Andersson-Svahn, H. (2014). Interfacing picoliter droplet microfluidics with addressable microliter compartments using fluorescence activated cell sorting. *Sensors and Actuators B: Chemical*, 194, 249–254.
- Barbot, A., Wales, D., Yeatman, E., & Yang, G.-Z. (2021). Microfluidics at Fiber Tip for Nanoliter Delivery and Sampling. *Advanced Science*, 8(10), 2004643.
- Bard, A. J., & Faulkner, L. R. (2001). *Electrochemical methods, fundamentals and applications*. John Wiley & Sons, Inc.
- Baret, J. C. (2012). Surfactants in droplet-based microfluidics. *Lab on a Chip*, 12(3), 422–433.
- Baroud, C. N., Gallaire, F., & Danga, R. (2010). Dynamics of microfluidic droplets. *Lab on a Chip*, 10(16), 2032.
- Basova, E. Y., & Foret, F. (2015). Droplet microfluidics in (bio)chemical analysis. *The Analyst*, 140(1), 22–38.
- Basser, P. J. (1992). Interstitial pressure, volume, and flow during infusion into brain tissue. *Microvascular Research*, 44(2), 143–165.

- Battat, S., Weitz, D. A., & Whitesides, G. M. (2022). Nonlinear Phenomena in Microfluidics. *Chemical Reviews*, 122(7), 6921–6937.
- Béland-Millar, A., Larcher, J., Courtemanche, J., Yuan, T., & Messier, C. (2017). Effects of Systemic Metabolic Fuels on Glucose and Lactate Levels in the Brain Extracellular Compartment of the Mouse. *Frontiers in Neuroscience*, 11, 1–17.
- Bell, S. E., Park, I., Rubakhin, S. S., Bashir, R., Vlasov, Y., & Sweedler, J. V. (2021). Droplet Microfluidics with MALDI-MS Detection: The Effects of Oil Phases in GABA Analysis. *ACS Measurement Science Au*, 1(3), 147–156.
- Benson, P., Kim, J. Y., Riveros, C., Camp, A., & Johnstone, D. M. (2020). Elucidating the time course of the transcriptomic response to photobiomodulation through gene co-expression analysis. *Journal of Photochemistry and Photobiology B: Biology*, 208, 111916.
- Bergman, H.-M. (2018). *Applications of nanospray desorption electrospray ionization mass spectrometry* (Doctoral dissertation). Uppsala University, Sweden.
- Bergman, N., Shevchenko, D., & Bergquist, J. (2014). Approaches for the analysis of low molecular weight compounds with laser desorption/ionization techniques and mass spectrometry. *Analytical and Bioanalytical Chemistry*, 406(1), 49–61.
- Berthier, J., & Silberzan, P. (2010). *Microfluidics for Biotechnology* (Second Edi). Artech House.
- Bertsch, A., Bongarzone, A., Duchamp, M., Renaud, P., & Gallaire, F. (2020). Feedback-free microfluidic oscillator with impinging jets. *Physical Review Fluids*, 5(5), 054202.
- Beulig, R. J., Warias, R., Heiland, J. J., Ohla, S., Zeitler, K., & Belder, D. (2017). A droplet-chip/mass spectrometry approach to study organic synthesis at nanoliter scale. *Lab on a Chip*, 17(11), 1996–2002.
- Blivet, G., Meunier, J., Roman, F. J., & Touchon, J. (2018). Neuroprotective effect of a new photobiomodulation technique against A β 25–35 peptide-induced toxicity in mice: Novel hypothesis for therapeutic approach of Alzheimer's disease suggested. *Alzheimer's & Dementia: Translational Research & Clinical Interventions*, 4(1), 54–63.
- Brown, E., Umino, Y., Loi, T., Solessio, E., & Barlow, R. (2005). Anesthesia can cause sustained hyperglycemia in C57/BL6J mice. *Visual Neuroscience*, 22(5), 615–618.
- Bruus, H. (2008). *Theoretical Microfluids*. Oxford University Press.

- Bucher, E. S., & Wightman, R. M. (2015). Electrochemical Analysis of Neurotransmitters. *Annual Review of Analytical Chemistry*, 8(1), 239–261.
- Bungay, P. M., Dedrick, R. L., Fox, E., & Balis, F. M. (2001). Probe Calibration in Transient Microdialysis In Vivo. *Pharmaceutical Research*, 18(3), 361–366.
- Bungay, P. M., Morrison, P. F., & Dedrick, R. L. (1990). Steady-state theory for quantitative microdialysis of solutes and water in vivo and in vitro. *Life Sciences*, 46(2), 105–119.
- Bungay, P. M., Morrison, P. F., Dedrick, R. L., Chefer, V. I., & Zapata, A. (2006). Chapter 2.2 Principles of quantitative microdialysis. *Handbook of behavioral neuroscience* (pp. 131–167).
- Bungay, P. M., Sumbria, R. K., & Bickel, U. (2011). Unifying the mathematical modeling of in vivo and in vitro microdialysis. *Journal of Pharmaceutical and Biomedical Analysis*, 55(1), 54–63.
- Burton, A., Won, S. M., Sohrabi, A. K., Stuart, T., Amirhossein, A., Kim, J. U., Park, Y., Gabros, A., Rogers, J. A., Vitale, F., Richardson, A. G., & Gutruf, P. (2021). Wireless, battery-free, and fully implantable electrical neurostimulation in freely moving rodents. *Microsystems & Nanoengineering*, 7, 62.
- Cabay, M. R., McRay, A., Featherstone, D. E., & Shippy, S. A. (2018). Development of μ -Low-Flow-Push–Pull Perfusion Probes for Ex Vivo Sampling from Mouse Hippocampal Tissue Slices. *ACS Chemical Neuroscience*, 9(2), 252–259.
- Canales, A., Jia, X., Froriep, U. P., Koppes, R. A., Tringides, C. M., Selvidge, J., Lu, C., Hou, C., Wei, L., Fink, Y., & Anikeeva, P. (2015). Multifunctional fibers for simultaneous optical, electrical and chemical interrogation of neural circuits in vivo. *Nature Biotechnology*, 33(3), 277–284.
- Cao, X., Qin, M., Li, P., Zhou, B., Tang, X., Ge, M., Yang, L., & Liu, J. (2018). Probing catecholamine neurotransmitters based on iron-coordination surface-enhanced resonance Raman spectroscopy label. *Sensors and Actuators, B: Chemical*, 268, 350–358.
- Catana, C. (2019). Development of Dedicated Brain PET Imaging Devices: Recent Advances and Future Perspectives. *Journal of Nuclear Medicine*, 60(8), 1044–1052.
- Cepeda, D. E., Hains, L., Li, D., Bull, J., Lentz, S. I., & Kennedy, R. T. (2015). Experimental evaluation and computational modeling of tissue damage from low-flow push-pull perfusion sampling in vivo. *Journal of Neuroscience Methods*, 242, 97–105.

- Chae, U., Shin, H., Choi, N., Ji, M.-J., Park, H.-M., Lee, S. H., Woo, J., Cho, Y., Kim, K., Yang, S., Nam, M.-H., Yu, H.-Y., & Cho, I.-J. (2021). Bimodal neural probe for highly co-localized chemical and electrical monitoring of neural activities in vivo. *Biosensors and Bioelectronics*, 191, 113473.
- Chae, U., Shin, H., Lee, H. J., Lee, J., Choi, N., Lee, Y. J., Lee, S. H., Woo, J., Cho, Y., Yoon, E.-S., Yu, H.-Y., & Cho, I.-J. (2016). A new MEMS neural probe system integrated with push-pull microfluidic channels and biosensors for real-time monitoring of neurochemicals. *2016 IEEE 29th International Conference on Micro Electro Mechanical Systems (MEMS)*, 329–332.
- Che, Y., Hou, L., Sun, F., Zhang, C., Liu, X., Piao, F., Zhang, D., Li, H., & Wang, Q. (2018). Taurine protects dopaminergic neurons in a mouse Parkinson's disease model through inhibition of microglial M1 polarization. *Cell Death and Disease*, 9(435).
- Chefer, V. I., Thompson, A. C., Zapata, A., & Shippenberg, T. S. (2009). Overview of Brain Microdialysis. *Current Protocols in Neuroscience*, 47(1), 1–7.
- Chen, C.-F. (2017). Dimensional Analysis and Constitutive Equations of Quantitative Microdialysis. *Insights of Biomedical Research*, 1(1), 5–11.
- Chen, C.-F., & Drew, K. L. (2008). Droplet-based microdialysis—Concept, theory, and design considerations. *Journal of Chromatography A*, 1209(1-2), 29–36.
- Chen, J. Z., Darhuber, A. A., Troian, S. M., & Wagner, S. (2004). Capacitive sensing of droplets for microfluidic devices based on thermocapillary actuation. *Lab on a Chip*, 4(5), 473–480.
- Chen, K. C. (2005). Evidence on extracellular dopamine level in rat striatum: implications for the validity of quantitative microdialysis. *Journal of Neurochemistry*, 92(1), 46–58.
- Chen, K. C. (2006). Effects of tissue trauma on the characteristics of microdialysis zero-net-flux method sampling neurotransmitters. *Journal of Theoretical Biology*, 238(4), 863–881.
- Chen, R., Xu, W., Xiong, C., Zhou, X., Xiong, S., Nie, Z., Mao, L., Chen, Y., & Chang, H.-C. (2012). High-Salt-Tolerance Matrix for Facile Detection of Glucose in Rat Brain Microdialysates by MALDI Mass Spectrometry. *Analytical Chemistry*, 84(1), 465–469.
- Chen, Z.-J., Gillies, G. T., Broaddus, W. C., Prabhu, S. S., Fillmore, H., Mitchell, R. M., Corwin, F. D., & Fatouros, P. P. (2004). A realistic brain tissue phantom for intraparenchymal infusion studies. *Journal of Neurosurgery*, 101(2), 314–322.

- Chen, Z., & Lee, J.-B. (2021). Biocompatibility of SU-8 and Its Biomedical Device Applications. *Micromachines*, 12(7), 794.
- Constantin, C. P., Aflori, M., Damian, R. F., & Rusu, R. D. (2019). Biocompatibility of Polyimides: A Mini-Review. *Materials*, 12(19), 3166.
- Convery, N., & Gadegaard, N. (2019). 30 years of microfluidics. *Micro and Nano Engineering*, 2, 76–91.
- Costa, A. R., Pinto-Costa, R., Sousa, S. C., & Sousa, M. M. (2018). The Regulation of Axon Diameter: From Axonal Circumferential Contractility to Activity-Dependent Axon Swelling. *Frontiers in Molecular Neuroscience*, 11(319), 1–7.
- Darlot, F., Moro, C., El Massri, N., Chabrol, C., Johnstone, D. M., Reinhart, F., Agay, D., Torres, N., Bekha, D., Auboiroux, V., Costecalde, T., Peoples, C. L., Anastascio, H. D. T., Shaw, V. E., Stone, J., Mitrofanis, J., & Benabid, A.-L. (2016). Near-infrared light is neuroprotective in a monkey model of Parkinson disease. *Annals of Neurology*, 79(1), 59–75.
- Dave, V. P., Ngo, T. A., Pernestig, A. K., Tilevik, D., Kant, K., Nguyen, T., Wolff, A., & Bang, D. D. (2019). MicroRNA amplification and detection technologies: opportunities and challenges for point of care diagnostics. *Laboratory Investigation*, 99(4), 452–469.
- de Freitas, L. F., & Hamblin, M. R. (2016). Proposed Mechanisms of Photobiomodulation or Low-Level Light Therapy. *IEEE Journal of Selected Topics in Quantum Electronics*, 22(3), 348–364.
- Delahaye, T., Lombardo, T., Sella, C., & Thouin, L. (2021). Electrochemical assessments of droplet contents in microfluidic channels. Application to the titration of heterogeneous droplets. *Analytica Chimica Acta*, 1155, 338344.
- Desbiolles, B. X., de Coulon, E., Maïno, N., Bertsch, A., Rohr, S., & Renaud, P. (2020). Nanovolcano microelectrode arrays: toward long-term on-demand registration of transmembrane action potentials by controlled electroporation. *Microsystems and Nanoengineering*, 6(67).
- Di Giovanni, G., & Di Matteo, V. (2013). *Microdialysis Techniques in Neuroscience*. Humana Press.
- Duchamp, M., Arnaud, M., Bobisse, S., Coukos, G., Harari, A., & Renaud, P. (2021). Microfluidic Device for Droplet Pairing by Combining Droplet Railing and Floating Trap Arrays. *Micromachines*, 12(9), 1076.

- Duchamp, M., Dahoun, T., Vaillier, C., Arnaud, M., Bobisse, S., Coukos, G., Harari, A., & Renaud, P. (2019). Microfluidic device performing on flow study of serial cell-cell interactions of two cell populations. *RSC Advances*, 9(70), 41066–41073.
- Ehlers, W., & Wagner, A. (2015). Multi-component modelling of human brain tissue: a contribution to the constitutive and computational description of deformation, flow and diffusion processes with application to the invasive drug-delivery problem. *Computer Methods in Biomechanics and Biomedical Engineering*, 18(8), 861–879.
- Elbuken, C., Glawdel, T., Chan, D., & Ren, C. L. (2011). Detection of microdroplet size and speed using capacitive sensors. *Sensors and Actuators, A: Physical*, 171(2), 55–62.
- Ellenbroek, B., & Youn, J. (2016). Rodent models in neuroscience research: is it a rat race? *Disease Models & Mechanisms*, 9(10), 1079–1087.
- Elvira, K. S., Gielen, F., Tsai, S. S. H., & Nightingale, A. M. (2022). Materials and methods for droplet microfluidic device fabrication. *Lab on a Chip*, 22(5), 859–875.
- Evans, S. a. G., & Murphy, L. J. (2008). Microelectrochemical Systems. *Handbook of biosensors and biochips*. John Wiley & Sons, Ltd.
- Fallegger, F., Schiavone, G., Pirondini, E., Wagner, F. B., Vachicouras, N., Serex, L., Zegarek, G., May, A., Constanthin, P., Palma, M., Khoshnevis, M., Van Roost, D., Yvert, B., Courtine, G., Schaller, K., Bloch, J., & Lacour, S. P. (2021). MRI-Compatible and Conformal Electrocorticography Grids for Translational Research. *Advanced Science*, 8(9), 1–9.
- Feng, S., Shirani, E., & Inglis, D. W. (2019). Droplets for sampling and transport of chemical signals in biosensing: A review. *Biosensors*, 9(2), 1–14.
- Fernandes, A. M. A. P., Vendramini, P. H., Galaverna, R., Schwab, N. V., Alberici, L. C., Augusti, R., Castilho, R. F., & Eberlin, M. N. (2016). Direct Visualization of Neurotransmitters in Rat Brain Slices by Desorption Electrospray Ionization Mass Spectrometry Imaging (DESI-MS). *Journal of The American Society for Mass Spectrometry*, 27(12), 1944–1951.
- Fisher, P. U., & Shippy, S. A. (2022). Extracellular Fluid Collection and Analysis of *Drosophila melanogaster* Brain Tissue with μ -Low-Flow Push–Pull Perfusion (μ LFPP). *Analytical Chemistry*, 94(9), 3767–3773.
- Frank, J. A., Antonini, M.-J., & Anikeeva, P. (2019). Next-generation interfaces for studying neural function. *Nature Biotechnology*, 37(9), 1013–1023.

- Franks, W., Schenker, I., Schmutz, P., & Hierlemann, A. (2005). Impedance characterization and modeling of electrodes for biomedical applications. *IEEE Transactions on Biomedical Engineering*, 52(7), 1295–1302.
- Franssila, S. (2010). *Introduction to Microfabrication*. John Wiley & Sons, Ltd.
- Fray, A. E., Boutelle, M., & Fillenz, M. (1997). Extracellular glucose turnover in the striatum of unanaesthetized rats measured by quantitative microdialysis. *The Journal of Physiology*, 504(3), 721–726.
- Frost, M. C., & Meyerhoff, M. E. (2015). Real-Time Monitoring of Critical Care Analytes in the Bloodstream with Chemical Sensors: Progress and Challenges. *Annual Review of Analytical Chemistry*, 8(1), 171–192.
- Garstecki, P., Fuerstman, M. J., Stone, H. a., & Whitesides, G. M. (2006). Formation of droplets and bubbles in a microfluidic T-junction—scaling and mechanism of break-up. *Lab on a Chip*, 6(3), 437–446.
- Gawad, S., Schild, L., & Renaud, P. (2001). Micromachined impedance spectroscopy flow cytometer for cell analysis and particle sizing. *Lab on a Chip*, 1(1), 76–82.
- Gill, E. L., Marks, M., Yost, R. A., Vedam-Mai, V., & Garrett, T. J. (2017). Monitoring Dopamine ex Vivo during Electrical Stimulation Using Liquid-Microjunction Surface Sampling. *Analytical Chemistry*, 89(24), 13658–13665.
- Glass, G. E. (2021). Photobiomodulation: A review of the molecular evidence for low level light therapy. *Journal of Plastic, Reconstructive & Aesthetic Surgery*, 74(5), 1050–1060.
- Glawdel, T. (2012). *Droplet production and transport in microfluidic networks with pressure driven flow control* (Doctoral dissertation). University of Waterloo.
- Goh, S. Y., Chao, Y. X., Dheen, S. T., Tan, E.-k., & Tay, S. S.-W. (2019). Role of MicroRNAs in Parkinson's Disease. *International Journal of Molecular Sciences*, 20(22), 5649.
- Gomez-Sjöberg, R., Leyrat, A. A., Pirone, D. M., Chen, C. S., & Quake, S. R. (2007). Versatile, Fully Automated, Microfluidic Cell Culture System. *Analytical chemistry*, 79(22), 8557–8563.
- Grayson, A., Shawgo, R., Johnson, A., Flynn, N., Li, Y., Cima, M., & Langer, R. (2004). A BioMEMS Review: MEMS Technology for Physiologically Integrated Devices. *Proceedings of the IEEE*, 92(1), 6–21.
- Gruetter, R., Adriany, G., Choi, I. Y., Henry, P. G., Lei, H., & Öz, G. (2003). Localized in vivo ¹³C NMR spectroscopy of the brain. *NMR in Biomedicine*, 16(6-7), 313–338.

- Gutruf, P., & Rogers, J. A. (2018). Implantable, wireless device platforms for neuroscience research. *Current Opinion in Neurobiology*, 50, 42–49.
- Ha, N. S., de Raad, M., Han, L. Z., Golini, A., Petzold, C. J., & Northen, T. R. (2021). Faster, better, and cheaper: harnessing microfluidics and mass spectrometry for biotechnology. *RSC Chemical Biology*, 2(5), 1331–1351.
- Hamblin, M. R. (2016). Shining light on the head: Photobiomodulation for brain disorders. *BBA Clinical*, 6, 113–124.
- Hamblin, M. R. (2019). Photobiomodulation for Alzheimer's Disease: Has the Light Dawned? *Photonics*, 6(3), 77.
- Hammarlund-Udenaes, M. (2017a). Microdialysis as an Important Technique in Systems Pharmacology—a Historical and Methodological Review. *AAPS Journal*, 19(5), 1294–1303.
- Hammarlund-Udenaes, M. (2017b). Microdialysis for pharmacokinetic and pharmacodynamic studies with focus on the CNS. *Compendium of in vivo monitoring in real-time molecular neuroscience - volume 2: microdialysis and sensing of neural tissues* (pp. 47–69). World Scientific.
- Han, R., Liang, J., & Zhou, B. (2021). Glucose Metabolic Dysfunction in Neurodegenerative Diseases—New Mechanistic Insights and the Potential of Hypoxia as a Prospective Therapy Targeting Metabolic Reprogramming. *International Journal of Molecular Sciences*, 22(11), 5887.
- Hansen, C. L., Skordalakest, E., Berger, J. M., & Quake, S. R. (2002). A robust and scalable microfluidic metering method that allows protein crystal growth by free interface diffusion. *Proceedings of the National Academy of Sciences of the United States of America*, 99(26), 16531–16536.
- Hartner, N. T., Wink, K., Raddatz, C.-R., Thoben, C., Schirmer, M., Zimmermann, S., & Belder, D. (2021). Coupling Droplet Microfluidics with Ion Mobility Spectrometry for Monitoring Chemical Conversions at Nanoliter Scale. *Analytical Chemistry*, 93(40), 13615–13623.
- Herfert, K., Mannheim, J. G., Kuebler, L., Marciano, S., Amend, M., Parl, C., Napieczynska, H., Maier, F. M., Vega, S. C., & Pichler, B. J. (2020). Quantitative Rodent Brain Receptor Imaging. *Molecular Imaging and Biology*, 22(2), 223–244.

- Huang, C. J., Chen, Y. H., Wang, C. H., Chou, T. C., & Lee, G. B. (2007). Integrated microfluidic systems for automatic glucose sensing and insulin injection. *Sensors and Actuators, B: Chemical*, 122(2), 461–468.
- Huh, D., Matthews, B. D., Mammoto, A., Montoya-Zavala, M., Hsin, H. Y., & Ingber, D. E. (2010). Reconstituting Organ-Level Lung Functions on a Chip. *Science*, 328(5986), 1662–1668.
- Hümmer, D., Kurth, F., Naredi-Rainer, N., & Dittrich, P. S. (2016). Single cells in confined volumes: microchambers and microdroplets. *Lab on a Chip*, 16(3), 447–458.
- Im, C., & Seo, J. M. (2016). A review of electrodes for the electrical brain signal recording. *Biomedical Engineering Letters*, 6(3), 104–112.
- Inagaki, N., Tasaka, S., & Baba, T. (2001). Surface modification of polyimide film surface by silane coupling reactions for copper metallization. *Journal of Adhesion Science and Technology*, 15(7), 749–762.
- Inglis, D. W., Warkiani, M. E., Qasaimeh, M. A., & Chen, W. (2021). *Microfluidics for Biosensing and Diagnostics*. MDPI.
- Jagust, W. J., & Landau, S. M. (2021). Temporal Dynamics of β -Amyloid Accumulation in Aging and Alzheimer Disease. *Neurology*, 96(9), e1347–e1357.
- Jeong, J. W., McCall, J. G., Shin, G., Zhang, Y., Al-Hasani, R., Kim, M., Li, S., Sim, J. Y., Jang, K. I., Shi, Y., Hong, D. Y., Liu, Y., Schmitz, G. P., Xia, L., He, Z., Gamble, P., Ray, W. Z., Huang, Y., Bruchas, M. R., & Rogers, J. A. (2015). Wireless Optofluidic Systems for Programmable In Vivo Pharmacology and Optogenetics. *Cell*, 162(3), 662–674.
- Johnstone, D. M., Moro, C., Stone, J., Benabid, A.-L., & Mitrofanis, J. (2016). Turning On Lights to Stop Neurodegeneration: The Potential of Near Infrared Light Therapy in Alzheimer's and Parkinson's Disease. *Frontiers in Neuroscience*, 9(500), 1–15.
- Jokinen, V., Suvanto, P., & Franssila, S. (2012). Oxygen and nitrogen plasma hydrophilization and hydrophobic recovery of polymers. *Biomicrofluidics*, 6(1), 016501.
- Joshi, S. (2018). *Free standing interconnects for stretchable electronics* (Doctoral dissertation). Delft University of Technology.
- Kadry, H., Noorani, B., & Cucullo, L. (2020). A blood–brain barrier overview on structure, function, impairment, and biomarkers of integrity. *Fluids and Barriers of the CNS*, 17(69), 1–24.

- Kalia, L. V. (2018). Biomarkers for cognitive dysfunction in Parkinson's disease. *Parkinsonism and Related Disorders*, 46, S19–S23.
- Kandel, E. R., Schwartz, J. H., Jessell, T. M., Siegelbaum, S., & Hudspeth, A. (2014). *Principles of Neural Science* (5th). McGraw Hill.
- Kang, Y. N., Chou, N., Jang, J.-W., Choe, H. K., & Kim, S. (2021). A 3D flexible neural interface based on a microfluidic interconnection cable capable of chemical delivery. *Microsystems & Nanoengineering*, 7(66).
- Kee, S. P., & Gavrilidis, A. (2008). Design and characterisation of the staggered herringbone mixer. *Chemical Engineering Journal*, 142(1), 109–121.
- Keller, A., Gröger, L., Tschernig, T., Solomon, J., Laham, O., Schaum, N., Wagner, V., Kern, F., Schmartz, G. P., Li, Y., Borchertding, A., Meier, C., Wyss-Coray, T., Meese, E., Fehlmann, T., & Ludwig, N. (2022). miRNATissueAtlas2: an update to the human miRNA tissue atlas. *Nucleic Acids Research*, 50(D1), D211–D221.
- Kellogg, R. a., Gómez-Sjöberg, R., Leyrat, A. a., & Tay, S. (2014). High-throughput microfluidic single-cell analysis pipeline for studies of signaling dynamics. *Nature protocols*, 9, 1713–1726.
- Kendrick, K. M. (1989). Use of microdialysis in neuroendocrinology. *Methods in enzymology* (pp. 182–205). Academic Press.
- Kennedy, R. T. (2013). Emerging trends in in vivo neurochemical monitoring by microdialysis. *Current Opinion in Chemical Biology*, 17(5), 860–867.
- Kennedy, R. T., Thompson, J. E., & Vickroy, T. W. (2002). In vivo monitoring of amino acids by direct sampling of brain extracellular fluid at ultralow flow rates and capillary electrophoresis. *Journal of Neuroscience Methods*, 114(1), 39–49.
- Kho, C. M., Enche Ab Rahim, S. K., Ahmad, Z. A., & Abdullah, N. S. (2017). A Review on Microdialysis Calibration Methods: the Theory and Current Related Efforts. *Molecular Neurobiology*, 54(5), 3506–3527.
- Khomiakova, N., Hanuš, J., Kuzminova, A., & Kylián, O. (2020). Investigation of Wettability, Drying and Water Condensation on Polyimide (Kapton) Films Treated by Atmospheric Pressure Air Dielectric Barrier Discharge. *Coatings*, 10(7), 619.
- Kikkeri, K., Wu, D., & Voldman, J. (2022). A sample-to-answer electrochemical biosensor system for biomarker detection. *Lab on a Chip*, 22, 100–107.

- Kopkova, A., Sana, J., Fadrus, P., Machackova, T., Vecera, M., Vybihal, V., Juracek, J., Vychytilova-Faltejskova, P., Smrcka, M., & Slaby, O. (2018). MicroRNA isolation and quantification in cerebrospinal fluid: A comparative methodical study. *PLoS ONE*, 13(12), 1–12.
- Kotake, N., Suzuki, T., Mabuchi, K., & Takeuchi, S. (2008). A flexible parylene neural probe combined with a microdialysis membrane. *12th International Conference on Miniaturized Systems for Chemistry and Life Sciences - The Proceedings of MicroTAS 2008 Conference*, 1687–1689.
- Kottegoda, S., Shaik, I., & Shippy, S. A. (2002). Demonstration of low flow push-pull perfusion. *Journal of Neuroscience Methods*, 121(1), 93–101.
- Kotzar, G., Freas, M., Abel, P., Fleischman, A., Roy, S., Zorman, C., Moran, J. M., & Melzak, J. (2002). Evaluation of MEMS materials of construction for implantable medical devices. *Biomaterials*, 23(13), 2737–2750.
- Kumar, V., & Sharma, N. N. (2015). Synthesis of hydrophilic to superhydrophobic SU8 surfaces. *Journal of Applied Polymer Science*, 132(18).
- Kushibiki, T., Hirasawa, T., Okawa, S., & Ishihara, M. (2013). Regulation of miRNA Expression by Low-Level Laser Therapy (LLLT) and Photodynamic Therapy (PDT). *International Journal of Molecular Sciences*, 14(7), 13542–13558.
- Labrot, V., Schindler, M., Guillot, P., Colin, A., & Joanicot, M. (2009). Extracting the hydrodynamic resistance of droplets from their behavior in microchannel networks. *Biomicrofluidics*, 3(1), 012804.
- Lausted, C., Lee, I., Zhou, Y., Qin, S., Sung, J., Price, N. D., Hood, L., & Wang, K. (2014). Systems Approach to Neurodegenerative Disease Biomarker Discovery. *Annual Review of Pharmacology and Toxicology*, 54(1), 457–481.
- Lee, H.-J., Bae, E.-J., & Lee, S.-J. (2014). Extracellular α -synuclein—a novel and crucial factor in Lewy body diseases. *Nature Reviews Neurology*, 10(2), 92–98.
- Lee, S., de Rutte, J., Dimatteo, R., Koo, D., & Di Carlo, D. (2022). Scalable Fabrication and Use of 3D Structured Microparticles Spatially Functionalized with Biomolecules. *ACS Nano*, 16(1), 38–49.
- Lee, W. H., Ngernsutivorakul, T., Mabrouk, O. S., Wong, J.-M. T., Dugan, C. E., Pappas, S. S., Yoon, H. J., & Kennedy, R. T. (2016). Microfabrication and in Vivo Performance of a

- Microdialysis Probe with Embedded Membrane. *Analytical Chemistry*, 88(2), 1230–1237.
- Lee, W. H., Slaney, T. R., Hower, R. W., & Kennedy, R. T. (2013). Microfabricated Sampling Probes for in Vivo Monitoring of Neurotransmitters. *Analytical Chemistry*, 85(8), 3828–3831.
- Leroy, A., Teixidor, J., Bertsch, A., & Renaud, P. (2021). In-flow electrochemical detection of chemicals in droplets with pyrolysed photoresist electrodes: application as a module for quantification of microsampled dopamine. *Lab on a Chip*, 21(17), 3328–3337.
- Lietsche, J., Gorka, J., Hardt, S., Karas, M., & Klein, J. (2014). Self-built microdialysis probes with improved recoveries of ATP and neuropeptides. *Journal of Neuroscience Methods*, 237, 1–8.
- Liljeroth, P., Johans, C., Slevin, C. J., Quinn, B. M., & Kontturi, K. (2002). Micro ring–disk electrode probes for scanning electrochemical microscopy. *Electrochemistry Communications*, 4(1), 67–71.
- Lindner, L., Cayrou, P., Jacquot, S., Birling, M.-C., Herault, Y., & Pavlovic, G. (2021). Reliable and robust droplet digital PCR (ddPCR) and RT-ddPCR protocols for mouse studies. *Methods*, 191, 95–106.
- Liu, C., Zhao, Y., Cai, X., Xie, Y., Wang, T., Cheng, D., Li, L., Li, R., Deng, Y., Ding, H., Lv, G., Zhao, G., Liu, L., Zou, G., Feng, M., Sun, Q., Yin, L., & Sheng, X. (2020). A wireless, implantable optoelectrochemical probe for optogenetic stimulation and dopamine detection. *Microsystems & Nanoengineering*, 6(1), 64.
- Liu, H., & Crooks, R. M. (2013). Highly reproducible chronoamperometric analysis in microdroplets. *Lab on a Chip*, 13(7), 1364–1370.
- Liu, W.-w., & Zhu, Y. (2020). “Development and application of analytical detection techniques for droplet-based microfluidics”-A review. *Analytica Chimica Acta*, 1113, 66–84.
- Liu, X., Hu, X., Xie, Z., Chen, P., Sun, X., Yan, J., & Zhou, S. (2016). In situ bifunctionalized carbon dots with boronic acid and amino groups for ultrasensitive dopamine detection. *Analytical Methods*, 8(15), 3236–3241.
- Liu, X., Tian, M., Gao, W., & Zhao, J. (2019). A Simple, Rapid, Fluorometric Assay for Dopamine by In Situ Reaction of Boronic Acids and cis -Diol. *Journal of Analytical Methods in Chemistry*, (6540397), 1–7.

- Lotankar, S., Prabhavalkar, K. S., & Bhatt, L. K. (2017). Biomarkers for Parkinson's Disease: Recent Advancement. *Neuroscience Bulletin*, 33(5), 585–597.
- Madou, M. J. (2018). *Fundamentals of Microfabrication*. CRC Press.
- Manz, A., Graber, N., & Widmer, H. (1990). Miniaturized total chemical analysis systems: A novel concept for chemical sensing. *Sensors and Actuators B: Chemical*, 1(1-6), 244–248.
- Marjańska, M., Auerbach, E. J., Valabrègue, R., Van de Moortele, P.-F., Adriany, G., & Garwood, M. (2012). Localized ^1H NMR spectroscopy in different regions of human brain in vivo at 7 T: T_2 relaxation times and concentrations of cerebral metabolites. *NMR in Biomedicine*, 25(2), 332–339.
- Martinez, V., Behr, P., Drechsler, U., Polesel-Maris, J., Potthoff, E., Vörös, J., & Zambelli, T. (2016). SU-8 hollow cantilevers for AFM cell adhesion studies. *Journal of Micromechanics and Microengineering*, 26(5), 055006.
- Martinez-Duarte, R., Teixidor, G. T., Mukherjee, P. P., Kang, Q., & Madou, M. J. (2010). Perspectives of Micro and Nanofabrication of Carbon for Electrochemical and Microfluidic Applications. *Microfluidics and microfabrication* (pp. 181–263). Springer US.
- Martinez-Duarte, R., & Madou, M. J. (2016). Finite-Volume Method for Numerical Simulation: Fundamentals. *Microfluidics and nanofluidics handbook* (pp. 151–188). CRC Press.
- Maynard, E. M., Nordhausen, C. T., & Normann, R. A. (1997). The Utah Intracortical Electrode Array: A recording structure for potential brain-computer interfaces. *Electroencephalography and Clinical Neurophysiology*, 102(3), 228–239.
- McCall, J. G., Qazi, R., Shin, G., Li, S., Ikram, M. H., Jang, K. I., Liu, Y., Al-Hasani, R., Bruchas, M. R., Jeong, J. W., & Rogers, J. A. (2017). Preparation and implementation of optofluidic neural probes for in vivo wireless pharmacology and optogenetics. *Nature Protocols*, 12(2), 219–237.
- McDonald, J. C., & Whitesides, G. M. (2002). Poly(dimethylsiloxane) as a Material for Fabricating Microfluidic Devices. *Accounts of Chemical Research*, 35(7), 491–499.
- McEwen, B. (2016). Central Role of the Brain in Stress and Adaptation. *Stress: concepts, cognition, emotion, and behavior* (pp. 39–55). Elsevier.

- McNay, E. C., Fries, T. M., & Gold, P. E. (2000). Decreases in rat extracellular hippocampal glucose concentration associated with cognitive demand during a spatial task. *Proceedings of the National Academy of Sciences*, 97(6), 2881–2885.
- McNay, E. C., & Gold, P. E. (1999). Extracellular glucose concentrations in the rat hippocampus measured by zero-net-flux: Effects of microdialysis flow rate, strain, and age. *Journal of Neurochemistry*, 72(2), 785–790.
- Menacherry, S., Hubert, W., & Justice, J. B. (1992). In vivo calibration of microdialysis probes for exogenous compounds. *Analytical Chemistry*, 64(6), 577–583.
- Mercanzini, A., Dransart, A., & Pollo, C. (2017). Directional Deep Brain Stimulation. *Innovative neuromodulation* (pp. 61–82). Elsevier.
- Mercanzini, A., Cheung, K., Buhl, D. L., Boers, M., Maillard, A., Colin, P., Bensadoun, J.-C., Bertsch, A., & Renaud, P. (2008). Demonstration of cortical recording using novel flexible polymer neural probes. *Sensors and Actuators A: Physical*, 143(1), 90–96.
- Mercanzini, A., Colin, P., Bensadoun, J.-C., Bertsch, A., & Renaud, P. (2009). In vivo electrical impedance spectroscopy of tissue reaction to microelectrode arrays. *IEEE Transactions on Biomedical Engineering*, 56(7), 1909–1918.
- Metz, S., Holzer, R., & Renaud, P. (2001). Fabrication of Flexible, Implantable Microelectrodes with Embedded Fluidic Microchannels. *Transducers '01 Eurosensors XV, The 11th International Conference on Solid-State Sensors and Actuators*, 1182–1185.
- Metz, S., Jiguet, S., Bertsch, A., & Renaud, P. (2004). Polyimide and SU-8 microfluidic devices manufactured by heat-depolymerizable sacrificial material technique. *Lab on a Chip*, 4(2), 114–120.
- Metz, S., Trautmann, C., Bertsch, A., & Renaud, P. (2004). Polyimide microfluidic devices with integrated nanoporous filtration areas manufactured by micromachining and ion track technology. *Journal of Micromechanics and Microengineering*, 14(3), 324–331.
- Mineev, I. R., Musienko, P., Hirsch, A., Barraud, Q., Wenger, N., Moraud, E. M., Gandar, J., Capogrosso, M., Milekovic, T., Asboth, L., Torres, R. F., Vachicouras, N., Liu, Q., Pavlova, N., Duis, S., Larmagnac, A., Vörös, J., Micera, S., Suo, Z., . . . Lacour, S. P. (2015). Electronic dura mater for long-term multimodal neural interfaces. *Science*, 347(6218), 159–163.

- Miranda, A., Kang, M. S., Blinder, S., Bouhachi, R., Soucy, J.-P., Aliaga-Aliaga, A., Massarweh, G., Stroobants, S., Staelens, S., Rosa-Neto, P., & Verhaeghe, J. (2019). PET imaging of freely moving interacting rats. *NeuroImage*, 191, 560–567.
- Moresco, J., Clausen, C. H., & Svendsen, W. (2010). Improved anti-stiction coating of SU-8 molds. *Sensors and Actuators B: Chemical*, 145(2), 698–701.
- Morgan, M. M., & Christie, M. J. (2010). Volume Transmission. *Encyclopedia of psychopharmacology* (pp. 1367–1367). Springer Berlin Heidelberg.
- Moro, C., Massri, N. E., Torres, N., Ratel, D., De Jaeger, X., Chabrol, C., Perraut, F., Bourgerette, A., Berger, M., Purushothuman, S., Johnstone, D., Stone, J., Mitrofanis, J., & Benabid, A.-L. (2014). Photobiomodulation inside the brain: a novel method of applying near-infrared light intracranially and its impact on dopaminergic cell survival in MPTP-treated mice. *Journal of Neurosurgery*, 120(3), 670–683.
- Morrison, P. F., Bungay, P. M., Hsiao, J. K., Mefford, I. N., Dykstra, K. H., & Dedrick, R. L. (1991). Quantitative microdialysis. *Techniques in the behavioral and neural sciences* (pp. 47–80). Elsevier.
- Morrison, P. F., Chen, M. Y., Chadwick, R. S., Lonser, R. R., & Oldfield, E. H. (1999). Focal delivery during direct infusion to brain: role of flow rate, catheter diameter, and tissue mechanics. *American Journal of Physiology-Regulatory, Integrative and Comparative Physiology*, 277(4), R1218–R1229.
- Mousavi, S. M., Amin Mahdian, S. M., Ebrahimi, M. S., Taghizadieh, M., Vosough, M., Sadri Nahand, J., Hosseindoost, S., Vosooghi, N., Javar, H. A., Larijani, B., Hadjighassem, M. R., Rahimian, N., Hamblin, M. R., & Mirzaei, H. (2022). Microfluidics for detection of exosomes and microRNAs in cancer: State of the art. *Molecular Therapy - Nucleic Acids*, 28, 758–791.
- Müller, J., Ballini, M., Livi, P., Chen, Y., Radivojevic, M., Shadmani, A., Viswam, V., Jones, I. L., Fiscella, M., Diggelmann, R., Stettler, A., Frey, U., Bakkum, D. J., & Hierlemann, A. (2015). High-resolution CMOS MEA platform to study neurons at subcellular, cellular, and network levels. *Lab on a Chip*, 15(13), 2767–2780.
- Nakatsuka, N., Abendroth, J. M., Yang, K. A., & Andrews, A. M. (2021). Divalent Cation Dependence Enhances Dopamine Aptamer Biosensing. *ACS Applied Materials and Interfaces*, 13(8), 9425–9435.

- Nakatsuka, N., Heard, K. J., Faillétaz, A., Momotenko, D., Vörös, J., Gage, F. H., & Vadodaria, K. C. (2021). Sensing serotonin secreted from human serotonergic neurons using aptamer-modified nanopipettes. *Molecular Psychiatry*, 26(7), 2753–2763.
- Nakatsuka, N., Yang, K.-A., Abendroth, J. M., Cheung, K. M., Xu, X., Yang, H., Zhao, C., Zhu, B., Rim, Y. S., Yang, Y., Weiss, P. S., Stojanović, M. N., & Andrews, A. M. (2018). Aptamer-field-effect transistors overcome Debye length limitations for small-molecule sensing. *Science*, 362(6412), 319–324.
- Nasrallah, I., & Dubroff, J. (2013). An Overview of PET Neuroimaging. *Seminars in Nuclear Medicine*, 43(6), 449–461.
- Ngernsutivorakul, T. (2018). *Microfabricated Sampling Probes for Monitoring Brain Chemistry at High Spatial and Temporal resolution* (Doctoral dissertation). University of Michigan.
- Ngernsutivorakul, T., Steyer, D. J., Valenta, A. C., & Kennedy, R. T. (2018). In Vivo Chemical Monitoring at High Spatiotemporal Resolution Using Microfabricated Sampling Probes and Droplet-Based Microfluidics Coupled to Mass Spectrometry. *Analytical Chemistry*, 90(18), 10943–10950.
- Ngernsutivorakul, T., White, T. S., & Kennedy, R. T. (2018). Microfabricated Probes for Studying Brain Chemistry: A Review. *ChemPhysChem*, 19(10), 1128–1142.
- Nicholson, C. (2001). Diffusion and related transport mechanisms in brain tissue. *Reports on Progress in Physics*, 64(7), 815–884.
- Nightingale, A. M., Leong, C. L., Burnish, R. A., Hassan, S. u., Zhang, Y., Clough, G. F., Boutelle, M. G., Voegeli, D., & Niu, X. (2019). Monitoring biomolecule concentrations in tissue using a wearable droplet microfluidic-based sensor. *Nature Communications*, 10(2741).
- Niu, X., Pereira, F., Edel, J. B., & de Mello, A. J. (2013). Droplet-Interfaced Microchip and Capillary Electrophoretic Separations. *Analytical Chemistry*, 85(18), 8654–8660.
- Niyonambaza, S. D., Kumar, P., Xing, P., Mathault, J., De Koninck, P., Boisselier, E., Boukadoum, M., & Miled, A. (2019). A Review of Neurotransmitters Sensing Methods for Neuro-Engineering Research. *Applied Sciences*, 9(21), 4719.
- Obaid, A., Hanna, M.-E., Wu, Y.-W., Kollo, M., Racz, R., Angle, M. R., Müller, J., Brackbill, N., Wray, W., Franke, F., Chichilnisky, E. J., Hierlemann, A., Ding, J. B., Schaefer, A. T., &

- Melosh, N. A. (2020). Massively parallel microwire arrays integrated with CMOS chips for neural recording. *Science Advances*, 6(12), eaay2789.
- Oh, K. W., Lee, K., Ahn, B., & Furlani, E. P. (2012). Design of pressure-driven microfluidic networks using electric circuit analogy. *Lab on a Chip*, 12(3), 515–545.
- Oueslati, A., Lovisa, B., Perrin, J., Wagnières, G., van den Bergh, H., Tardy, Y., & Lashuel, H. A. (2015). Photobiomodulation Suppresses Alpha-Synuclein-Induced Toxicity in an AAV-Based Rat Genetic Model of Parkinson's Disease (R. L. Mosley, Ed.). *PLOS ONE*, 10(10), e0140880.
- Ovechkina, V. S., Zakian, S. M., Medvedev, S. P., & Valetdinova, K. R. (2021). Genetically encoded fluorescent biosensors for biomedical applications. *Biomedicines*, 9(1528).
- Paluch, E. K., Nelson, C. M., Biais, N., Fabry, B., Moeller, J., Pruitt, B. L., Wollnik, C., Kudryasheva, G., Rehfeldt, F., & Federle, W. (2015). Mechanotransduction: use the force(s). *BMC Biology*, 13(47).
- Payne, E. M., Holland-Moritz, D. A., Sun, S., & Kennedy, R. T. (2020). High-throughput screening by droplet microfluidics: perspective into key challenges and future prospects. *Lab on a Chip*, 20(13), 2247–2262.
- Pereira, F., Niu, X., & DeMello, A. J. (2013). A Nano LC-MALDI Mass Spectrometry Droplet Interface for the Analysis of Complex Protein Samples. *PLoS ONE*, 8(5), e63087.
- Peretzki, A. J., Schmidt, S., Flachowsky, E., Das, A., Gerhardt, R. F., & Belder, D. (2020). How electrospray potentials can disrupt droplet microfluidics and how to prevent this. *Lab on a Chip*, 20(23), 4456–4465.
- Perry, M., Li, Q., & Kennedy, R. T. (2009). Review of recent advances in analytical techniques for the determination of neurotransmitters. *Analytica Chimica Acta*, 653(1), 1–22.
- Persike, M., Zimmermann, M., Klein, J., & Karas, M. (2010). Quantitative Determination of Acetylcholine and Choline in Microdialysis Samples by MALDI-TOF MS. *Analytical Chemistry*, 82(3), 922–929.
- Petit-Pierre, G. (2017). *A Microfluidic Brain Interface for In Vivo Recording of Neurochemical Activity* (Doctoral dissertation). EPFL, N°7816.
- Petit-Pierre, G., Bertsch, A., & Renaud, P. (2016). Neural probe combining microelectrodes and a droplet-based microdialysis collection system for high temporal resolution sampling. *Lab on a Chip*, 16(5), 917–924.

- Petit-Pierre, G., Colin, P., Laurer, E., Déglon, J., Bertsch, A., Thomas, A., Schneider, B. L., & Renaud, P. (2017). In vivo neurochemical measurements in cerebral tissues using a droplet-based monitoring system. *Nature Communications*, 8(1), 1239.
- Piendl, S. K., Schönfelder, T., Polack, M., Weigelt, L., van der Zwaag, T., Teutenberg, T., Beckert, E., & Belder, D. (2021). Integration of segmented microflow chemistry and online HPLC/MS analysis on a microfluidic chip system enabling enantioselective analyses at the nanoliter scale. *Lab on a Chip*, 21(13), 2614–2624.
- Pomfret, R., Miranpuri, G., & Sillay, K. (2013). The Substitute Brain and the Potential of the Gel Model. *Annals of Neurosciences*, 20(3), 118–122.
- Raman, R., Rousseau, E. B., Wade, M., Tong, A., Cotler, M. J., Kuang, J., Lugo, A. A., Zhang, E., Graybiel, A. M., White, F. M., Langer, R., & Cima, M. J. (2020). Platform for micro-invasive membrane-free biochemical sampling of brain interstitial fluid. *Science Advances*, 6(39), eabb0657.
- Rezaei, B., Pan, J. Y., Gundlach, C., & Keller, S. S. (2020). Highly structured 3D pyrolytic carbon electrodes derived from additive manufacturing technology. *Materials & Design*, 193, 108834.
- Rhodes, C. J. (2017). Magnetic Resonance Spectroscopy. *Science Progress*, 100(3), 241–292.
- Ribet, F., Stemme, G., & Roxhed, N. (2017). Ultra-miniaturization of a planar amperometric sensor targeting continuous intradermal glucose monitoring. *Biosensors and Bioelectronics*, 90, 577–583.
- Robinson, D. L., Venton, B. J., Heien, M. L. A. V., & Wightman, R. M. (2003). Detecting Subsecond Dopamine Release with Fast-Scan Cyclic Voltammetry in Vivo. *Clinical Chemistry*, 49(10), 1763–1773.
- Rogers, M. L., & Boutelle, M. G. (2017). Real time neurochemical monitoring using microdialysis. *Compendium of in vivo monitoring in real-time molecular neuroscience* (pp. 71–94). World Scientific.
- Roh, E., Song, D. K., & Kim, M.-S. (2016). Emerging role of the brain in the homeostatic regulation of energy and glucose metabolism. *Experimental & Molecular Medicine*, 48, e216.
- Ronne-Engström, E., Carlson, H., Yansheng, L., Ungerstedt, U., & Hillered, L. (1995). Influence of Perfusate Glucose Concentration on Dialysate Lactate, Pyruvate, Aspartate, and

- Glutamate Levels Under Basal and Hypoxic Conditions: A Microdialysis Study in Rat Brain. *Journal of Neurochemistry*, 65(1), 257–262.
- Rosen, G. D., & Williams, R. W. (2001). Complex trait analysis of the mouse striatum: independent QTLs modulate volume and neuron number. *BMC neuroscience*, 2(5).
- Roser, A. E., Caldi Gomes, L., Schünemann, J., Maass, F., & Lingor, P. (2018). Circulating miRNAs as Diagnostic Biomarkers for Parkinson's Disease. *Frontiers in Neuroscience*, 12(625).
- Routh, V. H. (2002). Glucose-sensing neurons: Are they physiologically relevant? *Physiology and Behavior*, 76(3), 403–413.
- Rowald, A., Komi, S., Demesmaeker, R., Baaklini, E., Hernandez-Charpak, S. D., Paoles, E., Montanaro, H., Cassara, A., Becce, E., Lloyd, B., Newton, T., Ravier, J., Kinany, N., D'Ercole, M., Paley, A., Hankov, N., Varescon, C., McCracken, L., Vat, M., ... Courtine, G. (2022). Activity-dependent spinal cord neuromodulation rapidly restores trunk and leg motor functions after complete paralysis. *Nature Medicine*, 28(2), 260–271.
- Saha-Shah, A., Green, C. M., Abraham, D. H., & Baker, L. A. (2016). Segmented flow sampling with push–pull theta pipettes. *The Analyst*, 141(6), 1958–1965.
- Salehpour, E., & Hamblin, M. (2020). Photobiomodulation for Parkinson's Disease in Animal Models: A Systematic Review. *Biomolecules*, 10(4), 610.
- Saliba, S. W., Vieira, E. L. M., Santos, R. P. d. M., Candelario-Jalil, E., Fiebich, B. L., Vieira, L. B., Teixeira, A. L., & de Oliveira, A. C. P. (2017). Neuroprotective effects of intrastriatal injection of rapamycin in a mouse model of excitotoxicity induced by quinolinic acid. *Journal of Neuroinflammation*, 14(25).
- Saugstad, J. A., Lusardi, T. A., Van Keuren-Jensen, K. R., Phillips, J. I., Lind, B., Harrington, C. A., McFarland, T. J., Courtright, A. L., Reiman, R. A., Yeri, A. S., Kalani, M. Y. S., Adelson, P. D., Arango, J., Nolan, J. P., Duggan, E., Messer, K., Akers, J. C., Galasko, D. R., Quinn, J. F., ... Hochberg, F. H. (2017). Analysis of extracellular RNA in cerebrospinal fluid. *Journal of Extracellular Vesicles*, 6(1), 1317577.
- Saylor, R. A., & Lunte, S. M. (2015). A review of microdialysis coupled to microchip electrophoresis for monitoring biological events. *Journal of Chromatography A*, 1382, 48–64.
- Saylor, R. A., Thomas, S. R., & Lunte, S. M. (2017). Separation-based methods combined with microdialysis sampling for monitoring neurotransmitters and drug delivery to the

- brain. *Compendium of in vivo monitoring in real-time molecular neuroscience* (pp. 1–45). World Scientific.
- Schmidt, A., Karas, M., & Dülcks, T. (2003). Effect of different solution flow rates on analyte ion signals in nano-ESI MS, or: when does ESI turn into nano-ESI? *Journal of the American Society for Mass Spectrometry*, 14(5), 492–500.
- Schultz, K. N., & Kennedy, R. T. (2008). Time-Resolved Microdialysis for In Vivo Neurochemical Measurements and Other Applications. *Annual Review of Analytical Chemistry*, 1, 627–661.
- Schultz, W. (2007). Multiple Dopamine Functions at Different Time Courses. *Annual Review of Neuroscience*, 30(1), 259–288.
- Schweizer, S., Calmes, S., Laudon, M., & Renaud, P. (1999). Thermally actuated optical microscanner with large angle and low consumption. *Sensors and Actuators A: Physical*, 76(1-3), 470–477.
- Schwerdt, H. N., Kim, M. J., Amemori, S., Homma, D., Yoshida, T., Shimazu, H., Yerramreddy, H., Karasan, E., Langer, R., Graybiel, A. M., & Cima, M. J. (2017). Subcellular probes for neurochemical recording from multiple brain sites. *Lab on a Chip*, 17(6), 1104–1115.
- Schwerdt, H. N., Zhang, E., Kim, M. J., Yoshida, T., Stanwicks, L., Amemori, S., Dagdeviren, H. E., Langer, R., Cima, M. J., & Graybiel, A. M. (2018). Cellular-scale probes enable stable chronic subsecond monitoring of dopamine neurochemicals in a rodent model. *Communications Biology*, 1, 144.
- Seok, T. J., Quack, N., Member, S., & Han, S. (2016). Highly Scalable Digital Silicon Photonic MEMS Switches. 34(2), 365–371.
- Shang, L., Cheng, Y., & Zhao, Y. (2017). Emerging Droplet Microfluidics. *Chemical Reviews*, 117(12), 7964–8040.
- Shannon, R. J., Carpenter, K. L. H., Guilfoyle, M. R., Helmy, A., & Hutchinson, P. J. (2013). Cerebral microdialysis in clinical studies of drugs: pharmacokinetic applications. *Journal of Pharmacokinetics and Pharmacodynamics*, 40(3), 343–358.
- Shetty, A. K., & Zanirati, G. (2020). The interstitial system of the brain in health and disease. *Aging and Disease*, 11(1), 200–211.

- Shin, H., Jeong, S., Lee, J.-H., Sun, W., Choi, N., & Cho, I.-j. (2021). 3D high-density microelectrode array with optical stimulation and drug delivery for investigating neural circuit dynamics. *Nature Communications*, 12(1), 492.
- Shin, M., & Venton, B. J. (2018). Electrochemical Measurements of Acetylcholine-Stimulated Dopamine Release in Adult *Drosophila melanogaster* Brains. *Analytical Chemistry*, 90(17), 10318–10325.
- Sim, J. Y., Haney, M. P., Park, S. I., McCall, J. G., & Jeong, J.-W. (2017). Microfluidic neural probes: in vivo tools for advancing neuroscience. *Lab Chip*, 17(8), 1406–1435.
- Slaney, T. R., Mabrouk, O. S., Porter-Stransky, K. A., Aragona, B. J., & Kennedy, R. T. (2013). Chemical Gradients within Brain Extracellular Space Measured using Low Flow Push–Pull Perfusion Sampling in Vivo. *ACS Chemical Neuroscience*, 4(2), 321–329.
- Sommer, A. P., Schemmer, P., Pavláth, A. E., Försterling, H.-D., Mester, Á. R., & Trelles, M. A. (2020). Quantum biology in low level light therapy: death of a dogma. *Annals of Translational Medicine*, 8(7).
- Song, P., Hershey, N. D., Mabrouk, O. S., Slaney, T. R., & Kennedy, R. T. (2012). Mass Spectrometry “Sensor” for in Vivo Acetylcholine Monitoring. *Analytical Chemistry*, 84(11), 4659–4664.
- Stayte, S., & Vissel, B. (2014). Advances in non-dopaminergic treatments for Parkinson’s disease. *Frontiers in Neuroscience*, 8, 1–29.
- Stenken, J. A., & Patton, S. L. (2017). Microdialysis flux considerations. *Compendium of in vivo monitoring in real-time molecular neuroscience* (pp. 337–374). World Scientific.
- Stenken, J. A., & Elkins, M. (2015). Measurement of Cytokines in the Brain. *Compendium of in vivo monitoring in real-time molecular neuroscience* (pp. 369–400). World Scientific.
- Steyer, D. J., & Kennedy, R. T. (2019). High-Throughput Nanoelectrospray Ionization-Mass Spectrometry Analysis of Microfluidic Droplet Samples. *Analytical Chemistry*, 91(10), 6645–6651.
- Stieglitz, T. (2004). Electrode materials for recording and stimulation. *Neuroprosthetics, theory and practice* (pp. 475–516). World Scientific.
- Su, Y., Bian, S., & Sawan, M. (2020). Real-time: In vivo detection techniques for neurotransmitters: A review. *Analyst*, 145(19), 6193–6210.

- Suea-Ngam, A., Rattanasart, P., Chailapakul, O., & Srisa-Art, M. (2015). Electrochemical droplet-based microfluidics using chip-based carbon paste electrodes for high-throughput analysis in pharmaceutical applications. *Analytica Chimica Acta*, 883, 45–54.
- Suzuki, A., Ivandini, T. A., Yoshimi, K., Fujishima, A., Oyama, G., Nakazato, T., Hattori, N., Kitazawa, S., & Einaga, Y. (2007). Fabrication, Characterization, and Application of Boron-Doped Diamond Microelectrodes for in Vivo Dopamine Detection. *Analytical Chemistry*, 79(22), 8608–8615.
- Syková, E., & Nicholson, C. (2008). Diffusion in Brain Extracellular Space. *Physiological Reviews*, 88(4), 1277–1340.
- Syslová, K., Rambousek, L., Bubeníková-Valešová, V., Šlamberová, R., Novotný, P., & Kačer, P. (2012). Dopamine analysis in neuroscience research. *Dopamine: functions, regulation and health effects* (pp. 81–111).
- Tamimi, F., Comeau, P., Le Nihouannen, D., Zhang, Y., Bassett, D., Khalili, S., Gbureck, U., Tran, S., Komarova, S., & Barralet, J. (2013). Perfluorodecalin and bone regeneration. *European Cells and Materials*, 25, 22–36.
- Tang, A., Bungay, P. M., & Gonzales, R. A. (2003). Characterization of probe and tissue factors that influence interpretation of quantitative microdialysis experiments for dopamine. *Journal of Neuroscience Methods*, 126(1), 1–11.
- Tao, S. L., Popat, K. C., Norman, J. J., & Desai, T. A. (2008). Surface Modification of SU-8 for Enhanced Biofunctionality and Nonfouling Properties. *Langmuir*, 24(6), 2631–2636.
- Taylor, D. P., Mathur, P., Renaud, P., & Kaigala, G. V. (2022). Microscale hydrodynamic confinements: shaping liquids across length scales as a toolbox in life sciences. *Lab on a Chip*, 22(8), 1415–1437.
- Teixidor, J., Bertsch, A., & Renaud, P. (2021a). Neural probe to sample brain fluid droplets on demand with high recovery fraction. *25th International Conference on Miniaturized Systems for Chemistry and Life Sciences (μTAS 2021)*, 709–710.
- Teixidor, J., Bertsch, A., & Renaud, P. (2021b). Neural probe to sample droplets on demand in vivo and quantify glucose by mass spectrometry. *NanoBioTech Montreux*.
- Teixidor, J., Novello, S., Ortiz, D., Menin, L., Lashuel, H. A., Bertsch, A., & Renaud, P. (2022). On-Demand Nanoliter Sampling Probe for the Collection of Brain Fluid. *Analytical Chemistry*, 94(29), 10415–10426.

- Teixidor, J., Novello, S., Ortiz, D., Menin, L., Lashuel, H. A., & Renaud, P. (2022). On demand nanoliter sampling probe for collection of brain fluid. *BioRxiv*, 1–17.
- Trouillon, R., & O'Hare, D. (2010). Comparison of glassy carbon and boron doped diamond electrodes: Resistance to biofouling. *Electrochimica Acta*, 55(22), 6586–6595.
- Trouillon, R., Lin, Y., Mellander, L. J., Keighron, J. D., & Ewing, A. G. (2013). Evaluating the Diffusion Coefficient of Dopamine at the Cell Surface During Amperometric Detection: Disk vs Ring Microelectrodes. *Analytical Chemistry*, 85(13), 6421–6428.
- Ueda, Y., Obrenovitch, T. P., Lok, S. Y., Sarna, G. S., & Symon, L. (1992). Changes in extracellular glutamate concentration produced in the rat striatum by repeated ischemia. *Stroke; a journal of cerebral circulation*, 23(8), 1125–30.
- Ungerstedt, U., & Pycock, C. (1974). Functional correlates of dopamine neurotransmission. *Bulletin der Schweizerischen Akademie der Medizinischen Wissenschaften*, 30(1-3), 44–55.
- Vachicouras, N., Tarabichi, O., Kanumuri, V. V., Tringides, C. M., Macron, J., Fallegger, F., Thenaisie, Y., Epprecht, L., McInturff, S., Qureshi, A. A., Paggi, V., Kuklinski, M. W., Brown, M. C., Lee, D. J., & Lacour, S. P. (2019). Microstructured thin-film electrode technology enables proof of concept of scalable, soft auditory brainstem implants. *Science Translational Medicine*, 11(514), eaax9487.
- Valenta, A. C., D'Amico, C. I., Dugan, C. E., Grinias, J. P., & Kennedy, R. T. (2021). A microfluidic chip for on-line derivatization and application to in vivo neurochemical monitoring. *The Analyst*, 146(3), 825–834.
- van den Brink, F. T. G., Phisonkunkasem, T., Asthana, A., Bomer, J. G., van den Maagdenberg, A. M. J. M., Tolner, E. A., & Odijk, M. (2019). A miniaturized push–pull-perfusion probe for few-second sampling of neurotransmitters in the mouse brain. *Lab on a Chip*, 19(8), 1332–1343.
- Vanapalli, S. A., Banpurkar, A. G., Van Den Ende, D., Duits, M. H., & Mugele, F. (2009). Hydrodynamic resistance of single confined moving drops in rectangular microchannels. *Lab on a Chip*, 9(7), 982–990.
- VanDersarl, J. J., Mercanzini, A., & Renaud, P. (2015). Integration of 2D and 3D Thin Film Glassy Carbon Electrode Arrays for Electrochemical Dopamine Sensing in Flexible Neuroelectronic Implants. *Advanced Functional Materials*, 25(1), 78–84.

- Vázquez-Guardado, A., Yang, Y., Bandodkar, A. J., & Rogers, J. A. (2020). Recent advances in neurotechnologies with broad potential for neuroscience research. *Nature Neuroscience*, 23(12), 1522–1536.
- Venton, B. J., & Cao, Q. (2020). Fundamentals of fast-scan cyclic voltammetry for dopamine detection. *Analyst*, 145(4), 1158–1168.
- Villanueva, L. G., Bausells, J., & Brugger, J. (2016). Grand Challenge in N/MEMS. *Frontiers in Mechanical Engineering*, 1(15).
- Vladislavljević, G. T., Khalid, N., Neves, M. A., Kuroiwa, T., Nakajima, M., Uemura, K., Ichikawa, S., & Kobayashi, I. (2013). Industrial lab-on-a-chip: Design, applications and scale-up for drug discovery and delivery. *Advanced Drug Delivery Reviews*, 65(11-12), 1626–1663.
- Walther, F., Davydovskaya, P., Zürcher, S., Kaiser, M., Herberg, H., Gigler, A. M., & Stark, R. W. (2007). Stability of the hydrophilic behavior of oxygen plasma activated SU-8. *Journal of Micromechanics and Microengineering*, 17(3), 524–531.
- Wan, J., Zhou, S., Mea, H. J., Guo, Y., Ku, H., & Urbina, B. M. (2022). Emerging Roles of Microfluidics in Brain Research: From Cerebral Fluids Manipulation to Brain-on-a-Chip and Neuroelectronic Devices Engineering. *Chemical Reviews*, 122(7), 7142–7181.
- Wang, G. (2019). High Temporal-Resolution Dynamic PET Image Reconstruction Using a New Spatiotemporal Kernel Method. *IEEE Transactions on Medical Imaging*, 38(3), 664–674.
- Wang, M., Hershey, N. D., Mabrouk, O. S., & Kennedy, R. T. (2011). Collection, storage, and electrophoretic analysis of nanoliter microdialysis samples collected from awake animals in vivo. *Analytical and Bioanalytical Chemistry*, 400(7), 2013–2023.
- Wang, M., Roman, G. T., Perry, M. L., & Kennedy, R. T. (2009). Microfluidic chip for high efficiency electrophoretic analysis of segmented flow from a microdialysis probe and in vivo chemical monitoring. *Analytical Chemistry*, 81(21), 9072–9078.
- Wang, M., Roman, G. T., Schultz, K., Jennings, C., & Kennedy, R. T. (2008). Improved Temporal Resolution for in Vivo Microdialysis by Using Segmented Flow. *Analytical Chemistry*, 80(14), 5607–5615.
- Wang, M., Slaney, T., Mabrouk, O., & Kennedy, R. T. (2010). Collection of nanoliter microdialysate fractions in plugs for off-line in vivo chemical monitoring with up to 2s temporal resolution. *Journal of Neuroscience Methods*, 190(1), 39–48.

- Wassum, K. M. (2017). Voltammetry reveals how mesolimbic dopamine relates to instrumental reward seeking. *Compendium of in vivo monitoring in real-time molecular neuroscience* (pp. 231–248). World Scientific.
- Wells, S. S., & Kennedy, R. T. (2020). High-Throughput Liquid–Liquid Extractions with Nanoliter Volumes. *Analytical Chemistry*, 92(4), 3189–3197.
- Weltin, A., & Kieninger, J. (2021). Electrochemical methods for neural interface electrodes. *Journal of Neural Engineering*, 18(5), 052001.
- Weltman, A., Yoo, J., & Meng, E. (2016). Flexible, Penetrating Brain Probes Enabled by Advances in Polymer Microfabrication. *Micromachines*, 7(10), 180.
- Whitesides, G. M. (2006). The origins and the future of microfluidics. *Nature*, 442(7101), 368–373.
- Wilson, G. S., & Michael, A. C. (2017). *Compendium of In Vivo Monitoring in Real-Time Molecular Neuroscience : Volume 2 - Microdialysis and Sensing of Neural Tissues*. World Scientific.
- Wotjak, C. T., Landgraf, R., & Engelmann, M. (2008). Listening to neuropeptides by microdialysis: Echoes and new sounds? *Pharmacology Biochemistry and Behavior*, 90(2), 125–134.
- Wu, G., Heck, I., Zhang, N., Phaup, G., Zhang, X., Wu, Y., Stalla, D. E., Weng, Z., Sun, H., Li, H., Zhang, Z., Ding, S., Li, D.-P., & Zhang, Y. (2022). Wireless, battery-free push-pull microsystem for membrane-free neurochemical sampling in freely moving animals. *Science Advances*, 8(8), eabn2277.
- Wu, Z., Lin, D., & Li, Y. (2022). Pushing the frontiers: tools for monitoring neurotransmitters and neuromodulators. *Nature Reviews Neuroscience*, 23(5), 257–274.
- Yoshimi, K., Naya, Y., Mitani, N., Kato, T., Inoue, M., Natori, S., Takahashi, T., Weitemier, A., Nishikawa, N., McHugh, T., Einaga, Y., & Kitazawa, S. (2011). Phasic reward responses in the monkey striatum as detected by voltammetry with diamond microelectrodes. *Neuroscience Research*, 71(1), 49–62.
- Zahn, J. D., Trebotich, D., & Liepmann, D. (2005). Microdialysis Microneedles for Continuous Medical Monitoring. *Biomedical Microdevices*, 7(1), 59–69.
- Zanetti, C., Spitz, S., Berger, E., Bolognin, S., Smits, L. M., Crepaz, P., Rothbauer, M., Rosser, J. M., Marchetti-Deschmann, M., Schwamborn, J. C., & Ertl, P. (2021). Monitoring

- the neurotransmitter release of human midbrain organoids using a redox cycling microsensor as a novel tool for personalized Parkinson's disease modelling and drug screening. *Analyst*, 146(7), 2358–2367.
- Zhang, S., Song, Y., Wang, M., Xiao, G., Gao, F., Li, Z., Tao, G., Zhuang, P., Yue, F., Chan, P., & Cai, X. (2018). Real-time simultaneous recording of electrophysiological activities and dopamine overflow in the deep brain nuclei of a non-human primate with Parkinson's disease using nano-based microelectrode arrays. *Microsystems & Nanoengineering*, 4(2017), 17070.
- Zhang, Y., Kim, S., Shi, W., Zhao, Y., Park, I., Brenden, C., Iyer, H., Jha, P., Bashir, R., Sweedler, J. V., & Vlasov, Y. (2022). Droplet-assisted electrospray phase separation using an integrated silicon microfluidic platform. *Lab on a Chip*, 22(1), 40–46.
- Zhang, Y., Jiang, N., & Yetisen, A. K. (2021). Brain neurochemical monitoring. *Biosensors and Bioelectronics*, 189, 113351.
- Zhao, C., Cheung, K. M., Huang, I.-W., Yang, H., Nakatsuka, N., Liu, W., Cao, Y., Man, T., Weiss, P. S., Monbouquette, H. G., & Andrews, A. M. (2021). Implantable aptamer–field-effect transistor neuroprobes for in vivo neurotransmitter monitoring. *Science Advances*, 7(48), 25–27.
- Zhao, L., & Wang, Z. (2019). MicroRNAs: Game Changers in the Regulation of α -Synuclein in Parkinson's Disease. *Parkinson's Disease*, 2019, 1743183.
- Zhu, P., & Wang, L. (2017). Passive and active droplet generation with microfluidics: a review. *Lab Chip*, 17(1), 34–75.
- Zhu, Y., & Fang, Q. (2013). Analytical detection techniques for droplet microfluidics—A review. *Analytica Chimica Acta*, 787, 24–35.
- Zoli, M., Torri, C., Ferrari, R., Jansson, A., Zini, I., Fuxe, K., & Agnati, L. F. (1998). The emergence of the volume transmission concept. *Brain research. Brain research reviews*, 26(2-3), 136–147.

List of publications

Papers included in this thesis

- Leroy, A., Teixidor, J., Bertsch, A., & Renaud, P. (2021). In-flow electrochemical detection of chemicals in droplets with pyrolysed photoresist electrodes: application as a module for quantification of microsampled dopamine. *Lab on a Chip*, 21(17), 3328–3337
- Teixidor, J., Novello, S., Ortiz, D., Menin, L., Lashuel, H. A., & Renaud, P. (2022). On demand nanoliter sampling probe for collection of brain fluid. *BioRxiv*, 1–17
- Teixidor, J., Novello, S., Ortiz, D., Menin, L., Lashuel, H. A., Bertsch, A., & Renaud, P. (2022). On-Demand Nanoliter Sampling Probe for the Collection of Brain Fluid. *Analytical Chemistry*, 94(29), 10415–10426

Conference proceedings

- Teixidor, J., Bertsch, A., & Renaud, P. (2021a). Neural probe to sample brain fluid droplets on demand with high recovery fraction. *25th International Conference on Miniaturized Systems for Chemistry and Life Sciences (μTAS 2021)*, 709–710
- Teixidor, J., Bertsch, A., & Renaud, P. (2021b). Neural probe to sample droplets on demand in vivo and quantify glucose by mass spectrometry. *NanoBioTech Montreux*

Acronyms

ACh	acetylcholine
ACN	acetonitrile
AD	Alzheimer's disease
AFM	atomic force microscope
AGC	automatic gain control
AP	Action Potential
ATP	adenosine triphosphate
BBB	Blood-Brain Barrier
BioMEMS	biological MEMS
CID	collision induced dissociation
CNS	central nervous system
DA	dopamine
DBS	Deep Brain Stimulation
DNA	deoxyribonucleic acids
DoD	Droplet on Demand
ECF	extracellular fluid
EES	Epidural Electrical Stimulation
ESI	electrospray ionization

FACS	fluorescence-activated cell sorting
fMRS	functional magnetic resonance spectroscopy
FSCV	Fast Scan Cyclic Voltammetry
GABA	gamma-aminobutyric acid
Glu	glutamate
ID	Inner diameter
IS	Internal standard
LoD	limit of detection
MEMS	microelectromechanical systems
miRNA	microRNA
mRNA	messenger RNA
nanoESI-FTMS	nanoelectrospray ionization Fourier transform mass spectrometry
nanoESI-MS	nanoelectrospray ionization mass spectrometry
OD	Outer diameter
PBM	photobiomodulation
PBS	Phosphate Buffered Saline
PCR	polymerase chain reaction
PD	Parkinson's disease
PDMS	polydimethylsiloxane
PET	Positron emission tomography
PFD	perfluoro(methyldecalin)
PFOTS	trichloro(1h,1h,2h,2h-perfluorooctyl)silane

PGMEA	Propylene Glycol Monomethyl Ether Acetate
PNS	peripheral nervous system
PR	photoresist
PRF	peak resistance frequency
PRM	Parallel Reaction Monitoring
qPCR	quantitative real-time PCR
REF	pseudo-reference electrode
RNA	ribonucleic acids
SIM	Selected Ion Monitoring
WE	working electrode

Joan Teixidor

PhD in Microsystems and
microelectronics.
EPF qualified Engineer.

Rue Saint-Paul 3
1700 Fribourg, Switzerland
+41 79 275 77 44

joan.teixidor@alumni.epfl.ch
[linkedin.com/in/joanteixidor/](https://www.linkedin.com/in/joanteixidor/)



Expertise in microsystems for
biomedical applications.

Adaptable to multidisciplinary
projects and with team management
abilities.

New experiences help me grow and
in exchange, I do my best to bring
them to the next level.

PROFESSIONAL EXPERIENCE

Doctoral assistant, École Polytechnique Fédérale de Lausanne (EPFL), Lausanne, Switzerland	2017 -2022
PhD project on the development of a new method to sample and measure chemicals in the brain, for more accurate quantitative molecular studies <i>in vivo</i> . Work achieved in the Laboratory for Microsystems 4 led by Prof. Philippe Renaud.	
<ul style="list-style-type: none">• Multidisciplinary project in microtechnology (probe fabrication, electronics, and microfluidics), life sciences (<i>in vivo</i> studies with mice), and analytical chemistry.• Side-project on porous silicon microcantilevers functionalized with peptides for detection of explosives in gas phase.• Design and supervision of 6 students projects (from 20% to 100% over 6 months).• In charge of 2 practicals for classes MEMS practicals I and II (MSc cycle): development of electrothermal microactuators, characterization of electrochemical glucose sensors.	
Research Intern, Institute of Supramolecular Science and Engineering, Strasbourg, France	2016 (6 mo)
Introduction of microfluidic know-how in the laboratory of nanostructures. Acquisition of nanofabrication skills and characterization techniques for plasmonic nanostructures (surface plasmon resonance arrays and Fabry-Pérot cavities).	
R&D Intern, Lunaphore Technologies SA, Ecublens, Switzerland	2015 (6 mo)
Development of the control electronics, the software, and a user-friendly interface to produce functional microfluidic systems for breast cancer diagnostic, for research and clinical settings.	
Scheduler in logistics, Richemont International Distribution, Villars-sur-Glâne, Switzerland	2010 -2014 (2 mo/y)
Manage the packing workload of a jewelry distribution center. Bilateral interactions with worldwide customers and suppliers for urgent matters. New employee training in 2014.	

SKILLS

Engineering	Control and design of microfluidic systems, Microfabrication technologies (BioMEMS, clean room), Analog and digital electronics, Sensor characterization, Mechatronics.
Biomedical technologies	Mammalian cell culture, Electrochemistry, Fluorescence microscopy, miRNA assays, Mass spectrometry on biological samples (nanoESI-FTMS, MALDI-TOF).
Informatics	C, C++, MATLAB, Assembly language, Python, LabVIEW, VBA, CAD Design (PTC Creo, AutoCAD, Inventor), COMSOL Multiphysics, Adobe Illustrator, Adobe Premiere Pro, Adobe After Effects, Microsoft Office, ImageJ, SAP.
Certifications	PRINCE2 Foundation (project management, 2021), RESAL module 1 (<i>in vivo</i> experimentation with rodents, 2019), Management of Innovation and Technology Transfer (EPFL Technology Transfer Office, 2020).
Soft skills	Active listening, teamwork, mediation, creative problem-solving, critical thinking.

LANGUAGES

French: native.	German: B2-C1.	Spanish: A2 oral and reading,
English: C1-C2.	Swiss-German: oral understanding.	A1 writing.

AWARDS AND SCHOLARSHIPS

Scholarship of the American Alumni Association of the Swiss Federal Institutes of Technology (A3SFIT) , received as funding for the MSc thesis at Stanford University (3 scholarships/year).	2015
Vincent Merkle Foundation Scholarship for MSc thesis at Stanford University.	2015
Debiopharm Excellence Scholarships awarded for outstanding academic results during BSc and renewed for MSc in 2014 (3 scholarships per year).	2013 -2015
Highschool excellence awards for best grades of the promotion and best French dissertation.	2010

EDUCATION

PhD in Microsystems and Microelectronics, EPFL, Lausanne, Switzerland	2017
<ul style="list-style-type: none">Publications in scientific journals and conferences, seminars in laboratories at Stanford, UC Berkeley, UC Santa Barbara, UC Los Angeles.	-2022
MSc in Microengineering, EPFL, Lausanne, Switzerland	2013
<ul style="list-style-type: none">Master thesis at Stanford University, USA, 2015-2016: organ-on-chip system for co-culture of epithelial cells to study mechanobiology of the gut.Major in Micro- and nanosystems, minor in biomedical technologies.Average grade of 5.81/6.	-2016
BSc in Microengineering, EPFL, Lausanne	2010
<ul style="list-style-type: none">Average grade of 5.48/6.	-2013

SCIENTIFIC PUBLICATIONS

-
- Teixidor, J., Novello, S., Ortiz, D., Menin, L., Lashuel, H. A., & Renaud, P. (2022). *On-Demand Nanoliter Sampling Probe for the Collection of Brain Fluid*. *Anal. Chem.*, 94(29), 10415-10426.
 - Teixidor, J., Bertsch, A., & Renaud, P. (2021). *Neural probe to sample droplets on demand in vivo and quantify glucose by mass spectrometry*. NanoBioTech-Montreux Conference.
 - Teixidor, J., Bertsch, A., & Renaud, P. (2021). *Neural probe to sample brain fluid droplets on demand with high recovery fraction*. 25th International Conference on Miniaturized Systems for Chemistry and Life Sciences (μTAS 2021), 709-710.
 - Leroy, A., Teixidor, J., Bertsch, A., & Renaud, P. (2021). *In-flow electrochemical detection of chemicals in droplets with pyrolysed photoresist electrodes: application as a module for quantification of microsampled dopamine*. *Lab on a Chip*, 21(17), 3328-3337.
 - Michaud, H. O., Teixidor, J., & Lacour, S. P. (2015). *Soft metal constructs for large strain sensor membrane*. *Smart Materials and Structures*, 24(3), 035020.
 - Michaud, H. O., Teixidor, J., & Lacour, S. P. (2015). *Soft flexion sensors integrating stretchable metal conductors on a silicone substrate for smart glove applications*. 2015 28th IEEE International Conference on Micro Electromechanical Systems (MEMS), 760-763.
 - Dupouy, D. G., Ciftlik, A. T., Teixidor, J., & Gijs, M. A. M. (2014). *Programming and use of Parylene C fluorescence as a quantitative on-chip reference*. *RSC Adv.*, 4(90), 49367-49373.

PERSONAL INTERESTS

-
- Swiss and Spanish, 31 years old.
 - Football for 25 years (many years as team captain and substitute coach). I'm a team player and in parallel, I also started road bike cycling 5 years ago.
 - Adventurous and curious, I also love to exchange experiences and acquire new points of view.
 - I like cooking, from daily meals to chef recipes, with humor as favorite spice. Cat person.